University of Alberta

Inverse Design Of Airfoil Thickness Distributions In Incompressible Flow

by

Lance Owen Portas

A thesis submitted to the Faculty of Graduate Studies and Research in partial fulfillment of the requirements for the degree of Master of Science.

Department of Mechanical Engineering

Edmonton, Alberta
Fall 2000

National Library of Canada
Acquisitions and Bibliographic Services
395 Wellington Street
Ottawa ON K1A 0N4
Canada

Bibliothèque nationale du Canada
Acquisitions et services bibliographiques
395, rue Wellington
Ottawa ON K1A 0N4
Canada

Your file Votre référence

Our file Notre référence

The author has granted a non-exclusive licence allowing the National Library of Canada to reproduce, loan, distribute or sell copies of this thesis in microform, paper or electronic formats.

L'auteur a accordé une licence non exclusive permettant à la Bibliothèque nationale du Canada de reproduire, prêter, distribuer ou vendre des copies de cette thèse sous la forme de microfiche/film, de reproduction sur papier ou sur format électronique.

The author retains ownership of the copyright in this thesis. Neither the thesis nor substantial extracts from it may be printed or otherwise reproduced without the author's permission.

L'auteur conserve la propriété du droit d'auteur qui protège cette thèse. Ni la thèse ni des extraits substantiels de celle-ci ne doivent être imprimés ou autrement reproduits sans son autorisation.

0-612-59866-7

Canada

University of Alberta

Library Release Form

Name of Author: Lance Owen Portas

Title of Thesis: Inverse Design Of Airfoil Thickness Distributions In Incompressible Flow

Degree: Master of Science

Year this Degree Granted: 2000

Permission is hereby granted to the University of Alberta to reproduce single copies of this thesis and to lend or sell such copies for private, scholarly, or scientific research purposes only.

The author reserves all other publication and other rights in association with the copyright in the thesis, and except as hereinbefore provided, neither the thesis nor any substantial portion thereof may be printed or otherwise reproduced in any material form whatever without the author's prior written permission.

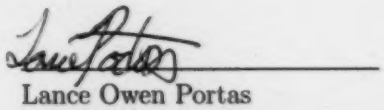

Lance Owen Portas
12 Greenridge Drive
Sherwood Park, Alberta
CANADA, T8A 5G1

Sept 13th/2000

There is no strife, no prejudice, no national conflict in outer space as yet. Its hazards are hostile to us all. Its conquest deserves the best of all mankind, and its opportunity for peaceful cooperation may never come again. But why, some say, the moon? Why choose this as our goal? And they may well ask why climb the highest mountain? Why 35 years ago, fly the Atlantic? Why does Rice play Texas?

We choose to go to the moon. We choose to go to the moon in this decade and do the other things, not because they are easy, but because they are hard, because that goal will serve to organize and measure the best of our energies and skills, because that challenge is one that we are willing to accept, one we are unwilling to postpone, and one which we intend to win, and the others too.

—John F. Kennedy – September 12, 1962

Abstract

An inverse method for designing incompressible airfoil thickness distributions has been developed. This technique is based on an implicit LU approximate factorization that uses specified surface velocities to calculate both the airfoil's thickness distribution and camber line.

Through the analysis of several groups of airfoils, a distinct relationship between thickness distribution, camber line and surface velocities has been discovered. The analysis of various airfoils proves that thickness distributions can be designed by specifying a single pair of surface velocities while camber lines can be designed by specifying a second, separate pair of surface velocities.

A surface velocity recreation technique has also been developed. The technique allows the surface velocities from the analysis of an entire group of airfoils to be recreated with a set of linear equations that are controlled by a single variable. The technique allows the designer to define the interior design space encompassed by a group of existing airfoil geometries. The designer can then use the combined influence of the existing airfoils to calculate a new airfoil geometry.

University of Alberta

Faculty of Graduate Studies and Research

The undersigned certify that they have read, and recommend to the Faculty of Graduate Studies and Research for acceptance, a thesis entitled Inverse Design Of Airfoil Thickness Distributions In Incompressible Flow submitted by Lance Owen Portas in partial fulfillment of the requirements for the degree of Master of Science.

Dr. J. Yokota (Supervisor)

Dr. Y.S. Wong

Dr. R. Toogood

Date Sept 12, 2000

To My Parents

Acknowledgements

I would like to express my sincerest thanks to my supervisor, Dr. Jeffrey W. Yokota. This work is based on a numerical method that he had already developed, and his knowledge and support was indispensable. I have learned enumerable lessons from Jeff, and hope to be able to apply all of the knowledge and experience he shared with me in my future work. I would like to thank Jeff for being my advisor, mentor and friend.

Thank you to my family, especially my parents and my sister, for their support over the years. They have provided more than enough encouragement and motivation, and have always been interested in the work that I have done. I am sure that without them, this endeavour would have proven insurmountable.

My colleagues from the CFDAM lab must be thanked for their interest and support as well. I have been lucky enough to have worked with several people throughout my graduate studies and I am grateful for the time I have spent with Seifu Bekele, Adam Medd, Chris Reaume, and Kevin Reid, and more recently Marty Lastiwka and Scott Bachand. I am thankful for the professional relationships I have formed with these men, as well as the friendships.

I would like to thank Dr. Roger Toogood and Dr. Yau Shu Wong for participating in my Oral Exam as committee members. I would also like to thank Dr. Lorenz Sigurdson for being the committee Chair and for all his help over the years.

CONTENTS

1 Introduction **1**

2 Characteristic Velocity Determination **9**
2.1 NACA 4-Digit Airfoils 10
2.2 NACA 5-Digit 16-Series Airfoils 58
2.3 NACA 4-Digit-Modified Airfoils 75
2.4 General Airfoils 92

3 Governing Equations **109**
3.1 Continuity Equation 109
3.2 Lamellar Decomposition 111
3.3 Dimensional Analysis 112
3.4 Generalized Coordinate System 113

4 Numerical Methods **117**
4.1 Approximate LU Factorization 118
4.2 Residual Construction (Analysis) 121
4.3 Numerical Stability of the LU Scheme 124
4.4 Multigrid Acceleration 130
4.5 Boundary And Initial Conditions For Analysis Of Airfoils . . 133
4.5.1 Periodic Boundary 133
4.5.2 Solid Boundary 134
4.5.3 Inflow Boundary 136
4.5.4 Outflow Boundary 137
4.5.5 Initial Condition 139
4.6 Sequence of Solution (Analysis) 139
4.7 Domain of Problem 140

5 Inverse Design Methods **142**
5.1 Input Velocity Specification 142
5.1.1 Bezier Curves 143
5.1.2 Velocity Recreation Technique 147
5.2 Residual Calculation (Design) 172
5.3 Geometry Calculation 173
5.4 Boundary And Initial Conditions For Design Of Airfoils 176
5.5 Sequence Of Solution (Design) 177

6 Results **180**
6.1 NACA 4-Digit Airfoils 180
6.1.1 NACA 3410 Airfoil 181
6.1.2 NACA 3406 Airfoil 187
6.1.3 NACA 3414 Airfoil 192
6.1.4 NACA 4-Digit Airfoil Design Space 198
6.2 NACA 4-Digit-Modified Airfoils 206
6.2.1 NACA 3410-44 Airfoil 206
6.2.2 NACA 3406-42 Airfoil 211
6.2.3 NACA 3414-46 Airfoil 217
6.2.4 NACA 4-Digit-Modified Airfoil Design Space 223
6.3 General Airfoils 231
6.3.1 GEN03 Airfoil 231
6.3.2 GEN01 Airfoil 236
6.3.3 GEN05 Airfoil 241
6.3.4 General Airfoil Design Space 247
6.4 Direct Calculation Of Geometry 255

7 Conclusions **259**

List of Figures

1.1 Airfoil Shape 1
1.2 Turbomachinery Blade Shape 2
1.3 Airfoil Components 5

2.1 NACA 3410 Airfoil 14
2.2 Thickness Distributions Of NACA 4-Digit Airfoils 15
2.3 u^+ Velocities Of NACA 4-Digit Airfoils 16
2.4 Difference In u^+ Velocities Of NACA 4-Digit Airfoils 18
2.5 u^- Velocities Of NACA 4-Digit Airfoils 19
2.6 Difference In u^- Velocities Of NACA 4-Digit Airfoils 20
2.7 v^+ Velocities Of NACA 4-Digit Airfoils 22
2.8 Difference In v^+ Velocities Of NACA 4-Digit Airfoils 23
2.9 v^- Velocities Of NACA 4-Digit Airfoils 25
2.10 Difference In v^- Velocities Of NACA 4-Digit Airfoils 27
2.11 $\bar{u}$ Velocities Of NACA 4-Digit Airfoils 29
2.12 Difference In $\bar{u}$ Velocities Of NACA 4-Digit Airfoils 30
2.13 Δu Velocities Of NACA 4-Digit Airfoils 32
2.14 Difference In Δu Velocities Of NACA 4-Digit Airfoils 33
2.15 $\bar{v}$ Velocities Of NACA 4-Digit Airfoils 36
2.16 Difference In $\bar{v}$ Velocities Of NACA 4-Digit Airfoils 37
2.17 Δv Velocities Of NACA 4-Digit Airfoils 39
2.18 Difference In Δv Velocities Of NACA 4-Digit Airfoils 41
2.19 Camber Lines of NACA 4-Digit Airfoils 43
2.20 $\bar{u}$ Velocities Of NACA 4-Digit Airfoils With Changing Camber Lines 45
2.21 Difference In $\bar{u}$ Velocities Of NACA 4-Digit Airfoils With Changing Camber Lines 46
2.22 Δu Velocities Of NACA 4-Digit Airfoils With Changing Camber Lines 48

2.23 Difference In Δu Velocities Of NACA 4-Digit Airfoils With Changing Camber Lines 49
2.24 $\bar{v}$ Velocities Of NACA 4-Digit Airfoils With Changing Camber Lines 51
2.25 Difference In $\bar{v}$ Velocities Of NACA 4-Digit Airfoils With Changing Camber Lines 52
2.26 Δv Velocities Of NACA 4-Digit Airfoils With Changing Camber Lines 54
2.27 Difference In Δv Velocities Of NACA 4-Digit Airfoils With Changing Camber Lines 55
2.28 NACA 16-310 Airfoil 60
2.29 Thickness Distributions Of NACA 5-Digit 16-Series Airfoils . 61
2.30 $\bar{u}$ Velocities Of NACA 5-Digit 16-Series Airfoils 62
2.31 Difference In $\bar{u}$ Velocities Of NACA 5-Digit 16-Series Airfoils 64
2.32 Δu Velocities Of NACA 5-Digit 16-Series Airfoils 65
2.33 Difference In Δu Velocities Of NACA 5-Digit 16-Series Airfoils 67
2.34 $\bar{v}$ Velocities Of NACA 5-Digit 16-Series Airfoils 69
2.35 Difference In $\bar{v}$ Velocities Of NACA 5-Digit 16-Series Airfoils 70
2.36 Δv Velocities Of NACA 5-Digit 16-Series Airfoils 73
2.37 Difference In Δv Velocities Of NACA 5-Digit 16-Series Airfoils 74
2.38 NACA 3410-44 Airfoil 77
2.39 Thickness Distributions Of NACA 4-Digit-Modified Airfoils . 78
2.40 $\bar{u}$ Velocities Of NACA 4-Digit-Modified Airfoils 79
2.41 Difference In $\bar{u}$ Velocities Of NACA 4-Digit-Modified Airfoils 81
2.42 Δu Velocities Of NACA 4-Digit-Modified Airfoils 82
2.43 Difference In Δu Velocities Of NACA 4-Digit-Modified Airfoils 83
2.44 $\bar{v}$ Velocities Of NACA 4-Digit-Modified Airfoils 86
2.45 Difference In $\bar{v}$ Velocities Of NACA 4-Digit-Modified Airfoils 87
2.46 Δv Velocities Of NACA 4-Digit-Modified Airfoils 89
2.47 Difference In Δv Velocities Of NACA 4-Digit-Modified Airfoils 90
2.48 Thickness Distributions Of General Airfoils 93
2.49 $\bar{u}$ Velocities Of General Airfoils 95
2.50 Difference In $\bar{u}$ Velocities Of General Airfoils 96
2.51 Δu Velocities Of General Airfoils 98
2.52 Difference In Δu Velocities Of General Airfoils 99
2.53 $\bar{v}$ Velocities Of General Airfoils 101
2.54 Difference In $\bar{v}$ Velocities Of General Airfoils 103
2.55 Δv Velocities Of General Airfoils 105

2.56 Difference In Δv Velocities Of General Airfoils 106

3.1 Grid Transformation 114

4.1 Flux Calculation 123
4.2 Growth Factor 129
4.3 Multigrid Grid Refinement 130
4.4 5-Level 6-Cycle 'W' Multigrid Scheme 133
4.5a Periodic Boundary Condition Of The Potential Field 134
4.5b Periodic Boundary Condition - Cont'd 135
4.6 Solid Boundary Condition 136
4.7 Typical Solution Mesh 141

5.1 Cubic Bezier Curve 145
5.2 Bezier Control Polygon Of NACA 3406 $\bar{u}$ Velocity 150
5.3 Bezier Control Polygon Of NACA 3410 $\bar{u}$ Velocity 151
5.4 Bezier Control Polygon Of NACA 3414 $\bar{u}$ Velocity 152
5.5 Bezier Recreation Of NACA 3410 $\bar{u}$ Velocity 158
5.6 Bezier Control Polygon Of NACA 3406 Δv Velocity 162
5.7 Bezier Control Polygon Of NACA 3410 Δv Velocity 163
5.8 Bezier Control Polygon Of NACA 3414 Δv Velocity 164
5.9 Bezier Recreation Of Δv Velocity 170

6.1 Original And Inversely Designed NACA 3410 Thickness Distributions 181
6.2a Difference In Original And Inversely Designed NACA 3410 Thickness Distributions 183
6.2b Difference In Analysis And Trended Inversely Designed NACA 3410 Thickness Distributions 183
6.3 Original And Inversely Designed NACA 3410 Camber Lines . 184
6.4a Difference In Original And Inversely Designed NACA 3410 Camber Lines 186
6.4b Difference In Analysis And Trended Inversely Designed NACA 3410 Camber Lines 186
6.5 Original And Inversely Designed NACA 3406 Thickness Distributions 188
6.6a Difference In Original And Inversely Designed NACA 3406 Thickness Distributions 189

6.6b Difference In Analysis And Trended Inversely Designed NACA 3406 Thickness Distributions 189
6.7 Original And Inversely Designed NACA 3406 Camber Lines . 190
6.8a Difference Of Original And Inversely Designed NACA 3406 Camber Lines 191
6.8b Difference Of Analysis And Trended Inversely Designed NACA 3406 Camber Lines 191
6.9 Original And Inversely Designed NACA 3414 Thickness Distributions 192
6.10a Difference Of Original And Inversely Designed NACA 3414 Thickness Distributions 194
6.10b Difference Of Analysis And Trended Inversely Designed NACA 3414 Thickness Distributions 194
6.11 Original And Inversely Designed NACA 3414 Camber Lines . 195
6.12a Difference In Original And Inversely Designed NACA 3414 Camber Lines 197
6.12b Difference In Analysis And Trended Inversely Designed NACA 3414 Camber Lines 197
6.13a Inversely Designed NACA 4-Digit Thickness Distributions - Decreasing Thickness Specification 199
6.13b Difference Of Inversely Designed NACA 4-Digit Thickness Distributions - Decreasing Thickness Specification 199
6.14a Inversely Designed NACA 4-Digit Camber Lines - Decreasing Thickness Specification 201
6.14b Difference Of Inversely Designed NACA 4-Digit Camber Lines - Decreasing Thickness Specification 201
6.15a Inversely Designed NACA 4-Digit Thickness Distributions - Increasing Thickness Specification 203
6.15b Difference Of Inversely Designed NACA 4-Digit Thickness Distributions - Increasing Thickness Specification 203
6.16a Inversely Designed NACA 4-Digit Camber Lines - Increasing Thickness Specification 205
6.16b Difference Of Inversely Designed NACA 4-Digit Camber Lines - Increasing Thickness Specification 205
6.17 Original And Inversely Designed NACA 3410-44 Thickness Distributions 207
6.18a Difference Of Original And Inversely Designed NACA 3410-44 Thickness Distributions 208

6.18b Difference Of Analysis And Trended Inversely Designed NACA 3410-44 Thickness Distributions 208
6.19 Original And Inversely Designed NACA 3410-44 Camber Lines 209
6.20a Difference In Original And Inversely Designed NACA 3410-44 Camber Lines 210
6.20b Difference In Analysis And Trended Inversely Designed NACA 3410-44 Camber Lines 210
6.21 Original And Inversely Designed NACA 3406-42 Thickness Distributions 211
6.22a Difference Of Original And Inversely Designed NACA 3406-42 Thickness Distributions 213
6.22b Difference Of Analysis And Trended Inversely Designed NACA 3406-42 Thickness Distributions 213
6.23 Original And Inversely Designed NACA 3406-42 Camber Lines 214
6.24a Difference In Original And Inversely Designed NACA 3406-42 Camber Lines 216
6.24b Difference In Analysis And Trended Inversely Designed NACA 3406-42 Camber Lines 216
6.25 Original And Inversely Designed NACA 3414-46 Thickness Distributions 217
6.26a Difference Of Original And Inversely Designed NACA 3414-46 Thickness Distributions 219
6.26b Difference Of Analysis And Trended Inversely Designed NACA 3414-46 Thickness Distributions 219
6.27 Original And Inversely Designed NACA 3414-46 Camber Lines 220
6.28a Difference In Original And Inversely Designed NACA 3414-46 Camber Lines 222
6.28b Difference In Analysis And Trended Inversely Designed NACA 3414-46 Camber Lines 222
6.29a Inversely Designed NACA 4-Digit-Modified Thickness Distributions - Decreasing Thickness Specification 224
6.29b Difference Of Inversely Designed NACA 4-Digit-Modified Thickness Distributions - Decreasing Thickness Specification . . . 224
6.30a Inversely Designed NACA 4-Digit-Modified Camber Lines - Decreasing Thickness Specification 226
6.30b Difference Of Inversely Designed NACA 4-Digit-Modified Camber Lines - Decreasing Thickness Specification 226

6.31a Inversely Designed NACA 4-Digit-Modified Thickness Distributions - Increasing Thickness Specification 228
6.31b Difference Of Inversely Designed NACA 4-Digit-Modified Thickness Distributions - Increasing Thickness Specification 228
6.32a Inversely Designed NACA 4-Digit-Modified Camber Lines - Increasing Thickness Specification 230
6.32b Difference Of Inversely Designed NACA 4-Digit-Modified Camber Lines - Increasing Thickness Specification 230
6.33 Original And Inversely Designed GEN03 Thickness Distributions 232
6.34a Difference Of Original And Inversely Designed GEN03 Thickness Distributions 233
6.34b Difference Of Analysis And Trended Inversely Designed GEN03 Thickness Distributions 233
6.35 Original And Inversely Designed GEN03 Camber Lines . . . 234
6.36a Difference In Original And Inversely Designed GEN03 Camber Lines 235
6.36b Difference In Analysis And Trended Inversely Designed GEN03 Camber Lines 235
6.37 Original And Inversely Designed GEN01 Thickness Distributions 236
6.38a Difference Of Original And Inversely Designed GEN01 Thickness Distributions 238
6.38b Difference Of Analysis And Trended Inversely Designed GEN01 Thickness Distributions 238
6.39 Original And Inversely Designed GEN01 Camber Lines . . . 239
6.40a Difference In Original And Inversely Designed GEN01 Camber Lines 240
6.40b Difference In Analysis And Trended Inversely Designed GEN01 Camber Lines 240
6.41 Original And Inversely Designed GEN05 Thickness Distributions 241
6.42a Difference Of Original And Inversely Designed GEN05 Thickness Distributions 243
6.42b Difference Of Analysis And Trended Inversely Designed GEN05 Thickness Distributions 243
6.43 Original And Inversely Designed GEN05 Camber Lines . . . 244

6.44a Difference In Original And Inversely Designed GEN05 Camber Lines 246
6.44b Difference In Analysis And Trended Inversely Designed GEN05 Camber Lines 246
6.45a Inversely Designed General Airfoil Thickness Distributions - Decreasing Thickness Specification 248
6.45b Difference Of Inversely Designed General Airfoil Thickness Distributions - Decreasing Thickness Specification 248
6.46a Inversely Designed General Airfoil Camber Lines - Decreasing Thickness Specification 250
6.46b Difference Of Inversely Designed General Airfoil Camber Lines - Decreasing Thickness Specification 250
6.47a Inversely Designed General Airfoil Thickness Distributions - Increasing Thickness Specification 252
6.47b Difference Of Inversely Designed General Airfoil Thickness Distributions - Increasing Thickness Specification 252
6.48a Inversely Designed General Airfoil Camber Lines - Increasing Thickness Specification 254
6.48b Difference Of Inversely Designed General Airfoil Camber Lines - Increasing Thickness Specification 254
6.49a Original And Inversely Designed Thickness Distributions From Two Calculation Methods 256
6.49b Difference In Original And Inversely Designed Thickness Distributions From Two Calculation Methods 256
6.50a Original And Inversely Designed Camber Lines From Two Calculation Methods 258
6.50b Difference In Original And Inversely Designed Camber Lines From Two Calculation Methods 258

List of Tables

2.1 NACA 4-Digit-Modified TE Slopes 76

4.1 Growth Factor Cases 127

5.1 Chordwise Location Of $\bar{u}$ Bezier Control Points 153
5.2 Velocity Magnitude Of $\bar{u}$ Bezier Control Points 153
5.3 $\bar{u}$ Velocity Bezier Control Points 156
5.4 Chordwise Location Of Δv Bezier Control Points 165
5.5 Vertical Location Of Δv Bezier Control Points 165
5.6 Δv Velocity Bezier Control Points 168

NOMENCLATURE

LATIN SYMBOLS

c ..... Chord Length

f, g ..... Residual Flux Components

f_{cl} ..... Calculated Camber Line

f_{th} ..... Calculated Thickness Distribution

FF ..... Multigrid Forcing Function

G ..... Growth Factor

I ..... Identity Matrix

$\tilde{I}$ ..... Multigrid Interpolation Operator

J ..... Jacobian Transfer Matrix

L ..... Lower Diagonal Operator

$\hat{n}$ ..... Surface Normal

N ..... Time Level

R ..... LU Scheme Residual Operator

Res ..... LU Residual

S ..... Control Surface

Δt ..... Timestep

T ..... Multigrid Solution Transfer Operator

$\tilde{T}$ ..... Multigrid Residual Transfer Operator

(u, v) ..... Cartesian Velocity Components

(u^+, v^+) ..... Upper Surface Velocities

(u^-, v^-) ..... Lower Surface Velocities

(U, V) ..... Transformed Velocity Components

U ..... Upper Diagonal Operator

U_∞ ..... Free Stream Velocity

$\forall$ ..... Control Volume

$\vec{V}$ ..... Velocity Field (2-D)

w ..... Relaxation Factor

W ..... Approximate Function

(x, y) ..... Cartesian Coordinates

Δx ..... Grid Spacing

GREEK SYMBOLS

α^* ..... Exponential Time Constant

β ..... Wave Number

δ ..... Finite Difference Operator; δ_i^+ forward, δ_i^- backward, δ_{ii} central

μ ..... Implicit Parameter

(ξ, η) ..... General Curvilinear Coordinates

ρ ..... Density

σ ..... Airfoil Surface Function

τ ..... Thickness Specification

ϕ ..... Irrotational Potential

ψ ..... Viscous Streamfunction Correction

CHAPTER 1

INTRODUCTION

In the study of aerodynamics, two general shapes exist. These two shapes are the airfoil and the turbomachinery blade. Airfoils or wing sections are used to generate lift. Turbomachinery blades are used to either extract energy (turbine) from or add energy (compressor) to a fluid. A generic airfoil shape can be seen in Figure 1.1. The two important characteristics of this aerodynamic shape are the lift and the drag. Figure 1.2 shows a turbomachinery blade. The enhanced curvature of the blade shape determines the amount of turning, and therefore the amount of energy transferred. This turning, as well as the drag induced by the blade, are the two important characteristics of a turbomachinery blade.

Figure 1.1: Airfoil Shape

Originally, airfoil shapes were designed graphically, using aesthetics to determine the final shape. The use of early wind tunnels allowed the designers of basic airfoil forms such as the Göttingen [1], [2] and Clark-Y [1] airfoils. These basic forms were modified by hand, and the different characteristics that matched the modifications were recorded. This method of design created a broad range of airfoils, but limited the ability to redesign. If an aerodynamicist needed a specific lift, pressure distribution or velocity profile then they would need to go through the recorded distributions or profiles until they found an airfoil that matched. Then, the airfoil that matched the closest would need to be adjusted by hand and retested until the exact criteria were met.

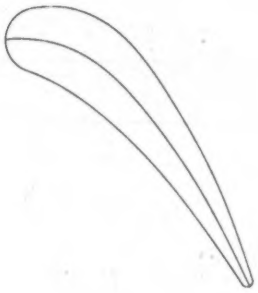

Figure 1.2: Turbomachinery Blade Shape

There are three widely used approaches towards aerodynamic design. These three approaches are experimental analysis, computational analysis and inverse design. The first approach involves the experimental analysis on an aerodynamic shape. One example of this would be testing an airfoil section in a wind tunnel [1]-[4]. This approach relies on the ability of

the designer to use past experience in the development of the final shape. The design process can involve physical modification of the airfoil and experimental determination of the aerodynamic characteristics. The designer needs to continue modifying the test section and running experiments until the required conditions such as a specific lift or drag profile are met.

The second approach to aerodynamic design, computational analysis, is similar to the first, in that it also involves analysis on an existing shape. This approach differs from experimental analysis in that instead of experimentally determining the aerodynamic characteristics, they are found computationally [5]-[7]. The computer analysis can determine characteristics such as drag, lift, and pressure distributions. This approach is less costly as it does not require any large experimental apparatus, but it still requires a designer with the knowledge and experience to modify the airfoil until the final design criteria are met.

The third approach to aerodynamic design is the use of a computational inverse design technique [8]-[17]. Inverse design is typically completed using computational methods, but some analytical methods exist. Instead of a designer analyzing the blade or airfoil and making changes to the geometry, with inverse design the designer specifies some aerodynamic performance criteria and then obtains the physical geometry needed to produce the specific criteria. Inverse design techniques can use various controls, such as pressure, velocity, lift, drag or turning profiles.

Perhaps the most difficult part of redesigning or optimizing an airfoil is the adjustment process. Since the airfoil geometries are often based simply on aesthetics it becomes difficult to control the aerodynamic performance.

Designers need a more precise concept to describe the aerodynamic shape in order to modify airfoil geometry. Redesign requires a more precise description of the airfoil in order to determine which geometric changes benefit or impair aerodynamic performance. One such description involves the use of camber and thickness distributions [1],[2].

Any basic aerodynamic shape is made up of two components. These two components, the camber or "mean" line and the thickness distribution, define the total shape. Figure 1.3 shows a basic airfoil shape, with the camber line line, chord line and thickness indicated. The chord line is a straight line that extends from the leading edge (front) to the trailing edge (back) of the airfoil. The camber is defined as the vertical distance from the chord line to the mean line. The thickness is the vertical distance from upper surface to the lower surface of the aerodynamic shape. Thickness and camber are generally specified as ratios dependent on the chord length. An airfoil with a 10% thickness ratio has a maximum thickness equal to one tenth of the overall chord length. These two components are present in both the turbomachinery blade and the airfoil.

The thickness and camber can be used to design aerodynamic shapes for specific purposes. The camber is used to determine whether the shape forms an airfoil (relatively low camber) or a turbomachinery blade (relatively high camber). The camber line is associated with the amount of lift in airfoils[2],[18]. The camber of an airfoil causes the air flowing past the airfoil to accelerate different amounts. The flow on the outside of the curved camber accelerates more than the flow on the inside, creating a velocity differential. Using Bernoulli's Theorem [19] it can be shown that the two different veloc-

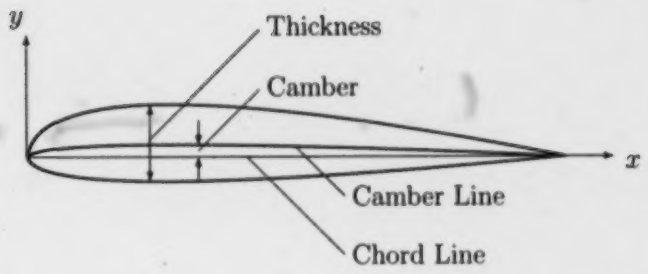

Figure 1.3: Airfoil Components

ities create two different pressures, a higher pressure on the bottom of the airfoil, and a lower pressure on the top. This pressure difference results in the lift of the airfoil. The camber also dictates the amount of turning in turbomachinery blades [2],[18],[20]. The angle of the flow meeting the blade matches the angle of the mean line at the leading edge, and the angle of the flow leaving the blade matches the angle of the mean line at the trailing edge. The higher the camber is, the larger the difference between these two angles, and the greater the amount of turning. Designing for camber is important to determine the performance of inviscid phenomena such as lift and turning.

Thickness is associated with the drag caused by the aerodynamic body [1] as well as other viscous effects [2] such as boundary layer separation, choking and shocking. An airfoil with a thickness that is too large can cause high drag lessening the efficiency of the airfoil [1]. Strong curvature in the geometry of the airfoil or blade can cause strong pressure gradients. If the

pressure gradient is adverse, the boundary layer attached to the airfoil or blade will separate [2]. Separation drops both lift and flow turning. For a turbomachinery blade the thickness prescribed may cause choking to occur [23]. The choking can be caused by the thickness distribution alone being too large for the passage, causing the flow to go sonic or the the combination of the thickness and the boundary layer may cause excessive blockage and choked flow. Choking lowers the efficiency of the turbomachinery. The thickness distribution can also cause shocks to form within the turbomachinery. The passage can be small enough that the flow goes supersonic between the blades, then once the blade is passed, the passage opens up, and the flow must shock in order to slow down. The shrinking of the passage can be cause by thickness distributions alone, or a combination of airfoil thickness and boundary layer blockage. Shocks occurring inside turbomachinery create strong energy losses [23]. Designing for thickness is important to determine the performance of viscous phenomena such as drag, separation, choking and shocking. Therefore both the camber and thickness distributions must be given equal consideration in determining a final design.

One inverse design technique, devised by Selig and Maughmer [10], uses velocity distributions to determine airfoil shapes based on conformal mapping methods. However, the use of conformal mapping only allows for the solution of surface characteristics along with the designed airfoil, not an entire flow field. A flow field solution is required to later determine the viscous effects and viscous performance of the airfoil or blade. The lack of a flow field also occurs with Eppler's [17] inverse design, which is also based on conformal mapping. While both of these methods are direct-inverse methods, meaning

that the entire airfoil surface is determined from the inverse design, they still lack a flow field solution, and therefore cannot be used as a precursor to viscous analysis. Another type of design is the use of an inverse panel method, such as the one described by Gopalarathnam and Selig [14]. This method also uses velocity distributions to determine the designed shape, but since it is a panel method, only the surface velocities are computed along with the airfoil shape, not the entire flow field. Again, the flow field is required to begin any sort of calculation of viscous performance, so methods without flow fields are undesirable.

The technique devised by Obayashi et al. [13] allows for the solution of the flow field and requires a pressure distribution around the airfoil as a control. This method also optimizes the airfoil for a minimum drag coefficient as the flow field is calculated but requires a specified thickness distribution to work. Since the thickness is specified, the method only designs for camber, not the entire airfoil shape. The limitation of this method is that the prescribed thickness distribution may be ill-suited to the design scenario. The generic thickness that is prescribed may be too thick, causing high drag, or it may have strong geometric curvatures, causing boundary layer separation. The thickness needs to be calculated as part of the design. Traditional examples of designing the camber while neglecting or prescribing the thickness include the use of lifting line theory [21] and thin airfoil theory [21]. Another example of designing for camber only is the circulation method devised by Dang [15]. In this case, a pressure loading distribution is used to design infinitely thin cascaded blades. This is an example of neglecting the effects of thickness, thus limiting the practical application of the design as the thickness will de-

termine whether or not the flow of the designed blade will choke within the passage or cause shocks to form. Another method developed by Dang [16] uses pressure loading and the Euler Turbomachinery Equations [23] to design turbomachinery blades. In this particular method, the thickness distribution is specified along with the loading, allowing the technique to solve for camber only. Again, a prescribed thickness may eliminate the application of a design. For this case of designing turbomachinery, the prescribed thickness may be too thick, causing the flow to approach sonic speeds and choke or possibly go supersonic causing shock waves to form. The thickness distribution may also cause thick boundary layers to form, creating the same choking or shocking to occur, or it may have steep geometry gradients causing boundary layer separation within the cascade. Methods using a prescribed thickness or neglecting thickness are useless because the thickness determines the viscous performance of the airfoil or blade, and therefore controls the validity of the final design by eliminating many applications.

In order to correctly design an airfoil or turbomachinery blade the design method needs the ability to design the thickness. An airfoil can be designed by camber alone but the thickness is the deciding factor on whether or not the design is practical. A camber distribution may match the given design criteria, such as a specific turning or velocity distribution, but different thickness distributions will eliminate possible applications by causing high drag, boundary layer separation, choked flow or shock waves. The design method must also calculate a converged flow field about the designed airfoil or blade. The flow field is necessary to later determine the viscous performance of the airfoil.

Chapter 2

Characteristic Velocity Determination

The design problem now becomes one of determining the best way to redesign the thickness of the airfoil or blade while simultaneously maintaining a camber as close to the designed camber as possible. The problems related to thickness such as separation, drag, choking and shocks are all viscous phenomena [1], [2], [23]. Unlike the scalar quantities such as turning and pressure differentials used to control the camber, more complex information is needed to determine the thickness distribution. One solution is to use specified velocities to design thickness. By specifying both the u and v components of the velocity, information on both the magnitude and direction of the flow field around the airfoil or blade can ensure the shape conforms to the viscous criteria. However, once the redesign control changes from the scalar pressure gradient to the non-scalar velocity field there is no guarantee that the fixed camber will match with the camber described by the velocity field and still satisfy conservation of mass. Therefore the camber line will need to be allowed to change according to the specified velocities. However, allowing both the camber and thickness to be influenced by the prescribed

velocity field creates an unconstrained problem. The local velocities that are used as controls can be manipulated in ways that are enumerably different, much like original geometries could be sculpted to fit certain design criteria.

The constraint applied to this technique is the requirement of maintaining the originally designed camber during the redesign of the thickness. This requires an investigation to determine if the velocities can be resolved to describe specific cambers and also be recombined to describe specific thicknesses as well. For this investigation the focus is on the u and v velocities along the upper and lower surfaces of an airfoil, or the u^+, u^-, v^+, and v^- velocities where '+' denotes the upper surface and '−' denotes the lower surface. The geometry of the surface of the airfoil can be described as

$$y = y_{cl} \pm y_{th} \tag{2.1}$$

where y can be either the upper or lower surface, y_{cl} is the camber line and y_{th} is the half-thickness. The half-thickness is defined as the vertical distance from the camber line to the surface of the airfoil. Individually the two surfaces can be described as

$$y^+ = y_{cl} + y_{th} \tag{2.2}$$

$$y^- = y_{cl} - y_{th} \tag{2.3}$$

2.1 NACA 4-Digit Airfoils

To study the relationship between the shape components of camber and thickness and surface velocities, a method of creating, controlling and adjusting airfoil shapes is needed. NACA airfoils satisfy this need. The NACA airfoil

family is a large series of wing sections created by the National Advisory Committee for Aeronautics[1], [22]. The family has several groups which encompass nearly every type or shape of airfoil. The first subset of NACA airfoils chosen is the 4-digit series of wing sections. This group was chosen because the airfoils can be generated mathematically, instead of requiring the use of tabulated coordinates, such as Eppler airfoils [17], or conformal transformations such as Joukowski airfoils [21]. Also the 4-digit series has a set of simple controls (namely the maximum camber height, the maximum camber location and the maximum thickness ratio) which can drastically modify the airfoil shape. The entire family of 4-digit wing sections can be described with only two equations, a thickness equation and a camber line equation[1],[22].

The thickness distribution equation[22] is given by

$$\left(\frac{y}{c}\right)_{th} = a_0\left(\frac{x}{c}\right)^{\frac{1}{2}} + a_1\left(\frac{x}{c}\right) + a_2\left(\frac{x}{c}\right)^2 + a_3\left(\frac{x}{c}\right)^3 + a_4\left(\frac{x}{c}\right)^4 \tag{2.4}$$

where $\left(\frac{y}{c}\right)_{th}$ is the thickness contribution to the airfoil, $\frac{x}{c}$ is the distance along the chord, and $a_0, \ldots, a_4$ are a series of constants. The a_i constants are determined by a set of boundary conditions imposed on the polynomial for an airfoil that has a thickness ratio of 0.20 (i.e. the maximum thickness is 20% of the chord length).

The boundary conditions[22] include

1. maximum thickness at 30% chord
2. slope of airfoil surface at location of maximum thickness
3. airfoil thickness at trailing edge
4. slope of airfoil surface at trailing edge

5. nose shape

The five boundary conditions determine the coefficients as

$$a_0 = 0.2969$$

$$a_1 = -0.1260$$

$$a_2 = -0.3516$$

$$a_3 = 0.2843$$

$$a_4 = 0.1015$$

The thickness distribution for an airfoil with a thickness-to-chord ratio other than 0.20 can be determined by scaling the 20% thick ordinates by the factor $\frac{T}{0.20}$ where T is the new thickness ratio. This makes the general thickness distribution equation

$$\left(\frac{y}{c}\right)_{th} = \frac{T}{0.20}\left[0.2969\sqrt{\frac{x}{c}} - 0.1260\left(\frac{x}{c}\right) - 0.3516\left(\frac{x}{c}\right)^2 + 0.2843\left(\frac{x}{c}\right)^3 + 0.1015\left(\frac{x}{c}\right)^4\right] \quad (2.5)$$

The NACA 4-digit series also has the ability to control both the location of maximum camber as well as the maximum camber height. The camber line is described as two parabolic curves tangent at the position of maximum camber [1]. The camber line equation[22] is written as

$$\left(\frac{y}{c}\right)_{cl} = \begin{cases} \frac{P}{M^2}\left[2M\left(\frac{x}{c}\right) - \left(\frac{x}{c}\right)^2\right] & ; \left(\frac{x}{c}\right) \leq M \\ \frac{M}{(1-P)^2}\left[1 - 2M + 2M\left(\frac{x}{c}\right) - \left(\frac{x}{c}\right)^2\right] & ; \left(\frac{x}{c}\right) \geq M \end{cases} \quad (2.6)$$

where M refers to the location of maximum camber and P refers to the value of maximum camber. The quantities of thickness (T), maximum camber (P)

and maximum camber location (M) are determined from the NACA four digit designation[22] as follows

NACA $abcd$

$$P = \frac{a}{100}$$
$$M = \frac{b}{10}$$
$$T = \frac{cd}{100}$$

A NACA 3410 airfoil has a maximum camber of 3% ($P = 0.03$) located at 40% chord ($M = 0.40$) and a maximum thickness of 10% ($T = 0.10$). A NACA 3410 airfoil can be seen in Figure 2.1.

The upper and lower surfaces of the airfoil are calculated using Equations 2.2 and 2.3 restated as a function of chord length as

$$\left(\frac{y}{c}\right)_{upper} = \left(\frac{y}{c}\right)_{cl} + \left(\frac{y}{c}\right)_{th} \tag{2.7}$$

$$\left(\frac{y}{c}\right)_{lower} = \left(\frac{y}{c}\right)_{cl} - \left(\frac{y}{c}\right)_{th} \tag{2.8}$$

The five 4-digit airfoils used are the NACA 3406, 3408, 3410, 3412 and 3414 airfoils. This selection represents the range (6% to 14% thick) of general airfoils used. All five have the same camber line defined with a maximum camber of 3% located at 40% of the chord length. The different thickness distributions can be seen in Figure 2.2.

After completing a potential flow analysis on each of the five airfoils at zero angle of attack, the four surface velocity components were compared to determine if any trends relating to thickness or camber occurred. The response of the upper u velocity (u^+) to increasing thickness can be seen in Figure 2.3.

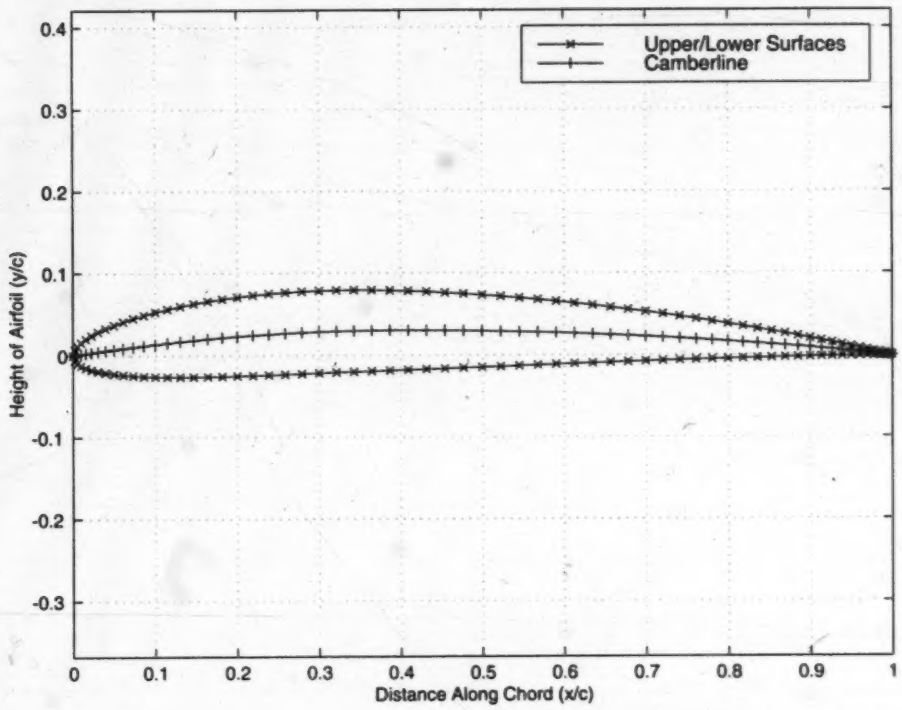

Figure 2.1: NACA 3410 Airfoil

The five velocities in Figure 2.3 all coincide at two points, at approximately 3% and 87% of the chord length. The occurrence of these characteristic points may be used to determine a method for trending the velocities according to thickness. The velocities also have a near-linear section that lasts from approximately 30% chord to 80% chord. The slope of this near-linear section increases with thickness. The common intersections of all five of the velocities, along with the increasing slope of the middle portion of the velocities is possibly the information necessary to trend the airfoil family,

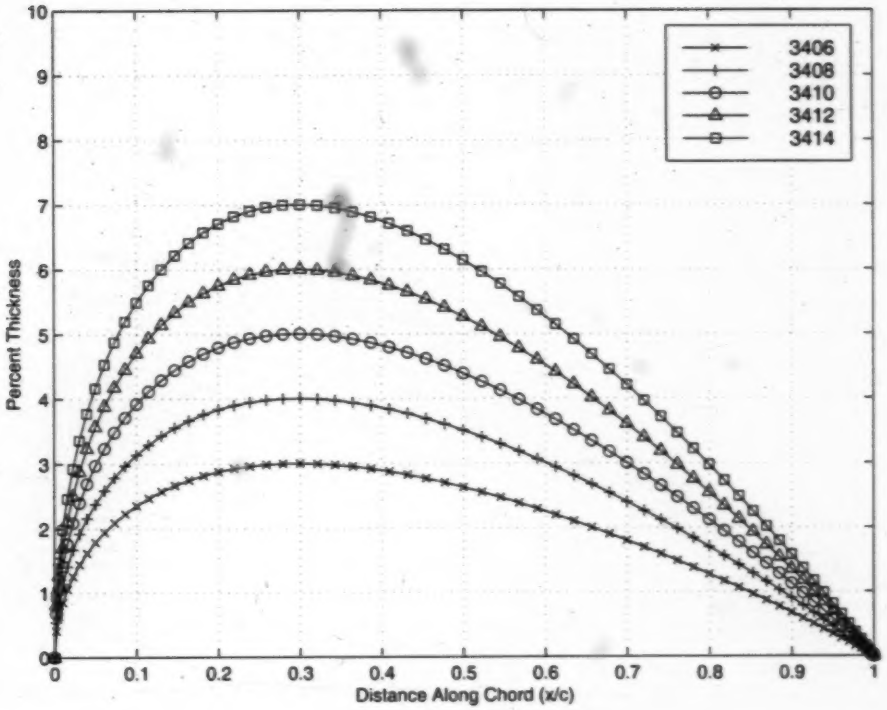

Figure 2.2: Thickness Distributions Of NACA 4-Digit Airfoils

but a more quantifiable comparison is needed. For each of the four velocity components being tested, a base velocity is chosen. The u^+ base velocity for the NACA 4-digit airfoils corresponds to the 3406 or the 6% thick airfoil. Each of the remaining four u^+ velocities is then compared to the base (6%) u^+ velocity according to the equation

$$u_{di}^+ = \frac{u_i^+ - u_{6\%}^+}{U_\infty} \times 100\% \tag{2.9}$$

where u_{di}^+ is the percent difference between the individual velocity (u_i^+) and

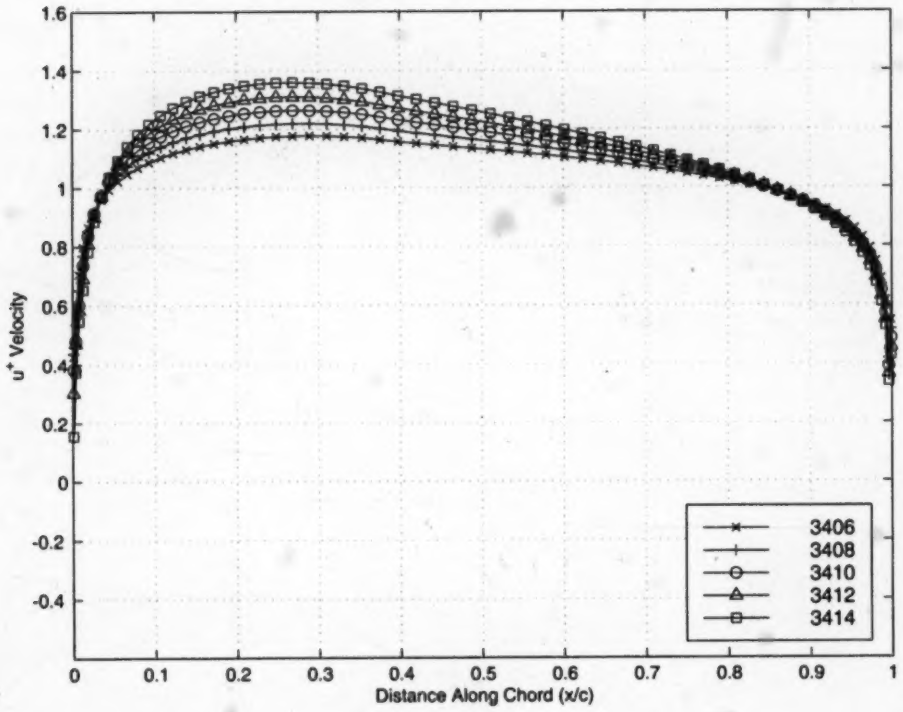

Figure 2.3: u^+ Velocities Of NACA 4-Digit Airfoils

the base velocity ($u^+_{6\%}$) and U_∞ represents the free stream velocity. The four u^+_d velocities can be seen in Figure 2.4.

Neglecting leading edge effects, the largest deviation that the u^+ velocities have from the base velocity occurs at approximately 25% chord. The range of difference at 25% chord is 4.3% to 18.5%. The 4.3% difference corresponds to the thinnest remaining airfoil, with a thickness ratio 2% greater than the base airfoil. The 18.5% difference corresponds to the thickest airfoil, with a thickness ratio 8% greater than the base airfoil. All of the velocities have a common point of approximately zero difference at 87% chord. All of the velocities also coincide at 3% chord length with a percent difference of 0.8%. The general trend from 3% chord to 87% chord is that the maximum deviation of the u^+ velocity from the base velocity increases with increasing thickness. From 87% chord to the trailing edge, the percent difference decreases with increasing thickness.

The next velocity component is the lower u or u^- velocity. As with the u^+ velocities, there are two points where all five of the velocities coincide. These points occur at 2% chord and 93% chord. Again, a mathematical comparison is needed, so one of the five velocities is chosen as a base velocity, and the difference of the remaining four velocities is calculated.

A plot showing the deviation of the u^- velocities from the base u^- velocity can be seen in Figure 2.6. The base u^- velocity is again chosen as the NACA 3406 airfoil. The percent difference of each of the four remaining u^- velocities is calculated with a variation of Equation 2.9 written as

$$u^-_{di} = \frac{u^-_i - u^-_{6\%}}{U_\infty} \times 100\% \tag{2.10}$$

The largest deviation that the u^- velocities have from the base velocity

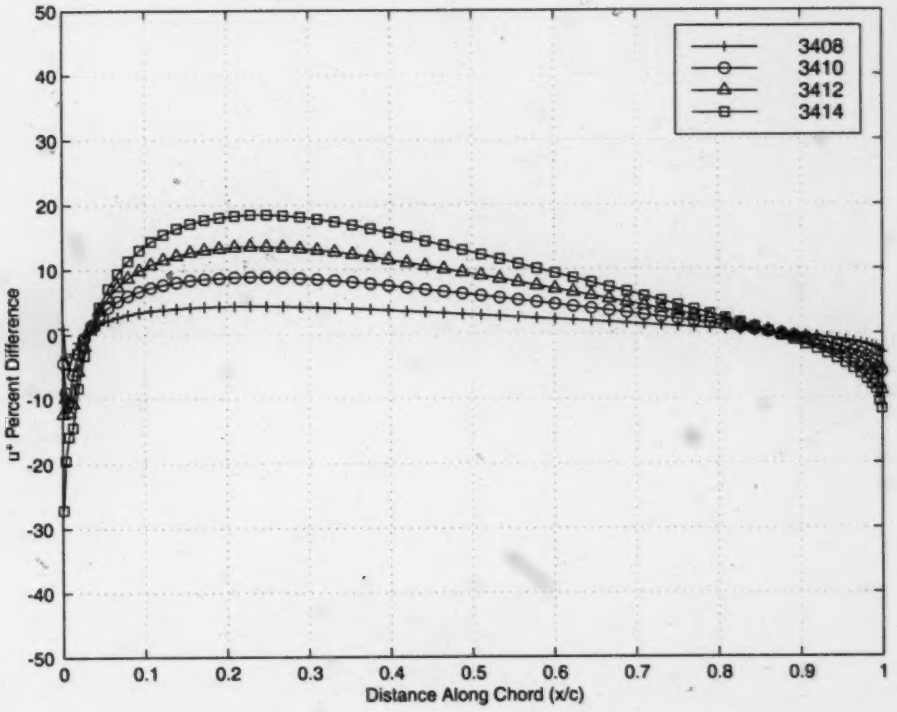

Figure 2.4: Difference In u^+ Velocities Of NACA 4-Digit Airfoils

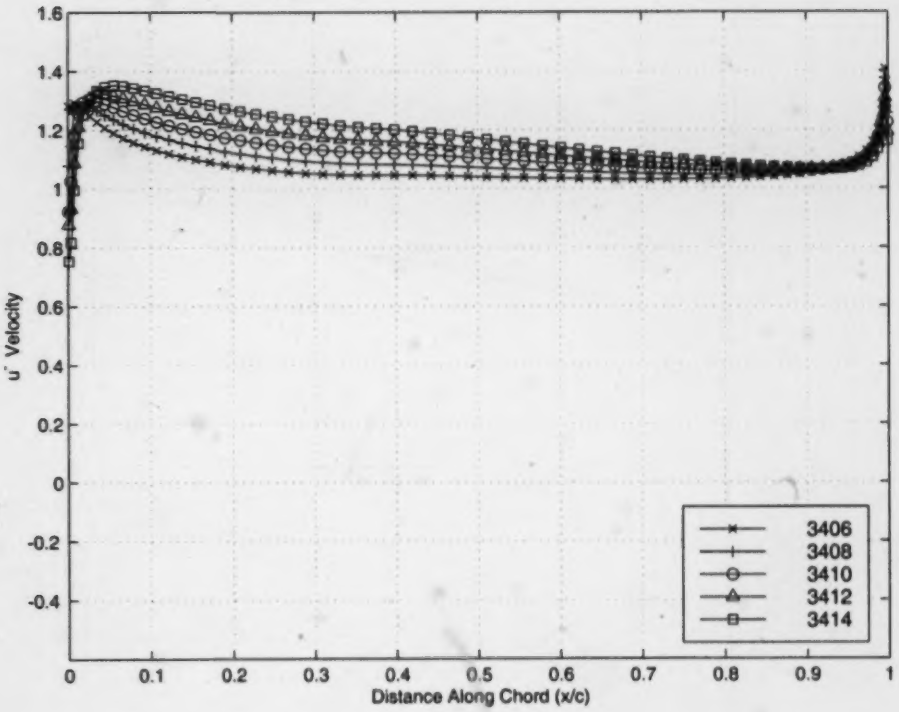

Figure 2.5: u^- Velocities Of NACA 4-Digit Airfoils

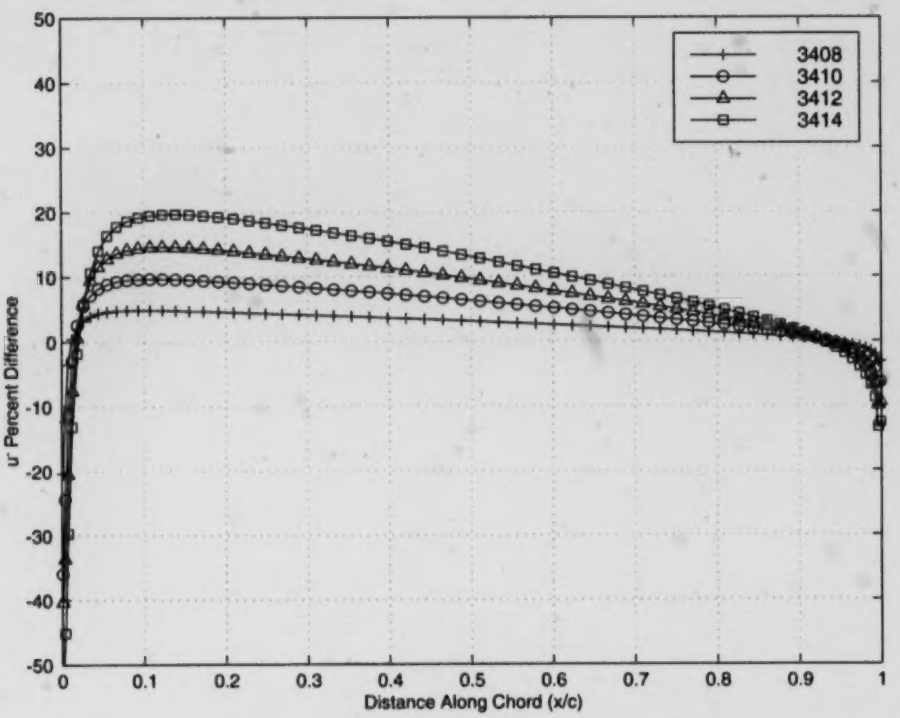

Figure 2.6: Difference In u^- Velocities Of NACA 4-Digit Airfoils

occurs at approximately 15% chord. The range of difference at 15% chord is 4.8% to 19.7%. The 4.8% difference corresponds to the thinnest airfoil, with a thickness ratio 2% greater than the base airfoil. The 19.7% difference corresponds to the thickest airfoil, with a thickness ratio 8% greater than the base airfoil. All of the velocities have a common point of approximately zero error at 92% chord. The four velocities also have a second common point of approximately 3.4% percent difference at 2% chord length. The general trend of the velocities from 2% chord to 92% chord is similar to the general trend of the u^+ velocities, the difference between each velocity and the base velocity increases with increasing thickness. Also, as with the u^+ velocities, from 93% chord to the trailing edge, the trend reverses, and the maximum difference decreases with increasing thickness.

The third velocity component for comparison is the upper v or v^+ velocity. The five v^+ velocities, each corresponding to different thickness ratios, can be seen in Figure 2.7. The five velocities only have a single common point, as opposed to the two common points of the u^+ and u^- velocities. The v^+ common point occurs at approximately 29% of the chord.

The velocities of the third velocity component, v^+, were compared in the same way that the u^+ and u^- velocities were compared. The base velocity corresponds to the 6% thick airfoil (NACA 3406), and the discrepancy between the base velocity and the remaining four velocities are calculated with an equation similar to Equation 2.10 written as

$$v_{di}^+ = \frac{v_i^+ - v_{6\%}^+}{U_\infty} \times 100\% \tag{2.11}$$

The percent differences calculated for the v^+ velocities can be seen in Figure 2.8.

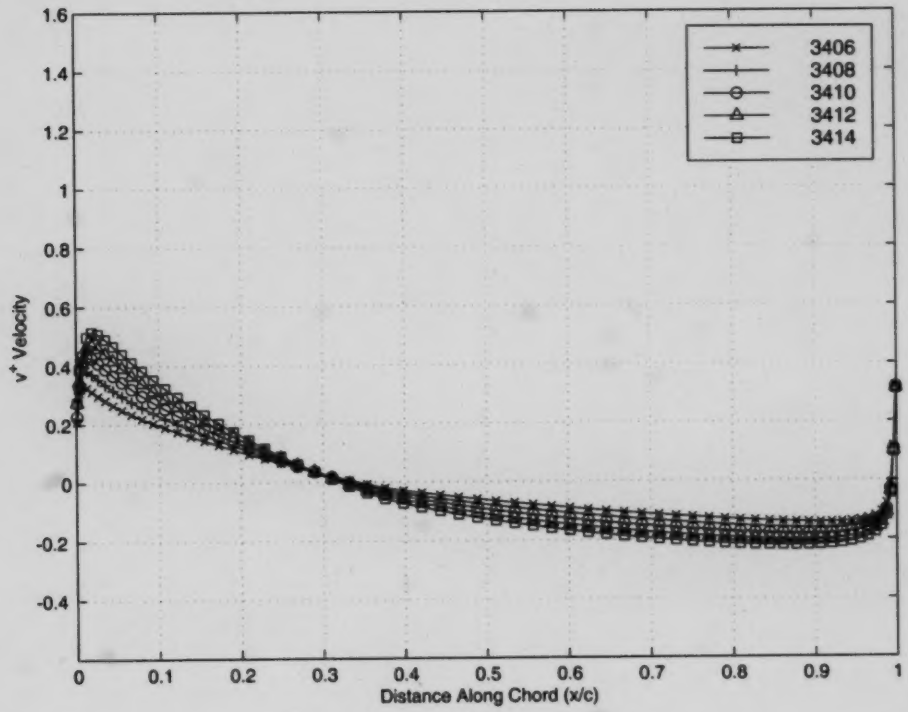

Figure 2.7: v^+ Velocities Of NACA 4-Digit Airfoils

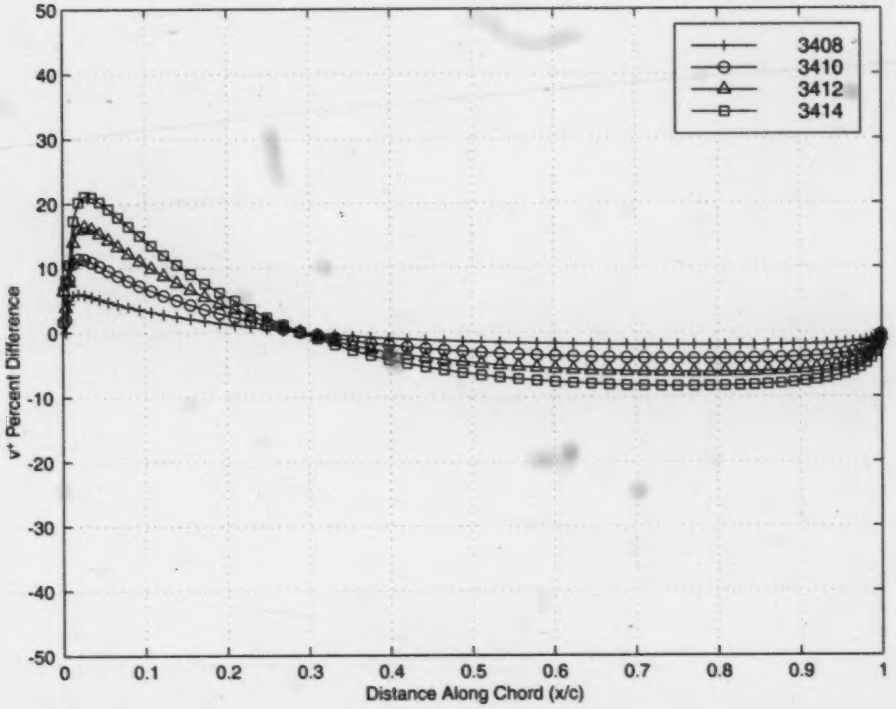

Figure 2.8: Difference In v^+ Velocities Of NACA 4-Digit Airfoils

All four of the v^+ percent differences have zero difference at 29% chord. This single common point effectively splits the plot into two separate sections. The first section, from 0% to 29% chord length has a maximum difference occurring at 2% of the chord. The range at 2% chord is from 5.9% difference to 21.1% difference. The 5.9% difference corresponds to the NACA 3408 airfoil, or an increase of 2% in the thickness ratio. The 21.1% difference corresponds to the NACA 3414 airfoil, or an increase in thickness ratio of 8%. The general trend in the first 29% of the chord is an increasing difference with increasing thickness ratio. From 29% chord to 100% chord the general trend is reversed. The greatest difference in this section occurs at 76% chord. The range at 76% chord is from -8.4% difference to -2.1% difference. The -8.4% difference is between the base velocity and the NACA 3414 airfoil reflecting an increase in the thickness ratio of 8%. The -2.1% difference corresponds to a thickness increase of 2%. The general trend from 29% chord length to the trailing edge is that the percent difference in the v^+ velocities decreases with increasing thickness.

The fourth and final velocity component is the lower v or v^- velocity. The response of the v^- velocity to changing thickness ratios can be seen in Figure 2.9. There is only a single common point that all five of the v^- velocities pass through. This point occurs at approximately 26% of the chord length.

The base velocity chosen for the v^- comparison is the v^- velocity of the NACA 3406 airfoil. The percent difference between the v^- velocity of the 6% thick airfoil and the remaining four v^- velocities is calculated using

$$v_{di}^- = \frac{v_i^- - v_{6\%}^-}{U_\infty} \times 100\% \tag{2.12}$$

A plot showing the percent difference between the remaining velocities and

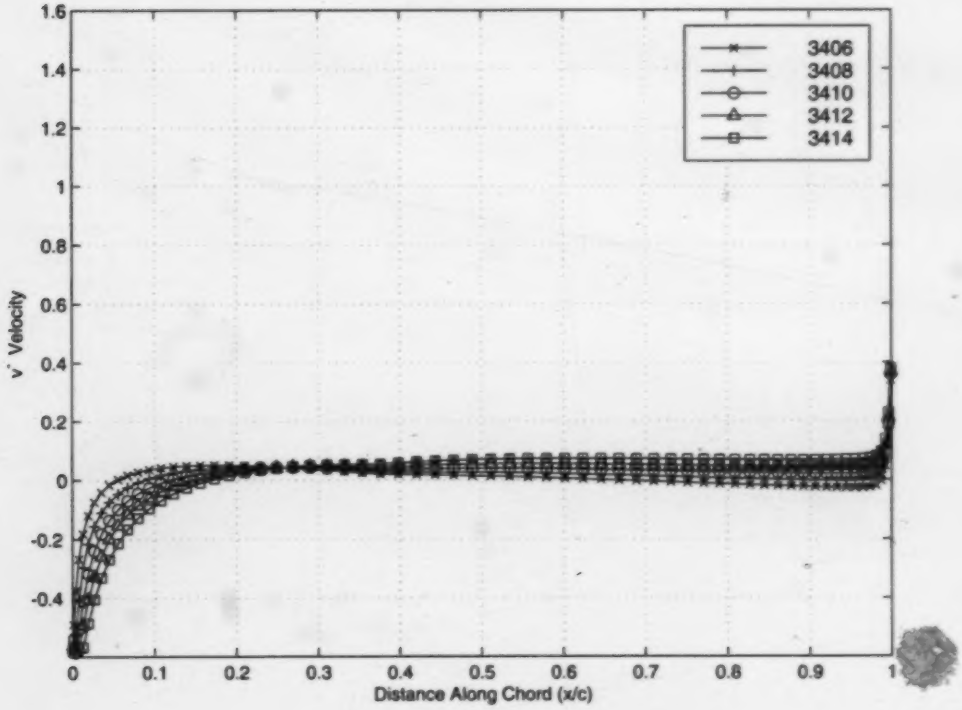

Figure 2.9: v^- Velocities Of NACA 4-Digit Airfoils

the base velocity can be seen in Figure 2.10.

At 26% chord, all four differences of velocities have a percent difference of zero. This zero-difference point separates the plot into two different sections. The first section has maximum differences at 1% of the chord length. The percent difference ranges from -38.6% to -14.5% at this 1% chord location. The largest difference, -38.6%, corresponds to the thickest airfoil, the NACA 3414. The -14.5% difference corresponds to the NACA 3408 airfoil. The general trend from the leading edge to 26% of the chord is that the percent difference decreases with increasing thickness ratio. The maximum difference between the 26% chord point of zero difference and the trailing edge occurs at 98% chord. At 98% chord the largest airfoil, 8% thicker than the base airfoil, has a maximum difference of 10.0%. The thinnest remaining airfoil, 2% thicker than the base airfoil, has a maximum difference of 2.6%. This range of 2.6% to 10.0% shows a general trend of increasing percent difference with increasing thickness ratio.

Looking at Figures 2.4, 2.6, 2.8 and 2.10 it becomes apparent that while there are possible trends between the velocity components and the airfoil thickness distributions, all four components are affected. Each of the plots of percent difference have maximum difference ranges of 14.2%, 14.9%, 15.2% and 24.2%. There is no visible split between velocities which describe thickness only and camber only. All four of the velocity components vary too greatly with thickness. Therefore, combinations of the four components are compared. Instead of looking at the surface velocities separately, they are combined to form $\bar{u}$, Δu, $\bar{v}$, and Δv. The four new velocity quantities are defined as

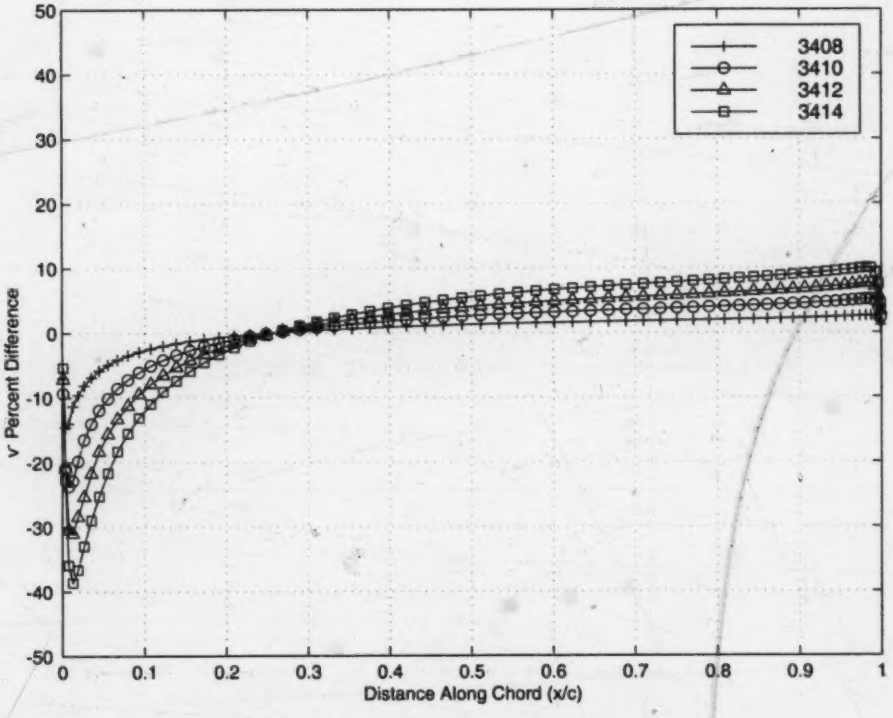

Figure 2.10: Difference In v^- Velocities Of NACA 4-Digit Airfoils

$$\bar{u} = \frac{u^+ + u^-}{2} \tag{2.13}$$

$$\Delta u = u^+ - u^- \tag{2.14}$$

$$\bar{v} = \frac{v^+ + v^-}{2} \tag{2.15}$$

$$\Delta v = v^+ - v^- \tag{2.16}$$

The use of the averages and differences of the velocities mimics the inviscid phenomena of turning and pressure difference, but the use of all four velocity components maintains the influence of the viscous phenomena.

The first velocity combination calculated and compared are the $\bar{u}$ velocities. The $\bar{u}$ velocity plot closely resembles the u^+ velocity plot. There are two locations where all five of the velocities appear to intersect, at 3% chord length and at 90% chord length. The velocities all have a similar shape as well. The five $\bar{u}$ velocities can be seen in Figure 2.11.

For comparison, the NACA 3406 or 6% thick airfoil is chosen as the base airfoil. The remaining four velocities are used to calculate a percent difference from the base velocity using the following equation

$$\bar{u}_{di} = \frac{\bar{u}_i - \bar{u}_{6\%}}{U_\infty} \times 100\% \tag{2.17}$$

The percent difference between the base velocity and the four remaining velocities can be seen in Figure 2.12.

There are two locations were the differences of the $\bar{u}$ velocities intersect. The first location is at 3% of the chord length with a difference of 1.7%. The second intersection is at 90% chord with a percent difference of zero. The two intersections divide the plot into three sections with difference ranges and

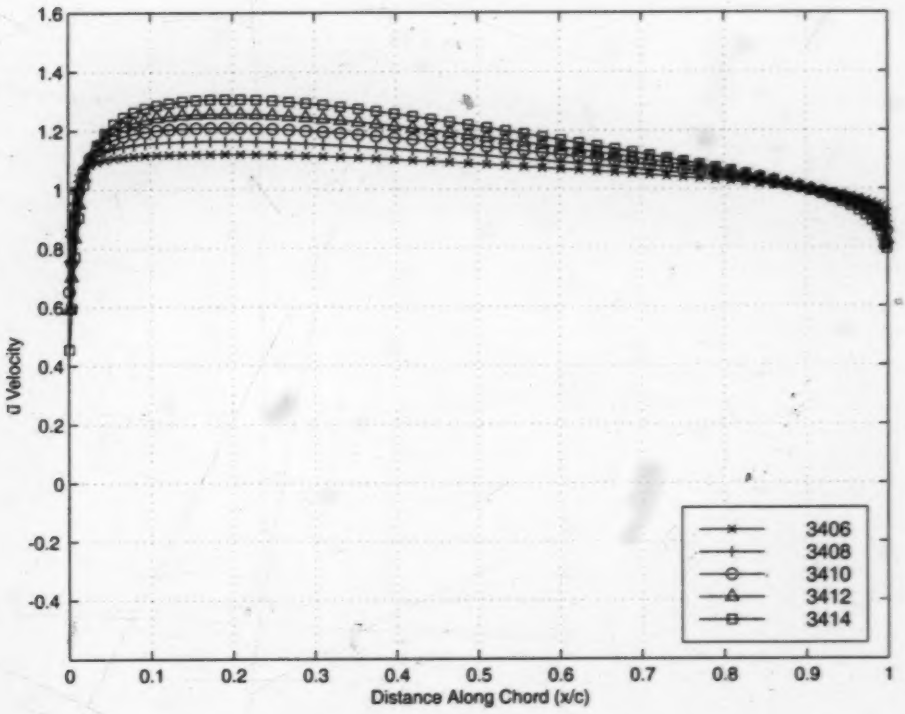

Figure 2.11: $\bar{u}$ Velocities Of NACA 4-Digit Airfoils

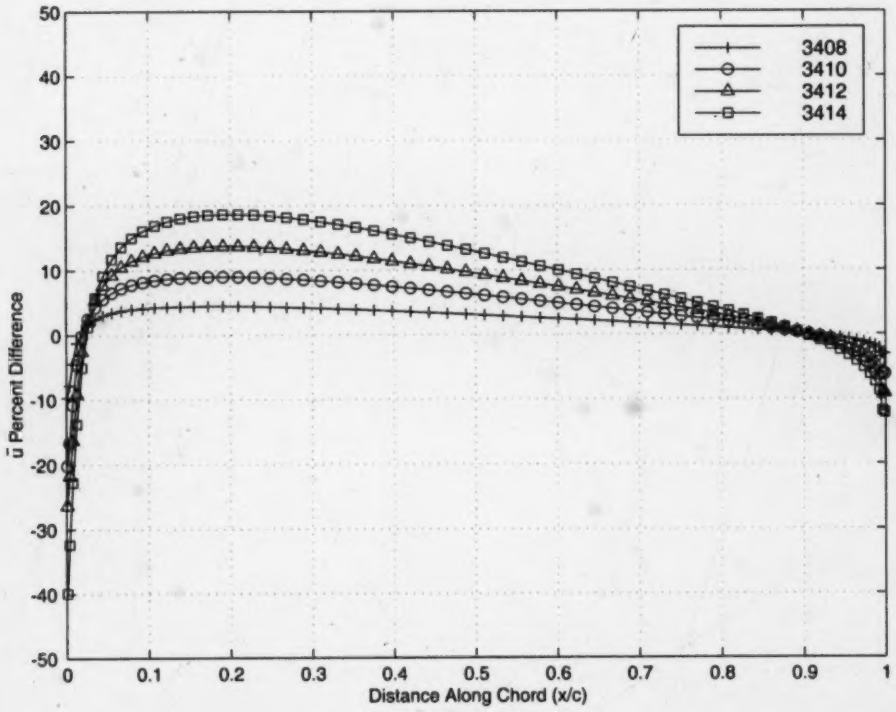

Figure 2.12: Difference In $\bar{u}$ Velocities Of NACA 4-Digit Airfoils

general trends for each. The first section is only 3% of the chord long, and is therefore neglected. The second section has maximum differences occurring at 20% of chord length. At 20% chord, the difference ranges from 4.4% to 18.6%. The 4.4% difference corresponds to the NACA 3408 airfoil, and the 18.6% difference corresponds to the NACA 3414 airfoil. The general trend between 3% chord and 90% is therefore increasing difference with increasing thickness ratio. The third section is from 90% of the chord length to the trailing edge. The greatest difference in this section occurs at the trailing edge, or 100% chord. The range of differences at 100% chord is from -12.2% to -3.1%. The -12.2% difference corresponds to the thickest airfoil, 8% thicker than the base airfoil. The -3.1% difference corresponds to the thinnest remaining airfoil, 2% thicker than the base airfoil. The general trend from 90% to 100% chord is decreasing percent difference with increasing thickness ratio.

The second velocity component combination is the Δu velocity. The Δu velocities plot, seen in Figure 2.13, shows a much smaller range than any other velocity component so far. Upon closer inspection, it becomes apparent that there are two locations where the five velocities intersect. These locations are at 24% chord and 43% chord.

The base velocity for the Δu difference calculation is the 6% thick airfoil. The percent difference is calculated using

$$\Delta u_{di} = \frac{\Delta u_i - \Delta u_{6\%}}{U_\infty} \times 100\% \tag{2.18}$$

The percent difference in the Δu velocity between the base velocity and the four remaining velocities can be seen in Figure 2.14.

All of the remaining Δu velocities have zero percent difference at both

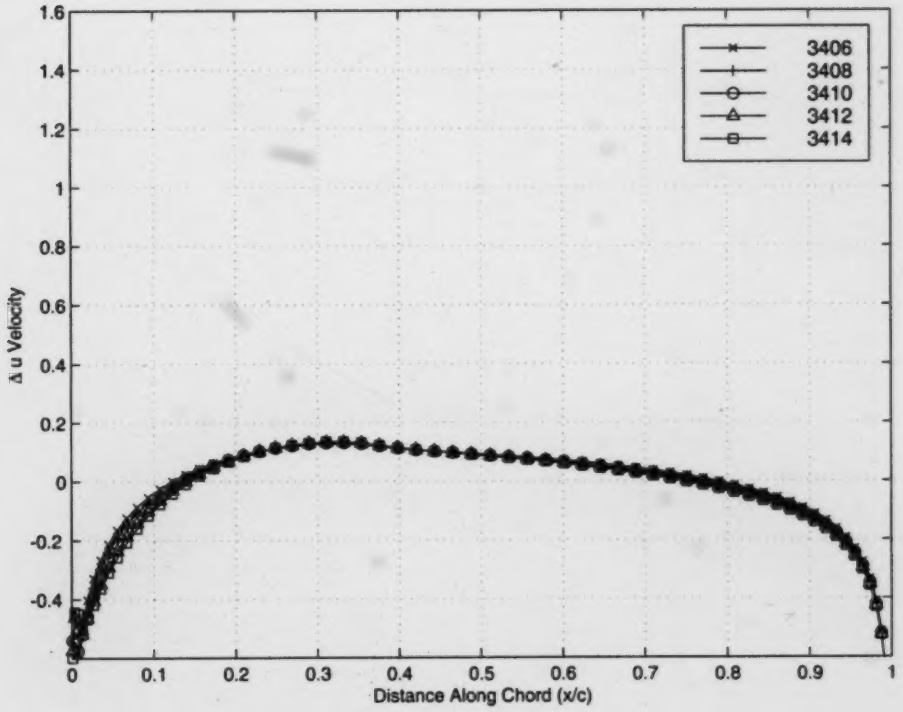

Figure 2.13: Δu Velocities Of NACA 4-Digit Airfoils

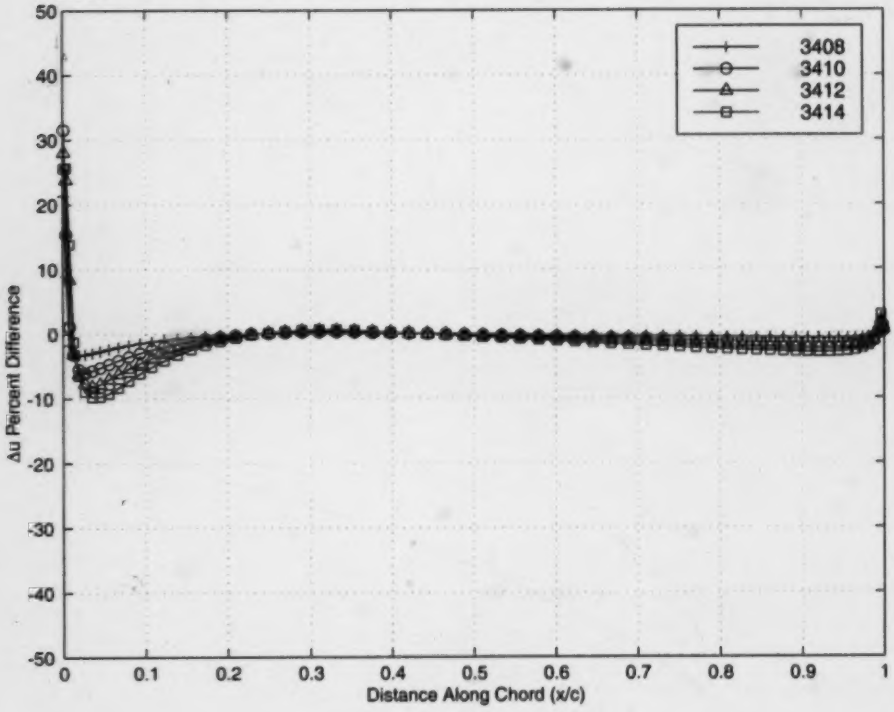

Figure 2.14: Difference In Δu Velocities Of NACA 4-Digit Airfoils

24% of the chord length and 43% of the chord length. Between the leading edge and 24% chord, the greatest difference occurs at 4% chord. The range of Δu differences at 4% chord are from -9.8% to -3.3%. The -9.8% difference corresponds to the NACA 3414 airfoil and the -3.3% difference corresponds to the NACA 3408 airfoil. This range of differences creates a general trend of decreasing percent difference with increasing thickness ratio between 0% chord and 24% chord. Between 24% of the chord length and 43% of the chord length, the general trend has reversed. The maximum difference in this area occurs at 32% chord. The maximum difference ranges from 0.2% to 0.6%. The 0.2% difference corresponds to the 8% thick airfoil and the 0.6% difference corresponds to the 14% thick airfoil. This creates a general trend of increasing percent difference with increasing thickness ratio. Between 43% of the chord length and 100% of the chord length, the maximum difference occurs at 32% chord. The maximum difference ranges from -2.9% to -0.8%. The -2.9% difference corresponds to the thickest airfoil and the -0.8% difference corresponds to the thinnest remaining airfoil. This creates a general trend of decreasing percent difference with increasing thickness ratio from 42% of the chord length to the trailing edge. This small range of percent difference, namely 0.4% and 2.1% in the last two sections of the plot, represents a strong change in how the velocity combination is effected by changing airfoil thickness. Instead of difference ranges of 15% or even 24%, the range of the Δu velocity difference is less than a tenth of that.

The third velocity combination is the $\bar{v}$ velocity. The $\bar{v}$ velocity behaves in a similar way to the Δu velocity when the thickness ratio of the airfoil is increased. The are three intersection points, at 8% chord, 35% chord and

81% chord. The five velocities appear very similar to each other, and do not cover a very large range of values. The $\bar{v}$ velocities can be seen in Figure 2.15.

The base velocity for the $\bar{v}$ difference calculation is the 6% thick airfoil. The percent difference is calculated using

$$\bar{v}_{di} = \frac{\bar{v}_i - \bar{v}_{6\%}}{U_\infty} \times 100\% \tag{2.19}$$

The percent difference in the $\bar{v}$ velocities between the base velocity and the four remaining velocities can be seen in Figure 2.16.

There are three locations where there is zero percent difference between the remaining four $\bar{v}$ velocities and the base velocity. These three locations occur at 8% of the chord length, 35% of the chord length and 81% of the chord length. In the first section of the percent difference plot, between the leading edge and 8% chord the greatest difference occurs at 1% chord. The range of differences at 1% chord is from -12.7% to -7.3%. The -12.7% difference corresponds to the NACA 3414 airfoil, and the -7.3% difference corresponds to the NACA 3408 airfoil. This range from -12.7% difference to -7.3% difference shows a trend of decreasing percent difference with increasing thickness ratio. In the next comparison section, from 8% chord to 35% chord, the maximum difference occurs at 15% chord. The percent difference at 15% chord varies from 0.4% to 1.5%. The 0.4% difference corresponds to the thinnest remaining airfoil, and the 1.5% difference corresponds to the thickest airfoil. This creates a general trend of increasing percent different with increasing thickness ration from 8% chord to 35% chord. The third region of the comparison plot lasts from 35% of the chord to 81% of the chord. The largest difference in this region occurs at 58% of the chord length. The

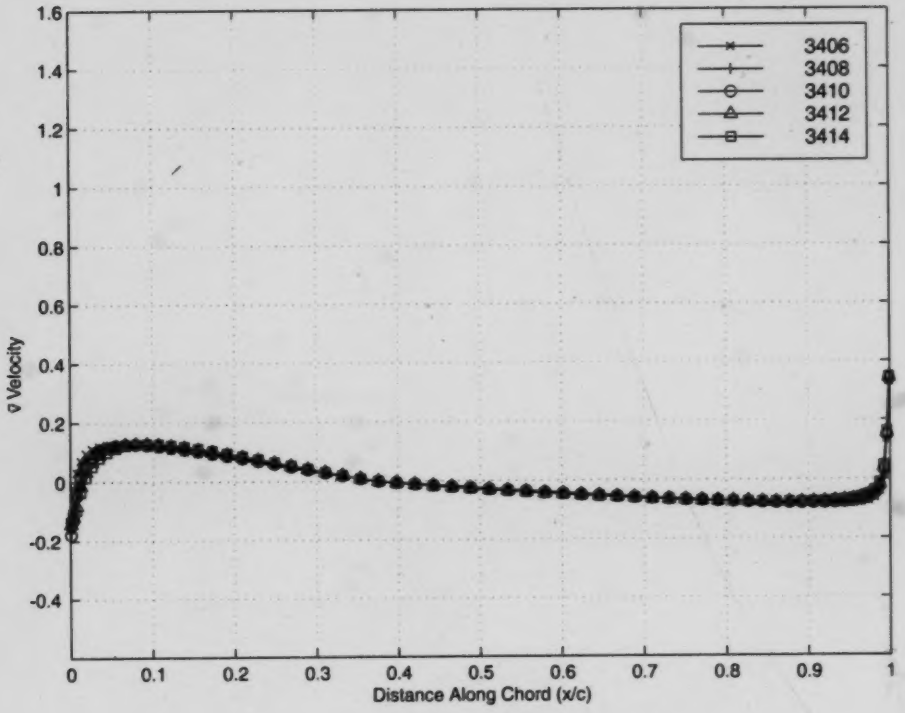

Figure 2.15: $\bar{v}$ Velocities Of NACA 4-Digit Airfoils

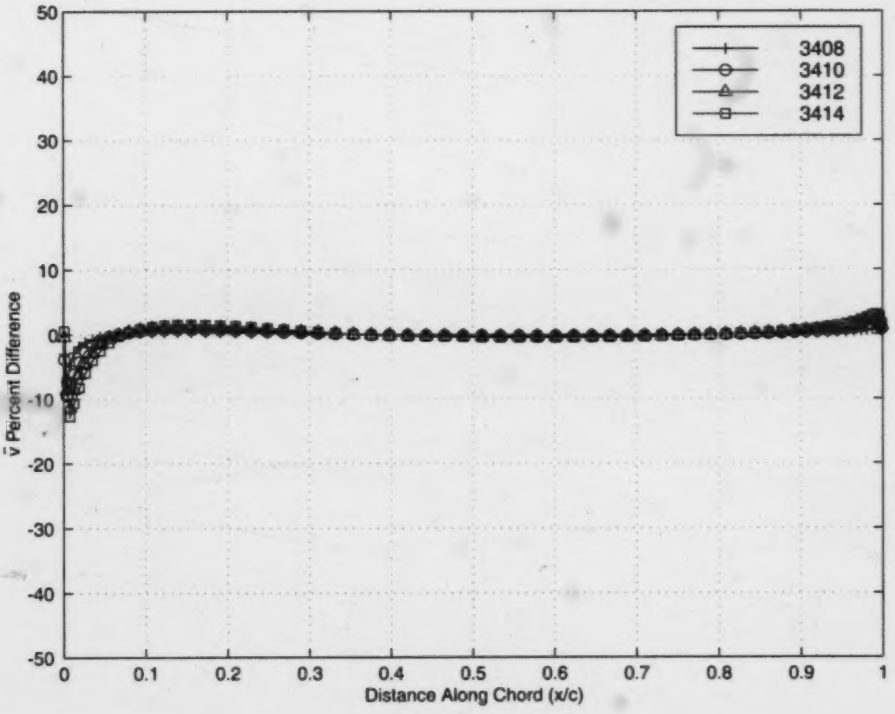

Figure 2.16: Difference In $\bar{v}$ Velocities Of NACA 4-Digit Airfoils

range of percent differences at 58% of the chord is from -0.5% for the 14% thick airfoil to -0.1% for the 8% thick airfoil. This range creates a general trend of decreasing percent difference for increasing airfoil thickness. The fourth and final region of the comparison plot lasts from 81% of the chord to the trailing edge. The maximum difference in this fourth section occurs at 99% of the chord length. The maximum difference at 99% chord has a range of 0.8% difference to 3.1% difference. The 0.8% difference corresponds to the airfoil 2% thicker than the base airfoil, and the 3.1% difference corresponds to the airfoil 8% thicker than the base airfoil. The range indicates a trend of increasing percent difference with increasing thickness ratio. The response of the $\bar{v}$ velocity to increasing thickness ratios is similar to the response of the Δu velocity. The difference ranges are much smaller than for the $\bar{u}$ velocity There are also more points where the velocities intersect, indicating that the velocities are very similar. In fact, neglecting the leading and trailing edge velocity increases of the $\bar{v}$ velocities, the maximum percent difference range is only 1.1%. There is a definite change in the effect that the different thickness distributions have on the velocity components when the combinations of Δu and $\bar{v}$ are calculated.

The fourth and final velocity component combination is Δv. There is only one location where the Δv velocities intersect, at 28% of the chord. The velocities cover a large velocity range, indicating a strong dependence on changing thickness. The five Δv velocities can be seen in Figure 2.17.

The base velocity for the $\bar{v}$ difference calculation is the NACA 3406 airfoil. The percent difference is calculated using

$$\Delta v_{di} = \frac{\Delta v_i - \Delta v_{6\%}}{U_\infty} \times 100\% \tag{2.20}$$

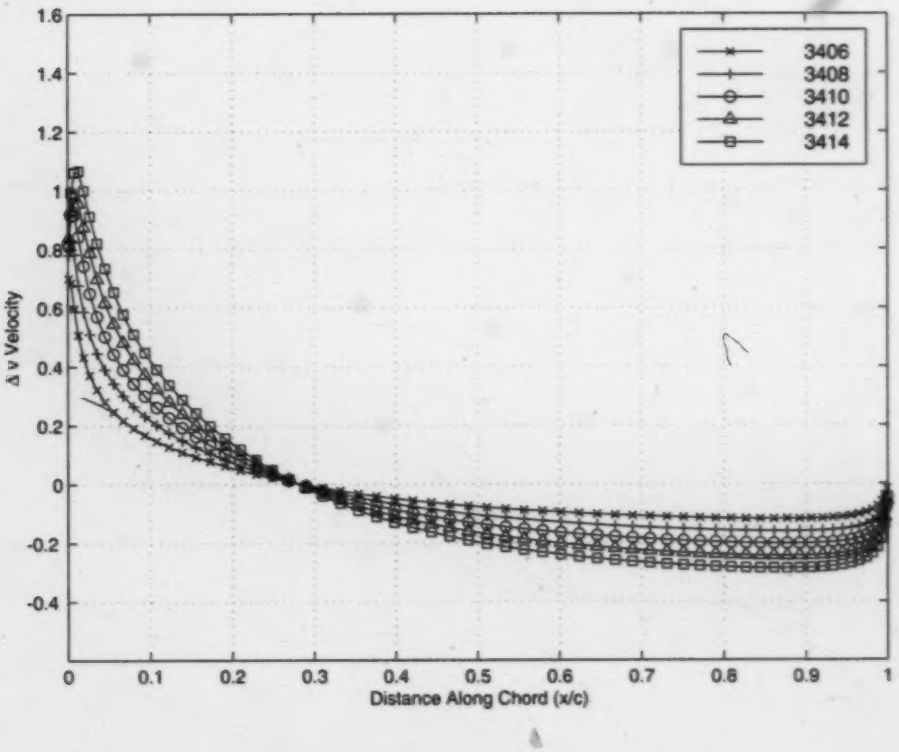

Figure 2.17: Δv Velocities Of NACA 4-Digit Airfoils

The percent difference in the Δv velocities between the base velocity and the four remaining velocities can be seen in Figure 2.18.

With the single intersection point at 28% of the chord length, the Δv velocity difference plot is split into two separate regions. The first section, from leading edge to 28% of the chord has a maximum percent difference occurring at 2% chord. The range of differences at 2% of the chord is from 18.4% difference for the NACA 3408 airfoil to 56.8% difference for the NACA 3414 airfoil. This represents a general trend of increasing percent difference for increasing airfoil thickness. The second section of the Δv difference plot has the opposite trend. The largest difference in the region from 28% chord to the trailing edge occurs at 88% of the chord. The range of differences at 88% chord is from -16.8% to -4.2%. The -16.8% difference corresponds to the 14% thick airfoil, and the -4.2% difference corresponds to the 8% thick airfoil. The general trend from 88% chord to the trailing edge is decreasing percent difference with increasing thickness ratio.

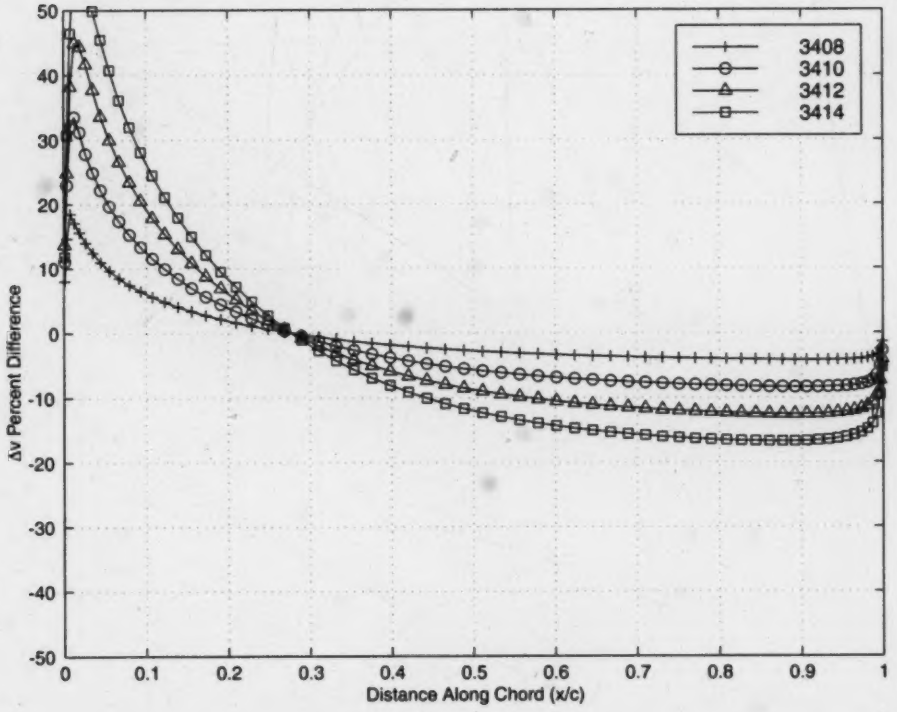

Figure 2.18: Difference In Δv Velocities Of NACA 4-Digit Airfoils

For the previous group of NACA 4-digit airfoils the thickness distribution changed while the camber line was held constant. The analysis velocity combinations of $\bar{u}$, Δu, $\bar{v}$, and Δv from the previous group show that only the $\bar{u}$ and Δv velocities change with the different thickness distributions while the Δu and $\bar{v}$ velocities remain relatively constant with the constant camber line. These velocities suggest that the thickness distribution can be designed by $\bar{u}$ and Δv velocities alone, while the camber line is described by Δu and $\bar{v}$ velocities. To determine the effect of changing camber lines, a second series of NACA 4-digit airfoils is analyzed. The five airfoils used to determine the relationship between surface velocities and camber line include the 1410, 2410, 3410, 4410, and 5410 airfoils. All five of these airfoils have an identical thickness distribution with a maximum thickness ratio of 10%. The airfoils all have a maximum camber height location of 40% chord. The only component that changes throughout the series of airfoils is the maximum camber line height. The camber line height ranges from 1% chord to 5% chord, respectively. The five camber lines can be seen in Figure 2.19.

From the analysis of this second group of NACA 4-digit airfoils the velocities prove that there is a definite relationship between specific velocity combinations and the thickness distribution and camber line of an airfoil. The $\bar{u}$, Δu, $\bar{v}$, and Δv velocities show that as the camber line height is changed, only the Δu and $\bar{v}$ velocities are strongly affected. The $\bar{u}$ and Δv velocities remain relatively constant for a constant thickness distribution.

The first velocity combination for camber line height comparison is the $\bar{u}$ velocity. As the camber height was increased, the $\bar{u}$ velocity remained nearly constant. The five $\bar{u}$ velocities corresponding to the five different camber

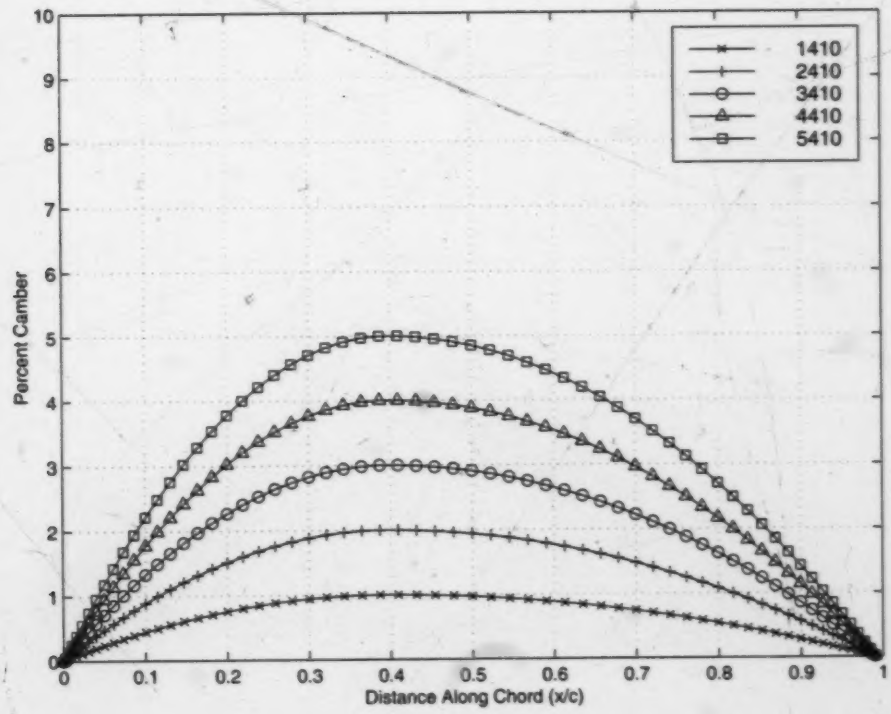

Figure 2.19: Camber Lines of NACA 4-Digit Airfoils

lines appear identical from approximately 30% of the chord length to 70% of the chord. The $\bar{u}$ velocities can be seen in Figure 2.20.

To calculate the effect that the changing camber line height has on $\bar{u}$ velocities, the NACA 1410 airfoil is chosen as the base airfoil. The percent difference of the remaining four velocities is calculated using

$$\bar{u}_{di} = \frac{\bar{u}_i - \bar{u}_{1\%}}{U_\infty} \times 100\% \tag{2.21}$$

where $\bar{u}_{di}$ is the percent difference, $\bar{u}_i$ is one of the four remaining velocities, $\bar{u}_{1\%}$ is the base velocity, and U_∞ is the free stream velocity. The difference in $\bar{u}$ velocity can be seen in Figure 2.21.

There are two locations where the difference in $\bar{u}$ is equal to zero for all four of the remaining velocities. These two locations occur at 31% chord and 47% chord. From the leading edge to 1% of the chord length, the largest percent difference occurs at 7% chord. The range of differences at 7% chord is from -3.0% to -0.4%. The -3.0% difference corresponds to the NACA 5410 airfoil. The -0.4% difference corresponds to the NACA 2410 airfoil. The general trend from 0% chord to 31% chord is decreasing percent difference with increasing camber line height. Between 31% chord and 47% chord, the maximum percent difference occurs at 35% chord. The difference at 35% chord ranges from 0.0% to 0.1%. The 0.0% difference corresponds to the 2% high camber line. The 0.1% difference corresponds to the 5% high camber line. The general trend from 31% chord to 47% chord is increasing percent difference with increasing camber line height. From 47% chord to the trailing edge, the largest percent difference occurs at 91% chord. The range of differences at 91% chord is from -1.3% to -0.2%. The -1.3% difference corresponds to the NACA 5410 airfoil. The -0.2% difference corresponds to

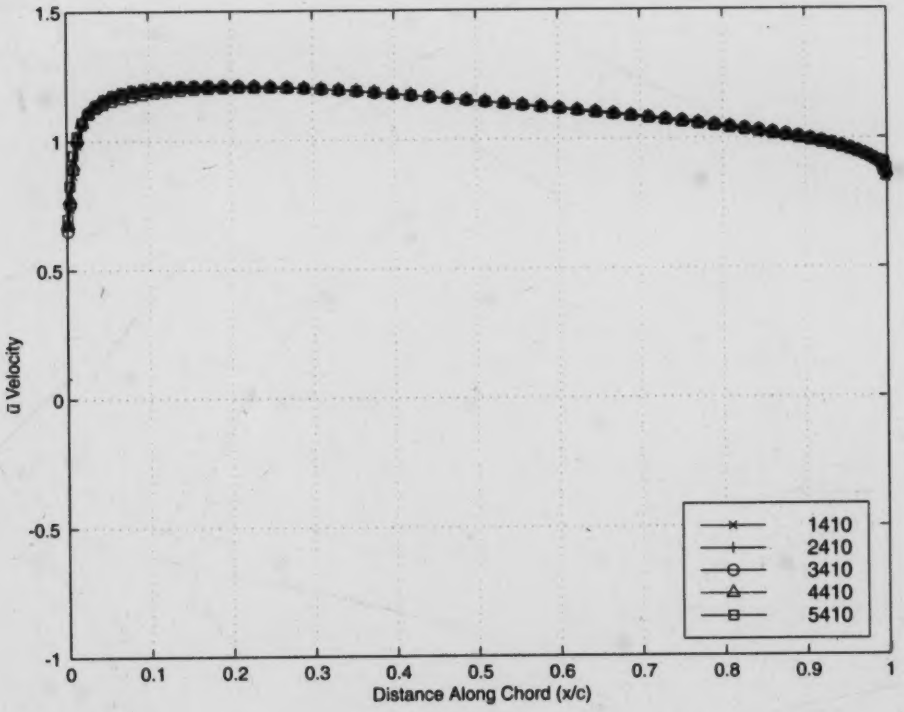

Figure 2.20: $\bar{u}$ Velocities Of NACA 4-Digit Airfoils With Changing Camber Lines

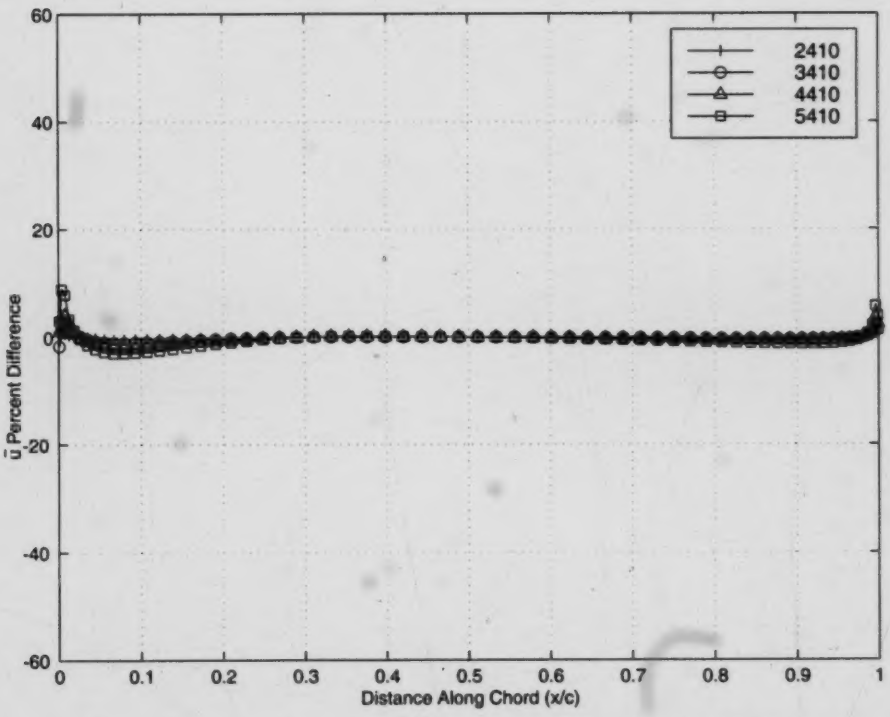

Figure 2.21: Difference In $\bar{u}$ Velocities Of NACA 4-Digit Airfoils With Changing Camber Lines

the NACA 2410 airfoil. The general trend from 47% chord to 100% chord is decreasing percent difference with increasing camber line height.

The second set of velocities compared are the Δu velocities. The five Δu velocities share two common intersection points. The intersection points occur at 13% and 76% of the chord length. The Δu velocities can be seen in Figure 2.22.

To calculate the effect that the changing camber line height has on Δu velocities, the NACA 1410 airfoil is again chosen as the base airfoil. The percent difference of the remaining four velocities is calculated using

$$\Delta u_{di} = \frac{\Delta u_i - \Delta u_{1\%}}{U_\infty} \times 100\% \tag{2.22}$$

where Δu_{di} is the percent difference, Δu_i is one of the four remaining velocities, $\Delta u_{1\%}$ is the base velocity, and U_∞ is the free stream velocity. The difference in Δu velocity can be seen in Figure 2.23.

The two intersection points of the Δu velocities create three sections in the plot. The first section, from leading edge to 13% chord has the largest percent differences at 0% chord. The range of percent differences at 0% chord is from -72.8% to -20.9%. The -72.8% difference corresponds to the NACA 5410 airfoil. The -20.9% difference corresponds to the NACA 2410 airfoil. The general trend from 0% chord to 13% chord is decreasing percent difference with increasing camber line height. The second region, from 13% chord to 76% chord has an opposite trend. The maximum percent difference in this section occurs at 33% of the length of the chord. The difference at 33% chord range from 4.4% to 17.5%. The 4.4% difference corresponds to the 2% high camber line. The 17.5% difference corresponds to the 5% high camber line. The general trend from 13% chord to 76% chord is increasing

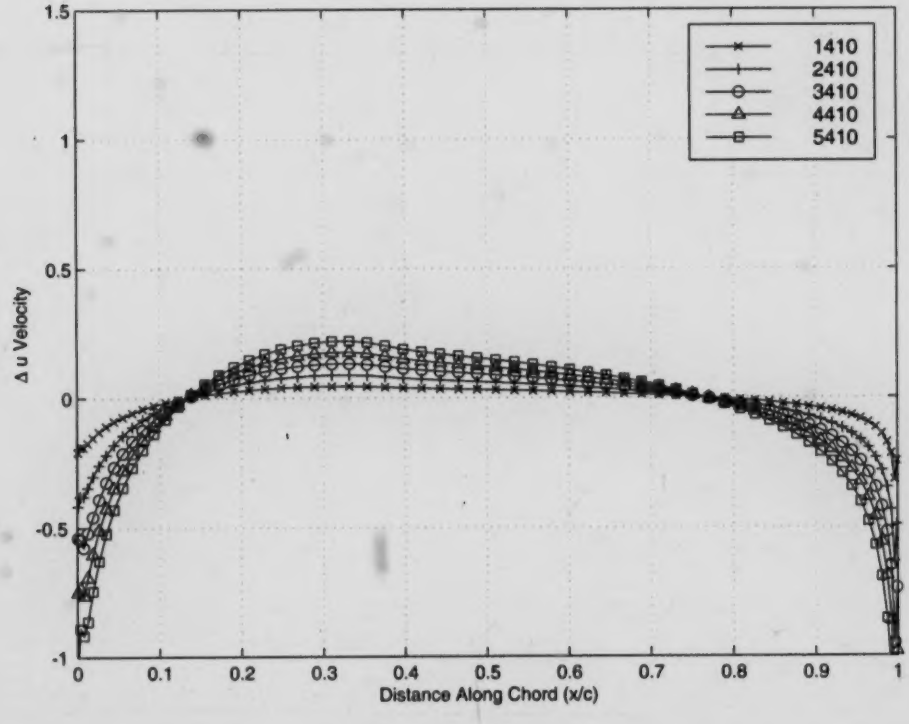

Figure 2.22: Δu Velocities Of NACA 4-Digit Airfoils With Changing Camber Lines

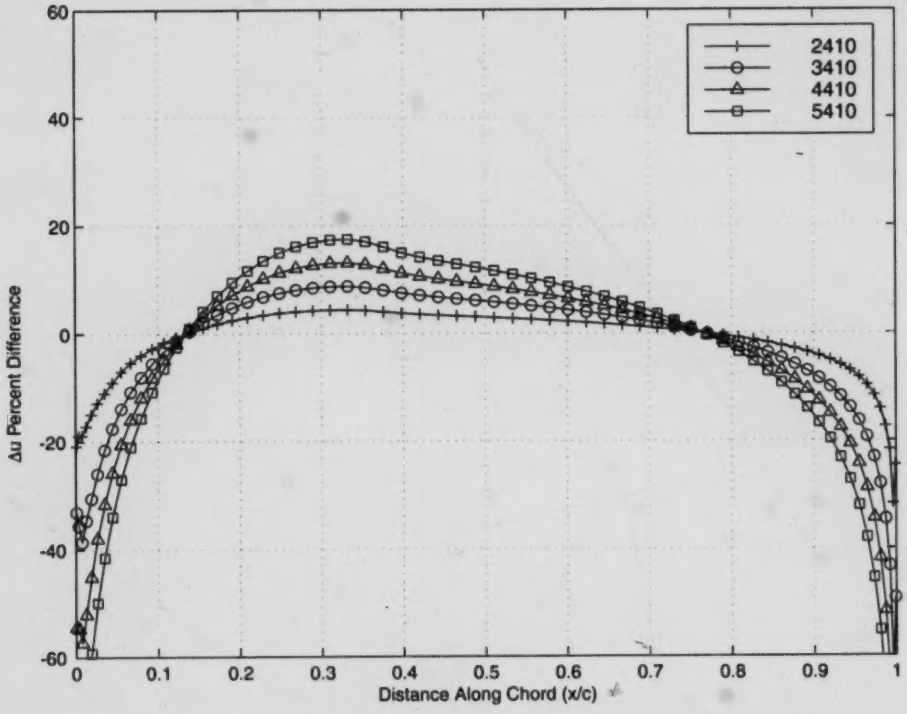

Figure 2.23: Difference In Δu Velocities Of NACA 4-Digit Airfoils With Changing Camber Lines

percent difference with increasing camber line height. The third and final section is from 76% chord to the trailing edge. The largest percent difference in this region occurs at 100% chord. The range of percent difference at 100% chord is from -98.0% to -31.7%. The -98.0% difference corresponds to the NACA 5410 airfoil. The -31.7% difference corresponds to the NACA 2410 airfoil. The general trend from 76% chord to 100% chord is decreasing percent difference with increasing camber line height.

The third set of velocities compared are the $\bar{v}$ velocities. The five $\bar{v}$ velocities share a single intersection point at 37% chord. The $\bar{v}$ velocities can be seen in Figure 2.24.

To calculate the effect that the changing camber line height has on $\bar{v}$ velocities, the NACA 1410 airfoil is again chosen as the base airfoil. The percent difference of the remaining four velocities is calculated using

$$\bar{v}_{di} = \frac{\bar{v}_i - \bar{v}_{1\%}}{U_\infty} \times 100\% \tag{2.23}$$

where $\bar{v}_{di}$ is the percent difference, $\bar{v}_i$ is one of the four remaining velocities, $\bar{v}_{1\%}$ is the base velocity, and U_∞ is the free stream velocity. The difference in $\bar{v}$ velocity can be seen in Figure 2.25.

The single intersection point of the $\bar{v}$ velocities creates two regions in the comparison plot. The first section, from leading edge to 37% chord has the largest percent differences at 8% chord. The range of percent differences at 8% chord is from 4.2% to 16.4%. The 4.2% difference corresponds to the NACA 2410 airfoil. The 16.4% difference corresponds to the NACA 5410 airfoil. The general trend from 0% chord to 37% chord is increasing percent difference with increasing camber line height. The second region exists from 37% chord to the trailing edge. The largest percent difference in this region

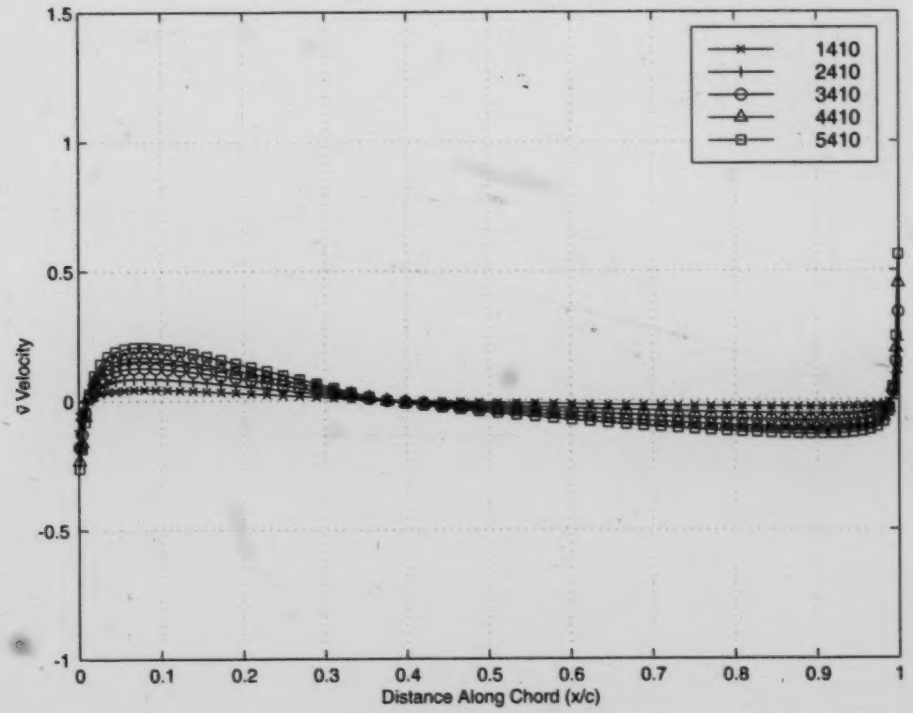

Figure 2.24: $\bar{v}$ Velocities Of NACA 4-Digit Airfoils With Changing Camber Lines

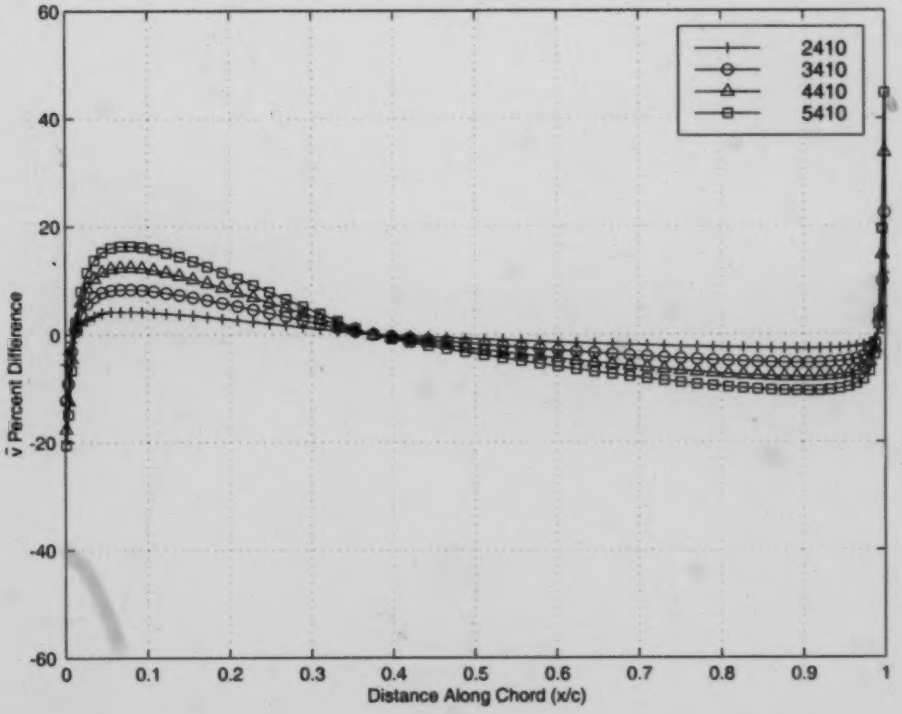

Figure 2.25: Difference In $\bar{v}$ Velocities Of NACA 4-Digit Airfoils With Changing Camber Lines

occurs at 90% chord. The range of percent difference at 90% chord is from -10.6% to -2.7%. The -10.6% difference corresponds to the NACA 5410 airfoil. The -2.7% difference corresponds to the NACA 2410 airfoil. The general trend from 37% chord to 100% chord is decreasing percent difference with increasing camber line height.

The fourth and final set of velocities compared are the Δv velocities. The five Δv velocities appear nearly identical from approximately 12% chord to approximately 80% chord. The Δv velocities can be seen in Figure 2.26.

To calculate the effect that the changing camber line height has on Δv velocities, the NACA 1410 airfoil is again chosen as the base airfoil. The percent difference of the remaining four velocities is calculated using

$$\Delta v_{di} = \frac{\Delta v_i - \Delta v_{1\%}}{U_\infty} \times 100\% \tag{2.24}$$

where Δv_{di} is the percent difference, Δv_i is one of the four remaining velocities, $\Delta v_{1\%}$ is the base velocity, and U_∞ is the free stream velocity. The difference in Δv velocity can be seen in Figure 2.27.

There are three locations where all of the Δv velocities coincide, creating zero percent difference. These three locations are at 14% chord, 38% chord and 74% chord. From the leading edge to 14% chord, the largest percent difference occurs at 1% chord. The range of differences at 1% chord is from -15.1% to -1.9%. The -15.1% difference corresponds to the NACA 5410 airfoil. The -1.9% difference corresponds to the NACA 2410 airfoil. The general trend from leading edge to 14% chord is decreasing percent difference with increasing camber line height. Between 14% chord and 38% chord, the maximum percent difference occurs at 23% of the chord length. The difference at 23% chord ranges from 0.2% to 1.5%. The 0.2% difference corresponds to

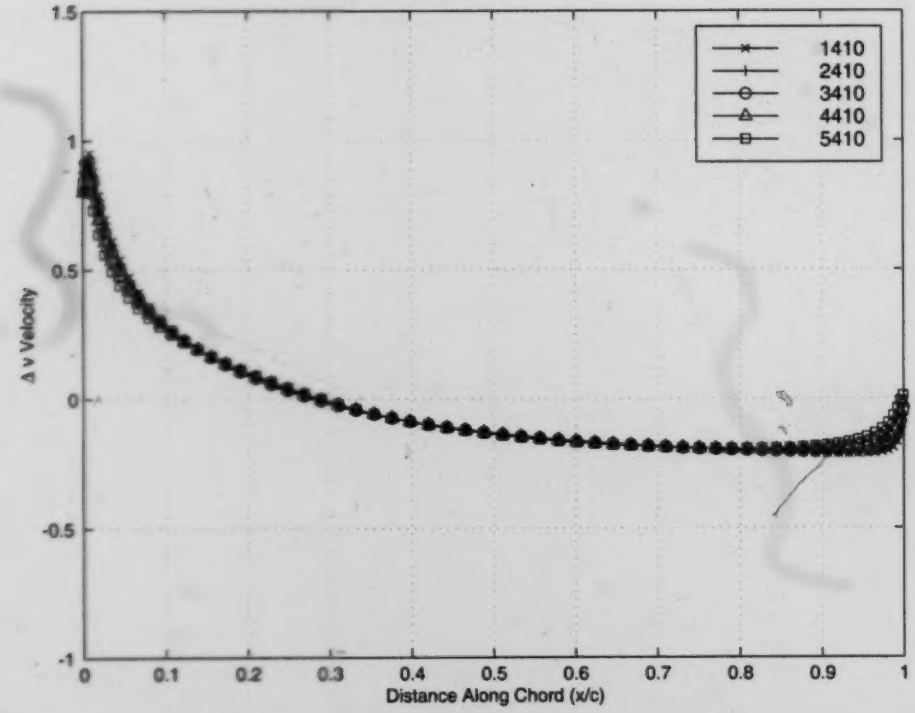

Figure 2.26: Δv Velocities Of NACA 4-Digit Airfoils With Changing Camber Lines

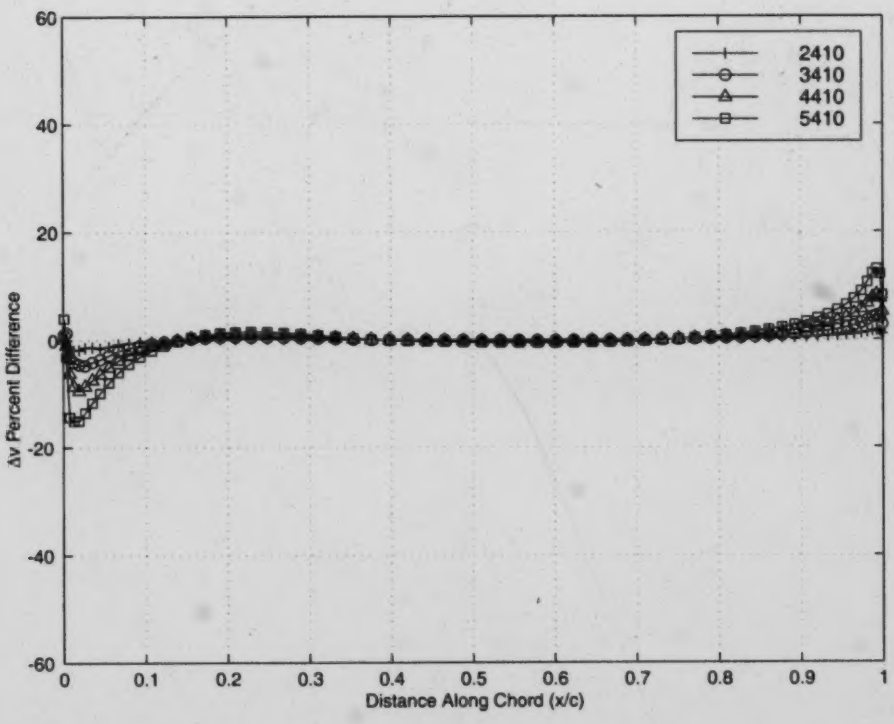

Figure 2.27: Difference In Δv Velocities Of NACA 4-Digit Airfoils With Changing Camber Lines

the 1% high camber line. The 1.5% difference corresponds to the 5% high camber line. The general trend from 14% chord to 38% chord is increasing percent difference with increasing camber line height. From 38% chord to 74% chord, the largest percent difference occurs at 58% chord. The range of differences at 58% chord is from -0.6% to -0.1%. The -0.6% difference corresponds to the NACA 5410 airfoil. The -0.1% difference corresponds to the NACA 2410 airfoil. The general trend from 38% chord to 74% chord is decreasing percent difference with increasing camber line height. Between 74% chord and the trailing edge, the maximum percent difference occurs at 99% of the length of the chord. The difference at 99% chord ranges from 1.6% to 13.0%. The 1.6% difference corresponds to the 1% high camber line. The 13.0% difference corresponds to the 5% high camber line. The general trend from 74% chord to 100% chord is increasing percent difference with increasing camber line height.

The analysis of the second group of NACA 4-digit airfoils proves that there is a definite relationship between specific velocities and specific airfoil characteristics. The analysis of five different thickness distributions show that only the $\bar{u}$ and Δv velocities are largely influenced by changing thickness distribution and that the Δu and $\bar{v}$ velocities remain relatively constant for a constant camber line. Conversely, the analysis of the five different camber lines show that only the Δu and $\bar{v}$ velocities are largely influenced by changing camber line height and that the $\bar{u}$ and Δv velocities remain relatively constant for a constant thickness distribution. These calculations suggest that thickness distributions can be designed by $\bar{u}$ and Δv velocities alone. These calculations also suggest that camber lines can be designed

by Δu and $\bar{v}$ velocities alone. Looking at the two groups of NACA 4-digit airfoils, there is no doubt of the fact that thickness distributions are related only to a single pair of surface velocity combinations, and camber lines are related only to the second pair of surface velocity combinations.

2.2 NACA 5-Digit 16-Series Airfoils

In comparing the average and difference combinations of the surface velocities instead of the velocities on their own, a distinct pattern has formed. Only two of the four quantities, namely $\bar{u}$ and Δv are strongly effected by changing thickness. The other two components, Δu and $\bar{v}$, are changed far less when comparing airfoils with constant camber. These characteristic trends that occur may be the constraint needed to maintain the original camber but still design for thickness. There is, however, the possibility that this characteristic trending is present in NACA 4-digit series airfoils only. This possibility may be due to the fact that the distributions are generated with a single set of equations, Equations 2.5 and 2.6. To test whether or not the averaged and differenced velocity phenomena only applies to 4-digit airfoils, a second family is tested. The second group of airfoils are the NACA 5-digit 16-series airfoils[1],[22]. This group of airfoils are also mathematically defined, but the functions used to calculate the thickness and camber are different from the 4-digit series. For a 5-digit 16-series airfoil, the maximum thickness is located at mid-chord, and the thickness distribution[22] is described in two parts as

$$\left(\frac{y}{c}\right)_{th} = \begin{cases} a_0\left(\frac{x}{c}\right)^{\frac{1}{2}} + a_1\left(\frac{x}{c}\right) + a_2\left(\frac{x}{c}\right)^2 + a_3\left(\frac{x}{c}\right)^3 & ; \left(\frac{x}{c}\right) \leq 0.5 \\ d_0 + d_1\left(1 - \frac{x}{c}\right) + d_2\left(1 - \frac{x}{c}\right)^2 + d_3\left(\frac{x}{c}\right)^3 & ; \left(\frac{x}{c}\right) \geq 0.5 \end{cases} \tag{2.25}$$

where $a_0, \cdots, a_3$ and $d_0, \cdots, d_3$ are coefficients determined from boundary conditions such as surface height, slope, and curvature and can be shown to become

$$d_0 = 0.010T$$

$$
\begin{aligned}
d_1 &= 2.325T \\
d_2 &= -3.420T \\
d_3 &= 1.460T \\
a_0 &= 0.990T \\
a_1 &= -0.239T \\
a_2 &= -0.041T \\
a_3 &= -0.559T
\end{aligned}
$$

where T is the thickness to chord ratio. The camber line[22] of the 5-digit 16-series airfoil is expressed as

$$\left(\frac{y}{c}\right)_{cl} = \frac{c_{l,i}}{4\pi}\left(1-\frac{x}{c}\right)^2 \ln\left(1-\frac{x}{c}\right) \tag{2.26}$$

where $c_{l,i}$ is called the design lift coefficient[22] and is given by

$$c_{l,i} = \frac{3M_i}{2} \tag{2.27}$$

where M_i is the camber index designated by the airfoil name. The thickness to chord ratio (T) and camber index (M_i) are determined from the NACA 5-digit 16-series designation[22] as follows

$$
\begin{aligned}
&\text{NACA} \quad 16-abc \\
M_i &= \tfrac{a}{10} \\
T &= \tfrac{cd}{100}
\end{aligned}
$$

A NACA 16-310 has a camber line with an index of 3 and a maximum thickness of 10%. A NACA 16-310 can be seen in Figure 2.28.

The five 5-digit 16-series airfoils that were tested were the 16-306, 16-308, 16-310, 16-312, and 16-314 airfoils. Both the camber lines and the thickness

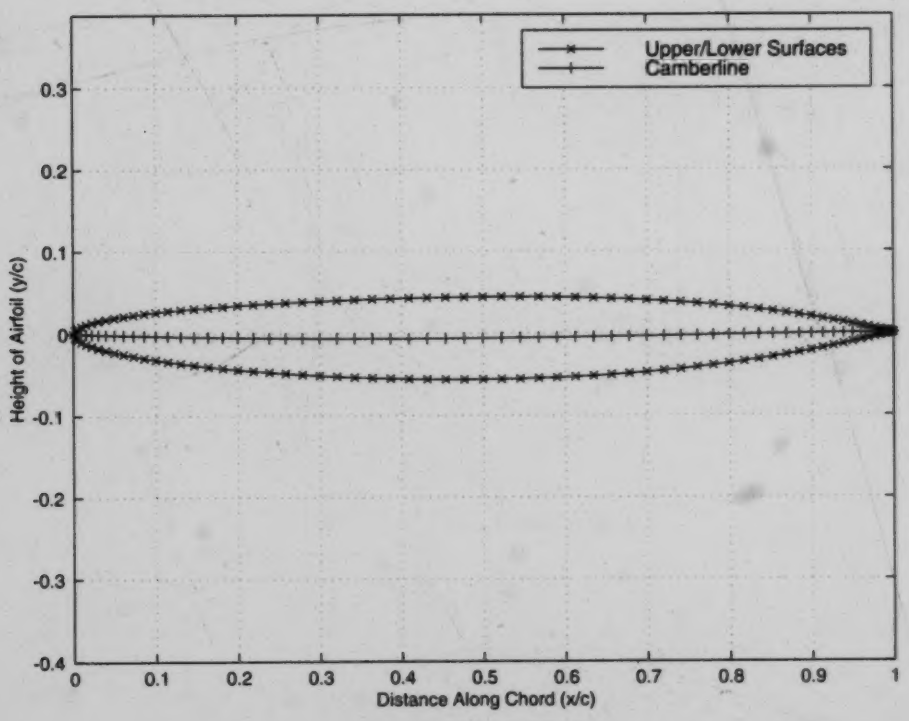

Figure 2.28: NACA 16-310 Airfoil

distributions of the 5-digit 16-series airfoils are calculated differently from the 4-digit airfoils. All five airfoils have identical camber lines and the range of thicknesses used can be seen in Figure 2.29.

As with the previous analysis of the NACA 4-digit airfoils, the focus shifts to determining the effect that changing thickness distributions have on the velocity quantities of $\bar{u}$, Δu, $\bar{v}$ and Δv. From the analysis of the 4-digit airfoils, it is obvious that there is a distinct separation between the $\bar{u}$ and Δv velocities being affected by increasing thickness and the Δu and $\bar{v}$ velocities

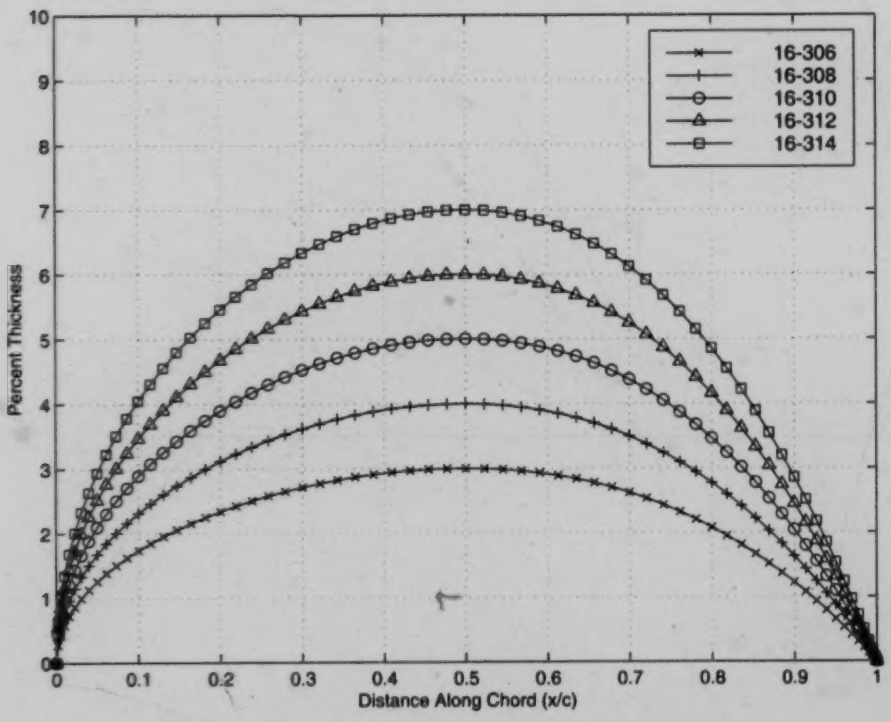

Figure 2.29: Thickness Distributions Of NACA 5-Digit 16-Series Airfoils

remaining relatively constant for a constant camber line. The four $\bar{u}$, Δu, $\bar{v}$ and Δv velocity quantities are calculated with Equations 2.13, 2.14, 2.15 and 2.16 respectively.

The first velocity combination for thickness comparison is the $\bar{u}$ velocity. As the thickness is increased, there is a noticeable effect. The $\bar{u}$ velocities share two common intersection points. The first point occurs at approximately 2% chord and the second at 91% chord. The five $\bar{u}$ velocities can be seen in Figure 2.30.

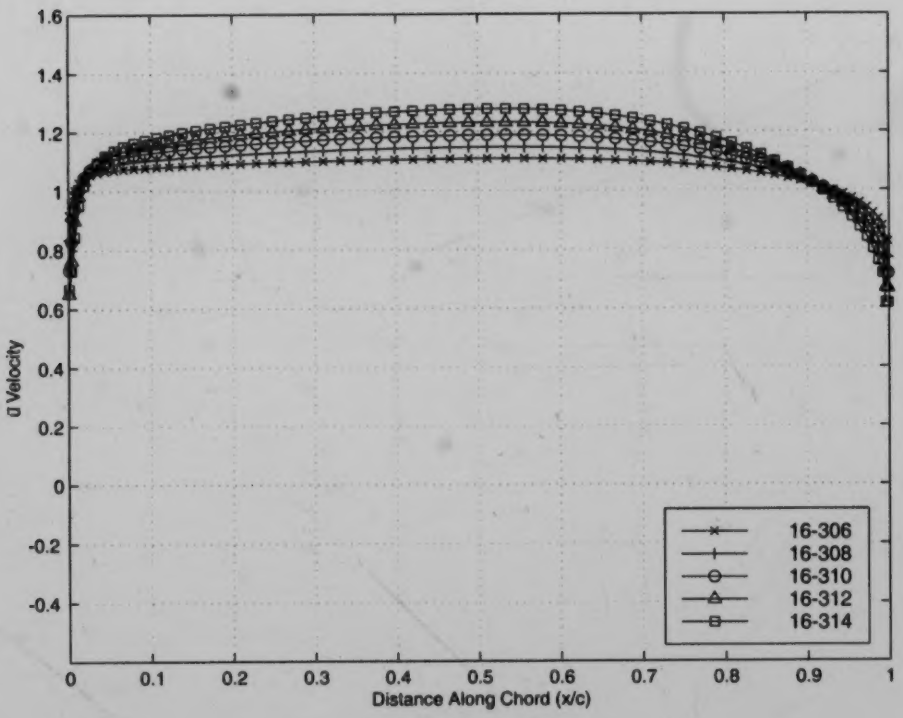

Figure 2.30: $\bar{u}$ Velocities Of NACA 5-Digit 16-Series Airfoils

In order to calculate the effect that the increasing thickness ratio has on the $\bar{u}$ velocities, the 6% thick, or NACA 16-306 airfoil velocity is chosen as the base velocity. The percent difference of the remaining four velocities is calculated using Equation 2.17. The resulting differences can be seen in Figure 2.31.

On the $\bar{u}$ velocity difference plot there are two locations where the percent difference is equal to zero. These two locations occur at 2% chord and at 91% chord. Between 2% of the chord length and 91% of the chord length, the maximum percent difference occurs at 52% chord. The range of percent difference at 52% chord is from 3.9% to 16.9%. The 3.9% difference corresponds to the thinnest remaining airfoil, the NACA 16-308. The 16.9% difference corresponds to the thickest airfoil, the NACA 16-314. The general trend from 2% of the chord to 91% chord is increasing percent difference with increasing thickness distribution. From 91% chord to the trailing edge, the general trend is reversed. The maximum percent difference between 91% chord and 100% chord occurs at the trailing edge. The range of percent difference at the trailing edge of the velocities is from -18.6% to -4.9%. The -18.6% difference corresponds to the 14% thick airfoil, and the -4.9% difference corresponds to the 8% thick airfoil. This range of differences creates a general trend of decreasing percent difference with increasing thickness ratio from 91% chord to the trailing edge.

The second set of velocities compared are the Δu velocities. As with the NACA 4-digit airfoils, the Δu velocities appear very similar for the entire series of different thicknesses. As Figure 2.32 shows, the five separate Δu velocities appear identical.

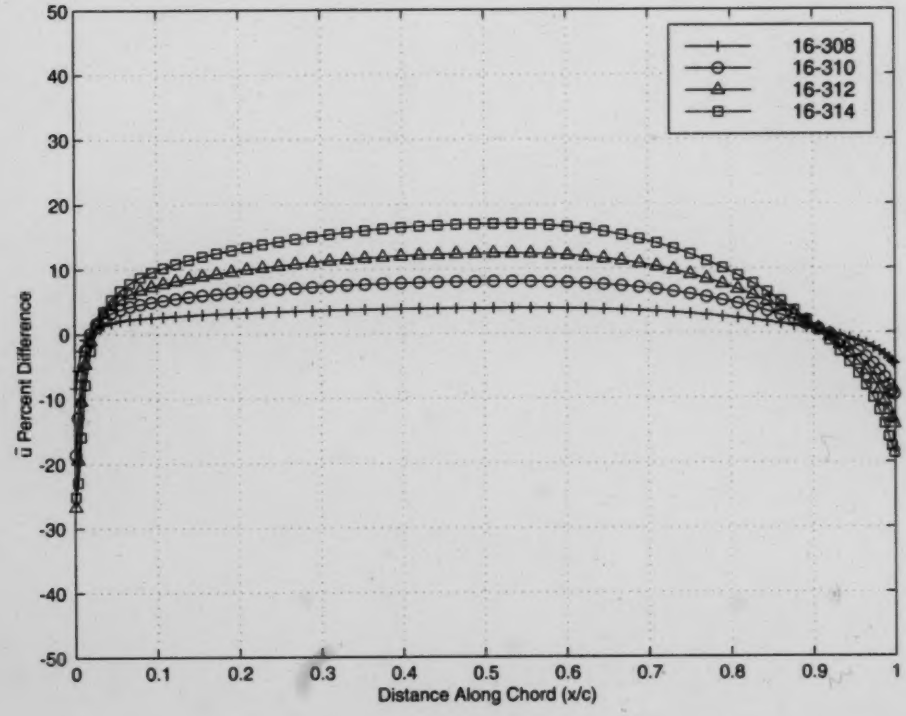

Figure 2.31: Difference In $\bar{u}$ Velocities Of NACA 5-Digit 16-Series Airfoils

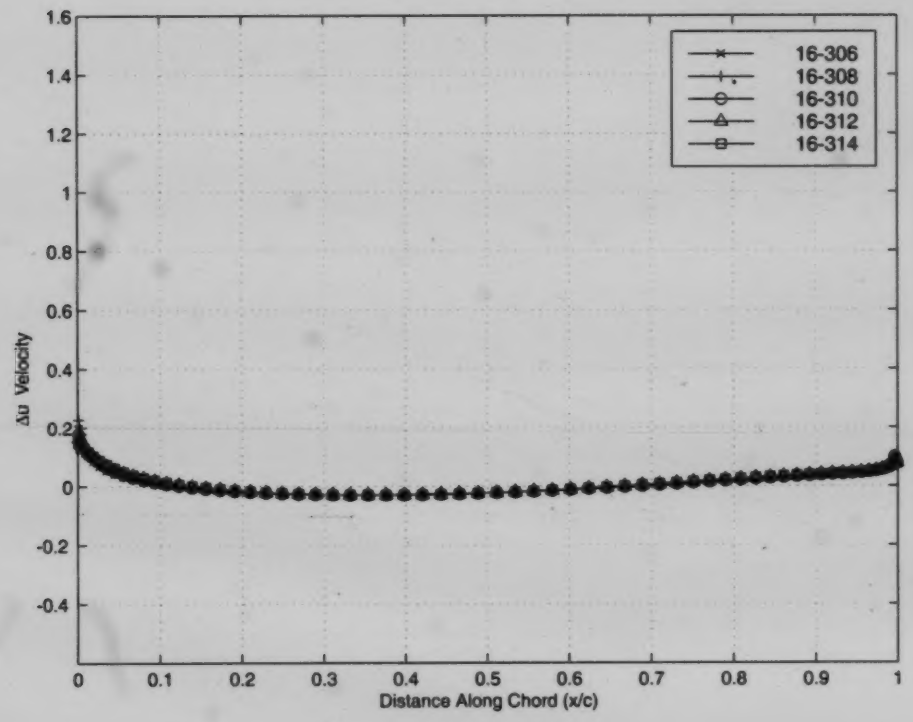

Figure 2.32: Δu Velocities Of NACA 5-Digit 16-Series Airfoils

The base airfoil chosen for comparison of the Δu velocities is again the 6% thick airfoil, the NACA 16-306. The percent difference of the other four velocities is calculated using Equation 2.18. The velocity difference plot of the Δu velocities can be seen in Figure 2.33.

The entire range of Δu velocity differences is quite narrow. The largest separation between the highest and lowest difference for the entire group is less than 2%. There are two locations where the four differences of velocity coincide with a magnitude of zero. These two points are at 31% of the chord length and at 52% of the chord length. These two zero-difference points effectively divide the plot into three sections. The first section, from 0% chord to 31% chord, displays the largest differences. The maximum percent difference in this region occurs at 3% chord. The range of percent differences at 3% chord is from 0.4% to 1.9%. The 0.4% difference corresponds to the airfoil 2% thicker than the base airfoil. The 1.9% difference corresponds to the airfoil 8% thicker than the base airfoil. The general trend from the leading edge to 31% chord is increasing percent difference with increasing thickness ratio. The second section exists from 31% chord to 52% chord and all four differences of velocity are confined within a tenth of a percent of zero. The largest percent difference in this region occurs at 41% of the chord length. The range of percent difference is from -0.1% to 0.0%. The -0.1% corresponds to the thickest airfoil, the NACA 16-314. The 0.0% difference corresponds to the thinnest remaining airfoil, the NACA 16-308. The general trend from 31% chord to 52% chord is decreasing percent difference with increasing thickness ratio. The third and final section of the Δu velocity difference plot lasts from 52% chord to the trailing edge. The maximum

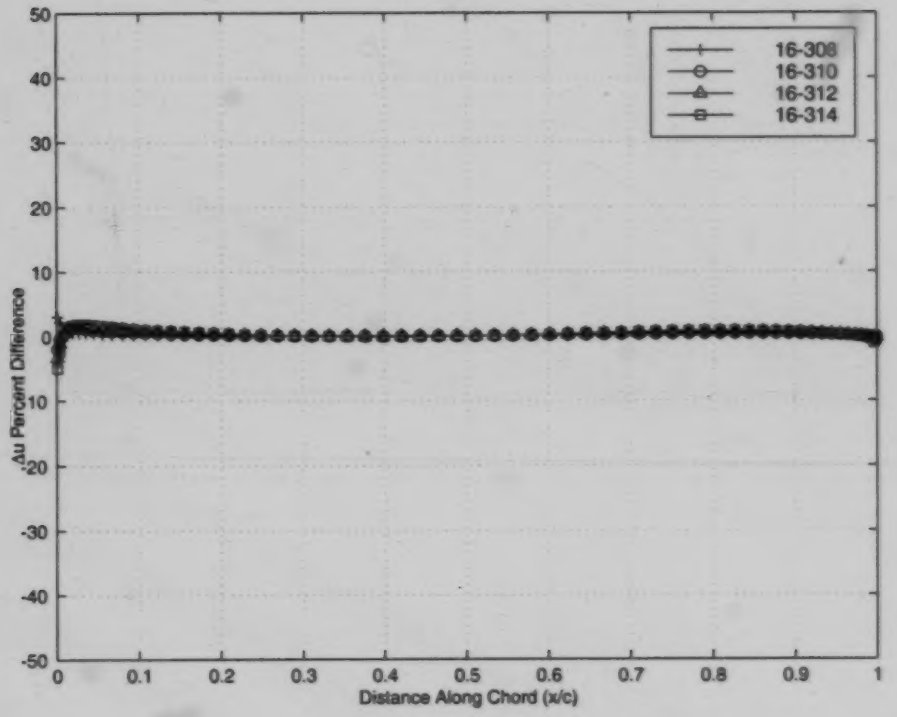

Figure 2.33: Difference In Δu Velocities Of NACA 5-Digit 16-Series Airfoils

percent difference in this region occurs at 82% chord. The percent difference at 82% chord ranges from 0.2% to 0.8%. The 0.2% difference corresponds to the 8% airfoil. The 0.8% difference corresponds to the 14% thick airfoil. The general trend from 52% chord to 100% chord is increasing percent difference with increasing airfoil thickness.

The third combination of surface velocity components that was analyzed for a dependence on thickness ratio are the $\bar{v}$ velocities. The $\bar{v}$ velocities seem to be affected by thickness ratio as little as the Δv velocities. As with the Δv velocities, all five $\bar{v}$ velocities appear to be equal. The five velocities corresponding to the five different airfoil thicknesses can be seen in Figure 2.34.

For comparison, the NACA 16-306 airfoil is chosen as the base airfoil. The remaining four velocities are used to calculated a percent difference from the base $\bar{v}$ velocity using Equation 2.19. The difference of the $\bar{v}$ velocities can be seen in Figure 2.35.

For the entire chord length, the largest difference between the base velocity and the remaining velocities is less than 2.5%. There are three locations where the percent difference for all four remaining velocities is equal to zero. These three locations occurs at 8% chord length, 38% chord length and 80% chord length. The three intersection points of zero difference separate the plot into four sections. In the first region, from the leading edge to 8% of the chord length, the maximum difference in the velocities occurs at 0% chord. The range of differences is from 0.1% to 2.4%. The 0.1% difference corresponds to the thinnest remaining airfoil, the NACA 16-308. The 2.4% difference corresponds to the thickest airfoil, the NACA 16-314. The general

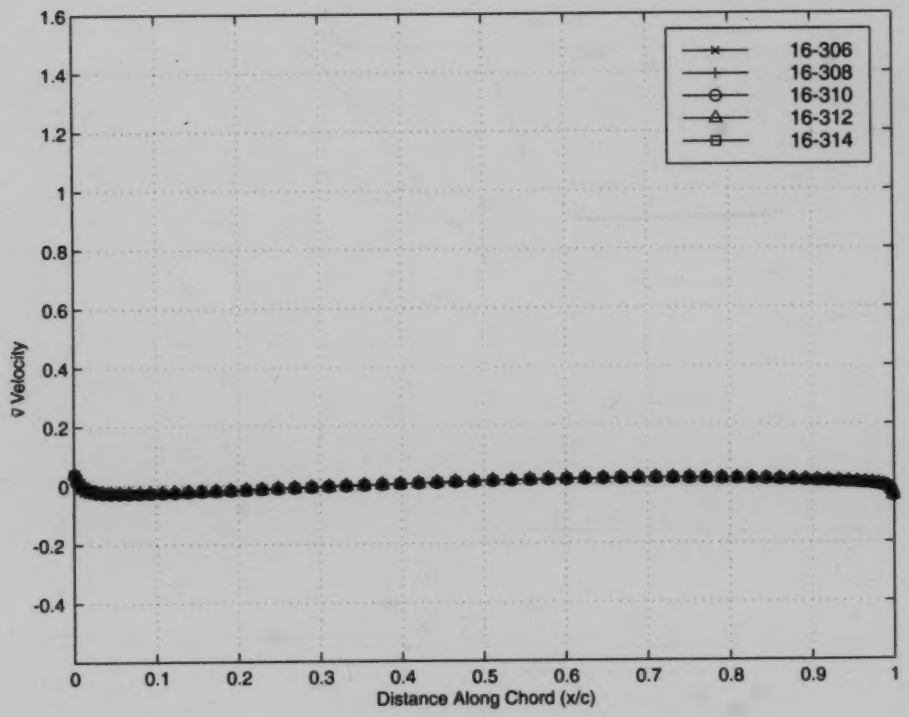

Figure 2.34: $\bar{v}$ Velocities Of NACA 5-Digit 16-Series Airfoils

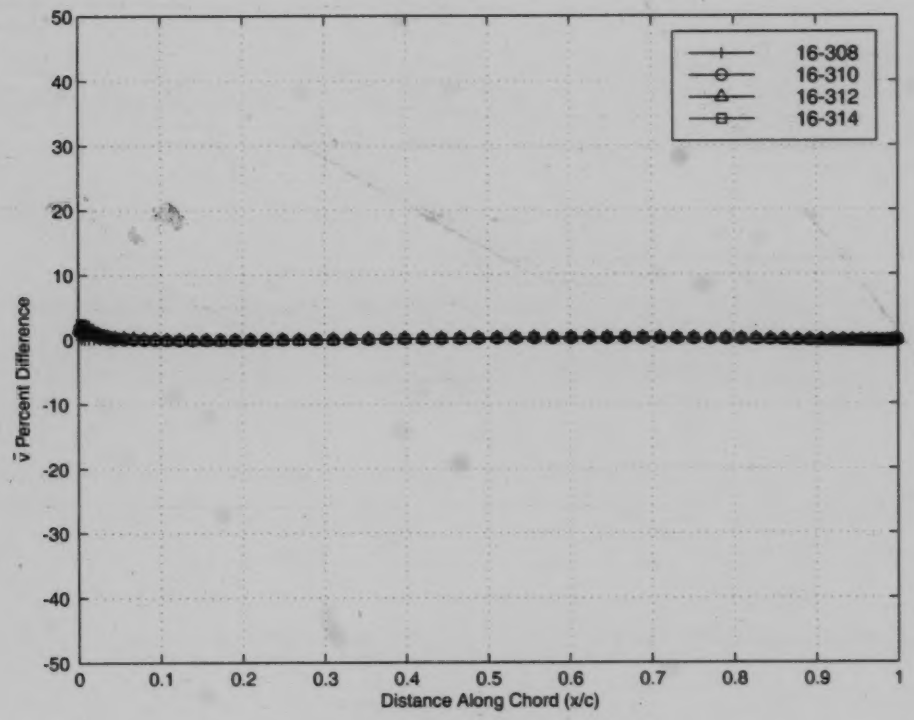

Figure 2.35: Difference In $\bar{v}$ Velocities Of NACA 5-Digit 16-Series Airfoils

trend from 0% chord to 8% chord is increasing percent difference with increasing thickness ratio. The second region is from 8% of the chord to 38% of the chord. The largest difference of the velocities in this region occurs at 21% of the chord. The range of differences at 21% chord length is from -0.3% to -0.1%. The -0.3% difference corresponds to the 14% thick airfoil. The -0.1% difference corresponds to the 8% thick airfoil. The general trend from 8% chord to 38% chord is decreasing percent difference with increasing thickness, although the maximum difference in the velocities only has a range of 0.2%. The third section lasts from 38% chord to 80% chord. This region also has a very small range of difference in velocity. The maximum difference occurs at 63% of the chord length. The range of differences at 63% chord is from 0.1% to 0.2%. The 0.1% difference corresponds to the airfoil 2% thicker than the base airfoil. The 0.2% difference corresponds to the airfoil 8% thicker than the base airfoil. The general trend from 38% chord length to 80% chord length is increasing percent difference with increasing airfoil thickness. The fourth and final section exists from 80% of the chord to the trailing edge. The greatest percent difference in this section occurs at 99% of the chord. The range of percent difference at 99% chord length is from -0.5% to -0.1%. The -0.5% difference corresponds to the NACA 16-314 airfoil. The -0.1% difference corresponds to the NACA 16-308 airfoil. The general trend from 80% chord to 100% chord is decreasing percent difference with increasing thickness.

The fourth and final velocity compared is the Δv velocity. The Δv velocities are similar only in shape. There is a large range of different velocities for the different airfoils. All five of the velocities do share a common point,

at 47% of the chord length. The five Δv velocities can be seen in Figure 2.36.

The base velocity of the Δv comparison corresponds to the NACA 16-306 airfoil. The percent difference of the remaining velocities is calculated with Equation 2.20. The four differences of the Δv velocities can be seen in Figure 2.35.

The common intersection of all four of the differences in velocity at 47% chord creates two nearly equal sections with opposite trends. The first region, from 0% chord to 47% of the chord length has maximum differences at the leading edge. The range of differences at 0% chord is from 14.8% to 51.7%. The 14.8% difference corresponds to the 8% thick airfoil. The 51.7% difference corresponds to the 14% thick airfoil. The general trend from 0% of the chord to 47% of the chord is increasing percent difference with increasing thickness. The second portion of the differences in Δv velocities lasts from 47% to the trailing edge. The largest percent differences in this region occur at 92% of the chord length. The range of differences at 92% chord is -29.7% to -7.7%. The -29.7% difference corresponds to the NACA 16-314 airfoil. The -7.7% difference corresponds to the NACA 16-308 airfoil. The general trend from 47% chord to 100% chord is decreasing percent difference with increasing airfoil thickness.

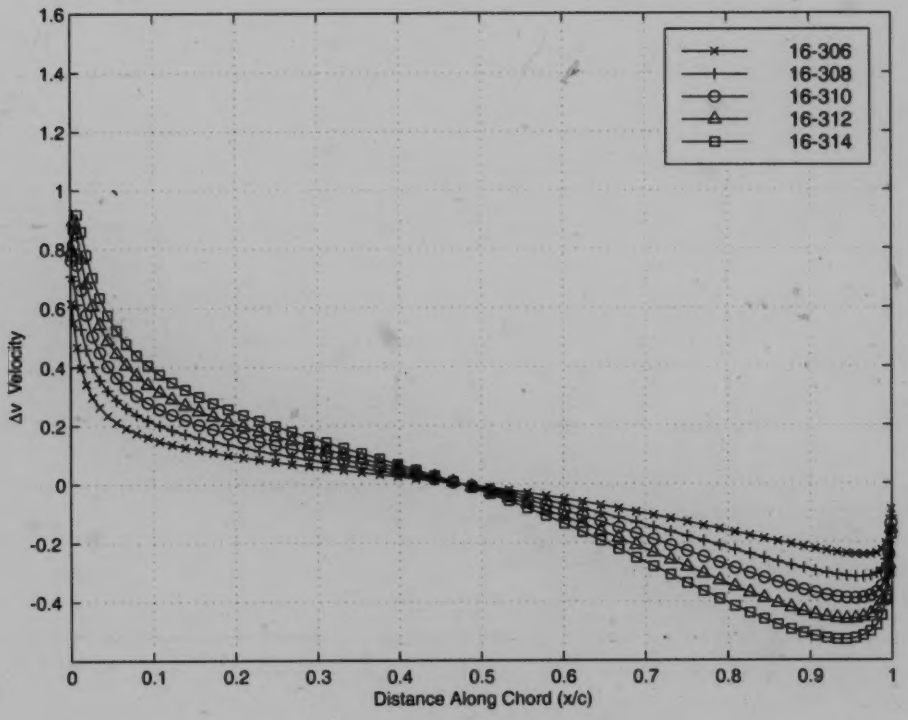

Figure 2.36: Δv Velocities Of NACA 5-Digit 16-Series Airfoils

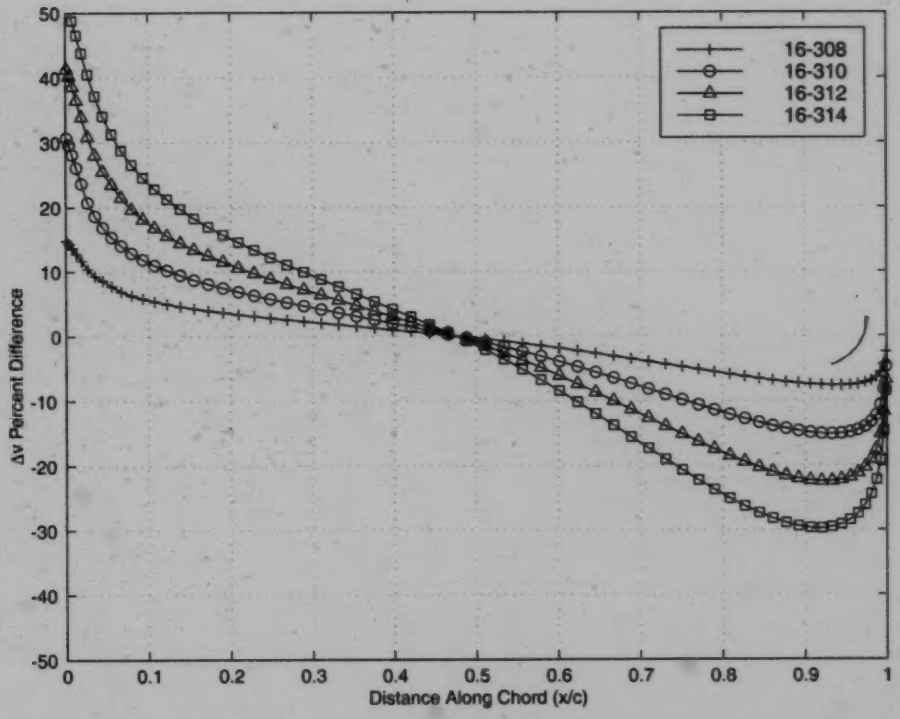

Figure 2.37: Difference In Δv Velocities Of NACA 5-Digit 16-Series Airfoils

2.3 NACA 4-Digit-Modified Airfoils

The use of NACA 4-digit and 5-digit 16-series airfoils show how increasing the thickness affects certain velocity quantities. For each of the two groups the thickness functions are distinct and merely scaled to create the test airfoils. There still exists the possibility that the characteristic surface velocity effect is not independent of airfoil type. To test this theory, a third group of airfoils were chosen where the thickness function was different for each airfoil. The NACA 4-digit-modified series[1],[22] of airfoils has the ability to not only create a series airfoils with increasing thickness, but the location of maximum thickness can be changed for each airfoil as well. This series of airfoils can describe a much larger range.

NACA 4-digit-modified airfoils have a thickness distribution similar to 5-digit 16-series airfoils defined[22] as

$$\left(\frac{y}{c}\right)_{th} = \begin{cases} a_0\left(\frac{x}{c}\right)^{\frac{1}{2}} + a_1\left(\frac{x}{c}\right) + a_2\left(\frac{x}{c}\right)^2 + a_3\left(\frac{x}{c}\right)^3 & ; \left(\frac{x}{c}\right) \leq M_{th} \\ d_0 + d_1\left(1-\frac{x}{c}\right) + d_2\left(1-\frac{x}{c}\right)^2 + d_3\left(\frac{x}{c}\right)^3 & ; \left(\frac{x}{c}\right) \geq M_{th} \end{cases} \tag{2.28}$$

where $a_0, \cdots, a_3$ and $d_0, \cdots, d_3$ are coefficients determined from boundary conditions and M_{th} is the location of maximum thickness. The boundary conditions used to solve for the thickness coefficients used in Equation 2.28 include maximum thickness, slope and curvature of airfoil surface, and leading edge radius[22] as determined by

$$R_{LE} = \frac{a_0^2}{2} = 1.1019\left(\frac{TI}{6}\right)^2 \tag{2.29}$$

where R_{LE} is the leading edge radius, a_0 is the coefficient from Equation 2.28, T is the maximum thickness, and I is the leading edge radius index

number. If the leading edge radius index is equal to zero (0), a sharp leading edge is present, while a six (6) refers to a leading edge radius matching that of the 4-digit series airfoils. Typically 6 is the largest index number used.

For 4-digit-modified airfoils the slope of the airfoil surface at the trailing edge of airfoil is controlled by the location of maximum thickness, according to Table 2.1[22].

M_{th}	d_1
0.2	0.200
0.3	0.234
0.4	0.315
0.5	0.465
0.6	0.700

Table 2.1: NACA 4-Digit-Modified TE Slopes

The camber line of a 4-digit-modified airfoil is calculated and determined in the same way as a 4-digit camber line. The exact function used to generate the camber line can be seen in Equation 2.6. The quantities of thickness (T), maximum camber (P), maximum camber location (M), maximum thickness location (M_{TH}) and leading edge radius index (I) are determined from the NACA four digit designation[22] as follows

$$
\begin{aligned}
\text{NACA} \quad & abcd - ef \\
P &= \tfrac{a}{100} \\
M &= \tfrac{b}{10} \\
T &= \tfrac{cd}{100} \\
I &= e \\
M_{th} &= \tfrac{f}{10}
\end{aligned}
$$

A NACA 3410-44 airfoil has a maximum camber of 3% ($P = 0.03$) located at 40% chord ($M = 0.40$), a maximum thickness of 10% ($T = 0.10$) located at 40% chord ($M_{th} = 0.40$) and a leading edge radius index of 4 ($I = 4$). A NACA 3410-44 airfoil can be seen in Figure 2.38.

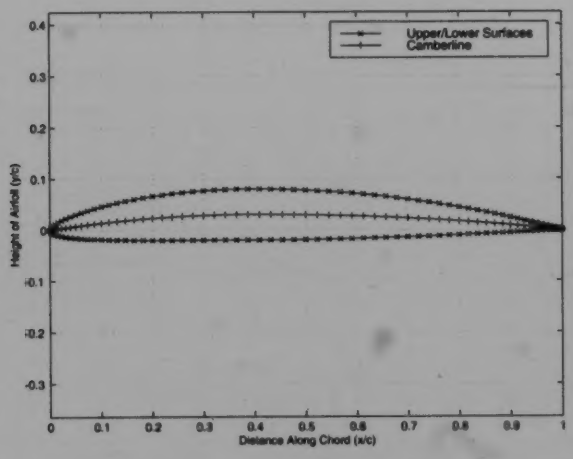

Figure 2.38: NACA 3410-44 Airfoil

The series of 4-digit-modified airfoils analyzed were the 3406-42, 3408-43, 3410-44, 3412-45, and 3414-46 airfoils. The different thickness distributions

created by changing both maximum thickness and maximum thickness location can be seen in Figure 2.39.

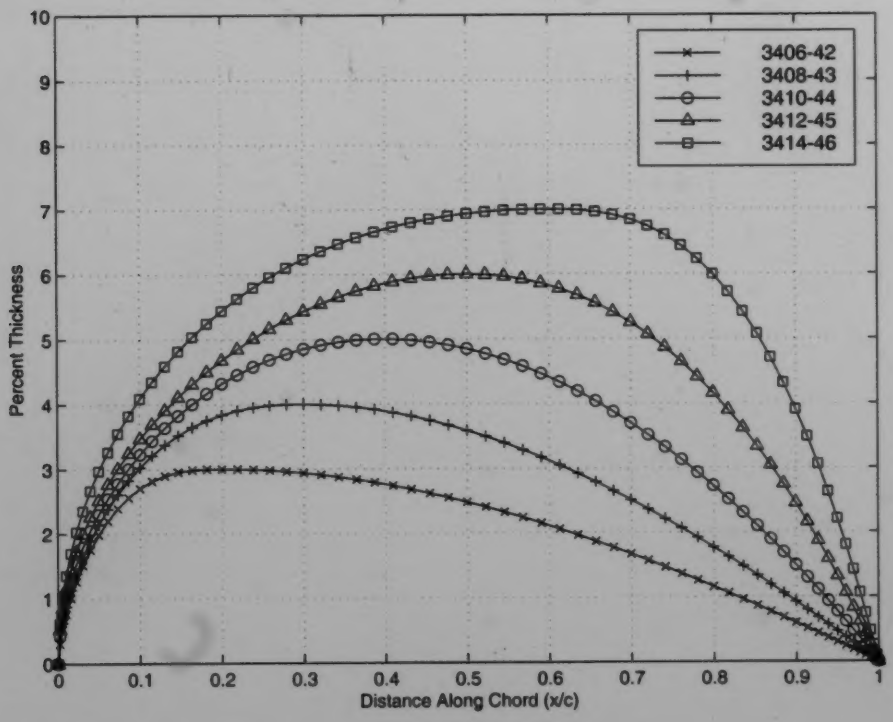

Figure 2.39: Thickness Distributions Of NACA 4-Digit-Modified Airfoils

The $\bar{u}$ velocity is the first velocity component that is used to compare the effect of different airfoil thicknesses. The five $\bar{u}$ velocities have a similar leading edge section, and all five share a common intersection point at approximately 90% of the length of the chord. The five $\bar{u}$ velocities can be seen in Figure 2.40.

The NACA 3406-42 airfoil is used as the base airfoil to calculate the

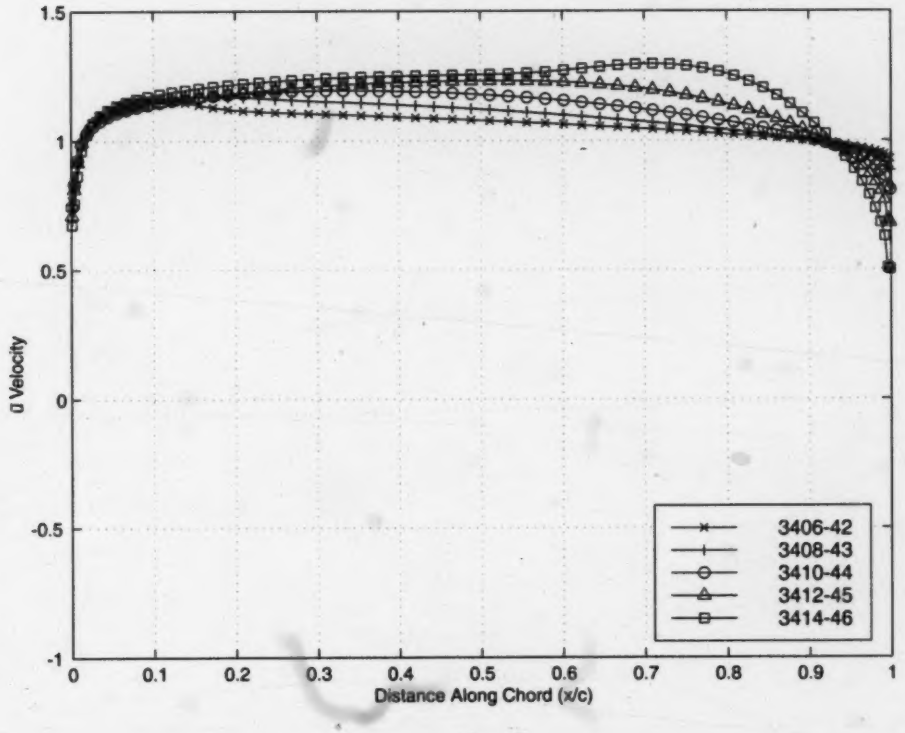

Figure 2.40: $\bar{u}$ Velocities Of NACA 4-Digit-Modified Airfoils

percent difference for each of the remaining airfoils. The percent difference is calculated using Equation 2.17. The difference in $\bar{u}$ velocities can be seen in Figure 2.41.

Although the leading edge portions of all four of the differences in velocity appear similar, there is only one location where the four differences coincide. The location of the zero difference intersection is at 93% chord. From the leading edge to 93% chord, the maximum percent difference occurs at 73% of the chord length. The range of differences at 93% chord is from 2.4% to 25.5%. The 2.4% difference corresponds to the 8% thick airfoil. The 25.5% difference corresponds to the 14% thick airfoil. The general trend from 0% chord to 93% chord is increasing percent difference with increasing thickness ratio. From 93% chord to the trailing edge, the largest difference occurs at 100% of the length of the chord. The range of percent differences in $\bar{u}$ velocity at the trailing edge is from -38.2% to -3.8%. The -38.2% difference corresponds to the thickest airfoil. The -3.8% difference corresponds to the thinnest remaining airfoil. The general trend from 93% chord to 100% chord is decreasing percent difference with increasing airfoil thickness.

The second velocity component compared is the Δu velocity. As with previous airfoil groups, the Δu velocity changes comparatively little with different thickness distributions. In Figure 2.42 the five Δu velocities appear to be nearly identical except for the last 25% of the chord. Figure 2.42 shows the Δu velocities corresponding to the five analysis airfoils.

For comparison, the NACA 3406-42 airfoil is chosen as the base airfoil. The percent difference of the four remaining airfoils is calculated using Equation 2.18. The difference in the Δu velocities can be seen in Figure 2.43.

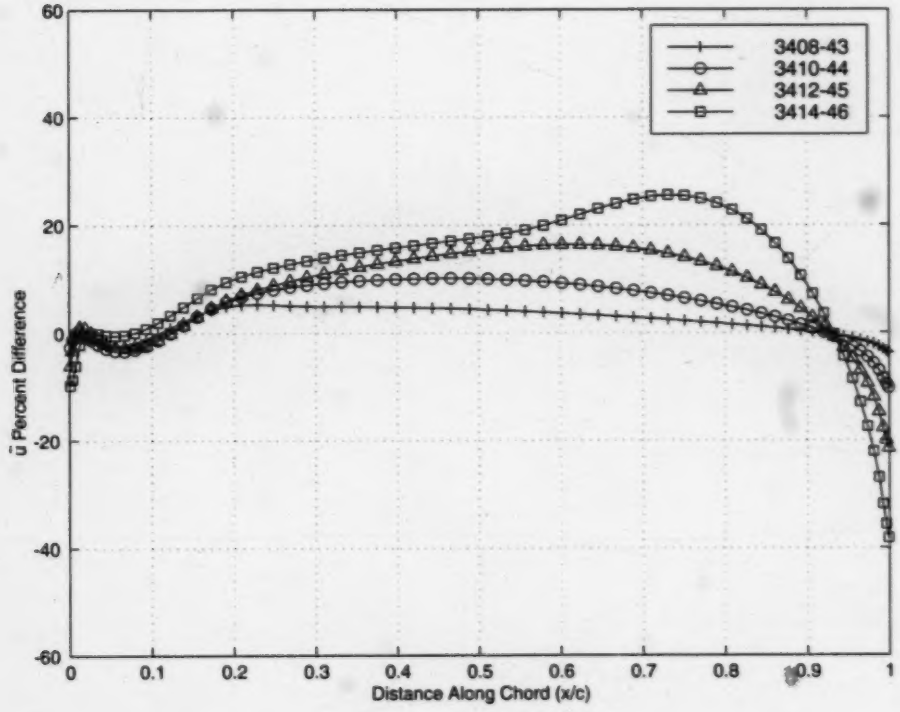

Figure 2.41: Difference In $\bar{u}$ Velocities Of NACA 4-Digit-Modified Airfoils

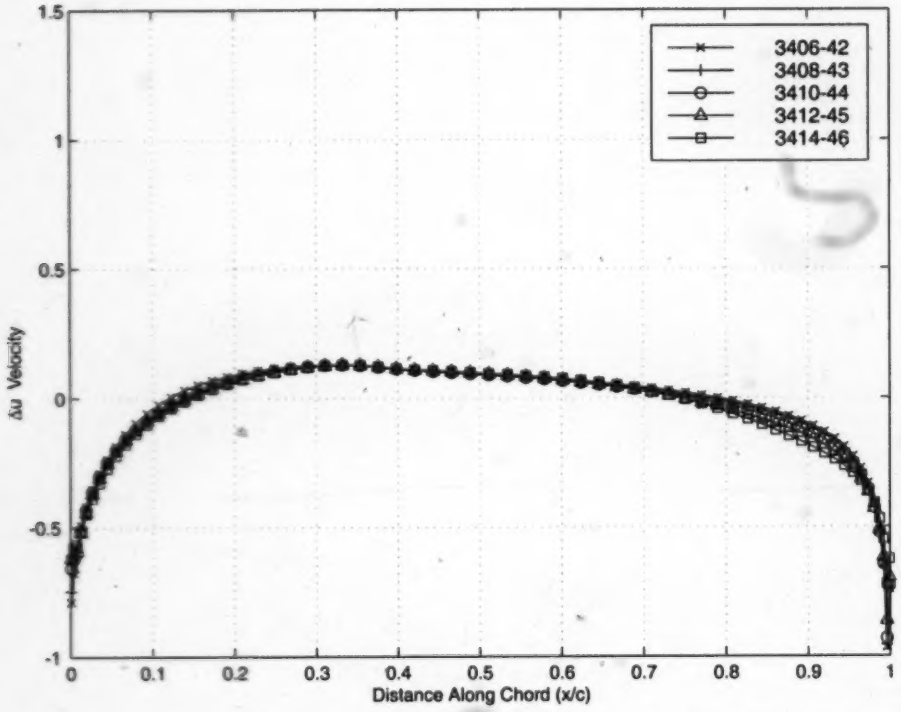

Figure 2.42: Δu Velocities Of NACA 4-Digit-Modified Airfoils

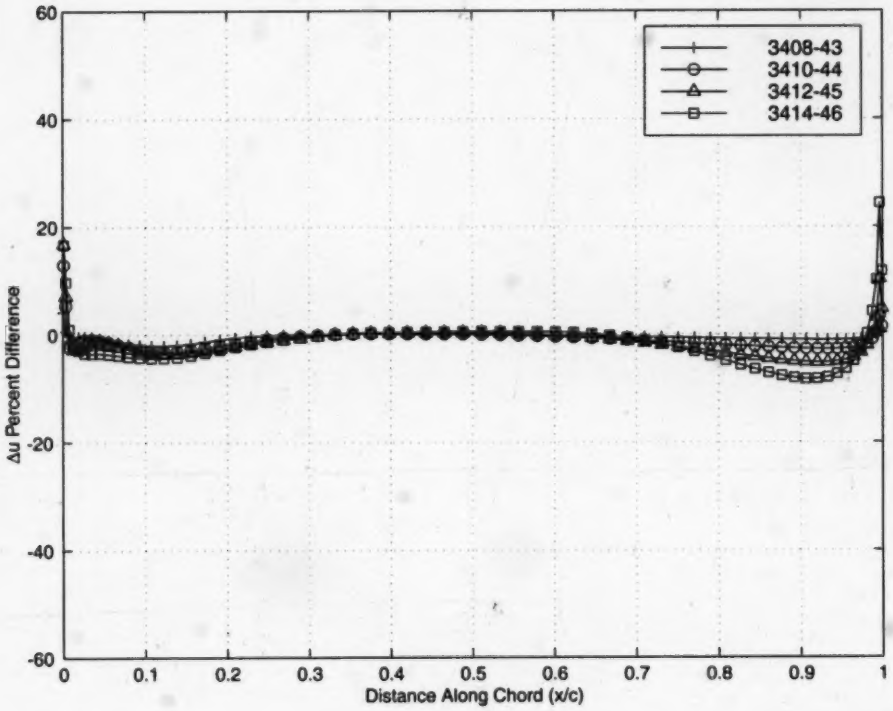

Figure 2.43: Difference In Δu Velocities Of NACA 4-Digit-Modified Airfoils

Neglecting the leading edge and trailing edge velocity spikes, there is one location where the four differences in velocity intersect with zero percent difference. This intersection occurs at 35% chord. There is also an inflection point for each of the four differences at approximately 70% of the chord, but there is no second intersection point. The largest difference between the leading edge and 35% of the chord length occurs at 11% of the chord. The differences in Δu velocity at 11% chord range from -4.5% to -2.1%. The -4.5% difference corresponds to the airfoil 8% thicker than the base airfoil. The -2.1% difference corresponds to the airfoil 2% thicker than the base airfoil. The general trend from 0% chord to 35% chord is decreasing percent difference with increasing airfoil thickness. Between 35% chord and 70% chord, the maximum difference occurs at 52% chord. The range of percent difference at 52% of the chord length is from 0.0% to 0.5%. The 0.0% difference corresponds to the thinnest remaining airfoil. The 0.5% difference corresponds to the thickest airfoil. The general trend from 35% chord to 70% chord is increasing percent difference with increasing thickness ratio. The last portion of the Δu velocity plot lasts from 70% chord to the trailing edge. The largest percent difference between 70% and 100% of the chord occurs at 91% chord length. The range of percent differences at 91% chord is from -8.4% to -1.2%. The -8.4% difference corresponds to the NACA 3414-46 airfoil. The -1.2% difference corresponds to the NACA 3408-43 airfoil. The general trend from 70% chord to 100% chord is decreasing percent difference with increasing thickness.

The third velocity combination is the $\bar{v}$ velocity. The $\bar{v}$ velocities behave similarly to the Δu velocities. The velocities appear nearly identical until

the 80% chord location where the effect of the different thicknesses becomes more noticeable. The $\bar{v}$ velocities can be seen in Figure 2.44.

The base velocity used for the calculation of differences in $\bar{v}$ velocities corresponds to the NACA 3406-42 airfoil. The differences are calculated using Equation 2.19. Figure 2.44 shows the calculated differences in $\bar{v}$ velocity.

There are two locations where all four of the difference in $\bar{v}$ velocities intersect with zero percent difference. The two locations occur at 48% of the chord length, and at 86% of the chord length. The two common points effectively divide the difference plot into three sections. The first region, from the leading edge to 48% chord, has a maximum difference at 23% chord. The range of differences at 23% of the length of the chord is from 0.5% to 1.0%. The 0.5% difference corresponds to the NACA 3408-43 airfoil. The 1.0% difference corresponds to the NACA 3414-46 airfoil. The general trend from 0% chord to 48% chord is increasing percent difference with increasing airfoil thickness. The second region of the differences in $\bar{v}$ velocities is from 48% of the chord to 86% of the chord. The largest percent difference in this region occurs at 75% of the chord length. The differences at 75% chord range from -1.5% to -0.2%. The -1.5% difference corresponds to the thickest airfoil. The -0.2% difference corresponds to the thinnest remaining airfoil. The general trend from 48% chord to 86% chord is decreasing percent difference with increasing thickness. The third and final region extends from 86% chord to the trailing edge. The maximum percent difference in this third section occurs at 99% of the chord length. The range of percent differences at 99% of the chord is from 1.1% to 10.6%. The 1.1% difference corresponds to the airfoil 2% thicker than the base airfoil. The 10.6% difference corresponds

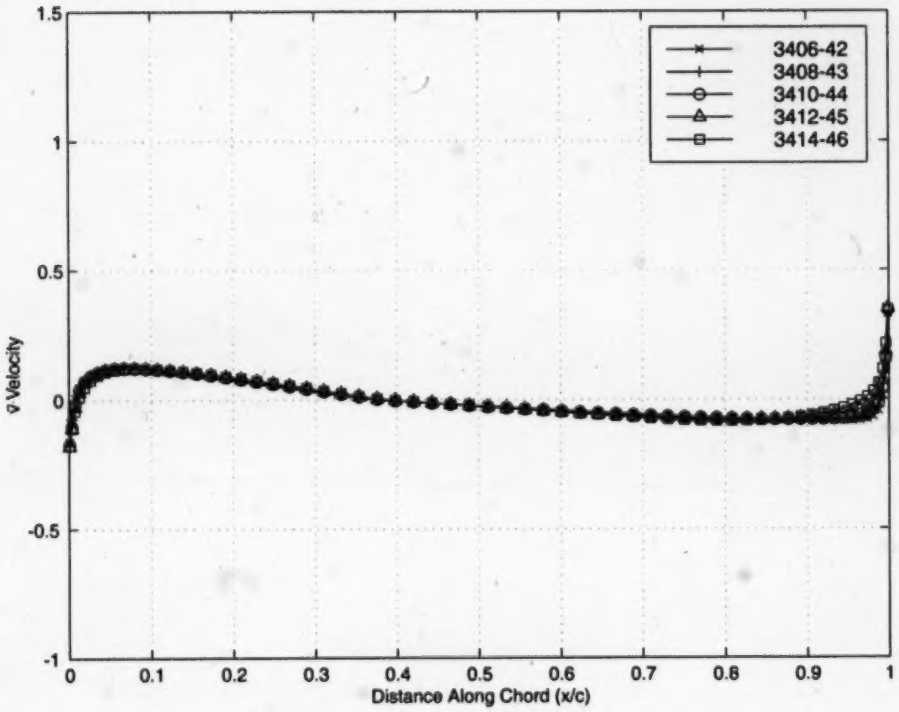

Figure 2.44: $\bar{v}$ Velocities Of NACA 4-Digit-Modified Airfoils

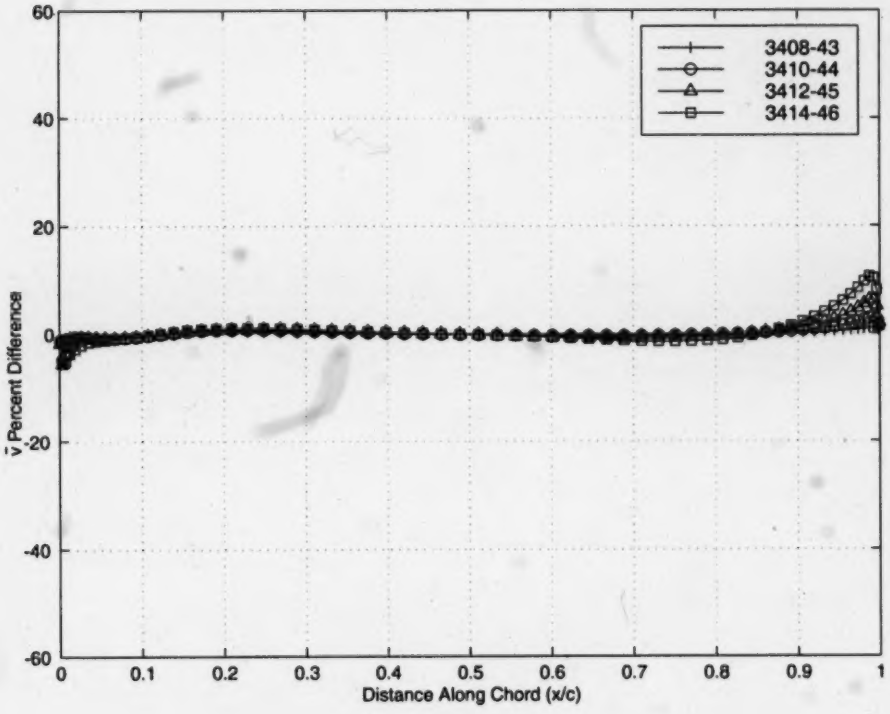

Figure 2.45: Difference In $\bar{v}$ Velocities Of NACA 4-Digit-Modified Airfoils

to the airfoil 8% thicker than the base airfoil. The general trend from 86% chord to 100% chord is increasing percent difference with increasing thickness ratio.

The fourth and final velocity component compared for thickness effects is the Δv velocity. The Δv velocities do not share any intersection points, and all five of the velocities have slightly different shapes. This is to be expected, as the five 4-digit-modified thickness distributions are not simply scaled versions of the same distribution. The five thickness distributions used for analysis in this group are airfoils have different maximum values, as well as different curves. The effect of the different thickness distributions has been seen to some extent in the previous comparison of other 4-digit-modified velocities, but the largest effect seems to have appeared in the Δv velocities. The Δv velocities corresponding to the 4-digit-modified airfoils can be seen in Figure 2.46.

The base velocity chosen for the Δv velocities is the 6% thick airfoil. The percent differences between the base velocity and the remaining four velocities is calculated using Equation 2.20. The difference in the Δv velocities can be seen in Figure 2.47.

Since there are no points where all four of the differences in velocities intersect, it is difficult to quantify the effect of the changing thickness ratios. There are two locations where the range of differences in the Δv velocity appear to be the largest. The first location is at 16% of the chord length. The range of differences at 16% chord is from 12.3% to 25.6%. The 12.3% difference corresponds to the 8% thick airfoil. The 25.6% difference corresponds to the 14% thick airfoil. The general trend at 16% of the chord is increasing

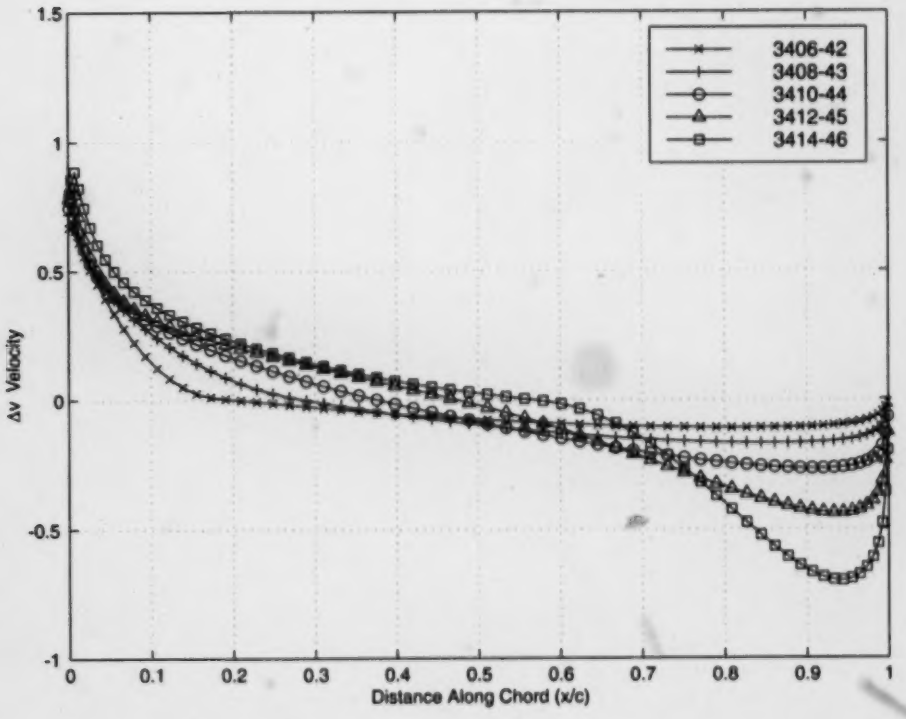

Figure 2.46: Δv Velocities Of NACA 4-Digit-Modified Airfoils

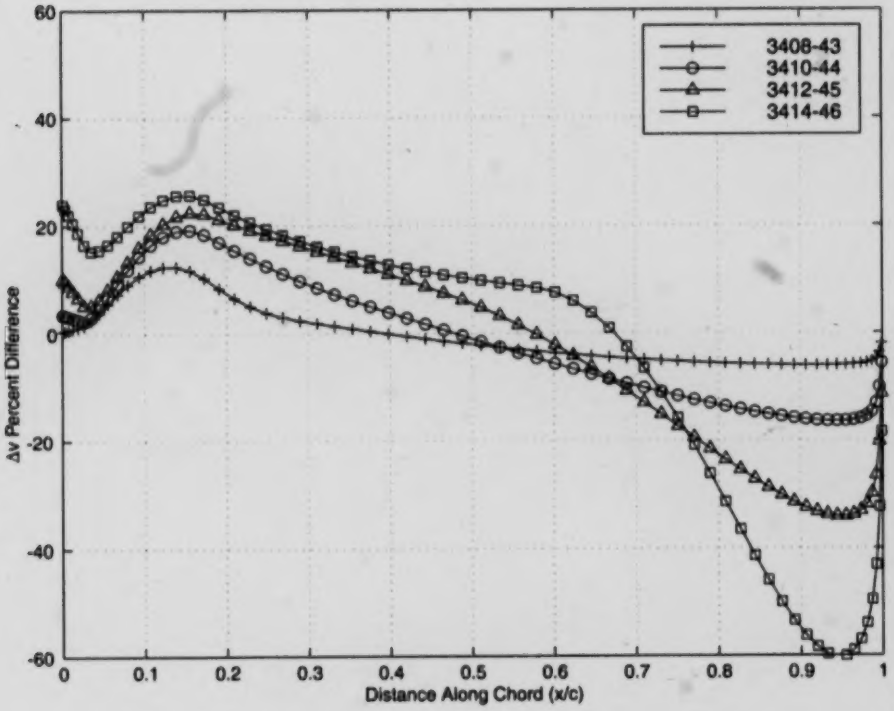

Figure 2.47: Difference In Δv Velocities Of NACA 4-Digit-Modified Airfoils

percent difference with increasing thickness ratio. The second location where the range of differences in Δv velocities appears to be at a maximum is at 94% of the chord length. At 94% of the chord, the range of percent difference is from -60.3% to -6.1%. The -60.3% difference corresponds to the NACA 3414-46 airfoil. The -6.1% difference corresponds to the NACA 3408-43 airfoil. The general trend at 94% chord is decreasing percent difference with increasing airfoil thickness.

The velocity comparisons of the NACA 4-digit-modified airfoils show larger percent difference between the velocities. These larger differences occur because the thickness distributions of the 4-digit-modified group have changing maximum thickness ratio as well as changing maximum thickness location. The thickness distributions are more varied, so the corresponding velocities are more varied as well. The large percent differences will not affect the trending as each individual velocity is recreated with a group-specific function before the series of recreated velocities are trended according to thickness ratio. For each airfoil group, the specific formulation of the trending function depends upon how accurately the trended velocity represents the analysis velocity. For more complex velocities, such as the NACA 4-digit-modified velocities, the trending function is adjusted so that the analysis velocities are accurately represented.

2.4 General Airfoils

The analysis of the three different groups of NACA airfoils show that the velocity components of $\bar{u}$ and Δv change with different thickness distributions but Δu and $\bar{v}$ remain constant. It has been shown that increasing maximum thickness at a fixed location as well as increasing maximum thickness with changing location both affect the two velocity quantities. By only investigating the NACA airfoils it is impossible to determine if the thickness and camber velocity dependence is linked to the mathematical descriptions of the thickness and camber. To test the possibility that this phenomena is strictly a NACA trait, a group of five general airfoils were chosen. The five different airfoils chosen were the NACA 3406 airfoil, Eppler E64 Low Reynolds Number airfoil [17], Eppler E212 Low Reynolds Number airfoil[17], Drela DAE11 Low Reynolds Number airfoil [7] and the Strand High Lift airfoil [25]. For test purposes, these five airfoils are referred to as GEN01 through GEN05, respectively. Each of the five general airfoils have different thicknesses and different camber lines. Since only the different thickness distributions are required, the thickness distributions and camber lines are determined from the airfoil coordinates, and only the thicknesses are taken. All five thickness distributions are then added to the camber line of the NACA 3406 airfoil to determine the test airfoils. The actual camber line does not matter, only the fact that the camber is identical for each of the five general airfoils. The five different thickness distributions can be seen in Figure 2.48.

The analysis results of the general airfoil group resembles those of the NACA groups. The constant camber line creates constant Δu and $\bar{v}$ velocities and the different thicknesses cause the $\bar{u}$ and Δv velocities to change

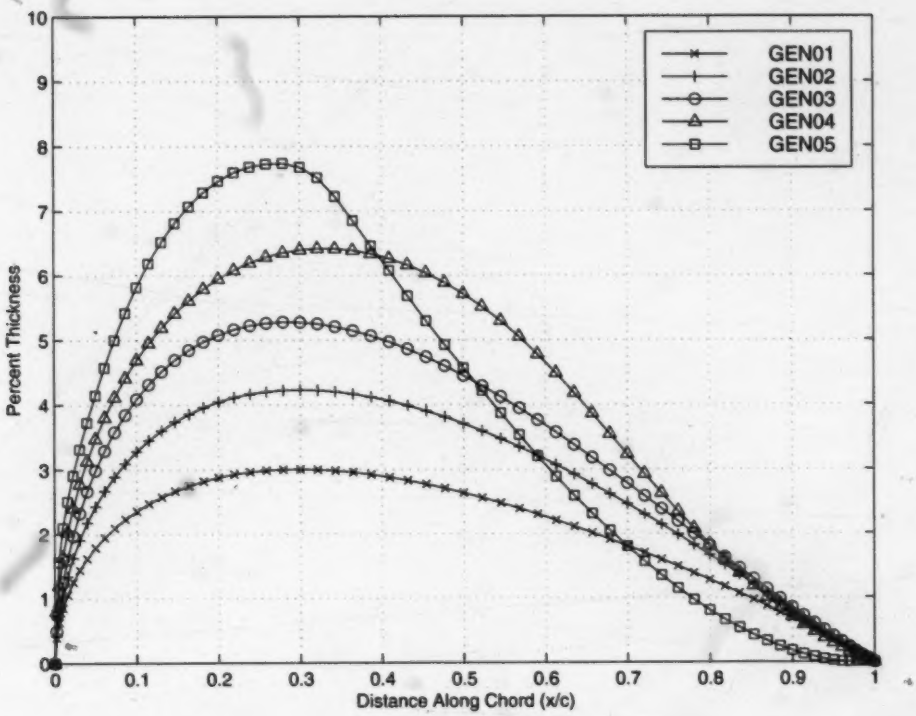

Figure 2.48: Thickness Distributions Of General Airfoils

for each airfoil. The strongly different shapes of the five general thickness distributions cause the calculated velocities to have different shapes as well. Because of the different velocity shapes, it is difficult to compare the sets of velocities using the same technique as the NACA 4-digit, 5-digit and 4-digit-modified groups. The general airfoil velocities do not have the same intersection points that all of the velocities share at zero percent difference that the other groups do. Therefore, the velocities are compared in regions separated by points where the most erratic difference in velocity crosses the

zero percent difference line.

The first velocity component is the $\bar{u}$ velocity. The only location where the five velocities have similar values is at the leading edge. The $\bar{u}$ velocities all have different curves and do not share a similar shape. The five $\bar{u}$ velocities can be seen in Figure 2.49.

The base velocity chosen for comparison corresponds to the GEN01 airfoil. The GEN01 airfoil is the thinnest airfoil of the group. The percent difference of the remaining four airfoils is calculated using

$$\bar{u}_{di} = \frac{\bar{u}_i - \bar{u}_{G01}}{U_\infty} \times 100\% \tag{2.30}$$

where $\bar{u}_{G01}$ refers to the $\bar{u}$ velocity of the base GEN01 airfoil, $\bar{u}_i$ refers to the $\bar{u}$ velocities of the remaining airfoils, and $\bar{u}_{di}$ refers to the percent different in velocity calculated. The four differences in $\bar{u}$ velocities can be seen in Figure 2.50.

The $\bar{u}$ velocity that has the largest percent difference from the base airfoil corresponds to the GEN05 airfoil. The GEN05 difference in velocity has zero percent difference at three locations. These three locations are used to divide the comparison into chordwise sections. The three locations where the difference in $\bar{u}$ velocity corresponding to the GEN05 airfoil occur at 4% chord, 53% chord, and 97% chord. Between 4% of the length of the chord and 53%, the largest percent difference occurs at 28% chord. The range of differences at 28% chord is from 5.3% to 30.0%. The 5.3% difference corresponds to the thinnest remaining airfoil. The 30% difference corresponds to the thickest airfoil. The general trend from 4% chord to 53% chord is increasing percent difference with increasing airfoil thickness. The second region exists from 53% chord to 97% chord. The largest percent difference between 53% of the chord

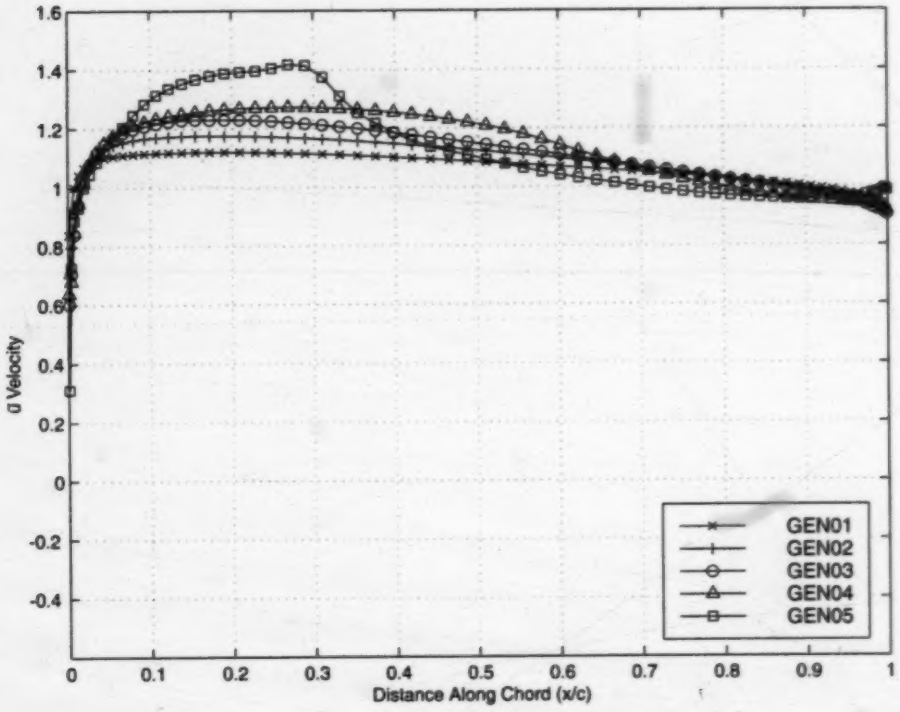

Figure 2.49: $\bar{u}$ Velocities Of General Airfoils

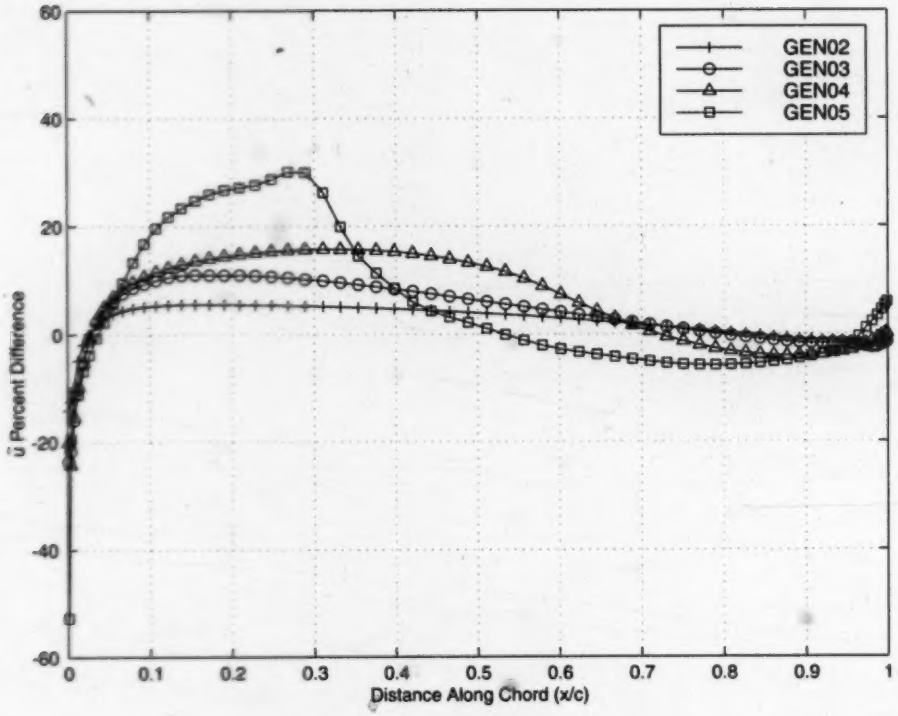

Figure 2.50: Difference In $\bar{u}$ Velocities Of General Airfoils

and 97% of the chord occurs at 78% chord. The percent difference at 97% chord ranges from -5.9% to -0.6%. The -5.9% difference corresponds to the GEN05 airfoil. The -0.6% difference corresponds to the GEN02 airfoil. The general trend from 53% chord to 97% chord is decreasing percent difference with increasing thickness ratio.

The second velocity compared is the Δv velocity. As with the three other airfoil groups, the Δv velocities are very similar for the five different airfoils, even though the $\bar{u}$ velocities have been shown to vary so greatly. The five Δu velocities can be seen in Figure 2.51.

The airfoil used as the base airfoil for the Δu velocities is the GEN01 airfoil. The percent difference between the base airfoil and each of the remaining airfoils is calculated using the following equation

$$\Delta u_{di} = \frac{\Delta u_i - \Delta u_{G01}}{U_\infty} \times 100\% \tag{2.31}$$

where Δu_{di} is the percent difference of the Δu velocities, Δu_i is the velocity of the four remaining airfoils, and Δu_{G01} is the velocity of the base airfoil. The four differences in Δu velocities can be seen in Figure 2.52.

As with the $\bar{u}$ velocity comparison the GEN05 airfoil velocity difference is used to categorize the trends in the comparison plot. The GEN05 velocity difference has zero percent difference from the base velocity at five locations, three occurring more than 5% from the leading and trailing edges. The three interior locations of zero percent difference occur at 23% chord, 37% chord and 85% chord. From leading edge to 23% chord, the largest percent difference occurs at 7% of the chord length. The range of differences at 7% chord is from -10.1% to -3.0%. The -10.1% difference corresponds to the GEN05 airfoil. The -3.0% difference corresponds to the GEN02 airfoil. The general

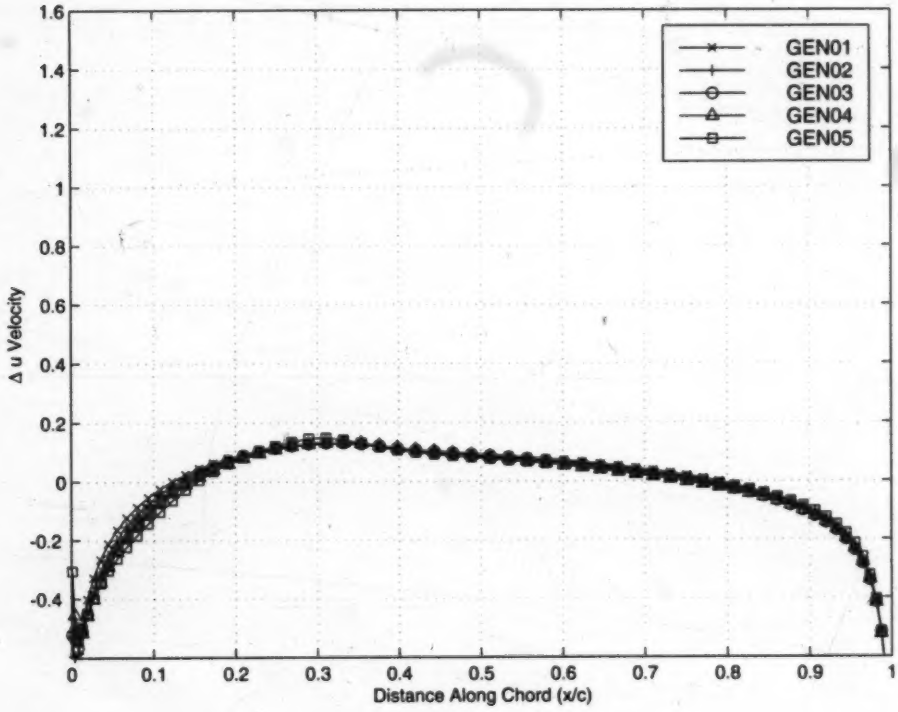

Figure 2.51: Δu Velocities Of General Airfoils

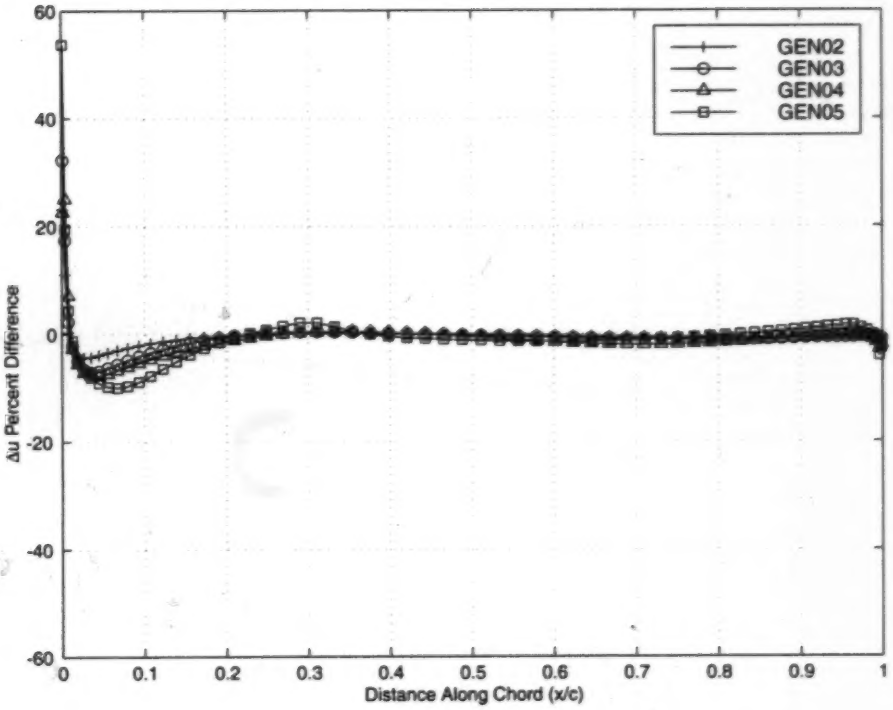

Figure 2.52: Difference In Δu Velocities Of General Airfoils

trend from 0% chord to 23% chord is decreasing percent difference with increasing airfoil thickness. Between 23% chord and 37% chord, the maximum percent difference occurs at 30% of the length of the chord. The percent difference at 30% chord ranges from 0.1% to 2.0%. The 0.1% difference corresponds to the thinnest remaining airfoil. The 2.0% difference corresponds to the thickest airfoil. The general trend from 23% chord to 37% chord is increasing percent difference with increasing thickness ratio. The third section lasts from 37% of the chord to 85% of the chord. The largest percent difference in this region occurs at 58% of the chord. The range of percent differences at 58% chord is from -1.4% to -0.3%. The -1.4% difference corresponds to the GEN05 airfoil. The -0.3% difference corresponds to the GEN02 airfoil. The general trend from 37% chord to 85% chord is decreasing percent difference with increasing airfoil thickness. The fourth and final region exists from 85% chord to the trailing edge. The maximum percent difference in this region occurs at 96% of the chord. The range of difference at 96% chord is from 0.7% to 1.6%. The 0.7% difference corresponds to the thinnest remaining airfoil. The 1.6% difference corresponds to the thickest remaining airfoil. The general trend from 85% chord to 100% chord is increasing percent difference with increasing thickness ratio.

The third velocity component is the $\bar{v}$ velocity. All five of the $\bar{v}$ velocities appear very similar even though they represent different thickness ratios, keeping with trends seen in the other airfoil groups. The five $\bar{v}$ velocities can be seen in Figure 2.53.

The base velocity chosen for comparison corresponds to the GEN01 airfoil. The percent difference of the four remaining airfoils is calculated using the

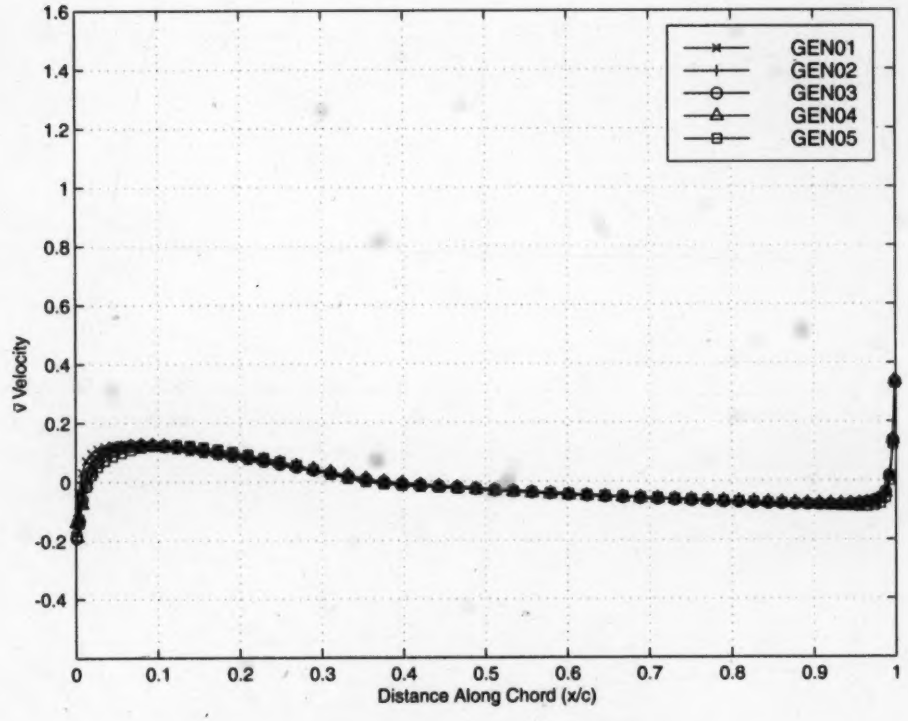

Figure 2.53: $\bar{v}$ Velocities Of General Airfoils

following equation

$$\bar{v}_{di} = \frac{\bar{v}_i - \bar{v}_{G01}}{U_\infty} \times 100\% \tag{2.32}$$

where $\bar{v}_{di}$ is the percent difference of the velocity, $\bar{v}_i$ is the velocity of one of the remaining four airfoils, and $\bar{v}_{G01}$ is the $\bar{v}$ velocity of the base GEN01 airfoil. The four differences in $\bar{v}$ velocities can be seen in Figure 2.54.

There are four interior locations where the GEN05 difference in $\bar{v}$ velocity is equal to zero. These five locations are at 9% chord, 30% chord, 63% chord, and 92% chord. The maximum range in difference for the $\bar{v}$ velocities does not exceed 3% anywhere between leading edge and trailing edge. From leading edge to 9% chord the largest percent difference occurs at 1% of the chord. The range of differences at 1% chord is from -10.6% to -7.8%. The -10.6% difference corresponds to the thickest airfoil. The -7.8% difference corresponds to the thinnest remaining airfoil. The general trend from 0% chord to 9% chord is decreasing percent difference with increasing thickness. Between 9% chord and 30% chord, the maximum percent difference occurs at 17% of the chord. The difference at 30% chord ranges from 0.4% to 2.0%. The 0.4% difference corresponds to the GEN02 airfoil. The 2.0% difference corresponds to the GEN05 airfoil. The general trend from 9% chord to 30% chord is increasing percent difference with increasing airfoil thickness. The third section of the comparison of $\bar{v}$ velocities is from 30% chord to 63% chord. The largest percent difference in this region occurs at 35% chord. The range of differences at 35% chord is from -0.9% to 0.0%. The -0.9% difference corresponds to the GEN05 airfoil. The 0.0% difference corresponds to the GEN02 airfoil. The general trend from 30% chord to 63% chord is decreasing percent difference with increasing airfoil thickness. The

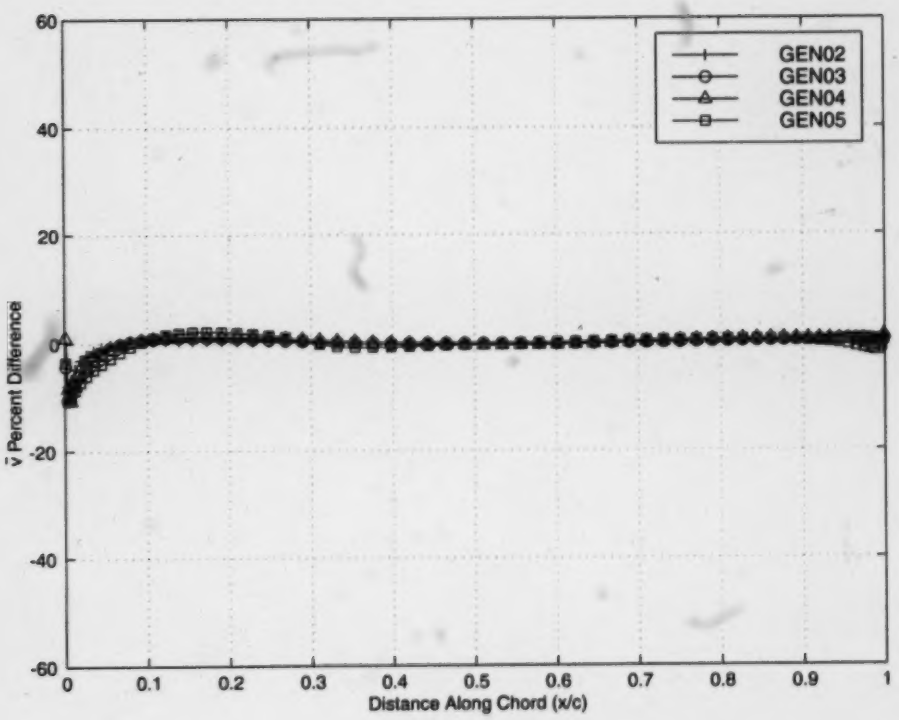

Figure 2.54: Difference In $\bar{v}$ Velocities Of General Airfoils

fourth region lasts from 63% chord to 92% chord. The maximum percent difference in this section occurs at 81% chord. The difference at 81% chord ranges from 0.0% to 0.4%. The 0.0% difference corresponds to the thinnest remaining airfoil. The 0.4% difference corresponds to the thickest airfoil. The general trend from 63% chord to 92% chord is increasing percent difference with increasing thickness ratio. The fifth and final region exists from 92% of the chord to the trailing edge. The largest difference in this section occurs at 99% chord. The range of differences at 99% chord is from -1.7% to 0.1%. The -1.7% difference corresponds to the GEN05 airfoil. The 0.1% difference corresponds to the GEN02 airfoil. The general trend from 92% chord to 100% chord is decreasing percent difference with increasing airfoil thickness.

The fourth and final velocity compared is the Δv velocity. The five different Δv velocities have different shapes and do not appear very similar. The Δv velocities can be seen in Figure 2.55.

The velocity chosen at the base velocity corresponds to the GEN01, or thinnest airfoil of the group. The percent difference in the Δv velocities is calculated using

$$\Delta v_{di} = \frac{\Delta v_i - \Delta v_{G01}}{U_\infty} \times 100\% \tag{2.33}$$

where Δv_{di} refers to the percent difference in Δv velocity, Δv_i refers to a Δv velocity corresponding to one of the remaining airfoils and Δv_{G01} refers to the Δv velocity of the base, or GEN01, airfoil. The differences in Δv velocities can be seen in Figure 2.56.

There are only two points where the GEN05 difference in Δv velocity is equal to zero. These two points occur at 24% chord and 83% chord. Between the leading edge and 24% chord, the maximum percent difference occurs at

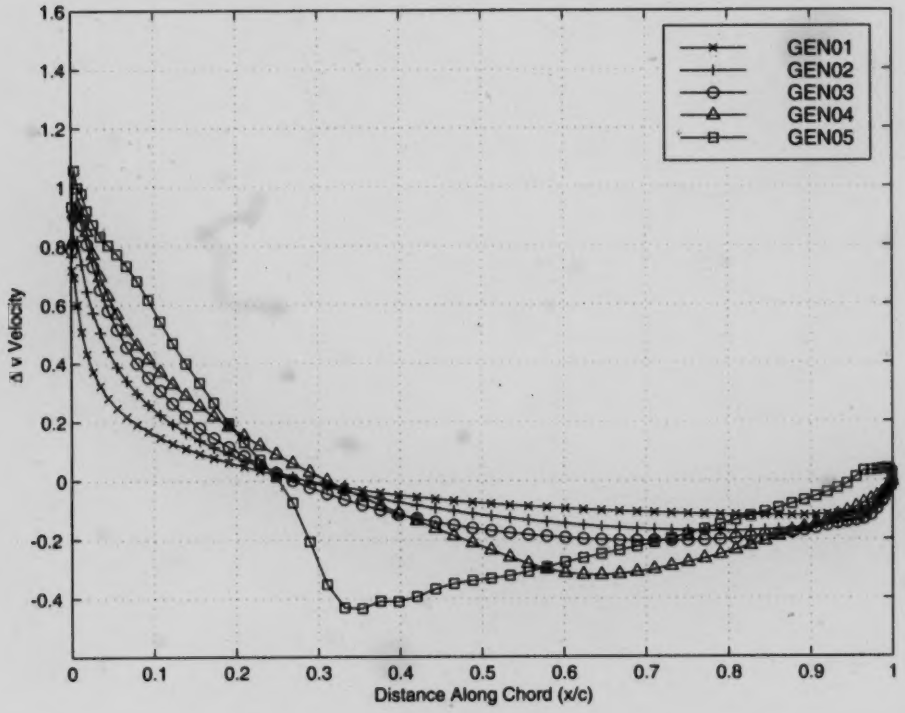

Figure 2.55: Δv Velocities Of General Airfoils

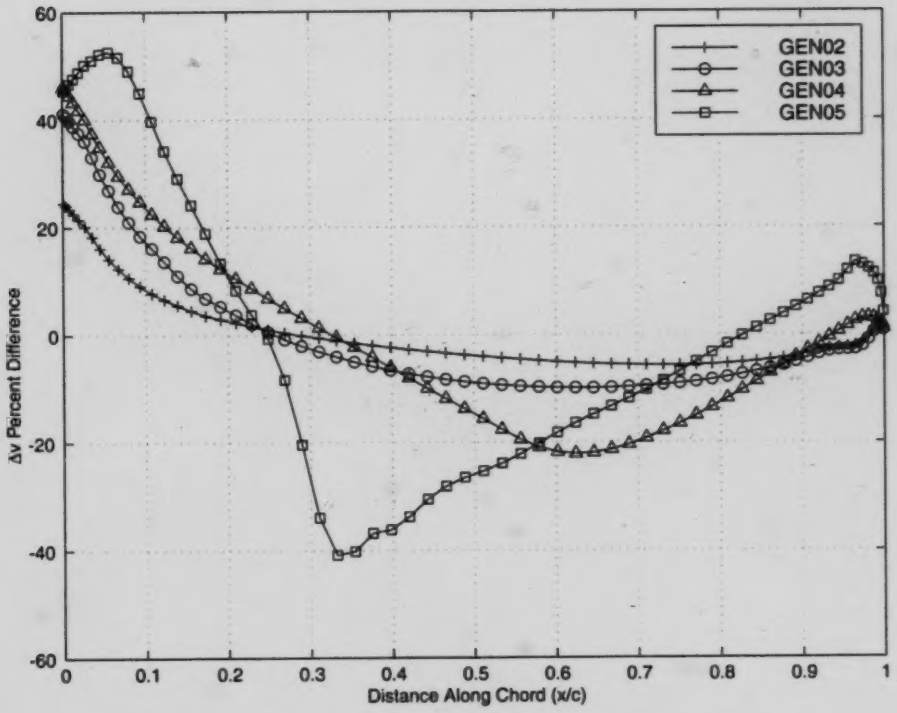

Figure 2.56: Difference In Δv Velocities Of General Airfoils

6% chord. The range of difference at 6% chord is from 13.4% to 52.6%. The 13.4% difference corresponds to the GEN02 airfoil. The 52.6% difference corresponds to the GEN05 airfoil. The general trend from 0% of the chord to 24% of the chord is increasing percent difference with increasing airfoil thickness. From 24% chord to 83% chord the largest difference range occurs at 33% of the chord. The differences at 33% chord range from -40.9% to -0.5%. The -40.9% difference corresponds to the thickest airfoil. The -0.5% difference corresponds to the thinnest remaining airfoil. The general trend from 24% chord to 83% chord is decreasing percent difference with increasing thickness ratio. The last region is from 83% of the length of the chord to the trailing edge. The maximum percent difference in this section occurs at 96% of the chord. The range of differences at 96% chord is from -2.8% to 13.4%. The -2.3% difference corresponds to the GEN02 airfoil. The 13.4% difference corresponds to the GEN05 airfoil. The general trend from 83% chord to 100% chord is increasing percent difference with increasing airfoil thickness.

As with the NACA 4-digit-modified airfoils, the General group of airfoils show velocities that have larger percent differences than either the NACA 4-digit or 5-digit 16-series airfoils. The large range of percent differences between the velocities of the General group of airfoils are due to the highly varied shapes of the thickness distributions. By looking at Figure 2.48 it can be seen that each of the thickness distributions of the General airfoil group have different maximum thickness ratios as well as different locations of maximum thickness. The large percent differences of the General airfoil group will not affect the trending of the velocities because the trending function will

be altered so that the trending technique creates as little error as possible. The specific shapes of the General group analysis velocities will be used to determine the exact method of recreating the velocities.

CHAPTER 3

GOVERNING EQUATIONS

The velocity plots discussed in the previous chapter were calculated using a finite volume approach to solving the potential flow in a cascade of airfoils. The potential flow equation is formulated using the Law of Conservation of Mass to determine the flow field in a single channel between two airfoils. The single channel is represented as a control volume.

3.1 Continuity Equation

In a control volume, the Law of Conservation of Mass can be written in integral form as

$$\frac{\partial}{\partial t}\iiint_{\forall} \rho \, d\forall + \iint_{S} \rho \vec{V} \cdot dS = 0 \tag{3.1}$$

where t represents time, ρ is the density of the fluid, $\vec{V}$ is the vector form of the velocity field, $\forall$ is the control volume and S denotes the control surface. The surface integral can be changed into a volume integral using the

divergence theorem, giving

$$\frac{\partial}{\partial t}\iiint_{\forall} \rho \, d\forall + \iiint_{\forall} \nabla \cdot \left(\rho \vec{V}\right) d\forall = 0 \tag{3.2}$$

For the problem being studied, the control volume is steady, so Equation 3.2 becomes

$$\iiint_{\forall} \left[\frac{\partial}{\partial t}(\rho) + \nabla \cdot \left(\rho \vec{V}\right)\right] d\forall = 0 \tag{3.3}$$

For any arbitrary control volume, the integral is equal to zero, so the integrand must also be equal to zero giving

$$\frac{\partial \rho}{\partial t} + \nabla \cdot \left(\rho \vec{V}\right) = 0 \tag{3.4}$$

In order to calculate the correct flow field for the problem, an equation of state of the fluid is needed. This state equation can add convergence difficulty, therefore it is preferable to express Equation 3.4 in a more expanded form. The expanded form allows the density characteristics of the problem to be considered. With this in mind, the differential operator in Equation 3.4 can be expanded to give

$$\frac{\partial \rho}{\partial t} + \rho\left(\nabla \cdot \vec{V}\right) + \vec{V}\left(\nabla \cdot \rho\right) = 0 \tag{3.5}$$

For this problem, ρ is constant for all time within the domain space. Therefore

$$\nabla \cdot \rho = 0 \tag{3.6}$$

$$\frac{\partial \rho}{\partial t} = 0 \tag{3.7}$$

With these two conditions, Equation 3.5 simplifies to

$$\rho \nabla \cdot \vec{V} = 0 \tag{3.8}$$

Removing the constant density ρ gives the continuity equation

$$\nabla \cdot \vec{V} = 0 \tag{3.9}$$

3.2 Lamellar Decomposition

The velocity field, $\vec{V}$ originally mentioned in Equation 3.1 is composed of two flow variables. The two variables are the free stream velocity (U_∞) and an irrotational potential (ϕ). These two variables comprise a complex-lamellar decomposition of the flow field according to the following equation

$$\vec{V} = U_\infty + \nabla\phi \tag{3.10}$$

The continuity equation, Equation 3.9, can be expanded to become

$$\nabla \cdot \vec{V} = \frac{\partial u}{\partial x} + \frac{\partial v}{\partial y} \tag{3.11}$$

From the decomposition described in Equation 3.10 the two cartesian velocity components, u and v are defined as

$$u = U_\infty + \frac{\partial \phi}{\partial x} \tag{3.12}$$

$$v = \frac{\partial \phi}{\partial y} \tag{3.13}$$

Using the u and v definitions of Equations 3.12 and 3.13, Equation 3.11 becomes

$$\nabla \cdot \vec{V} = \frac{\partial}{\partial x}\left(U_\infty + \frac{\partial \phi}{\partial x}\right) + \frac{\partial}{\partial y}\left(\frac{\partial \phi}{\partial y}\right) \tag{3.14}$$

$$= \frac{\partial U_\infty}{\partial x} + \frac{\partial^2 \phi}{\partial x^2} + \frac{\partial^2 \phi}{\partial y^2} \tag{3.15}$$

This equation is used to model the continuity. The final form of the continuity equation has the second degree partial derivatives combined, written as

$$\nabla \cdot \vec{V} = \frac{\partial U_\infty}{\partial x} + \nabla^2 \phi \tag{3.16}$$

3.3 Dimensional Analysis

In order to express the continuity equation in a non-dimensional form, two dimensional constants must be used, a characteristic length and velocity. The characteristic length used is denoted as c and represents the distance from the leading edge to the trailing edge of the airfoil. The characteristic velocity used is the freestream velocity U_∞. These two values are used to remove any dimensional dependence that the solution of the problem may have because of the flow variables used. The flow variables are distance (x, y) and velocity (u, v). The non-dimensional quantities are as follows:

$$x^* = \frac{x}{c} \tag{3.17}$$

$$y^* = \frac{y}{c} \tag{3.18}$$

$$u^* = \frac{u}{U_\infty} \tag{3.19}$$

$$v^* = \frac{v}{U_\infty} \tag{3.20}$$

The above equations can be rearranged for substitution into the continuity equation giving

$$x = x^* c \tag{3.21}$$

$$y = y^* c \tag{3.22}$$

$$u = u^* U_\infty \tag{3.23}$$

$$v = v^* U_\infty \tag{3.24}$$

The continuity equation can be tested for dimensional dependence using the above substitutions. The test is used to determine whether or not non-dimensional constants must be inserted in order for the equation to be solved and still be dimensionally consistent. Equation 3.11 can be written with the dimensional constants as

$$\begin{aligned} \nabla \cdot \vec{V} &= \frac{\partial (u^* U_\infty)}{\partial (x^* c)} + \frac{\partial (v^* U_\infty)}{\partial (y^* c)} \\ &= \frac{\partial u^*}{\partial x^*} \left(\frac{U_\infty}{c} \right) + \frac{\partial v^*}{\partial y^*} \left(\frac{U_\infty}{c} \right) \end{aligned} \tag{3.25}$$

The term $\frac{U_\infty}{c}$ is present in both terms of Equation 3.25 and referring to Equation 3.9 it is known that $\nabla \cdot \vec{V}$ is equal to zero. Therefore the $\frac{U_\infty}{c}$ term can be factored and the continuity equation becomes

$$\nabla \cdot \vec{V} = \frac{U_\infty}{c} \left(\frac{\partial u^*}{\partial x^*} + \frac{\partial v^*}{\partial y^*} \right) \tag{3.26}$$

3.4 Generalized Coordinate System

In solving the continuity equation, the coordinate system must be transformed from the physical domain to the computational domain. This involves transforming the system from cartesian (x, y) coordinates to general curvilinear (ξ, η) coordinates. The effect of the transformation , as demonstrated in Figure 3.1, creates a uniform coordinate system where the grid spacings are both equal to unity, or

$$\Delta\xi = \Delta\eta = 1 \tag{3.27}$$

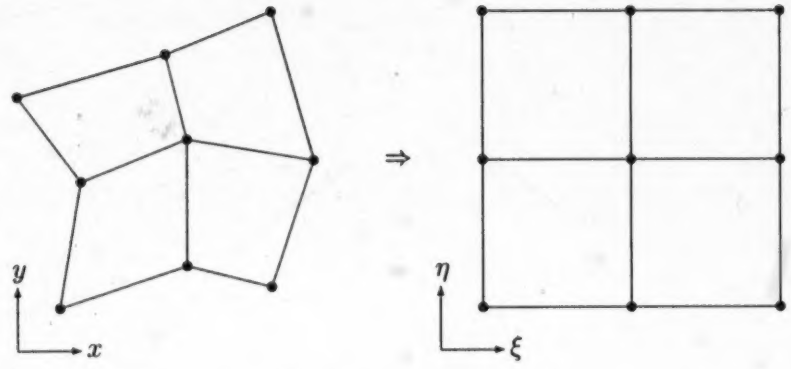

Figure 3.1: Grid Transformation

The transformation is completed through the use of a Jacobian transformation matrix. The Jacobian matrix is defined as

$$J \equiv \frac{\partial(x,y)}{\partial(\xi,\eta)} \equiv \begin{bmatrix} \frac{\partial x}{\partial \xi} & \frac{\partial x}{\partial \eta} \\ \frac{\partial y}{\partial \xi} & \frac{\partial y}{\partial \eta} \end{bmatrix} \tag{3.28}$$

The inverse of the Jacobian, denoted J^{-1} is defined as follows

$$J^{-1} \equiv \begin{bmatrix} \frac{\partial \xi}{\partial x} & \frac{\partial \xi}{\partial y} \\ \frac{\partial \eta}{\partial x} & \frac{\partial \eta}{\partial y} \end{bmatrix} = \frac{1}{\|J\|} \begin{bmatrix} \frac{\partial y}{\partial \eta} & \frac{-\partial x}{\partial \eta} \\ \frac{-\partial y}{\partial \xi} & \frac{\partial x}{\partial \xi} \end{bmatrix} \tag{3.29}$$

where $\|J\|$ is the determinant of the Jacobian, given as

$$\|J\| = \left(\frac{\partial x}{\partial \xi}\frac{\partial y}{\partial \eta} - \frac{\partial x}{\partial \eta}\frac{\partial y}{\partial \xi} \right) \tag{3.30}$$

The two cartesian derivatives $\frac{\partial}{\partial x}$ and $\frac{\partial}{\partial y}$ can be expressed in terms of the (ξ, η) system as follows

$$\frac{\partial}{\partial x} = \frac{\partial}{\partial \xi}\frac{\partial \xi}{\partial x} + \frac{\partial}{\partial \eta}\frac{\partial \eta}{\partial x} \tag{3.31}$$

$$\frac{\partial}{\partial y} = \frac{\partial}{\partial \xi}\frac{\partial \xi}{\partial y} + \frac{\partial}{\partial \eta}\frac{\partial \eta}{\partial y} \tag{3.32}$$

using Equation 3.29, the following terms can be replaced using the listed substitutes

$$\frac{\partial \xi}{\partial x} = \frac{1}{\|J\|}\left(\frac{\partial y}{\partial \eta}\right) \tag{3.33}$$

$$\frac{\partial \xi}{\partial y} = \frac{1}{\|J\|}\left(-\frac{\partial x}{\partial \eta}\right) \tag{3.34}$$

$$\frac{\partial \eta}{\partial x} = \frac{1}{\|J\|}\left(-\frac{\partial y}{\partial \xi}\right) \tag{3.35}$$

$$\frac{\partial \eta}{\partial y} = \frac{1}{\|J\|}\left(\frac{\partial x}{\partial \xi}\right) \tag{3.36}$$

so the derivatives become

$$\frac{\partial}{\partial x} = \frac{1}{\|J\|}\left[\frac{\partial}{\partial \xi}\left(\frac{\partial y}{\partial \eta}\right) + \frac{\partial}{\partial \eta}\left(-\frac{\partial y}{\partial \xi}\right)\right] \tag{3.37}$$

$$\frac{\partial}{\partial y} = \frac{1}{\|J\|}\left[\frac{\partial}{\partial \xi}\left(-\frac{\partial x}{\partial \eta}\right) + \frac{\partial}{\partial \eta}\left(\frac{\partial x}{\partial \xi}\right)\right] \tag{3.38}$$

The transformed derivatives are used to derive a transformed continuity equation which can be written as

$$\nabla \cdot \vec{V} = \frac{1}{\|J\|}\left[\frac{\partial \|J\| U}{\partial \xi} + \frac{\partial \|J\| V}{\partial \eta}\right] \tag{3.39}$$

or rearranged into

$$\|J\| \, \nabla \cdot \vec{V} = \frac{\partial \|J\| U}{\partial \xi} + \frac{\partial \|J\| V}{\partial \eta} \tag{3.40}$$

where U and V are the contravariant velocities defined as

$$\begin{bmatrix} U \\ V \end{bmatrix} = J^{-1} \begin{bmatrix} u \\ v \end{bmatrix} \tag{3.41}$$

The two lamellar velocities u and v contain cartesian partial differentials, as can be seen in Equations 3.12 and 3.13. These cartesian differentials are transformed using Equations 3.37 and 3.38 to give

$$u = U_\infty + \frac{1}{\|J\|}\left[\frac{\partial\phi}{\partial\xi}\frac{\partial y}{\partial\eta} + \frac{\partial\phi}{\partial\eta}\left(-\frac{\partial y}{\partial\xi}\right)\right] \tag{3.42}$$

$$v = \frac{1}{\|J\|}\left[\frac{\partial\phi}{\partial\xi}\left(-\frac{\partial x}{\partial\eta}\right) + \frac{\partial\phi}{\partial\eta}\frac{\partial x}{\partial\xi}\right] \tag{3.43}$$

CHAPTER 4

NUMERICAL METHODS

The continuity equation, Equation 3.9, is used to solve for the potential field or ϕ variable. With the potential an inviscid, irrotational velocity field is constructed using

$$\vec{V}_{inviscid} = U_\infty + \nabla\phi \tag{4.1}$$

The potential is solved using a implicit approximate LU factorization algorithm. The convergence of this algorithm is accelerated to a steady state using a multigrid scheme. However, Equation 3.9 must be expressed in a time dependent form for it to be solved using these methods. Since the solution being sought involves the potential function, ϕ is the variable that will be changing from one iteration to the next as the scheme converges. This gives the time dependent form of the continuity as

$$\frac{\partial\phi}{\partial t} = \nabla \cdot \vec{V} \tag{4.2}$$

When the potential has converged to a steady state, or

$$\frac{\partial\phi}{\partial t} = 0 \tag{4.3}$$

then the continuity condition will also be satisfied according to Equation 4.2.

4.1 Approximate LU Factorization

The LU scheme being used has the ability to be fully explicit, fully implicit or semi-implicit. The implicit nature of the scheme is controlled using an implicit parameter, μ. The inclusion of μ and use of the potential form of continuity described in Equation 3.16 changes Equation 4.2 into

$$\frac{\partial \phi}{\partial t} = \left((1-\mu) \left[\frac{\partial U_\infty}{\partial x} + \frac{\partial^2 \phi}{\partial x^2} + \frac{\partial^2 \phi}{\partial y^2} \right]^N + \mu \left[\frac{\partial U_\infty}{\partial x} + \frac{\partial^2 \phi}{\partial x^2} + \frac{\partial \phi^2}{\partial y^2} \right]^{N+1} \right) \quad (4.4)$$

where N and $N+1$ refer to the current and future time iterations, respectively. The LU scheme is fully implicit when $\mu = 1$, and fully explicit when $\mu = 0$. The $\frac{\partial \phi}{\partial t}$ term can be approximated as a finite difference such as

$$\frac{\partial \phi}{\partial t} = \frac{\phi^{N+1} - \phi^N}{\Delta t} \quad (4.5)$$

where N and $N+1$ refer to successive time iterations and Δt is the time step. The Equation 4.5 approximation allows Equation 4.4 to be expanded into

$$\phi^{N+1} - \phi^N =$$

$$\Delta t \left((1-\mu) \left[\frac{\partial U_\infty}{\partial x} + \frac{\partial^2 \phi}{\partial x^2} + \frac{\partial^2 \phi}{\partial y^2} \right]^N + \mu \left[\frac{\partial U_\infty}{\partial x} + \frac{\partial^2 \phi}{\partial x^2} + \frac{\partial \phi^2}{\partial y^2} \right]^{N+1} \right) \quad (4.6)$$

Collecting terms with the implicit factor, and linearizing the implicit terms about the last timestep gives

$$\Delta \phi^N - \mu \Delta t \left[\left(\frac{\partial^2 \phi}{\partial x^2} + \frac{\partial^2 \phi}{\partial y^2} \right)^{N+1} - \left(\frac{\partial^2 \phi}{\partial x^2} + \frac{\partial^2 \phi}{\partial y^2} \right)^N \right] =$$

$$\Delta t \left(\frac{\partial U_\infty}{\partial x} + \frac{\partial^2 \phi}{\partial x^2} + \frac{\partial \phi^2}{\partial y^2} \right)^N \quad (4.7)$$

where $\Delta\phi^N$ is the potential field correction for time N, and is defined as

$$\Delta\phi^N = \phi^{N+1} - \phi^N \tag{4.8}$$

The bracketed terms on the right hand side of Equation 4.7 are called the residual and are specifically constructed to maintain numerical conservation and accuracy. The use of Equation 4.8 allows the simplification of Equation 4.7, and the addition of a relaxation factor, w, gives

$$\left[I - \mu\frac{\Delta t}{\Delta x^2}\left(\delta_{xx} + \delta_{yy}\right)\right]\Delta\phi^N = w\frac{\Delta t}{\Delta x^2}\,\mathrm{Res}^N \tag{4.9}$$

where I is the identity matrix and δ_{xx}, δ_{yy} are the second order central differencing terms written in delta form. The delta form terms are defined as

$$\delta_{xx}\Delta\phi = \Delta\phi_{i+1} - 2\Delta\phi_i + \Delta\phi_{i-1} \tag{4.10}$$

$$\delta_{yy}\Delta\phi = \Delta\phi_{j+1} - 2\Delta\phi_j + \Delta\phi_{j-1} \tag{4.11}$$

The left hand side of Equation 4.9 is factored to create an approximation that will allow for solution using an explicit sweep. The approximate factorized equation is

$$\left[I + \mu\frac{\Delta t}{\Delta x^2}\left(\delta_x^- + \delta_y^-\right)\right]\left[I - \mu\frac{\Delta t}{\Delta x^2}\left(\delta_x^+ + \delta_y^+\right)\right]\Delta\phi^N = w\frac{\Delta t}{\Delta x^2}\,\mathrm{Res}^N \tag{4.12}$$

where $\delta_x^-, \delta_y^-, \delta_x^+$, and δ_y^+ are first order differencing terms written in delta form. The four first order delta form terms are defined as

$$\delta_x^+\Delta\phi = \Delta\phi_{i+1} - \Delta\phi_i \tag{4.13}$$

$$\delta_x^-\Delta\phi = \Delta\phi_i - \Delta\phi_{i-1} \tag{4.14}$$

$$\delta_y^+ \Delta\phi = \Delta\phi_{j+1} - \Delta\phi_j \tag{4.15}$$

$$\delta_y^- \Delta\phi = \Delta\phi_j - \Delta\phi_{j-1} \tag{4.16}$$

This equation is solved in two steps. The first step uses the residual at time N to solve for a temporary potential correction called $\Delta\phi'$. The second step then uses the temporary correction to solve for the true potential field correction.

$$\begin{aligned} &(1) \quad \left[I + \mu\tfrac{\Delta t}{\Delta x^2}\left(\delta_x^- + \delta_y^-\right)\right]\Delta\phi' = w\tfrac{\Delta t}{\Delta x^2}\,\mathrm{Res}^N \\ &(2) \quad \left[I - \mu\tfrac{\Delta t}{\Delta x^2}\left(\delta_x^+ + \delta_y^+\right)\right]\Delta\phi^N = \Delta\phi' \end{aligned} \tag{4.17}$$

In the transformed system, Equation 4.17 becomes

$$\begin{aligned} &(1) \quad \left[I + \mu\tfrac{\Delta t}{\Delta x^2}\left(A_1\delta_\xi^- + A_2\delta_\eta^-\right)\right]\Delta\phi' = w\tfrac{\Delta t}{\Delta x^2}\,(\mathrm{Res}^*)^N \\ &(2) \quad \left[I - \mu\tfrac{\Delta t}{\Delta x^2}\left(A_1\delta_\xi^+ + A_2\delta_\eta^+\right)\right]\Delta\phi^N = \Delta\phi' \end{aligned} \tag{4.18}$$

where A_1 and A_2 are defined as

$$A_1 = \frac{\left(-\frac{\partial x}{\partial \eta}\right)^2 + \left(\frac{\partial y}{\partial \eta}\right)^2}{\|J\|} \tag{4.19}$$

$$A_2 = \frac{\left(\frac{\partial x}{\partial \xi}\right)^2 + \left(-\frac{\partial y}{\partial \xi}\right)^2}{\|J\|} \tag{4.20}$$

and the new residual, Res^* is calculated using the transformed continuity equation, Equation 3.40. The A terms and the new residual calculation are derived using the transformation techniques discussed in Section 3.4.

Step (1) of Equation 4.18 can be solved with an explicit sweep because the δ^- factorization creates a lower triangular matrix. Similarly, the δ^+ factorization in step (2) creates an upper triangular matrix. The potential correction is then used to update the potential field in the following manner

$$\phi^{N+1} = \phi^N + \Delta\phi^N \tag{4.21}$$

4.2 Residual Construction (Analysis)

Calculating a solution for the potential field requires the discretization of the continuity equation. For this work, a finite volume method was used. The benefit of a finite volume formulation is the ability to calculate all of the terms of the residual as fluxes through the cell faces. The residual in Equation 4.18 represents the continuity equation, restated as

$$\text{Res}^* = \|J\| \nabla \cdot \vec{V} \tag{4.22}$$

The residual can be written in a more generalized form as

$$\text{Res}^* = \frac{\partial f}{\partial \xi} + \frac{\partial g}{\partial \eta} \tag{4.23}$$

where f and g are the tangential and normal fluxes, respectively. The fluxes can be expressed in terms of velocities and geometric terms, and combining Equations 4.22, 4.23 and Equation 3.40 gives

$$\|J\| \nabla \cdot \vec{V} = \frac{\partial \|J\| U}{\partial \xi} + \frac{\partial \|J\| V}{\partial \eta} \tag{4.24}$$

where $\|J\|$ is the determinant of the Jacobian transformation matrix, defined in Equation 3.30, and U, V are the contravariant velocities. The fluxes can be written in terms of U and V as

$$f = \|J\| \, U \tag{4.25}$$

$$g = \|J\| \, V \tag{4.26}$$

Using Equation 3.41 the f and g fluxes can be written as

$$\begin{bmatrix} f \\ g \end{bmatrix} = \|J\| \, J^{-1} \begin{bmatrix} u \\ v \end{bmatrix} \tag{4.27}$$

where J^{-1} is the inverse of the Jacobian transformation matrix and u, v are cartesian velocities. The g flux can be expanded to become

$$g = \|J\| \left[\frac{1}{\|J\|} \left(-\frac{\partial y}{\partial \xi} u + \frac{\partial x}{\partial \xi} v \right) \right] \tag{4.28}$$

For airfoil analysis the normal flux along the surface of the airfoil is set equal to zero to mimic the solid surface of the airfoil. The no-flux condition is achieved by using the u and v velocities to set V equal to zero at the surface of the airfoil. The u and v velocities are used to only affect the V or normal contravariant velocity, and therefore the g or normal flux at the solid surface. Everywhere else, and for the U contravariant velocity, the cartesian velocities are constructed using the current potential field.

Approximating the flux partial derivatives as finite differences, Equation 4.23 becomes

$$\text{Res}^* = \frac{\Delta f}{\Delta \xi} + \frac{\Delta g}{\Delta \eta} \tag{4.29}$$

where Δf and Δg are fluxes through the entire cell. Figure 4.1 shows a diagram of a single computational cell. The location of the Δf and Δg terms can be seen in Figure 4.1(i). From Equation 3.27 it is known that $\Delta \xi$ and $\Delta \eta$ are equal to one in the computational domain. The cell flux terms in Equation 4.29 can be replaced with the flux through the cell face terms, as

$$\Delta f = f_R - f_L \tag{4.30}$$

$$\Delta g = g_T - g_B \tag{4.31}$$

where the R, L, T and B subscripts refer to the right, left, top and bottom walls of the cell respectively. This can seen in Figure 4.1(ii). Using Equations

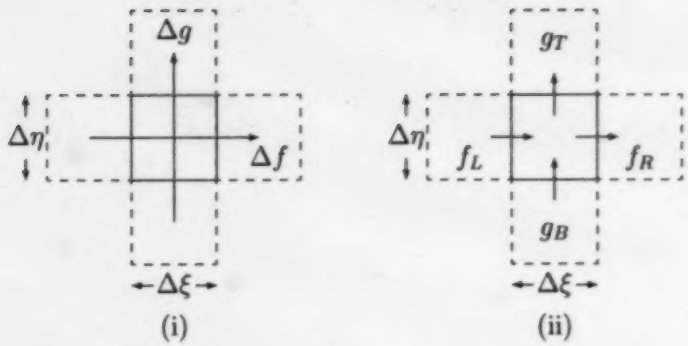

Figure 4.1: Flux Calculation

3.27, 4.30 and 4.31, Equation 4.29 becomes

$$\text{Res}^* = f_R - f_L + g_T - g_B \tag{4.32}$$

The four fluxes listed above must all be calculated on the cell faces. The ϕ variable, as well as some geometric terms for a particular cell do not lie on the corresponding cell faces for a particular flux calculation, however. This means that the fluxes must be constructed such that they occur in the correct location on the cell. Since the potential equation is elliptic, information is passed in all directions. Therefore, linear interpolation of variables can be used in the construction of the residual.

4.3 Numerical Stability of the LU Scheme

In order for a numerical scheme to be considered stable, the error can not be allowed to grow exponentially in time, that is

$$\text{error}^{N+1} \leq \text{error}^{N} \tag{4.33}$$

where N and $N+1$ describe successive time steps. For an initial value problem, such as the one one being studied here, a scheme can be called stable if the absolute value of the error remains bounded as

1. $t \to \infty$, for a fixed Δt

2. $\Delta t \to 0$, for a fixed t

The Lax Equivalence Theorem states that for a well-posed initial value problem with constant coefficients, if a numerical approximation is consistent then stability is a sufficient condition for numerical convergence. The unsteady implicit approximation, Equation 4.18, is not consistent with the artificial unsteady equation modelled in Equation 4.2. However, when the numerical scheme converges to a steady state solution the steady state residual is consistent with the continuity equation. To determine the stability of the numerical approximation, a Von Neumann Stability analysis is completed. The Von Neumann stability involves completing a Fourier decomposition in space. This analysis applies specifically to problems with periodic boundaries and constant coefficients. The analysis assumes that the problem has a separable solution of the form

$$W = e^{\alpha^* t} e^{i\beta x} \tag{4.34}$$

In Equation 4.34, W is the approximate function, i is an imaginary number, α^* is an exponential time constant and β is the wave number. For the N^{th} time step, the time t is defined as $N\Delta t$ to give

$$\begin{aligned} e^{\alpha^* t} e^{i\beta x} &= e^{\alpha^* N\Delta t} e^{i\beta x} \\ &= \left(e^{\alpha^* \Delta t}\right)^N e^{i\beta x} \end{aligned} \tag{4.35}$$

for a constant α^* and Δt, an new constant, G, can be defined as the growth factor in the following way

$$G = e^{\alpha^* \Delta t} \tag{4.36}$$

such that at time step N,

$$G^N = \left(e^{\alpha^* \Delta t}\right)^N \tag{4.37}$$

With the substitution of G, Equation 4.34 becomes

$$W_j = G^N e^{i\beta x} \tag{4.38}$$

Equation 4.38 can be used to describe W at any time (N) as well as at any location (j). The error between two successive time steps can now be defined in terms of the growth factor. For error not to grow exponentially in time, Equation 4.33 can be written in terms of the growth factor as

$$|G|^{N+1} \leq |G|^N \tag{4.39}$$

which becomes the growth factor condition

$$|G| \leq 1 \tag{4.40}$$

The continuity equation can be modelled for numerical stability analysis as a one-dimensional diffusion equation. The model equation used is

$$\frac{\partial W}{\partial t} = \frac{\partial^2 W}{\partial x^2} \tag{4.41}$$

Using the LU factorization scheme, the model equation can be written in operator form as

$$\mathrm{LU}\Delta W_j = \mathrm{R}W_j \tag{4.42}$$

where L, U, and R refer to the lower diagonal matrix, the upper diagonal matrix and the residual respectively. In delta form, the model equation is written

$$\left[I + \mu\frac{\Delta t}{\Delta x^2}\delta_x^-\right]\left[I - \mu\frac{\Delta t}{\Delta x^2}\delta_x^+\right]\left(W_j^{N+1} - W_j^N\right) = w\frac{\Delta t}{\Delta x^2}\delta_{xx}W_j \tag{4.43}$$

where Δx refers to the grid spacing and is assumed to be constant. The left hand terms of Equation 4.43 expand so that the delta form model equation can be written

$$\left[I - \mu\frac{\Delta t}{\Delta x^2}\delta_x^+ + \mu\frac{\Delta t}{\Delta x^2}\delta_x^- - \mu^2\frac{\Delta t^2}{\Delta x^4}\delta_{xx}\right]\left(W_j^{N+1} - W_j^N\right) =$$

$$w\frac{\Delta t}{\Delta x^2}\delta_{xx}W_j \tag{4.44}$$

Using Equation 4.38 the delta form model equation becomes

$$\left[1 - \left(\mu\frac{\Delta t}{\Delta x^2} + \mu^2\frac{\Delta t^2}{\Delta x^4}\right)\left(e^{i\beta\Delta x} + e^{-i\beta\Delta x} - 2\right)\right](G-1) =$$

$$w\frac{\Delta t}{\Delta x^2}\left(e^{i\beta\Delta x} + e^{-i\beta\Delta x} - 2\right) \tag{4.45}$$

The exponential terms in the previous equation can be replaced with trigonometric functions, using the substitution

$$e^{i\beta\Delta x} = \cos\beta\Delta x + i\sin\beta\Delta x \tag{4.46}$$

Using the trigonometric identity

$$\sin^2\theta = \frac{1-\cos 2\theta}{2} \tag{4.47}$$

the growth factor of the model equation is defined in the following way

$$G = \frac{1+4\left(\mu^2\left(\frac{\Delta t}{\Delta x^2}\right)^2 + \mu\frac{\Delta t}{\Delta x^2} - w\frac{\Delta t}{\Delta x^2}\right)\sin^2\frac{\beta\Delta x}{2}}{1+4\left(\mu^2\left(\frac{\Delta t}{\Delta x^2}\right)^2 + \mu\frac{\Delta t}{\Delta x^2}\right)\sin^2\frac{\beta\Delta x}{2}} \tag{4.48}$$

A plot of different growth factors can be seen in Figure 4.2. The different growth factors correspond to different combinations of μ, w and $\frac{\Delta t}{\Delta x^2}$. The cases are defined as follows

Case	μ	w	$\frac{\Delta t}{\Delta x^2}$
1	1.0	1.0	6.0
2	1.0	2.0	6.0
3	0.5	1.0	6.0
4	0.5	2.0	5.8

Table 4.1: Growth Factor Cases

Figure 4.2 shows that the numerical scheme is stable for each of the cases, as the growth factor $|G|$ is never greater than one. The growth factor parameters can be used to accelerate the convergence of the calculation by decreasing the area under the growth factor curve. It can be seen in Figure

4.2 that the best growth factor is given by the parameters of Case 4. However, these growth factors apply to the one-dimensional model equation only. The growth factor used for calculations must be empirically chosen with numerical test cases. For the calculations discussed here, the growth factor parameters used are those of Case 1, namely $\mu = 1.0$, $w = 1.0$ and $\frac{\Delta t}{\Delta x^2} = 6.0$. These values were chosen by completing sample calculations.

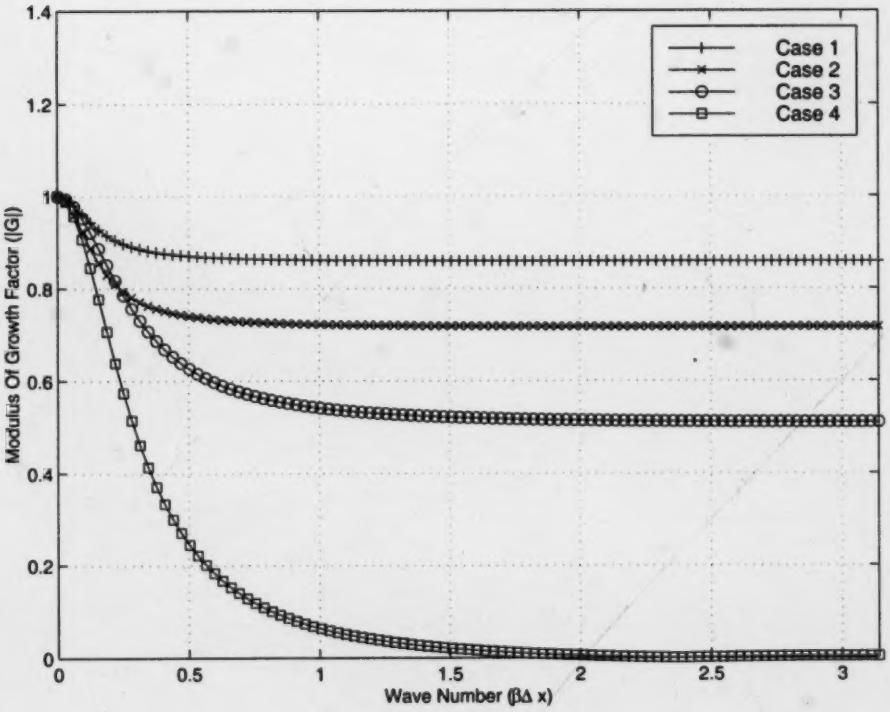

Figure 4.2: Growth Factor

4.4 Multigrid Acceleration

The continuity equation, Equation 3.9 is an elliptic equation, which is converged to a steady state. The solution of a steady state equation is controlled by the boundary conditions imposed. Multigrid allows convergence acceleration by increasing the speed at which the effects of the boundary conditions are spread throughout the entire domain [27]. This acceleration is achieved by coarsening the grid. A coarser grid has fewer cells to convect the information across, allowing a converged solution to be calculated quicker. The multigrid technique used for this problem involves geometric coarsening. A simple three-stage coarsening can be seen in Figure 4.3. The h, $h-1$ and $h-2$ variables refer to the grid level. The h level of the grid is the finest grid, and each level lower is labelled as $h-n$ where n represents the number of times cells have been geometrically combined.

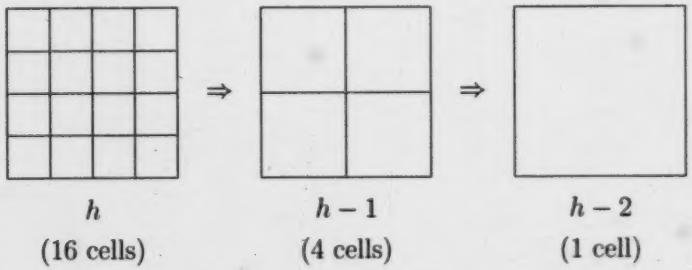

Figure 4.3: Multigrid Grid Refinement

The first step in a multigrid cycle is the calculation of a solution correction on the fine grid as well as the new solution. The LU scheme is used written

in operator form as

$$\mathrm{LU}_h \Delta\phi_h^N = \Delta t \mathrm{Res}_h^N \tag{4.49}$$

$$\phi_h^{N+1} = \phi_h^N + \Delta\phi_h^N \tag{4.50}$$

The new solution is passed down to the next coarsest grid using an area weighted accumulation method or

$$\phi_{h-1}^t = T_{h-1}^h \phi_h \tag{4.51}$$

where ϕ_{h-1}^t represents the transferred ϕ solution on the coarser $(h-1)$ grid and T represents the accumulation method. The residuals that were calculated on the fine grid are then combined using direct summation to get residuals corresponding to the cells of the coarser grid. This step is written in operator form as

$$\mathrm{Res}_{h-1}^t = \tilde{T}_{h-1}^h \mathrm{Res}_h \tag{4.52}$$

where $\tilde{T}$ refers to the residual combination operator. The transferred solution is used to calculate a coarse grid residual, denoted Res_{h-1}^c.

$$\begin{aligned} \mathrm{Res}_{h-1}^c &= \mathrm{Res}\left(\phi_{h-1}^t\right)_{h-1} \\ &= \mathrm{Res}\left(T_{h-1}^h \phi_h\right)_{h-1} \end{aligned} \tag{4.53}$$

A forcing function (FF) is calculated as the difference between the transferred residual and the calculated residual. This is written as

$$\begin{aligned} FF_{h-1} &= \mathrm{Res}_{h-1}^t - \mathrm{Res}_{h-1}^c \\ &= \tilde{T}_{h-1}^h \mathrm{Res}_h - \mathrm{Res}\left(T_{h-1}^h \phi_h\right)_{h-1} \end{aligned} \tag{4.54}$$

A new solution correction ($\Delta\phi_{h-1}$) is calculated on the coarse grid, using the LU method and a right hand side term containing a new residual calculated on the coarse grid and the forcing function.

$$\begin{aligned} \mathrm{LU}_{h-1}\Delta\phi_{h-1} &= \Delta t\left(\mathrm{Res}_{h-1} + FF_{h-1}\right) \\ &= \Delta t\left(\mathrm{Res}_{h-1} + \tilde{T}^{h}_{h-1}\mathrm{Res}_{h} - \mathrm{Res}\left(T^{h}_{h-1}\phi_{h}\right)_{h-1}\right) \end{aligned} \tag{4.55}$$

The new coarse grid solution (ϕ'_{h-1}) is calculated using the solution correction.

$$\phi'_{h-1} = \phi_{h-1} + \Delta\phi_{h-1} \tag{4.56}$$

The steps outlined in Equations 4.51 through 4.56 are repeated until the lowest grid level (coarsest grid) is reached. After calculating a solution on the coarsest grid, the correction can begin to be passed to the finer meshes. An interpolation scheme, denoted $\tilde{I}$ is used to pass the correction.

$$\phi'_{h} = \phi_{h} + \tilde{I}^{h-1}_{h}\left(\phi'_{h-1} - T^{h}_{h-1}\phi_{h}\right) \tag{4.57}$$

The interpolation is continued until the finest mesh is reached. The exact sequence of transferring solutions down to coarser grids then passing corrections back up to finer grids is best explained in a schematic diagram. The specific multigrid scheme used in this work contains five grids and six transfer/interpolate cycles and is called a 'W' cycle [27]. The 'W' refers to the shape, as shown in Figure 4.4 of the path that the multigrid technique uses to accelerate convergence.

It must be said that the interpolating and transferring methods used are not inverse of each other, or

$$\phi_{h} \neq \tilde{I}^{h-1}_{h}T^{h}_{h-1}\phi_{h} \tag{4.58}$$

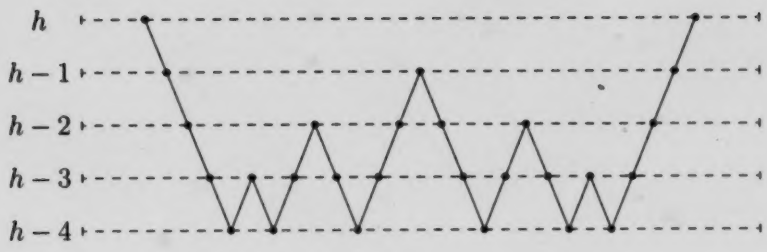

Figure 4.4: 5-Level 6-Cycle 'W' Multigrid Scheme

4.5 Boundary And Initial Conditions For Analysis Of Airfoils

There are four separate boundary conditions that are used in finding the solution for the potential field for the analysis of airfoils. The inflow, outflow, solid and periodic boundaries all have numerical treatments designed to mimic the physical interfaces. The initial condition describes the flow field variables used at the start of the first iteration when calculating the converged solution.

4.5.1 Periodic Boundary

The periodic boundary condition is constructed to represent the ability of fluid to pass between separate channels in a turbine cascade. Instead of creating an entire cascade filled with numerous passages, the flow in a single

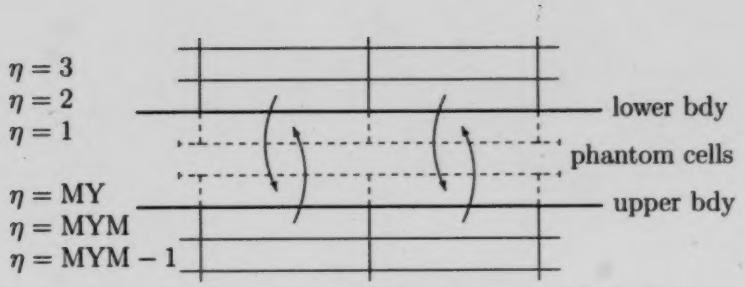

Figure 4.5a: Periodic Boundary Condition Of The Potential Field

channel is calculated. The true flow is simulated by having whatever flow information that leaves through the top of the channel enter through the bottom, and vice-versa. Computationally, the boundary cells of the lower edge are filled with the information from the cells along the upper edge. Similarly, the boundary cells of the upper edge are filled with the information from the cells along the lower edge. The process used to simulate the 'passage flow' or periodic boundary condition can be seen in Figures 4.5a and 4.5b. Figure 4.5a shows the two boundaries separated and where flow field boundary information is situated. Figure 4.5b shows what the periodic boundary is supposed to represent with the simulated grid cell-overlap. Periodic boundary conditions are present from the inlet to the leading edge of the airfoil, and from the trailing edge of the airfoil to the outlet.

4.5.2 Solid Boundary

For the analysis of the airfoil, the physical surface of the airfoil is represented in the computational domain with a solid boundary condition. The boundary condition imposed ensures that the velocity component normal to the surface

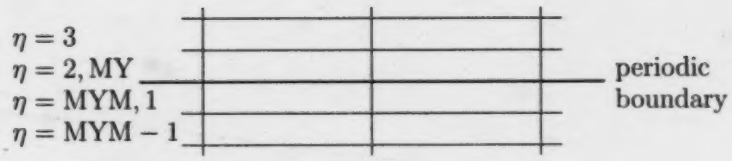

Figure 4.5b: Periodic Boundary Condition - Cont'd

of the airfoil must be equal to zero at the surface of the airfoil. This allows the fluid to travel along the surface, but not through the surface. This condition can be expressed mathematically as

$$\vec{V} \cdot \hat{n}\Big|_{solid} = 0 \tag{4.59}$$

where $\hat{n}$ represents the surface normal. Including the inviscid lamellar decomposition, Equation 4.1, gives

$$U_\infty \cdot \hat{n} + \frac{\partial \phi}{\partial \hat{n}}\bigg|_{solid} = 0 \tag{4.60}$$

The normal direction differential of the potential field is written in terms of ξ and η as

$$U_\infty \cdot \hat{n} + \frac{\partial \phi}{\partial \xi}\frac{\partial \xi}{\partial \hat{n}} + \frac{\partial \phi}{\partial \eta}\frac{\partial \eta}{\partial \hat{n}} \tag{4.61}$$

The geometric $\frac{\partial \xi}{\partial \hat{n}}$ and $\frac{\partial \eta}{\partial \hat{n}}$ terms can be expressed in terms of an angle γ [28]. The location of the γ angle can be seen in Figure 4.6. Using γ, the $\hat{n}$ terms become

$$\frac{\partial \xi}{\partial \hat{n}} = \tan\gamma \tag{4.62}$$

$$\frac{\partial \eta}{\partial \hat{n}} = \frac{1}{\cos\gamma} \tag{4.63}$$

Substitution of Equations 4.62 and 4.63 change Equation 4.61 into

$$\left.\frac{\partial \phi}{\partial \eta}\right|_{solid} = \left(-U_\infty \cdot \hat{n} - \frac{\partial \phi}{\partial \xi} \tan \gamma\right) \cos \gamma \tag{4.64}$$

so that the boundary potential normal to the surface is calculated using both the free stream velocity (U_∞) and the tangential velocity $\left(\frac{\partial \phi}{\partial \xi}\right)$.

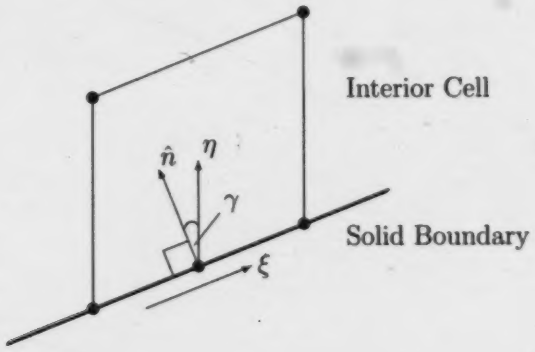

Figure 4.6: Solid Boundary Condition

4.5.3 Inflow Boundary

The analysis inflow boundary condition is constructed to model a uniform flow that would be present at the inlet. The uniform flow condition maintains that the potential remains constant across the inlet or

$$u\Big|_{inlet} = U_\infty \tag{4.65}$$

However, u is defined in Equation 3.12 as

$$u = U_\infty + \frac{\partial \phi}{\partial x} \tag{4.66}$$

Therefore the boundary condition becomes

$$\left.\frac{\partial \phi}{\partial x}\right|_{inlet} = 0 \tag{4.67}$$

The inlet portion of the domain is a purely horizontal section where the x and ξ directions are parallel. The transformed inflow boundary condition becomes

$$\left.\frac{\partial \phi}{\partial x}\right|_{inlet} = \left.\frac{\partial \phi}{\partial \xi}\right|_{inlet} = 0 \tag{4.68}$$

4.5.4 Outflow Boundary

The analysis outflow boundary condition is constructed to mimic the same uniform flow as the inlet condition. The outflow condition forces the potential to remain constant across the outlet, written as

$$u\Big|_{outlet} = U_\infty \tag{4.69}$$

Again, the cartesian velocity definition of Equation 3.12 gives the potential boundary condition as

$$\left.\frac{\partial \phi}{\partial x}\right|_{outlet} = 0 \tag{4.70}$$

Transforming the above equation into general curvilinear coordinates gives

$$\frac{\partial \phi}{\partial x} = \frac{\partial \phi}{\partial \xi}\frac{\partial \xi}{\partial x} + \frac{\partial \phi}{\partial \eta}\frac{\partial \eta}{\partial x} \tag{4.71}$$

Using the Jacobian substitutions from Section 3.4 and the above expansion, the boundary condition becomes

$$\frac{\partial \phi}{\partial \xi}\left(\frac{1}{\|J\|}\frac{\partial y}{\partial \eta}\right) + \frac{\partial \phi}{\partial \eta}\left(\frac{-1}{\|J\|}\frac{\partial y}{\partial \xi}\right) = 0 \tag{4.72}$$

Since the determinant of the transfer matrix, $\|J\|$, is present in both terms, it can be factored out. Rearranging gives

$$\left.\frac{\partial\phi}{\partial\xi}\right|_{outlet} = \frac{\partial y}{\partial\xi}\left(\frac{1}{\frac{\partial y}{\partial\eta}}\right)\frac{\partial\phi}{\partial\eta} \tag{4.73}$$

In order to calculate the $\frac{\partial\phi}{\partial\eta}$ term, it is assumed that the v component of the outlet velocity can be described as

$$v|_{outlet} = -U_\infty \tan\tilde{\alpha} \tag{4.74}$$

where $\tilde{\alpha}$ is the turning angle of flow. Transforming the lamellar form of Equation 4.74 to be similar to Equation 4.71 gives

$$\frac{\partial\phi}{\partial\xi}\frac{\partial\xi}{\partial y} + \frac{\partial\phi}{\partial\eta}\frac{\partial\eta}{\partial y} = -U_\infty \tan\tilde{\alpha} \tag{4.75}$$

Using the inverse Jacobian substitutions, the above equation becomes

$$\frac{\partial\phi}{\partial\xi}\left(\frac{-1}{\|J\|}\frac{\partial x}{\partial\eta}\right) + \frac{\partial\phi}{\partial\eta}\left(\frac{1}{\|J\|}\frac{\partial x}{\partial\xi}\right) = -U_\infty \tan\tilde{\alpha} \tag{4.76}$$

The outflow boundary is always vertical, so the η-wise gridline is vertical, or

$$\frac{\partial x}{\partial\eta} = 0 \tag{4.77}$$

so that Equation 4.76 can be written

$$\frac{\partial\phi}{\partial\eta} = \left(\frac{-\|J\|}{\frac{\partial x}{\partial\xi}}\right) U_\infty \tan\tilde{\alpha} \tag{4.78}$$

The above equation can be used with Equation 4.73 to give

$$\left.\frac{\partial\phi}{\partial\xi}\right|_{outlet} = \frac{\partial y}{\partial\xi}\left(\frac{1}{\frac{\partial y}{\partial\eta}}\right)\left(\frac{-\|J\|}{\frac{\partial x}{\partial\xi}}\right) U_\infty \tan\tilde{\alpha} \tag{4.79}$$

Restating the definition of the Jacobian determinant, Equation 3.30 as

$$\|J\| = \left(\frac{\partial x}{\partial\xi}\frac{\partial y}{\partial\eta} - \frac{\partial x}{\partial\eta}\frac{\partial y}{\partial\xi}\right)$$

it can be seen that using Equation 4.77, $\|J\|$ becomes

$$\|J\| = \frac{\partial x}{\partial \xi}\frac{\partial y}{\partial \eta} \tag{4.80}$$

The above equation allows the simplification of Equation 4.79 to

$$\left.\frac{\partial \phi}{\partial \xi}\right|_{outlet} = -\frac{\partial y}{\partial \xi} U_\infty \tan\tilde{\alpha} \tag{4.81}$$

4.5.5 Initial Condition

The initial condition for the flow field is imposed on the potential only. The starting potential is a field that is everywhere equal to zero. According to the lamellar nature of the velocity field, this corresponds to a uniform flow everywhere within the domain. Mathematically, the initial potential condition can be expressed as

$$\phi\big|_{initial} \equiv 0 \tag{4.82}$$

4.6 Sequence of Solution (Analysis)

A solution for the analysis of a cascade of airfoils is calculated in the following sequence

1. Initialize variables - such as the flux variables, the residuals and the potential field
2. Obtain grid - either as input or created according to the NACA definitions
3. Create coarse grids - according to the number required to perform the multigrid analysis

4. Calculate geometric terms - in order to determine the transformed velocities and flux calculations

5. Set boundary conditions - in the following order; inflow boundary , outflow boundary, periodic boundary from inflow to leading edge, solid boundary from leading edge to trailing edge, periodic boundary from trailing edge to outflow, and finally outflow boundary

6. Calculate residuals - with the flux across the solid boundary equal to zero

7. Solve LU factorization - to determine potential field correction

8. Update solution - to create new potential flow field .

Steps 5 to 8 are repeated within the multigrid cycle until the convergence criteria is obtained. For this experiment, the criteria is nine orders of magnitude of convergence for the maximum residual.

4.7 Domain of Problem

The physical domain of the problem consists of a fluid passage between two airfoils, at zero angle of attack, within an infinite cascade. The distance from the inlet to the leading edge of the airfoil is one chord length, and the distance from the trailing edge of the airfoil to the outlet is two chord lengths. The vertical distance between airfoils, or the spacing-to-chord ratio is three-quarters (0.75) of a chord length. The numerical grid is a sheared-H style mesh consisting of 144 by 32 cells with 64 cells covering the airfoil from leading to trailing edge. There is grid clustering, both in the horizontal

and vertical directions. The vertical clustering creates cell packing near the surfaces of the airfoil, while the horizontal clustering creates cell packing towards the leading and trailing edges of the airfoil. Figure 4.7 shows two identical meshes, stacked one upon the other to show the airfoil used. The airfoil used in Figure 4.7 is a NACA 3410 airfoil.

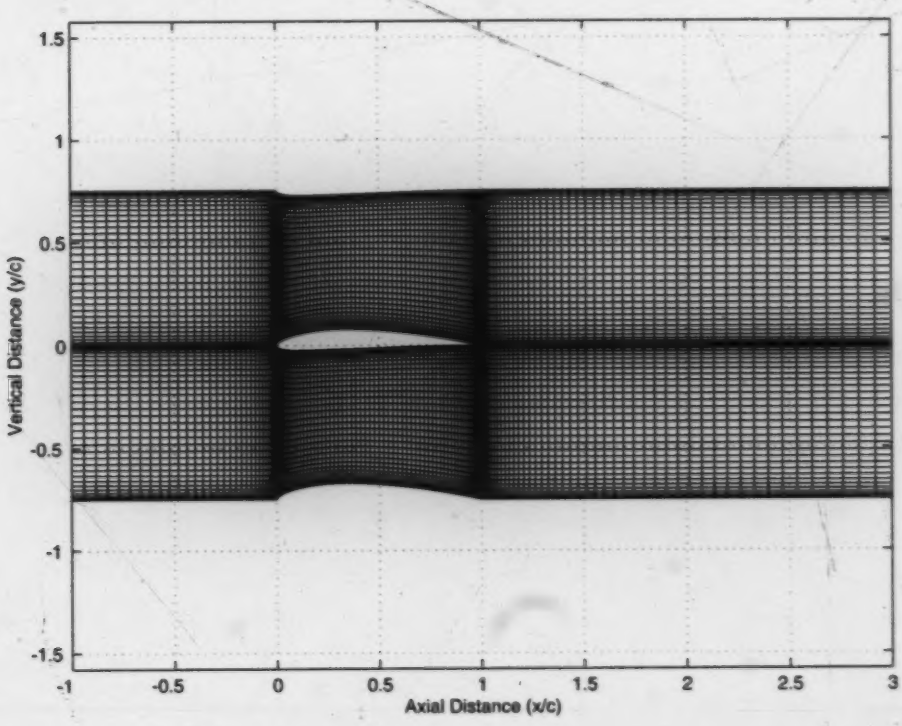

Figure 4.7: Typical Solution Mesh

CHAPTER 5

INVERSE DESIGN METHODS

The inverse design technique is formulated to take advantage of the knowledge that by combining the four cartesian surface velocities of u^+, u^-, v^+ and v^- into the components of $\bar{u}$, Δu, $\bar{v}$, and Δv the design of airfoil camber can be separated from the design of airfoil thickness. The inverse technique is a method of calculating geometry by specifying surface velocities. The actual geometry is determined by calculation of a thickness distribution and camber line by the specification of $\bar{u}$, Δu, $\bar{v}$, and Δv velocities. The inverse method differs from the analysis method by the addition of the velocity input, as well as the geometry calculation method, a different set of boundary conditions and a different residual flux formulation. The inverse technique also has a different solution sequence that calculates a geometry from specified surface velocities.

5.1 Input Velocity Specification

The design calculation of an airfoil geometry requires the specification of $\bar{u}$, Δu, $\bar{v}$, and Δv velocities from the leading edge to the trailing edge of an

airfoil. After analyzing airfoils in each of the four different groups, it became clear that only two velocity components are required to determine different thickness distributions. The analysis showed that for a constant camber line, the Δu and $\bar{v}$ velocities remained relatively constant while the $\bar{u}$ and Δv velocities changed with the changing thickness ratio. This means that an entire group of airfoils with the same camber line can be redesigned with a single Δu and $\bar{v}$ velocity specification. The different thickness distributions in the group are created by only altering the $\bar{u}$ and Δv velocities. Knowing that only the different $\bar{u}$ and Δv velocities determine the thickness of the group of airfoils, a method of recreating the analysis velocities without needing the catalogue of data, as well as similar curves that would describe similar airfoils, is required. Also this method of creating the $\bar{u}$ and Δv velocities for the inverse design requires a simple control. The method of recreating the analysis velocities focuses on determining smooth continuous functions that describe how the $\bar{u}$ and Δv velocities changed with different thickness ratios. The $\bar{u}$ and Δv velocities are trended according to the thickness ratio of the airfoil that each velocity represents. The final result of the trending is a system of equations that can recreate each of the five different $\bar{u}$ and Δv velocities determined in the analysis of the airfoil family, as well as other airfoils with thickness distributions between the five analysis airfoils. The entire system of equations is based on thickness.

5.1.1 Bezier Curves

When the $\bar{u}$ velocity and Δv velocities were first being analyzed, it became apparent that basic functions such as polynomials and other general curves

were unable to correctly define the data curves to the precision needed. The focus on curve fitting then shifted to Bezier curves. Beziers are parametric curves that can create complex shapes while using only a few simple controls[29]. The basis of the Bezier is a family of curves called Bernstein polynomials[29]. These polynomials are contained within a control polygon, where the vertices of the polygon are the control points of the Bezier. This polygon defines the shape of the curve, as well as supplying the end points. The Bezier function[29] is written as

$$C(\zeta) = \sum_{i=0}^{k} B_{i,k}(\zeta)\, P_i\,,\ \zeta \in [0,1] \tag{5.1}$$

where C is the parametric curve, k is the degree of the curve, B is the Bezier coefficient, ζ is the parameter, and P_i are the control points. When $\zeta = 0$, C gives the starting point of the curve, and when $\zeta = 1$, C gives the endpoint of the curve. The ζ parameter represents the distance along the curve. The Bezier coefficient[29] is given by

$$B_{i,k}(\zeta) = \binom{k}{i} \zeta^i\, (1-\zeta)^{k-i} \tag{5.2}$$

where $\binom{k}{i}$ is the binomial coefficient function[29]

$$\binom{k}{i} = \frac{k!}{i!(k-i)!} \tag{5.3}$$

The number of vertices in the control polygon reflect the order of the curve, $(k+1)$ vertices mean a k^{th} order Bernstein polynomial and a k^{th} order Bezier[29].

Since a Bezier is a parametric curve, y is not a function of x. Instead, both x and y are functions of ζ. Also, $C(\zeta)$ represents the entire curve, but it is actually made up of two parts, $C_x(\zeta)$ and $C_y(\zeta)$. For these two parts, the

control points $(P_0, \ldots, P_k)$ are split into $(P_{x,0}, \ldots, P_{x,k})$ and $(P_{y,0}, \ldots, P_{y,k})$. The two functions $C_x(\zeta)$ and $C_y(\zeta)$ are calculated as

$$C_x(\zeta) = \sum_{i=0}^{k} B_{i,k}(\zeta)\, P_{x,i} \tag{5.4}$$

$$C_y(\zeta) = \sum_{i=0}^{k} B_{i,k}(\zeta)\, P_{y,i} \tag{5.5}$$

A fully expanded 3^{rd} order (cubic) Bezier curve is written

$$C_x(\zeta) = (1-\zeta)^3 P_{x,0} + 3\zeta(1-\zeta)^2 P_{x,1} + 3\zeta^2(1-\zeta)P_{x,2} + \zeta^3 P_{x,3} \tag{5.6}$$

$$C_y(\zeta) = (1-\zeta)^3 P_{y,0} + 3\zeta(1-\zeta)^2 P_{y,1} + 3\zeta^2(1-\zeta)P_{y,2} + \zeta^3 P_{y,3} \tag{5.7}$$

The function resembles a cubic polynomial and uses four control points, $(P_0, \ldots, P_3)$ to determine the shape. A cubic Bezier curve can be seen in Figure 5.1. The Bezier equations (Equations 5.6 and 5.7) calculate two separate

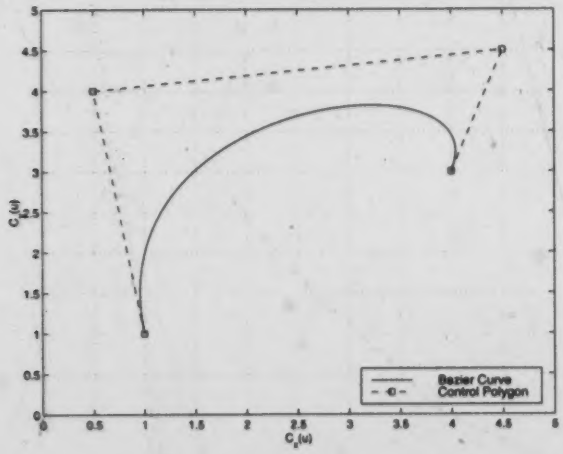

Figure 5.1: Cubic Bezier Curve

parametric curves making the velocity curves difficult to match. Therefore,

the method is reformulated. Instead of both the C_x and C_y curves being dependent on an arbitrary ζ, the method is derived so that C_y is dependent on C_x, making y a function of x. This formulation is necessary to provide the ability to recreate the velocity for insertion in the inverse design code. The characteristics of ζ have to be mirrored in the new Bezier parameter, $\bar{\zeta}$. These characteristics include the need to be monotonically increasing or $\bar{\zeta}_i \geq \bar{\zeta}_{i-1}$. The $\bar{\zeta}$ must also be a real number, and be between zero and one, or $\bar{\zeta} \in [0, 1]$. The new parameter is calculated from the C_x curve, knowing the P_x control points and the x location of the data. The parameter is then used to create the C_y curve using the P_y control points.

The assumption is made that for any point A on the cubic Bezier curve C, there is a corresponding value of $\bar{\zeta}$. This relationship is given by the C_x equation

$$A_x = \left(1-\bar{\zeta}_A\right)^3 P_{x,0} + 3\bar{\zeta}_A\left(1-\bar{\zeta}_A\right)^2 P_{x,1} + 3\bar{\zeta}_A^2\left(1-\bar{\zeta}_A\right) P_{x,2} + \bar{\zeta}_A^3 P_{x,3} \quad (5.8)$$

This equation can be rewritten as a polynomial in $\bar{\zeta}$ as

$$\begin{aligned} A_x \;=\; & \left(-P_{x,0} + 3P_{x,1} - 3P_{x,2} + P_{x,3}\right)\bar{\zeta}_A^3 + \left(3P_{x,0} - 6P_{x,1} + 3P_{x,2}\right)\bar{\zeta}_A^2 \\ & + \left(-3P_{x,0} - 3P_{x,1}\right)\bar{\zeta}_A + P_{x,0} \end{aligned} \quad (5.9)$$

The above equation can be rearranged to form

$$\begin{aligned} 0 \;=\; & \left(-P_{x,0} + 3P_{x,1} - 3P_{x,2} + P_{x,3}\right)\bar{\zeta}_A^3 + \left(3P_{x,0} - 6P_{x,1} + 3P_{x,2}\right)\bar{\zeta}_A^2 \\ & + \left(-3P_{x,0} - 3P_{x,1}\right)\bar{\zeta}_A + \left(P_{x,0} - A_x\right) \end{aligned} \quad (5.10)$$

The roots of Equation 5.10 are found, and the value of $\bar{\zeta}$ that matches the needed characteristics of the parameter is used. This new $\bar{\zeta}_A$ value represents the A_x location on the C_x curve. The value of A_y is found using $\bar{\zeta}_A$. This

calculation means that A_y is a function of $\bar{\zeta}_A$, and $\bar{\zeta}_A$ is a function of A_x, or in general, $y = f(x)$. This process is used to generate a $y = f(x)$ curve for any given x range. The y in this case being a $\bar{u}$ or Δv velocity.

5.1.2 Velocity Recreation Technique

Each of the airfoil groups analyzed were tested with five different thickness distributions. For every thickness there is a corresponding $\bar{u}$ and Δv velocity that can be used to calculate a separate set of control points that define a control polygon. Using the control points for each thickness, a system for trending the airfoil family is determined.

For the $\bar{u}$ velocity plot four control points were calculated and used to create a sixth order Bezier curve. The high order Bezier curve was needed in order to create the correct curvature. The first control point (A) of the $\bar{u}$ velocity is the leading edge point. The exact chordwise location and $\bar{u}$ velocity magnitude are used to define this point, respectively, as

$$P_{A,x} = x_{LE} \tag{5.11}$$

$$P_{A,v} = \bar{u}_{LE} \tag{5.12}$$

where LE refers to the leading edge point of the $(x, \bar{u})$ velocity data.

The second point (B) is the intersection of two tangential lines. The first line extends from the leading edge velocity point and has the identical slope of the leading edge section of the velocity curve. The second line is tangential to the $\bar{u}$ velocity curve at 50% chord. These two lines, the leading edge tangential line and the 50% chord tangential line, are extended until they intersect. This point of intersection is the second control point. The

slope at the leading edge (m_{LE}) is calculated with the first two data points of the $\bar{u}$ velocity data in the following way

$$m_{LE} = \frac{\bar{u}_{LE+1} - \bar{u}_{LE}}{x_{LE+1} - x_{LE}} \tag{5.13}$$

where LE and $LE+1$ describe the first and second points of the $(x, \bar{u})$ data, respectively. A linear function of the form $y = mx + b$ is used to describe the lines tangent to the $\bar{u}$ velocity for the calculation of both the intersection control points. The intercept for the tangent line at the leading edge (b_{LE}) is calculated using

$$b_{LE} = \bar{u}_{LE} - m_{LE} \cdot x_{LE} \tag{5.14}$$

The slope at 50% of the chord ($m_{50\%}$) is calculated with the two data points that bracket the 50% chord point, using an equation similar to Equation 5.13. The intercept of the line tangent to the $\bar{u}$ velocity curve at 50% chord ($b_{50\%}$) is calculated with an equation similar to Equation 5.14. The first intersection control point, P_B, is calculated as

$$P_{B,x} = \frac{b_{50\%} - b_{LE}}{m_{LE} - m_{50\%}} \tag{5.15}$$

and

$$P_{B,v} = m_{LE} \cdot P_{B,x} + b_{LE} \tag{5.16}$$

The third control point (C) of the $\bar{u}$ velocity curve is also an intersection point of two tangential lines. The first line is tangential to the $\bar{u}$ velocity curve at 50% chord. The second line extends from the trailing edge point of the $\bar{u}$ velocity curve with a tangential slope. The intersection point of the 50% chord tangential line and the trailing edge tangential line is the third

control point. The slope at the trailing edge (m_{TE}) is calculated with the final two points of the $\bar{u}$ data and an equation similar to Equation 5.13. The intercept of the line tangent to the $\bar{u}$ velocity curve at the trailing edge (b_{TE}) is calculated with an equation similar to Equation 5.14. The second intersection control point, P_C, is calculated as

$$P_{C,x} = \frac{b_{TE} - b_{50\%}}{m_{50\%} - m_{TE}} \tag{5.17}$$

and

$$P_{C,v} = m_{TE} \cdot P_{C,x} + b_{TE} \tag{5.18}$$

The fourth and final control point (D) of the $\bar{u}$ control polygon is the trailing edge point of the $\bar{u}$ velocity curve. As with the leading edge (first) control point, both the chordwise location and $\bar{u}$ velocity magnitude are used to define each point. The chordwise position and velocity magnitude of this point are defined as

$$P_{D,x} = x_{TE} \tag{5.19}$$

$$P_{D,v} = \bar{u}_{TE} \tag{5.20}$$

The $\bar{u}$ velocity plots from NACA 3406, 3410, and 3414 airfoils can be seen in Figures 5.2 through 5.4. The figures also show the control polygons calculated with the $\bar{u}$ velocity curves. The four control points that are calculated for each $\bar{u}$ velocity are labelled and shown with asterisks.

(text resumes on page 153)

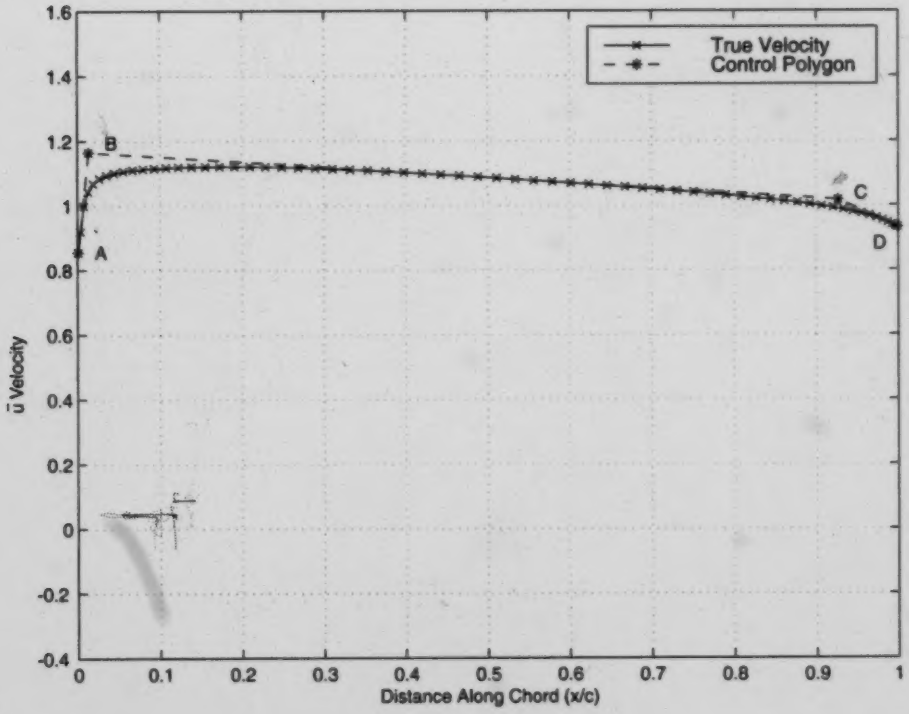

Figure 5.2: Bezier Control Polygon Of NACA 3406 $\bar{u}$ Velocity

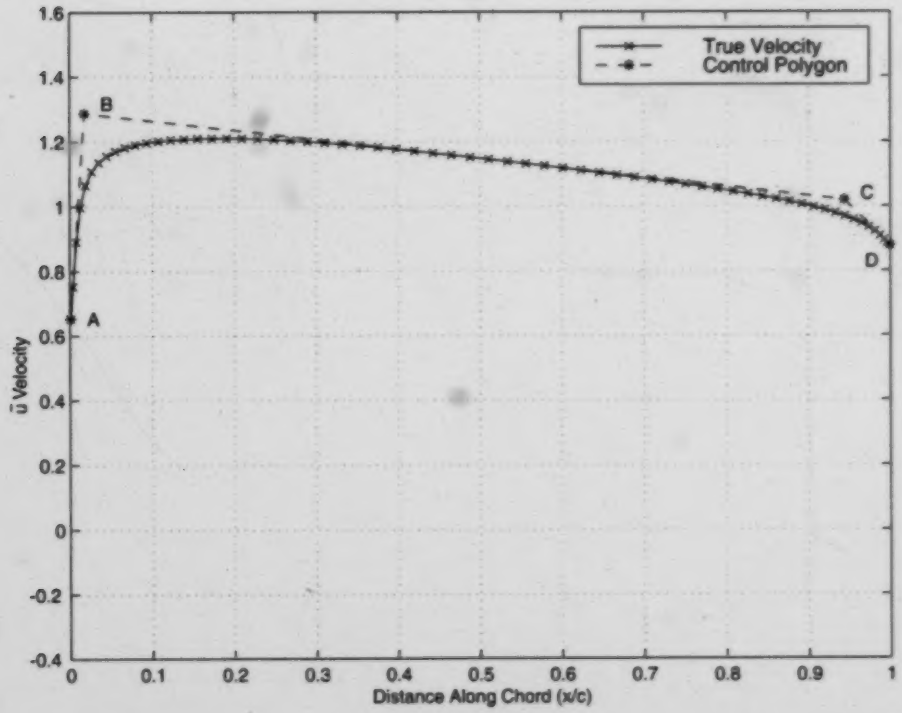

Figure 5.3: Bezier Control Polygon Of NACA 3410 $\bar{u}$ Velocity

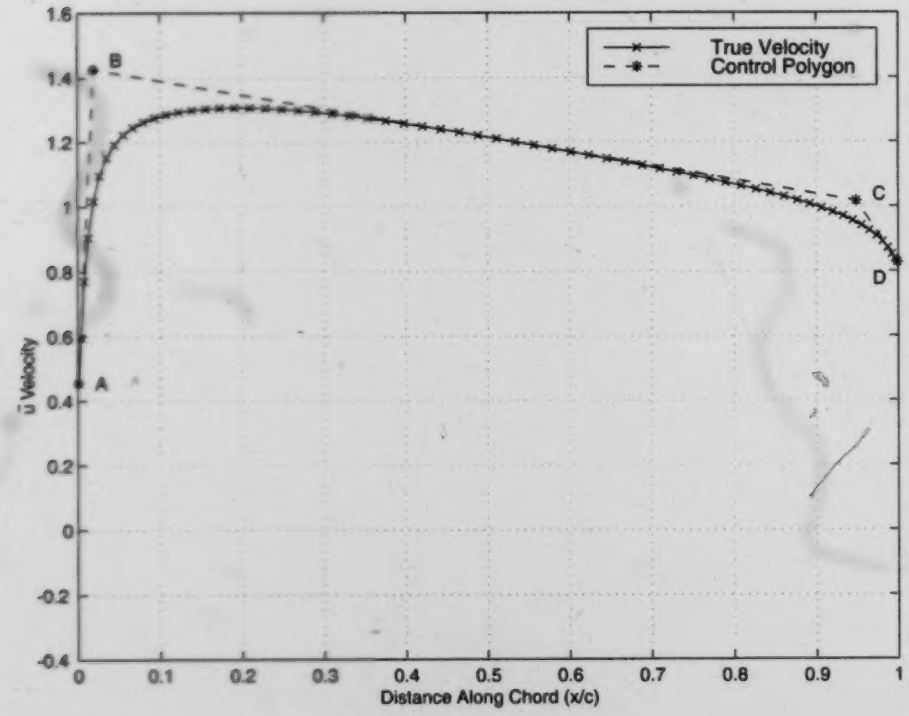

Figure 5.4: Bezier Control Polygon Of NACA 3414 $\bar{u}$ Velocity

The set of control points calculated from the $\bar{u}$ velocities can be seen in Tables 5.1 and 5.2. The control points from each $\bar{u}$ velocity are listed with their corresponding thickness ratios.

TH	Control Point Location (x/c)			
(%)	P_A	P_B	P_C	P_D
6	0.0010	0.0136	0.9263	0.9990
8	0.0010	0.0157	0.9385	0.9990
10	0.0010	0.0178	0.9437	0.9990
12	0.0010	0.0192	0.9466	0.9990
14	0.0010	0.0193	0.9486	0.9990

Table 5.1: Chordwise Location Of $\bar{u}$ Bezier Control Points

TH	Control Point Location $(\bar{u})$			
(%)	P_A	P_B	P_C	P_D
6	0.8542	1.1644	1.0168	0.9315
8	0.7570	1.2241	1.0185	0.9051
10	0.6522	1.2873	1.0193	0.8788
12	0.5907	1.3544	1.0187	0.8529
14	0.4551	1.4263	1.0165	0.8272

Table 5.2: Velocity Magnitude Of $\bar{u}$ Bezier Control Points

The thickness ratios are used to create polynomials that describe the chordwise locations and velocity magnitudes of the control points as functions of a specified thickness, τ. The polynomials that describe the control points for the recreation of the entire series of NACA 4-digit $\bar{u}$ velocities are determined as follows

$$P_{A,x} = 1.000 \times 10^{-3} \tag{5.21}$$

$$P_{A,v} = -5.962 \times 10^{-4}\tau^2 - 3.630 \times 10^{-2}\tau + 1.089 \tag{5.22}$$

$$P_{B,x} = -1.412 \times 10^{-5}\tau^3 + 3.392 \times 10^{-4}\tau^2 - 1.614 \times 10^{-3}\tau + 1.414 \times 10^{-2} \tag{5.23}$$

$$P_{B,v} = 3.270 \times 10^{-2}\tau + 9.463 \times 10^{-1} \tag{5.24}$$

$$P_{C,x} = -9.180 \times 10^{-6}\tau^4 + 4.314 \times 10^{-4}\tau^3 - 7.675 \times 10^{-3}\tau^2 + 6.257 \times 10^{-2}\tau + 7.459 \times 10^{-1} \tag{5.25}$$

$$P_{C,v} = -9.666 \times 10^{-6}\tau^3 + 1.249 \times 10^{-4}\tau^2 + 5.100 \times 10^{-4}\tau + 1.011 \tag{5.26}$$

$$P_{D,x} = 9.990 \times 10^{-1} \tag{5.27}$$

$$P_{D,v} = -1.303 \times 10^{-2}\tau + 1.009 \tag{5.28}$$

The sixth order Bezier curve is created by increasing the weighting on some of the four $\bar{u}$ control points. Generally, every control point has an equal weighting of one, meaning that each control point is used only once, and an n^{th} order Bezier curve requires $n+1$ control points, as explained in the previous section. In order to correctly recreate the five different $\bar{u}$ velocities the general Bezier form needed to be adjusted. To make the recreated $\bar{u}$ velocity curves more closely resemble the original velocities, the first intersection point was given a triple weighting and the second intersection point was given a double weighting creating a sixth order Bezier out of four control points. The formulation of the Bezier control points can be seen in Table 5.3.

The sixth order Bezier curve used to recreate the $\bar{u}$ velocities is written as

$$\begin{aligned}\bar{u} = \; & \left(1-\bar{\zeta}\right)^6 P_0 + 6\bar{\zeta}\left(1-\bar{\zeta}\right)^5 P_1 + 15\bar{\zeta}^2\left(1-\bar{\zeta}\right)^4 P_2 \\ & +20\bar{\zeta}^3\left(1-\bar{\zeta}\right)^3 P_3 + 15\bar{\zeta}^4\left(1-\bar{\zeta}\right)^2 P_4 + 6\bar{\zeta}^5\left(1-\bar{\zeta}\right) P_5 \\ & +\bar{\zeta}^6 P_6\end{aligned} \tag{5.29}$$

P_i	Control Polygon Point
P_0	leading edge point (P_A)
P_1	first intersection point (P_B)
P_2	first intersection point (P_B)
P_3	first intersection point (P_B)
P_4	second intersection point (P_C)
P_5	second intersection point (P_C)
P_6	trailing edge point (P_D)

Table 5.3: $\bar{u}$ Velocity Bezier Control Points

The multiple weighting of some of the control points allows for Equation 5.29 to be restated as

$$\bar{u} = \left(1-\bar{\zeta}\right)^6 P_A + \bar{\zeta}\left(1-\bar{\zeta}\right)^3 \left(11\bar{\zeta}^2 + 3\bar{\zeta} - 6\right) P_B$$

$$+3\bar{\zeta}^4 \left(1-\bar{\zeta}\right)\left(5-3\bar{\zeta}\right) P_C + \bar{\zeta}^6 P_D \qquad (5.30)$$

Figure 5.5 shows the NACA 3410 $\bar{u}$ velocity curve recreated by the Bezier function, along with the original velocity and the control polygon. While the recreated velocity is not identical to the analysis velocity, the purpose of the Bezier is to mimic the basic shape and more importantly the trend of the $\bar{u}$ velocities as the thickness ratio is increased. The maximum error produced in the trending of $\bar{u}$ velocities of NACA 4-Digit airfoils did not exceed 2%. The trending of the $\bar{u}$ velocities of the NACA 4-digit-modified group has a maximum error between the true velocities and the trended velocities of 7%

for all velocities except for the NACA 3414-46 airfoil. The error produced in the trending of the NACA 3414-46 airfoil was 13%. The percent error between the analysis $\bar{u}$ velocities of the General airfoil group and the trended $\bar{u}$ velocities is 5% or less, except for the GEN05 airfoil. There is 20% error between the trended GEN05 $\bar{u}$ velocity and the analysis $\bar{u}$ velocity. The large error in the trending of the $\bar{u}$ velocities of the NACA 4-digit-modified and General airfoil groups is produced by using the same Bezier control polygon for velocities that have different shapes. By using the same function to describe the velocities of the entire group, the Bezier curves best matched velocities with similar shapes. The errors present in the trending of the $\bar{u}$ velocities for all of the groups of airfoils are within acceptable limits.

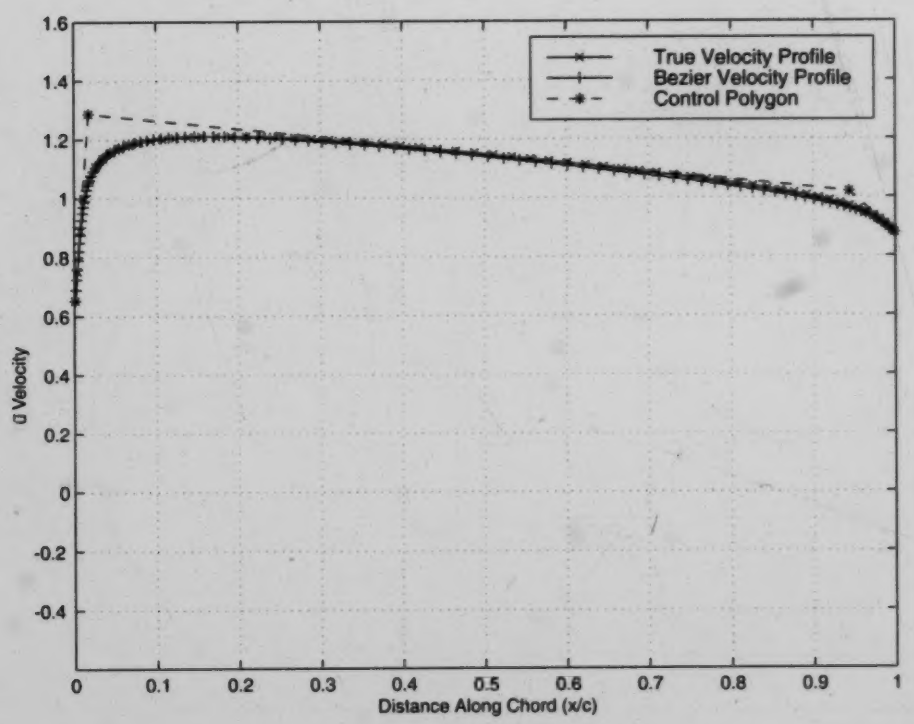

Figure 5.5: Bezier Recreation Of NACA 3410 $\bar{u}$ Velocity

For the Δv velocity plot five control points were calculated and used to create an eighth order Bezier curve. The five control points were calculated using four tangential lines. The first tangential line begins at the leading edge of the Δv velocity curve and has a slope matching that of the leading edge section. The second line is tangential to the Δv velocity plot at the 50% chord point. The third line is tangential to the Δv velocity curve at 80% of the chord length. The fourth and final tangential line begins at the trailing edge of the Δv velocity curve and has a slope identical to the Δv curve at 100% chord. The first control point (A) is the leading edge point of the Δv velocity. The chordwise location and Δv velocity magnitude are used to define this point as

$$P_{A,x} = x_{LE} \tag{5.31}$$

$$P_{A,v} = \Delta v_{LE} \tag{5.32}$$

where LE refers to the leading edge point of the $(x, \Delta v)$ velocity data.

The second control point (B) is the intersection of the leading edge tangent and the 50% chord tangential line. The slope of the line tangent to the Δv velocity curve at the leading edge (m_{LE}) is calculated with the first two data points of the Δv velocity in the following way

$$m_{LE} = \frac{\Delta v_{LE+1} - \Delta v_{LE}}{x_{LE+1} - x_{LE}} \tag{5.33}$$

where LE and $LE + 1$ describe the first and second points of the $(x, \Delta v)$ data, respectively. A linear function of the form $y = mx + b$ is also used to describe the lines tangent to the Δv velocity for the calculation of all the

intersection control points. The intercept for the tangent line at the leading edge (b_{LE}) is calculated using

$$b_{LE} = \Delta v_{LE} - m_{LE} \cdot x_{LE} \tag{5.34}$$

The slope at 50% of the chord ($m_{50\%}$) is calculated with the two data points that bracket the 50% chord point, using an equation similar to Equation 5.13. The intercept of the line tangent to the Δv velocity curve at 50% chord ($b_{50\%}$) is calculated with an equation similar to Equation 5.14. The first intersection control point, P_B is calculated as

$$P_{B,x} = \frac{b_{50\%} - b_{LE}}{m_{LE} - m_{50\%}} \tag{5.35}$$

and

$$P_{B,v} = m_{LE} \cdot P_{B,x} + b_{LE} \tag{5.36}$$

The third control point (C) is the intersection of the 50% chord tangent line and the line tangent to the Δv velocity curve at 80% of the chord. The slope at 80% of the chord ($m_{80\%}$) is calculated with the two data points that bracket the 80% chord point, using an equation similar to Equation 5.13. The intercept of the line tangent to the Δv velocity curve at 80% chord ($b_{80\%}$) is calculated with an equation similar to Equation 5.14. The second intersection control point, P_C is calculated as

$$P_{C,x} = \frac{b_{80\%} - b_{50\%}}{m_{50\%} - m_{80\%}} \tag{5.37}$$

and

$$P_{C,v} = m_{80\%} \cdot P_{C,x} + b_{80\%} \tag{5.38}$$

The fourth control (D) point is the intersection of the 80% chord tangent line and the trailing edge tangent. The slope at the trailing edge (m_{TE}) is calculated with the final two points of the Δv data, using an equation similar to Equation 5.13. The intercept of the line tangent to the Δv velocity curve at the trailing edge (b_{TE}) is calculated with an equation similar to Equation 5.14. The third intersection control point, P_D is calculated as

$$P_{D,x} = \frac{b_{TE} - b_{80\%}}{m_{80\%} - m_{TE}} \tag{5.39}$$

and

$$P_{D,v} = m_{TE} \cdot P_{D,x} + b_{TE} \tag{5.40}$$

The fifth and final control point (E) is the trailing edge point. As with the $\bar{u}$ velocity control points, both the chordwise location and the Δv velocity magnitude are needed to define this point as

$$P_{E,x} = x_{TE} \tag{5.41}$$

$$P_{E,v} = \Delta v_{TE} \tag{5.42}$$

Figures 5.6 through 5.8 show the Δv velocity plots of NACA 3406, 3410, and 3414 airfoils along with the control polygons calculated. The five control points for each Δv velocity are indicated by asterisks and are labelled A through E.

(text resumes on page 165)

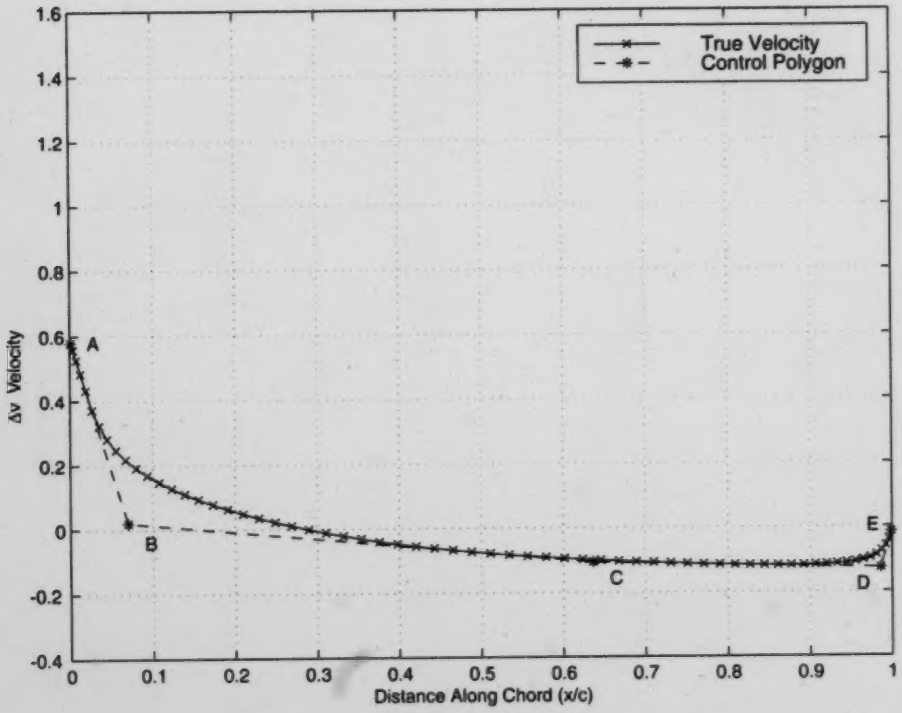

Figure 5.6: Bezier Control Polygon Of NACA 3406 Δv Velocity

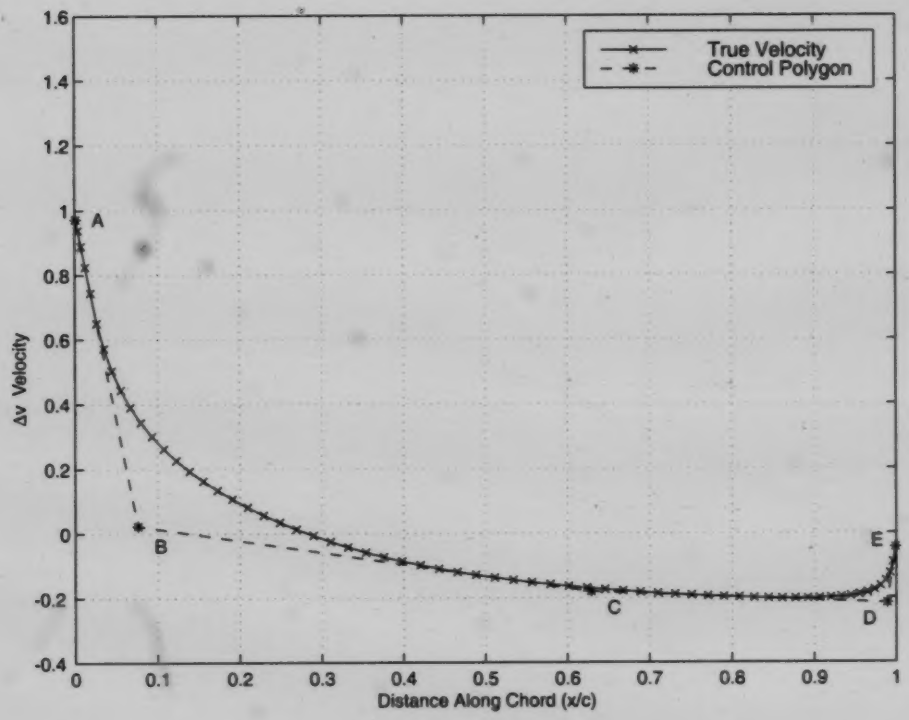

Figure 5.7: Bezier Control Polygon Of NACA 3410 Δv Velocity

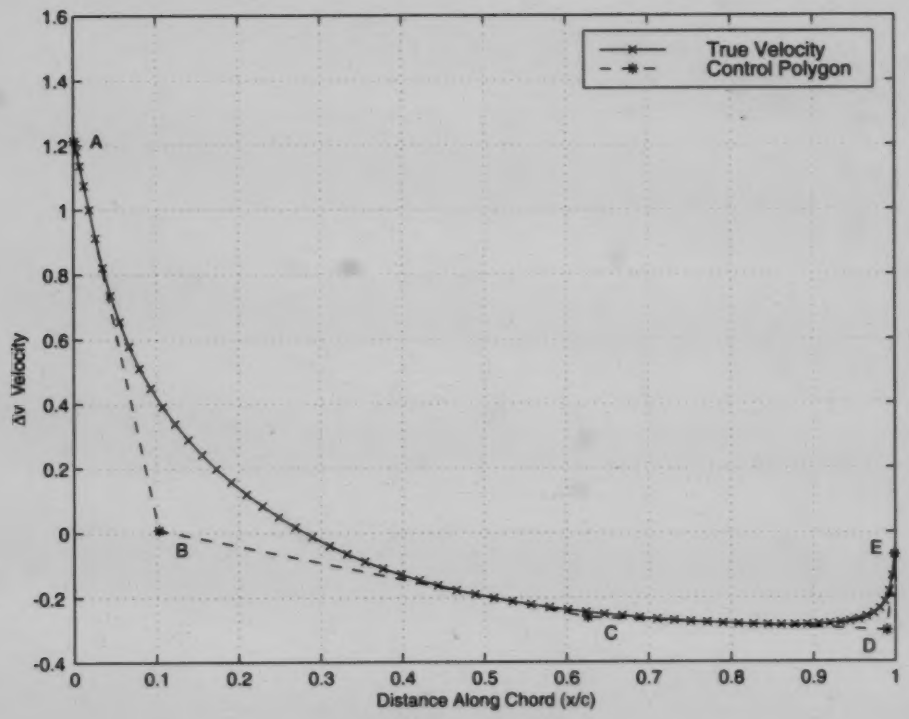

Figure 5.8: Bezier Control Polygon Of NACA 3414 Δv Velocity

The set of control points calculated from the Δv velocities can be seen in Tables 5.4 and 5.5. The control points from each Δv velocity are listed with their corresponding thickness ratios.

TH	Control Point Location (x/c)				
(%)	P_A	P_B	P_C	P_D	P_E
6	0.0010	0.0701	0.6367	0.9863	0.9990
8	0.0010	0.0744	0.6318	0.9882	0.9990
10	0.0010	0.0764	0.6290	0.9890	0.9990
12	0.0010	0.0925	0.6272	0.9894	0.9990
14	0.0010	0.1033	0.6260	0.9896	0.9990

Table 5.4: Chordwise Location Of Δv Bezier Control Points

TH	Control Point Location (Δv)				
(%)	P_A	P_B	P_C	P_D	P_E
6	0.5785	0.0189	-0.1070	-0.1279	-0.0169
8	0.7731	0.0211	-0.1432	-0.1726	-0.0311
10	0.9718	0.0225	-0.1810	-0.2169	-0.0466
12	1.0876	0.0162	-0.2206	-0.2608	-0.0576
14	1.2134	0.0087	-0.2620	-0.3040	-0.0700

Table 5.5: Vertical Location Of Δv Bezier Control Points

The thickness ratios are used to create polynomials that describe the chordwise locations and velocity magnitudes of the control points as functions of a specified thickness, τ. The polynomials that describe the control points for the recreation of the entire series of NACA 4-digit Δv velocities are determined as follows

$$P_{A,x} = 1.000 \times 10^{-3} \tag{5.43}$$

$$P_{A,v} = -3.937 \times 10^{-3}\tau^2 + 1.580 \times 10^{-1}\tau - 2.295 \times 10^{-1} \tag{5.44}$$

$$P_{B,x} = -9.310 \times 10^{-5}\tau^4 + 3.692 \times 10^{-3}\tau^3 - 5.277 \times 10^{-2}\tau^2$$

$$+3.248 \times 10^{-1}\tau - 6.559 \times 10^{-1} \tag{5.45}$$

$$P_{B,v} = 3.540 \times 10^{-5}\tau^4 - 1.418 \times 10^{-3}\tau^3 + 2.020 \times 10^{-2}\tau^2$$

$$-1.213 \times 10^{-1}\tau + 2.801 \times 10^{-1} \tag{5.46}$$

$$P_{C,x} = -1.464 \times 10^{-5}\tau^3 + 5.878 \times 10^{-4}\tau^2 - 8.465 \times 10^{-3}\tau$$

$$+6.694 \times 10^{-1} \tag{5.47}$$

$$P_{C,v} = -1.936 \times 10^{-2}\tau + 1.084 \times 10^{-2} \tag{5.48}$$

$$P_{D,x} = -1.212 \times 10^{-6}\tau^4 + 5.782 \times 10^{-5}\tau^3 - 1.056 \times 10^{-3}\tau^2$$

$$+8.877 \times 10^{-3}\tau + 9.601 \times 10^{-1} \tag{5.49}$$

$$P_{D,v} = -2.202 \times 10^{-2}\tau + 3.810 \times 10^{-3} \tag{5.50}$$

$$P_{E,x} = 9.990 \times 10^{-1} \tag{5.51}$$

$$P_{E,v} = 3.321 \times 10^{-7}\tau^3 + 6.241 \times 10^{-5}\tau^2 - 7.984 \times 10^{-3}\tau$$

$$+2.865 \times 10^{-2} \tag{5.52}$$

The eighth order Bezier is also constructed by increasing the weighting of several of the control points. The multiply defined control points are needed to accurately recreate the Δv velocities. The specific weighting of the control points is a double weighting on both the first and third intersection points, as well as a triple weighting on the second intersection point. The eighth order Bezier points are listed in Table 5.6.

P_i	Control Polygon Point
P_0	leading edge point (P_A)
P_1	first intersection point (P_B)
P_2	first intersection point (P_B)
P_3	second intersection point (P_C)
P_4	second intersection point (P_C)
P_5	second intersection point (P_C)
P_6	third intersection point (P_D)
P_7	third intersection point (P_D)
P_8	trailing edge point (P_E)

Table 5.6: Δv Velocity Bezier Control Points

The eighth order Bezier curve used to recreate the Δv velocities is written as

$$\begin{aligned}\Delta v = \; & \left(1-\bar{\zeta}\right)^8 P_0 + 8\bar{\zeta}\left(1-\bar{\zeta}\right)^7 P_1 + 28\bar{\zeta}^2\left(1-\bar{\zeta}\right)^6 P_2 \\ & +56\bar{\zeta}^3\left(1-\bar{\zeta}\right)^5 P_3 + 70\bar{\zeta}^4\left(1-\bar{\zeta}\right)^4 P_4 + 56\bar{\zeta}^5\left(1-\bar{\zeta}\right)^3 P_5 \\ & +28\bar{\zeta}^6\left(1-\bar{\zeta}\right)^2 P_6 + 8\bar{\zeta}^7\left(1-\bar{\zeta}\right) P_7 + \bar{\zeta}^8 P_8 \end{aligned} \tag{5.53}$$

As with the $\bar{u}$ velocity recreation, the multiple weighting of some of the control points allows some simplification. Equation 5.29 can be rewritten as

$$\Delta v = \left(1-\bar{\zeta}\right)^8 P_A + 4\bar{\zeta}\left(1-\bar{\zeta}\right)^6\left(5\bar{\zeta}+2\right) P_B$$

$$+14\bar{\zeta}^3\left(1-\bar{\zeta}\right)^3\left(3\bar{\zeta}^2-3\bar{\zeta}-4\right) P_C$$

$$+4\bar{\zeta}^6\left(1-\bar{\zeta}\right)\left(7-5\bar{\zeta}\right) P_D + \bar{\zeta}^8 P_E \qquad (5.54)$$

Figure 5.9 shows the NACA 3410 Δv velocity curve recreated by the Bezier function, along with the original velocity and the control polygon. The maximum error produced in the trending of the NACA 4-digit Δv velocities is 5%. The error produced in the trending of the NACA 4-digit-modified Δv velocities ranged from 3% to 11% for the five airfoils in the group. The General group of airfoils had a larger maximum error for the GEN01 and GEN05, with errors of 15% and 19%, respectively. The error created in trending the Δv velocities of the three remaining airfoils has a maximum error of 8%. The errors present in the trending of the Δv velocities for all of the groups of airfoils are within acceptable limits.

Since there are five values for each control point, the highest order polynomial that can be constructed is quartic. The five difference values for each control point correspond to the five different airfoils in the family. The data set of five thicknesses and five values of the same control point is used in a linear least-squares regression to determine the coefficients of the polynomial that describes the relation between thickness and control point. For each control point, the order of the polynomial is determined to assure 99% accuracy of the relation between thickness ratio and control point value.

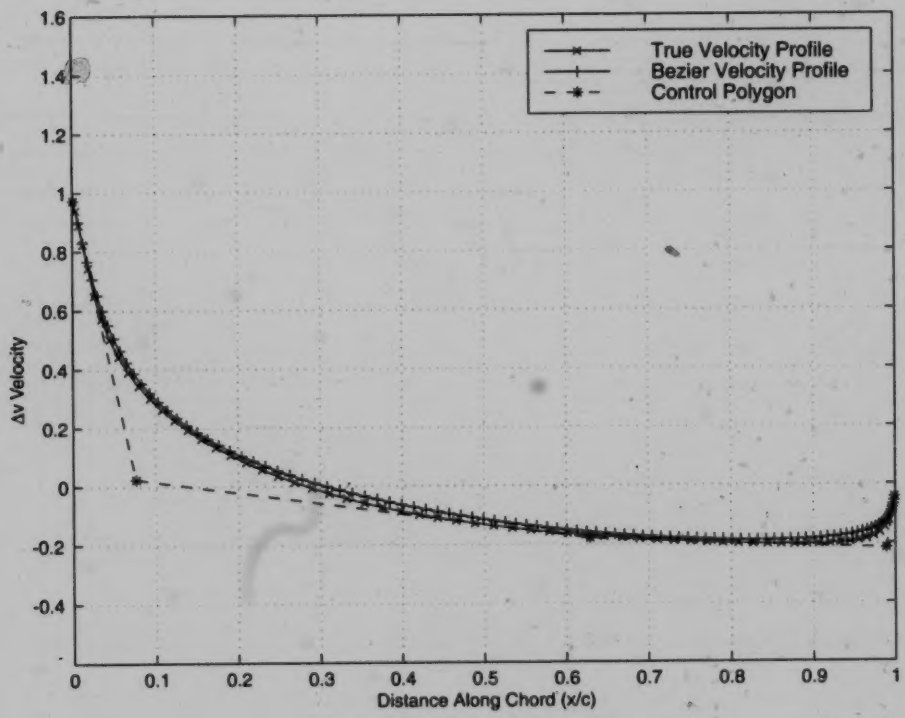

Figure 5.9: Bezier Recreation Of Δv Velocity

The use of the control point polynomials and the Bezier functions has two important benefits. The first benefit is that any one of the five $\bar{u}$ or Δv velocities can be recreated by specifying the thickness ratio. The second benefit is that since the polynomials that describe the control point values are smooth and continuous, any thickness ratio between the smallest and largest airfoils used will create a $\bar{u}$ or Δv velocity.

The technique to recreate $\bar{u}$ and Δv velocities is used with all of the airfoil families analyzed. For each family, the entire range of $\bar{u}$ and Δv velocities is trended and the system of polynomials created allows for both the recreation of analysis velocities and the calculation of intermediate velocities that can be used to design airfoils existing between the analysis airfoils. This process allows the inverse design to be controlled using a single value, the thickness ratio. By adjusting this single control, different velocity profiles are created, and different geometries are calculated.

5.2 Residual Calculation (Design)

The residual calculated during the design of airfoils is constructed the same as the residual calculated during the analysis of airfoils everywhere except at the surface of the airfoil. In analysis calculations the normal flux at the surface of the airfoil is set equal to zero to mimic a solid surface. The normal-direction flux equation, Equation 4.28, is restated as

$$g = \|J\| \left[\frac{1}{\|J\|} \left(-\frac{\partial y}{\partial \xi} u + \frac{\partial x}{\partial \xi} v \right) \right]$$

where $\|J\|$ is the determinant of the Jacobian transformation matrix, $\frac{\partial y}{\partial \xi}$ and $\frac{\partial x}{\partial \xi}$ are geometric terms calculated in the transformation into generalized coordinates, and u and v are cartesian velocities. In analysis of airfoils, the u and v velocities are set equal to zero in the calculation of the fluxes at the surface. In the design of airfoils, the u and v velocities are set equal to the input surface velocities for the calculation of the fluxes at the surface of the airfoil. The specification of the input velocities controls the inverse design method. The specified surface velocities are added to the flux terms so that while still controlling the inverse calculation the flow field is allowed to slowly adapt and maintain continuity. If the specified velocities were used anywhere else, there would be no guarantee that the conservation of mass would be maintained, and the resulting airfoil that is calculated may or may not be an appropriate solution. Without maintaining continuity, the calculated geometry may not describe a true physical airfoil.

5.3 Geometry Calculation

During a calculation, whether in inverse design or analysis mode, the convergence of the residual is calculated every iteration after completing a single multigrid W-cycle. In inverse design mode, if the convergence criteria has not been met, the current potential field is used to calculate a new airfoil geometry. More specifically, the potential field is used to calculate a set of cartesian velocities along the surface of the existing airfoil. These surface velocities are then used to calculate a new camber line and thickness distribution. For this geometry calculation, a surface description similar to one devised by Dang [16] is used. The solid surface of the airfoil is expressed as a function σ in terms of the thickness distribution and camber line, written as

$$\sigma^{\pm} = y - (f_{cl} \pm f_{th}) \tag{5.55}$$

where σ^+ and σ^- refer to the upper and lower surfaces of the airfoil respectively. The f_{cl} term refers to the new camber line that is a function of x only. The f_{th} term refers to the new thickness distribution that is also a function of x only.

The solid surface of the airfoil is material surface. The material derivative is used to describe the material surface such that

$$\frac{D\sigma}{Dt} = 0 \tag{5.56}$$

The material derivative can then be expanded to become

$$\frac{\partial \sigma}{\partial t} + u\frac{\partial \sigma}{\partial x} + v\frac{\partial \sigma}{\partial y} = 0 \tag{5.57}$$

Substitution of the definition of σ, Equation 5.55, turns Equation 5.57 into

$$\frac{\partial \sigma}{\partial t} + u\left(\frac{\partial y}{\partial x} - \frac{\partial f_{cl}}{\partial x} \mp \frac{\partial f_{th}}{\partial x}\right) + v\left(\frac{\partial y}{\partial y} - \frac{\partial f_{cl}}{\partial y} \mp \frac{\partial f_{th}}{\partial y}\right) = 0 \tag{5.58}$$

Since f_{cl} and f_{th} are functions of x only, Equation 5.58 can be simplified and rewritten in a time dependent form as

$$\frac{\partial \sigma}{\partial t} + u\left(-\frac{\partial f_{cl}}{\partial x} \mp \frac{\partial f_{th}}{\partial x}\right) + v = 0 \tag{5.59}$$

This geometry calculation has no time dependence however, so the σ surface is considered to be a constant or

$$\frac{\partial \sigma}{\partial t} = 0 \tag{5.60}$$

which allows Equation 5.59 to become

$$u\frac{\partial f_{cl}}{\partial x} \pm \frac{\partial f_{th}}{\partial x} = v \tag{5.61}$$

Equation 5.61 is now in the basic form used to calculate the new geometry. The upper and lower surfaces can be expressed in terms of the surface velocities, respectively, as

$$u^+\frac{\partial f_{cl}}{\partial x} + u^+\frac{\partial f_{th}}{\partial x} = v^+ \tag{5.62}$$

$$u^-\frac{\partial f_{cl}}{\partial x} - u^-\frac{\partial f_{th}}{\partial x} = v^- \tag{5.63}$$

where u^+, v^+ refer to the upper surface velocities and u^-, v^- refer to the lower surface velocities. Equations 5.62 and 5.63 are combined in order to create the velocity components that were used in the trending of the airfoil velocities. The combined geometry equations are written as

$$\bar{u}\frac{\partial f_{cl}}{\partial x} + \frac{\Delta u}{2}\frac{\partial f_{th}}{\partial x} = \bar{v} \tag{5.64}$$

$$\frac{\Delta u}{2}\frac{\partial f_{cl}}{\partial x} + \bar{u}\frac{\partial f_{th}}{\partial x} = \frac{\Delta v}{2} \tag{5.65}$$

For solution, the surface velocity components are constructed out of the updated potential field at the end of every iteration. The surface velocities are calculated using Equations 3.42 and 3.43 restated as

$$u = U_\infty + \frac{1}{\|J\|}\left[\frac{\partial\phi}{\partial\xi}\frac{\partial y}{\partial\eta} + \frac{\partial\phi}{\partial\eta}\left(-\frac{\partial y}{\partial\xi}\right)\right]$$

$$v = \frac{1}{\|J\|}\left[\frac{\partial\phi}{\partial\xi}\left(-\frac{\partial x}{\partial\eta}\right) + \frac{\partial\phi}{\partial\eta}\frac{\partial x}{\partial\xi}\right]$$

The f_{cl} and f_{th} terms in Equations 5.64 and 5.65 can be expressed as finite differences as

$$\frac{\partial f}{\partial x} = \frac{f_i - f_{i-1}}{x_i - x_{i-1}} \tag{5.66}$$

Using the finite difference expansion, the two surface equations, Equations 5.64 and 5.65, are solved simultaneously in the form

$$\begin{bmatrix} \bar{u} & \frac{\Delta u}{2} \\ \frac{\Delta u}{2} & \bar{u} \end{bmatrix}\cdot\begin{bmatrix} f_{cl,i} \\ f_{th,i} \end{bmatrix} = \begin{bmatrix} \bar{v}\,(x_i - x_{i-1}) + \bar{u} f_{cl,i-1} + \frac{\Delta u}{2} f_{th,i-1} \\ \frac{\Delta v}{2}\,(x_i - x_{i-1}) + \frac{\Delta u}{2} f_{cl,i-1} + \bar{u} f_{th,i-1} \end{bmatrix} \tag{5.67}$$

The surface equations can also be solved separately as

$$f_{cl,i} = f_{cl,i-1} + \frac{\left(\bar{u}\cdot\bar{v} - \frac{\Delta u\cdot\Delta v}{4}\right)(x_i - x_{i-1})}{\bar{u}^2 - \frac{\Delta u^2}{4}} \tag{5.68}$$

$$f_{th,i} = f_{th,i-1} + \frac{\left(\frac{\bar{u}\cdot\Delta v}{2} - \frac{\Delta u\cdot\bar{v}}{2}\right)(x_i - x_{i-1})}{\bar{u}^2 - \frac{\Delta u^2}{4}} \tag{5.69}$$

The new surface is calculated by marching from the leading edge of the airfoil to the trailing edge. In a single sweep, a new thickness and new camber line are determined. The new thickness distribution and camber line describe the airfoil that matches the current potential field. As the potential field converges, the thickness and camber line adapt until the convergence criteria

is met. Once the nine orders of residual convergence have been reached, the final airfoil design is the geometry described by the specified input surface velocities. The final converged potential field is the solution of the flow around the final airfoil geometry.

5.4 Boundary And Initial Conditions For Design Of Airfoils

The boundary and initial conditions prescribed for the design of airfoils are nearly identical to the conditions prescribed for the analysis of airfoils. The only condition that changes is the inlet boundary condition. The analysis inlet condition was that the flow was to be uniform with a magnitude equal to the free stream velocity U_∞. The inverse inlet boundary condition is that the potential field at the inlet is equal to zero, expressed mathematically as

$$\phi\Big|_{inlet} = 0 \tag{5.70}$$

The design outlet boundary condition remains the same as for analysis. The outlet boundary condition states that the flow along the entire outlet was to be uniform with speed U_∞. This condition can be written

$$u\Big|_{outlet} = U_\infty \tag{5.71}$$

The periodic boundary condition for inverse design is the same as for airfoil analysis. The periodic boundary cells are used to mimic fluid flow between passages of a cascade. The flow information that exits the channel through the top of the passage enters through the bottom and vice-versa. This boundary condition is prescribed on both the upper and lower edges

of the passage from the inlet to the leading edge of the airfoil and from the trailing edge to the outlet.

The solid boundary condition for the design of airfoils is again the condition that the velocity component normal to the surface of the airfoil is equal to zero at the surface of the airfoil, or

$$\vec{V} \cdot \hat{n}\Big|_{solid} = 0 \tag{5.72}$$

The solid boundary condition is prescribed on both surfaces of the airfoil from leading edge to trailing edge.

The initial condition specified for the design of airfoils is that the potential field is everywhere equal to zero, or

$$\phi\Big|_{initial} \equiv 0 \tag{5.73}$$

Since most of the design boundary conditions are identical to the conditions prescribed in the analysis of airfoils, further details of the boundary conditions can be seen in Section 4.5.

5.5 Sequence Of Solution (Design)

A solution for the design of an airfoil geometry through the specification of surface velocities is calculated in the following sequence

1. Initialize variables - such as the flux variable, the residuals and the potential field

2. Obtain specified surface velocities - in the $\bar{u}$, Δu, $\bar{v}$, and Δv form and calculate the u^+, u^-, v^+, and v^- velocities

3. Obtain grid - either as input or create according to the NACA definitions

4. Create coarse grids - according to the multigrid specification

5. Calculate geometric terms - in order to determine the contravariant velocities and solve the transformed equations

6. Set boundary conditions - in the following order; inflow boundary, outflow boundary, periodic boundary from inlet to leading edge, solid boundary from leading edge to trailing edge, and finally the periodic boundary from trailing edge to outlet

7. Calculate residuals - with the specified input velocities in the flux terms

8. Solve LU factorization - to determine potential field correction

9. Update solution - to create new potential flow field

10. Calculate cartesian velocities - from updated potential field

11. Calculate new thickness distribution and camber line - from cartesian velocities

12. Create new grid - from new thickness distribution and camber line

13. Calculate geometric terms - in order to determine the contravariant velocities and solve the transformed equations

14. Create coarse grids - according to the multigrid specification

15. Calculate geometric terms - in order to determine the contravariant velocities and solve the transformed equations

16. Set boundary conditions - in the following order; inflow boundary, outflow boundary, periodic boundary from inlet to leading edge, solid boundary from leading edge to trailing edge, and finally the periodic boundary from trailing edge to outlet

17. Calculate residuals - with the specified input velocities in the flux terms

18. Solve LU factorization - to determine potential field correction

19. Update solution - to create new potential flow field

20. Calculate cartesian velocities - from updated potential field

21. Calculate new thickness distribution and camber line - from cartesian velocities

Steps 12 to 21 are repeated within the multigrid cycle until the convergence criteria is obtained and a final geometry is calculated. For this problem, the convergence criteria is a decrease of nine orders of magnitude in the maximum residual.

CHAPTER 6

RESULTS

6.1 NACA 4-Digit Airfoils

The first step in verifying the accuracy of this inverse method is to determine whether the calculation of an airfoil geometry is possible using a set of converged analysis surface velocities as input. The second step in verification is to test the validity of the velocity trending.

From the analysis of the different groups of airfoils it has been shown that the thickness distribution is directly related to the $\bar{u}$ and Δv velocities, and the camber line is directly related to the Δu and $\bar{v}$ velocities. Therefore a set of airfoils with different thickness distributions and identical camber lines can be designed with a set of specified surface velocities that have different $\bar{u}$ and Δv velocities, and identical Δu and $\bar{v}$ velocities. For the entire series of NACA 4-digit airfoil design tests, the Δu and $\bar{v}$ velocities are held constant. Every 4-digit design input file contains the Δu and $\bar{v}$ velocities calculated during the analysis of the NACA 3410 airfoil. The $\bar{u}$ and Δv velocities change for every test case, but the Δu and $\bar{v}$ velocities do not change.

6.1.1 NACA 3410 Airfoil

The purpose of the first set of test cases is to recreate a NACA 3410 airfoil. For the first calculation, the specified input velocities are taken directly from the analysis of a NACA 3410 airfoil. The $\bar{u}$, Δv, $\bar{v}$ and Δv velocities are all from a converged solution of the flow around a NACA 3410 airfoil. For the second calculation, the specified input velocities have $\bar{u}$ and Δv velocities that are created using the trending system of equations pertaining to the NACA 4-digit airfoils. The 4-digit equations were used to calculate the $\bar{u}$ and Δv velocities corresponding to a 10% thick airfoil. The Δv and $\bar{v}$ velocities are the analysis NACA 3410 velocities. The calculated thicknesses from the two inverse calculation can be seen in Figure 6.1 along with the thickness distribution of the original NACA 3410 airfoil.

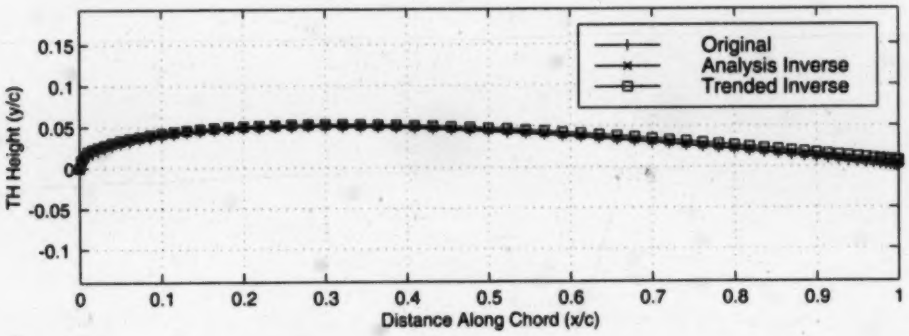

Figure 6.1: Original And Inversely Designed NACA 3410 Thickness Distributions

The three thickness distributions appear very similar. The difference between the thickness inversely designed using the analysis $\bar{u}$ and Δv velocities

and the original thickness is calculated using

$$y_{th,d} = \frac{y_{th,a} - y_{th,o}}{c} \times 100\% \tag{6.1}$$

where $y_{th,d}$ is the percent difference, $y_{th,o}$ is the original thickness distribution, $y_{th,a}$ is the thickness inversely designed with the analysis $\bar{u}$ and Δv velocities, and c is the chord length. The maximum percent difference calculated is 0.6%, as seen in Figure 6.2a.

The difference between the thickness designed with the analysis $\bar{u}$ and Δv velocities and the thickness designed with the trended $\bar{u}$ and Δv velocities is calculated with

$$y_{th,d} = \frac{y_{th,t} - y_{th,a}}{c} \times 100\% \tag{6.2}$$

where $y_{th,d}$ is the percent difference, $y_{th,a}$ is the thickness inversely designed with the analysis $\bar{u}$ and Δv velocities, $y_{th,t}$ is the thickness designed with the trended $\bar{u}$ and Δv velocities, and c is the chord length. The maximum percent difference calculated is 0.5%, as seen in Figure 6.2b.

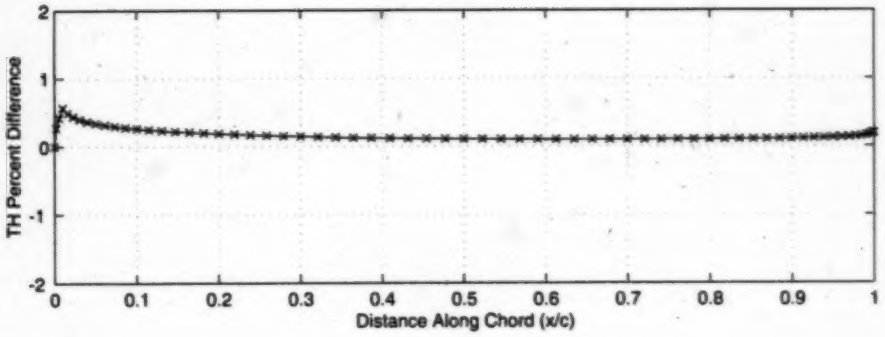

Figure 6.2a: Difference In Original And Inversely Designed NACA 3410 Thickness Distributions

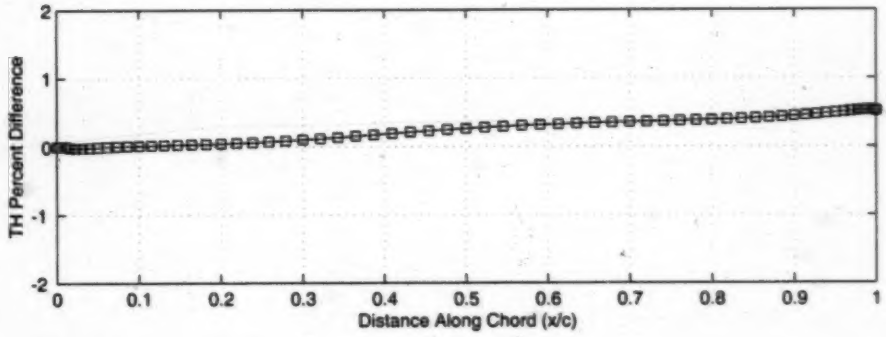

Figure 6.2b: Difference In Analysis And Trended Inversely Designed NACA 3410 Thickness Distributions

The calculated camber lines from the two inverse calculations can be seen in Figure 6.3 along with the camber line of the original NACA 3410 airfoil.

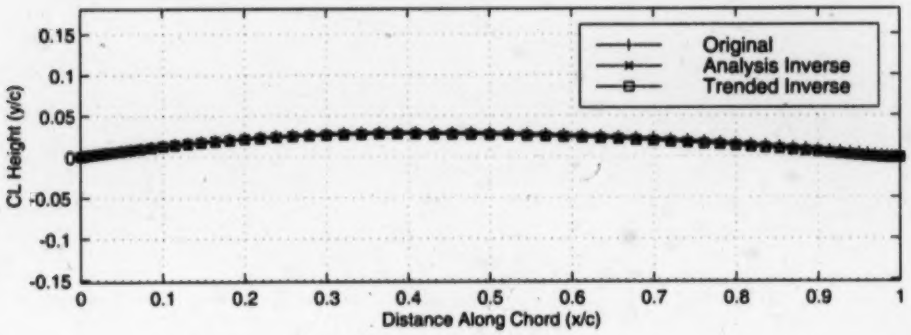

Figure 6.3: Original And Inversely Designed NACA 3410 Camber Lines

The difference between the camber inversely designed using the analysis $\bar{u}$ and Δv velocities and the original camber is calculated using

$$y_{cl,d} = \frac{y_{cl,a} - y_{cl,o}}{c} \times 100\% \tag{6.3}$$

where $y_{cl,d}$ is the percent difference, $y_{cl,o}$ is the original camber line, $y_{cl,a}$ is the camber inversely designed with the analysis $\bar{u}$ and Δv velocities, and c is the chord length. The maximum percent difference calculated is 0.3%, as seen in Figure 6.4a.

The difference between the camber designed with the analysis $\bar{u}$ and Δv velocities and the camber designed with the trended $\bar{u}$ and Δv velocities is calculated with

$$y_{cl,d} = \frac{y_{cl,t} - y_{cl,a}}{c} \times 100\% \tag{6.4}$$

where $y_{cl,d}$ is the percent difference, $y_{cl,a}$ is the camber inversely designed with the analysis $\bar{u}$ and Δv velocities, $y_{cl,t}$ is the camber designed with the trended $\bar{u}$ and Δv velocities, and c is the chord length. The maximum percent difference calculated is less than 0.1%, as seen in Figure 6.4b.

From these tests it can be concluded that both analysis and trended velocities can be used to accurately recreate both the thickness distribution and the camber line of a NACA 3410 airfoil.

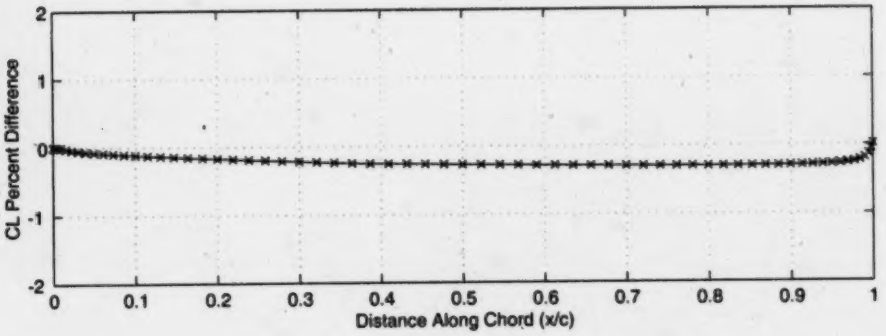

Figure 6.4a: Difference In Original And Inversely Designed NACA 3410 Camber Lines

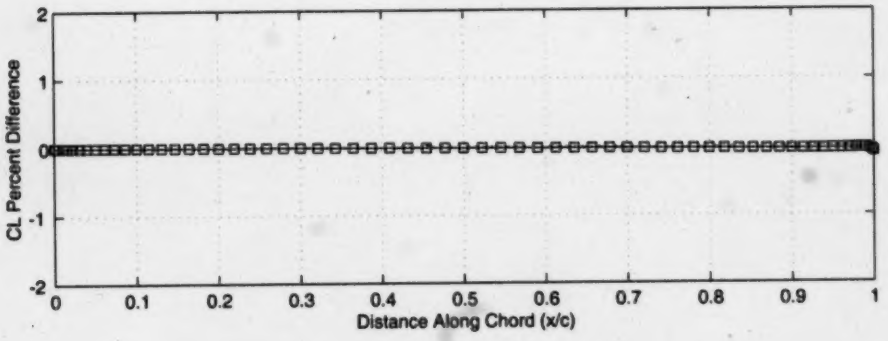

Figure 6.4b: Difference In Analysis And Trended Inversely Designed NACA 3410 Camber Lines

6.1.2 NACA 3406 Airfoil

After being able to inversely design a NACA 3410 airfoil specifying both analysis and trended $\bar{u}$ and Δv velocities, the ability of the inverse method to design other airfoils in the group needs to be tested. The purpose of the next set of test cases is to design a NACA 3406 airfoil, the thinnest airfoil from the 4-digit group. The specified Δu and $\bar{v}$ velocities for this set of test cases are taken from the converged solution of the analysis of a NACA 3410 airfoil. The 3410 Δu and $\bar{v}$ velocities are used to test the theory that since all airfoils in the 4-digit group have identical camber lines, they can be designed with identical Δu and $\bar{v}$ velocities. For the first inverse design calculation of a NACA 3406 airfoil, the $\bar{u}$ and Δv velocities are taken from the analysis of a NACA 3406 airfoil. For the second inverse design calculation of a NACA 3406 airfoil, the $\bar{u}$ and Δv velocities are calculated with the system of equations that describe the velocity trending. By specifying a thickness of 6%, the NACA 4-digit trending method calculates both a $\bar{u}$ and Δv velocity. The calculated thicknesses from the two inverse calculations can be seen in Figure 6.5 along with the thickness distribution of the original NACA 3406 airfoil.

The difference between the thickness inversely designed using the analysis $\bar{u}$ and Δv velocities and the original thickness is calculated using Equation 6.1. The maximum percent difference calculated is 0.5%, as seen in Figure 6.6a.

The difference between the thickness designed with the analysis $\bar{u}$ and Δv velocities and the thickness designed with the trended $\bar{u}$ and Δv velocities is calculated with Equation 6.2. The maximum percent difference calculated is

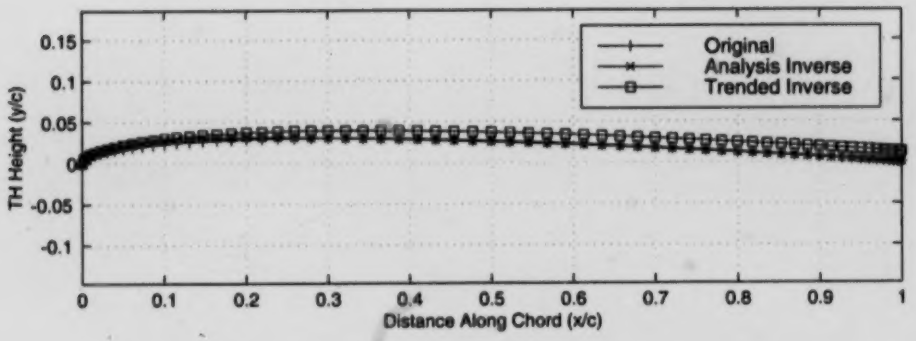

Figure 6.5: Original And Inversely Designed NACA 3406 Thickness Distributions

1.3%, as seen in Figure 6.6b.

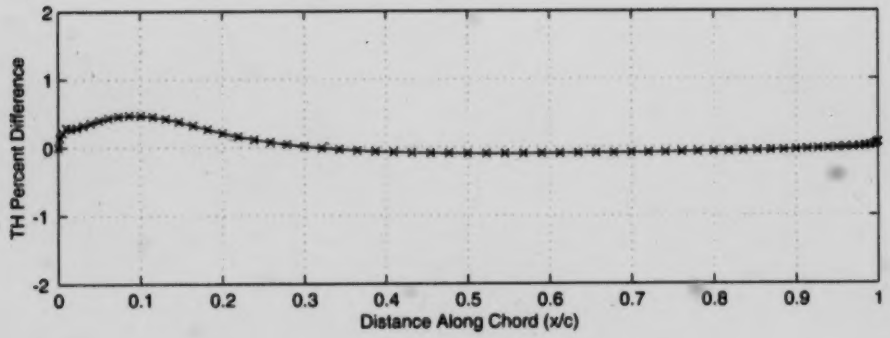

Figure 6.6a: Difference In Original And Inversely Designed NACA 3406 Thickness Distributions

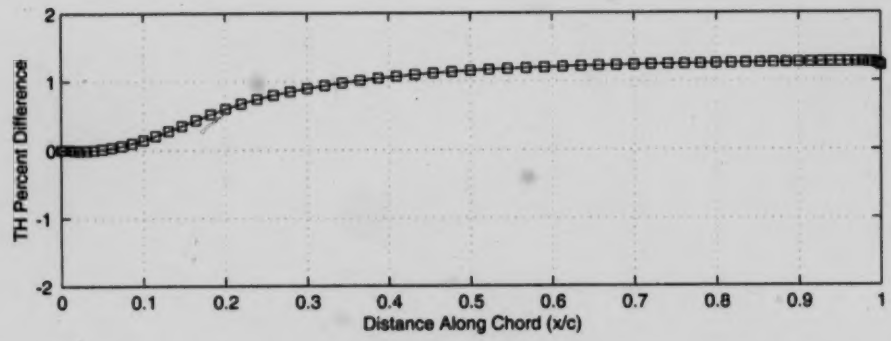

Figure 6.6b: Difference In Analysis And Trended Inversely Designed NACA 3406 Thickness Distributions

The calculated camber lines from the two inverse calculations can be seen in Figure 6.7 along with the camber line of the original NACA 3406 airfoil.

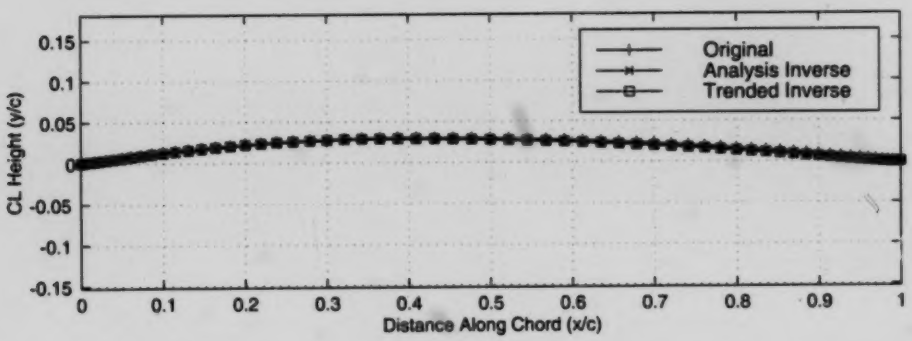

Figure 6.7: Original And Inversely Designed NACA 3406 Camber Lines

The difference between the camber inversely designed using the analysis $\bar{u}$ and Δv velocities and the original camber is calculated using Equation 6.3. The maximum percent difference calculated is 0.3%, as seen in Figure 6.8a.

The difference between the camber designed with the analysis $\bar{u}$ and Δv velocities and the camber designed with the trended $\bar{u}$ and Δv velocities is calculated with Equation 6.4. The maximum percent difference calculated is less than 0.1%, as seen in Figure 6.8b. These results prove that the analysis $\bar{u}$ and Δv velocities of a NACA 3406 airfoil can accurately reproduce the thickness distribution and camber line. Also, the $\bar{u}$ and Δv velocities created from the trending of the group can be used to accurately recreate a NACA 3406 airfoil. These results also show that the NACA 3406 camber line can be accurately redesigned using the Δu and $\bar{v}$ velocities from the analysis of the NACA 3410 airfoil, with either the analysis or trended $\bar{u}$ and Δv velocities.

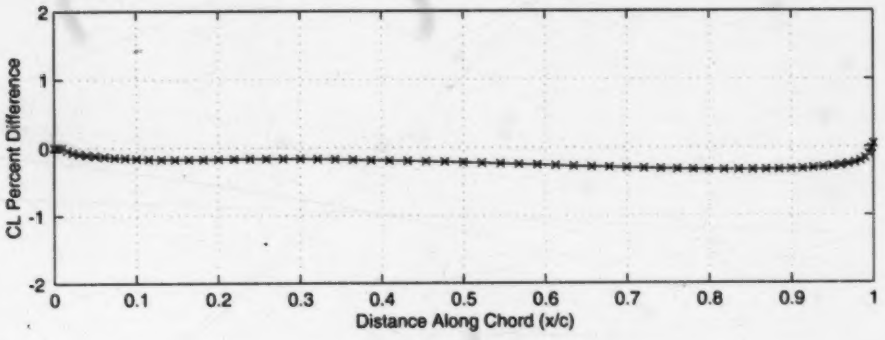

Figure 6.8a: Difference Of Original And Inversely Designed NACA 3406 Camber Lines

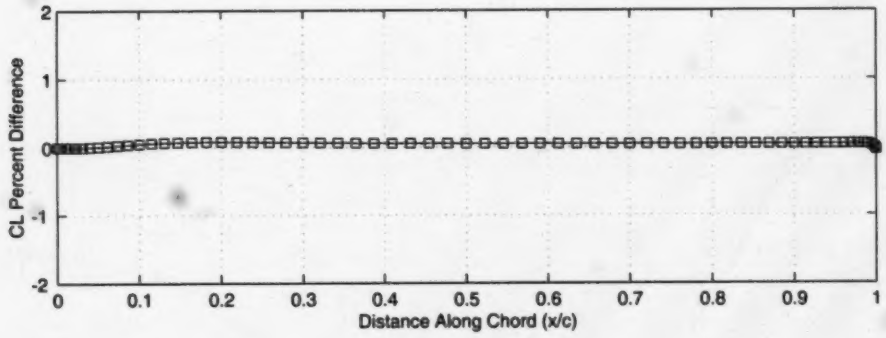

Figure 6.8b: Difference Of Analysis And Trended Inversely Designed NACA 3406 Camber Lines

6.1.3 NACA 3414 Airfoil

The purpose of the next set of test cases is to inversely calculate a NACA 3414 airfoil. For this set of test cases, the Δu and $\bar{v}$ velocities will still be taken from the analysis of a NACA 3410 airfoil. The first calculation has $\bar{u}$ and Δv velocities that were taken from the analysis of a NACA 3414 airfoil. The second calculation has $\bar{u}$ and Δv velocities that were created using the trending equations with a specified thickness ratio of 14%. The calculated thicknesses from the two inverse calculations can be seen in Figure 6.9 along with the thickness distribution of the original NACA 3414 airfoil.

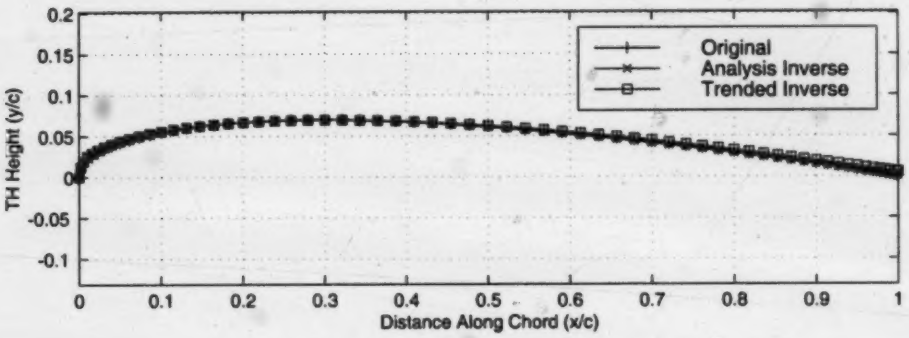

Figure 6.9: Original And Inversely Designed NACA 3414 Thickness Distributions

The difference between the thickness inversely designed using the analysis $\bar{u}$ and Δv velocities and the original thickness is calculated using Equation 6.1. The maximum percent difference calculated is 0.6%, as seen in Figure 6.10a.

The difference between the thickness designed with the analysis $\bar{u}$ and Δv

velocities and the thickness designed with the trended $\bar{u}$ and Δv velocities is calculated with Equation 6.2. The maximum percent difference calculated is 0.6%, as seen in Figure 6.10b.

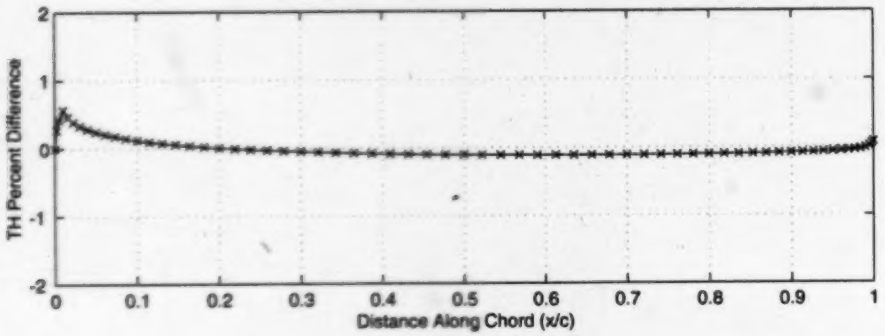

Figure 6.10a: Difference Of Original And Inversely Designed NACA 3414 Thickness Distributions

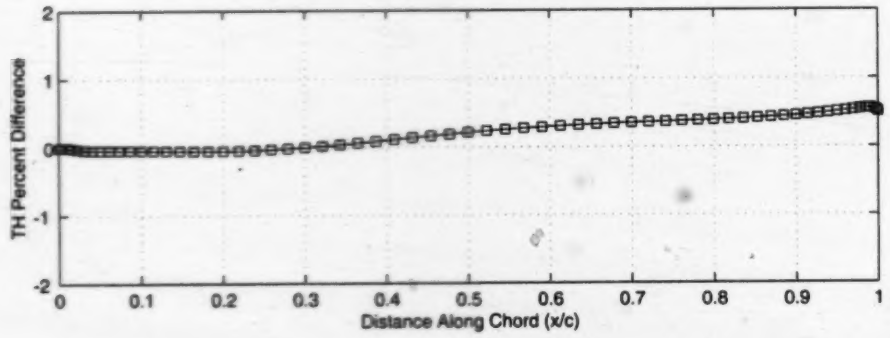

Figure 6.10b: Difference Of Analysis And Trended Inversely Designed NACA 3414 Thickness Distributions

The calculated camber lines from the two inverse calculations can be seen in Figure 6.11 along with the camber line of the original NACA 3414 airfoil.

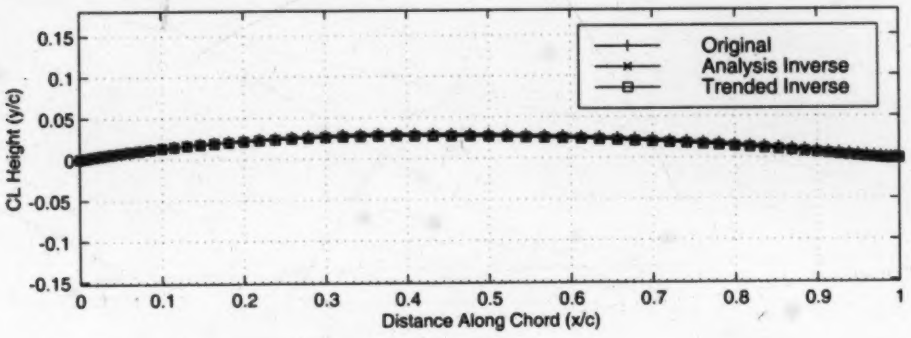

Figure 6.11: Original And Inversely Designed NACA 3414 Camber Lines

The difference between the camber inversely designed using the analysis $\bar{u}$ and Δv velocities and the original camber is calculated using Equation 6.3. The maximum percent difference calculated is 0.2%, as seen in Figure 6.12a.

The difference between the camber designed with the analysis $\bar{u}$ and Δv velocities and the camber designed with the trended $\bar{u}$ and Δv velocities is calculated with Equation 6.4. The maximum percent difference calculated is less than 0.1%, as seen in Figure 6.12b.

These six test cases show that both the inverse method and the trending of the NACA 4-digit $\bar{u}$ and Δv velocities can be used to accurately recreate any of the original NACA 4-digit analysis airfoils. The percent difference between the analysis velocity designs and the original airfoils is small enough to be considered negligible. The difference created by specifying trended velocities is easily explained by the error present in the trending techniques. The

assumption that the Δu and $\bar{v}$ velocities would remain constant as long as the camber line was constant is correct. The use of analysis $\bar{u}$ and Δv velocities for the inverse calculation proved that the full range of thicknesses in the airfoil group could be accurately recreated with specification of identical Δu and $\bar{v}$ velocities. The difference in camber lines increased slightly when the trended $\bar{u}$ and Δv velocities were used, but the percent differences remained within acceptable limits. Thus it can be seen that $\bar{u}$ and Δv velocities can be used to design thickness distributions alone, and Δu and $\bar{v}$ velocities determine the camber line. Also, both analysis and trended velocities can be used to accurately recreate the entire group of NACA 4-digit airfoils.

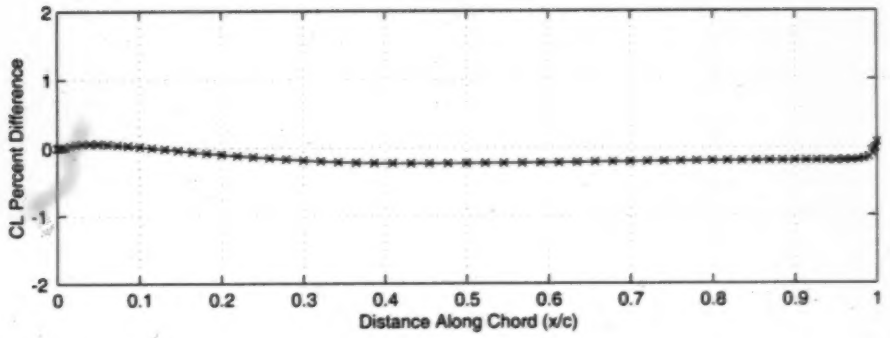

Figure 6.12a: Difference In Original And Inversely Designed NACA 3414 Camber Lines

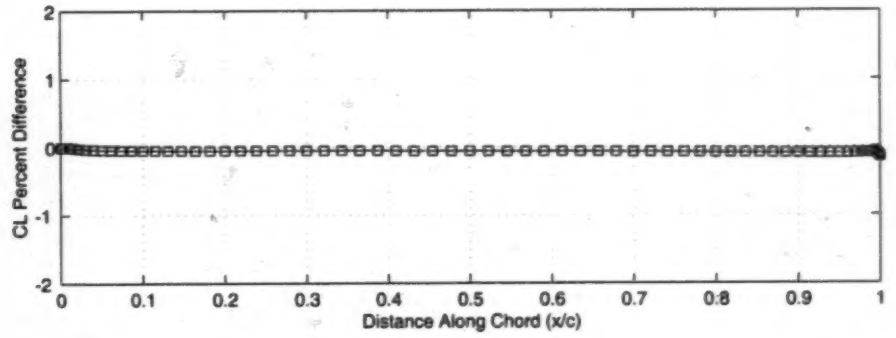

Figure 6.12b: Difference In Analysis And Trended Inversely Designed NACA 3414 Camber Lines

6.1.4 NACA 4-Digit Airfoil Design Space

The next step in verifying the accuracy of the inverse design method and trending technique is to use the system of equations created by trending the NACA 4-digit $\bar{u}$ and Δv velocities to design airfoils that were not included in the trending. The trending used airfoils that were 6%, 8%, 10%, 12% and 14% thick. It has already been shown that the 6%, 10% and 14% thick airfoils can be accurately recreated using the velocity trending, but the equations used to create the trended input velocities are smooth so any thickness ratio, or fraction of a thickness ratio, within the group can be specified. For this set of calculations, the $\bar{u}$ and Δv velocities all come from the 4-digit trending but the trending is used to calculate $\bar{u}$ and Δv velocities corresponding to thickness ratios of 8%, 8.5% and 9%. Two of these thickness ratios are not present in the analysis velocities used in the trending. The Δu and $\bar{v}$ velocities for these calculations are taken from the analysis of a NACA 3410 airfoil. The inversely designed thickness distributions, as well as the thickness distribution of the original NACA 3410 airfoil can be seen in Figure 6.13a.

The difference between each of the three designed thickness distributions and the NACA 3410 airfoil is calculated with

$$y_{th,di} = \frac{y_{th,i} - y_{th,o}}{c} \times 100\% \tag{6.5}$$

where $y_{th,di}$ is the percent difference, $y_{th,i}$ is each of the designed thickness distributions, $y_{th,o}$ is the original NACA 3410 thickness distribution, and c is the chord length. The calculated difference between each of the designed thickness distributions and the NACA 3410 thickness distribution can be seen in Figure 6.13b.

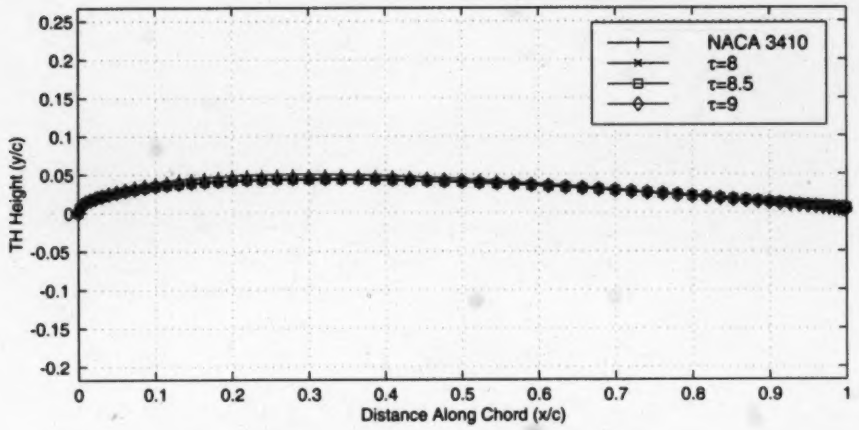

Figure 6.13a: Inversely Designed NACA 4-Digit Thickness Distributions - Decreasing Thickness Specification

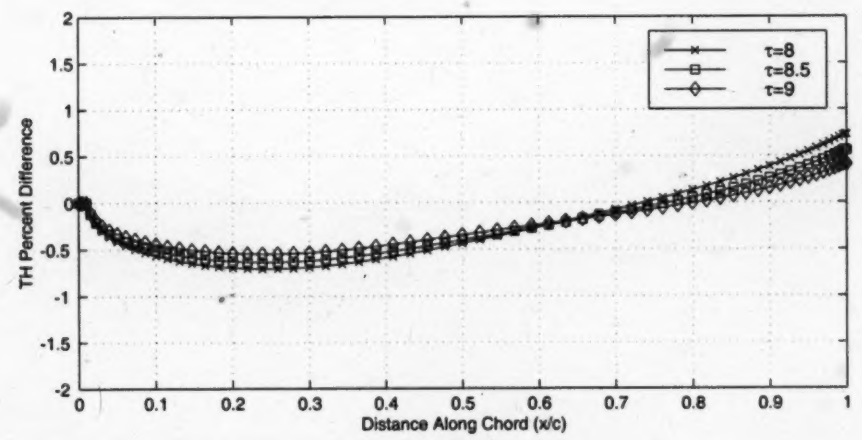

Figure 6.13b: Difference Of Inversely Designed NACA 4-Digit Thickness Distributions - Decreasing Thickness Specification

The percent differences show that the trending specification of 9%, 8.5%, and 8% created airfoils that decreased in thickness. The relationship between specified thickness and designed thickness is not one-to-one. The thickness designed by specifying 8% in the trending is not exactly 2% thinner than the NACA 3410 airfoil, nor is it exactly 1% thinner than the thickness designed by specifying 9%. However the ability to utilize recreated velocities to work within the design space is still a very valuable tool. A decrease in specified thickness ratio does in fact create a thinner airfoil.

The inversely designed camber lines corresponding to the specified thickness ratios, as well as the camber line of the original NACA 3410 airfoil can be seen in Figure 6.14a. The difference between each of the designed camber lines and the NACA 3410 camber line is calculated using

$$y_{cl,di} = \frac{y_{cl,i} - y_{cl,o}}{c} \times 100\% \tag{6.6}$$

where $y_{cl,di}$ is the percent difference, $y_{cl,i}$ is each of the designed camber lines, $y_{cl,o}$ is the original NACA 3410 camber line, and c is the chord length. The differences can be seen in Figure 6.14b. The maximum difference between any of the designed camber lines and the original camber line is less than 0.4%. This provides further proof of the accuracy of the inverse method, and the validity of the assumption that the camber line can be described by Δu and $\bar{v}$ velocities alone.

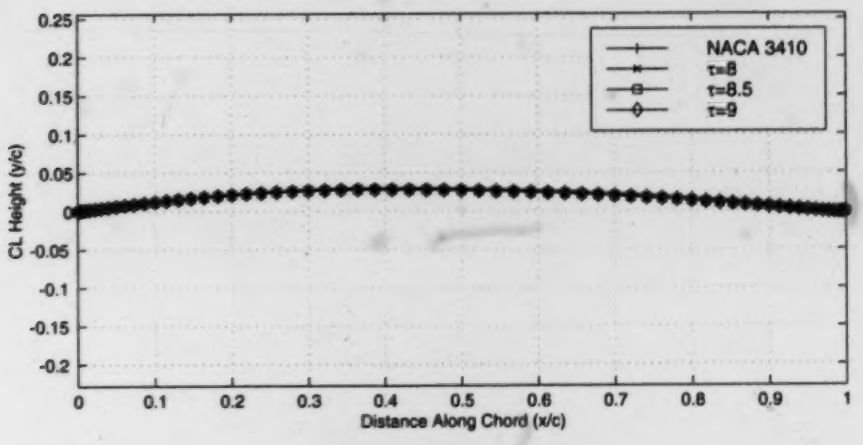

Figure 6.14a: Inversely Designed NACA 4-Digit Camber Lines - Decreasing Thickness Specification

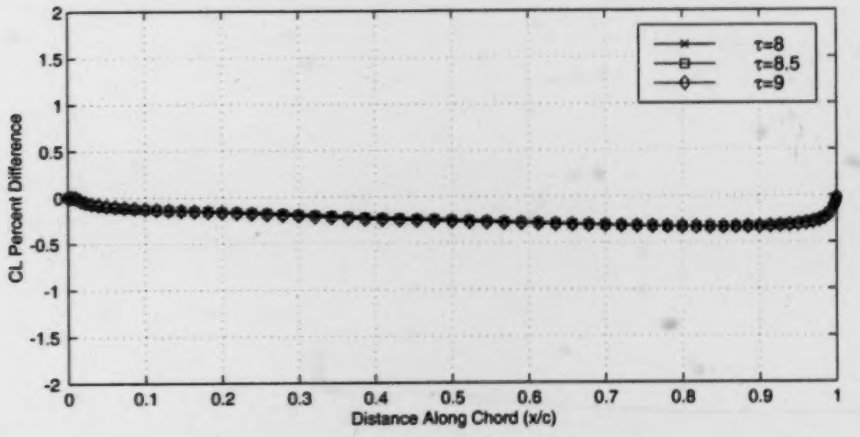

Figure 6.14b: Difference Of Inversely Designed NACA 4-Digit Camber Lines - Decreasing Thickness Specification

The design space test was repeated for thickness ratios greater than 10%. The three specified thickness ratios included 11%, 11.5% and 12%. As with the previous design space test, the NACA 4-digit velocity trending equations were used to create the $\bar{u}$ and Δv velocities. The Δu and $\bar{v}$ velocities for all three calculations were taken from the analysis of a NACA 3410 airfoil. The designed thickness distributions, as well as the thickness distribution of the original NACA 3410 airfoil can be seen in Figure 6.15a. The difference between each of the designed thicknesses and the NACA 3410 thickness was calculated using Equation 6.5. The difference of each of the designed thickness distributions can be seen in Figure 6.15b.

As with the decreasing thickness design space test, the relationship between specified thickness for the trended velocities and the designed thickness distribution is not one-to-one. However, the validity of the trending method is verified by the fact that as the specified thickness was increased, the designed thickness distribution increased as well. Thus these results show that the specified thickness of the trending technique can be used to adjust the designed thickness distribution so that any airfoil geometry can be calculated that exists between the airfoils of the original group.

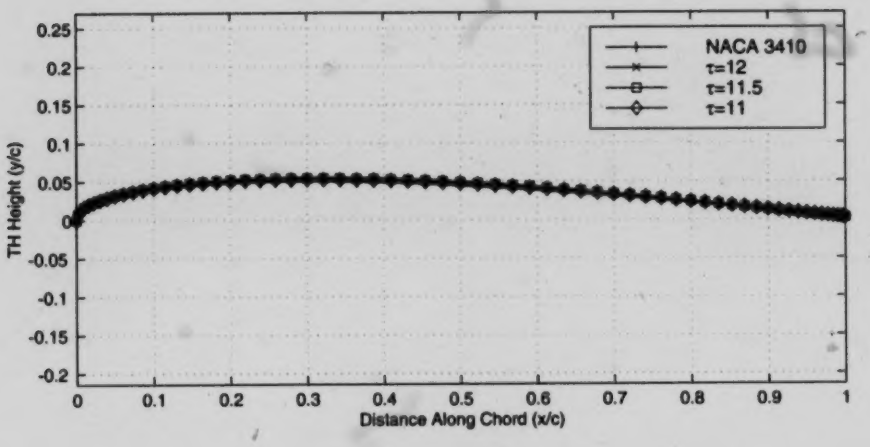

Figure 6.15a: Inversely Designed NACA 4-Digit Thickness Distributions - Increasing Thickness Specification

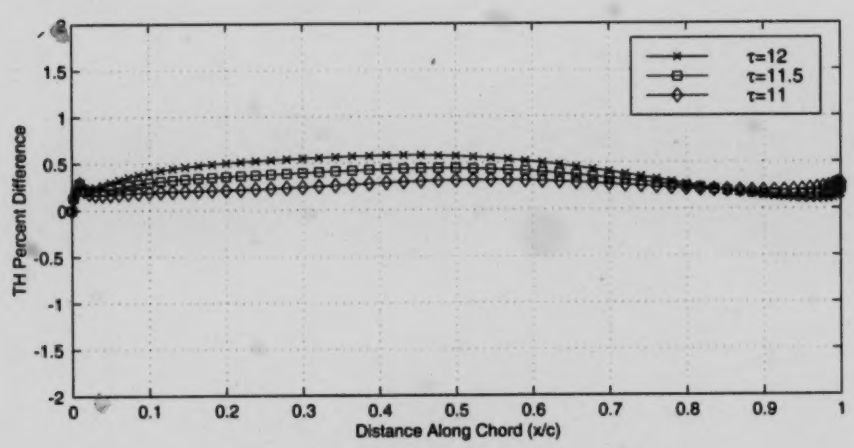

Figure 6.15b: Difference Of Inversely Designed NACA 4-Digit Thickness Distributions - Increasing Thickness Specification

The inversely designed camber lines corresponding to the specified thickness ratios, as well as the camber line of the original NACA 3410 airfoil can be seen in Figure 6.16a. The difference between each of the designed camber lines and the NACA 3410 camber line is calculated using Equation 6.6. The differences can be seen in Figure 6.16b. The maximum difference between any of the designed camber lines and the original camber line is 0.3%. The designed camber lines provide further proof of the accuracy of the inverse method, and add to the validity of the assumption that the camber line can be described by Δu and $\bar{v}$ velocities alone.

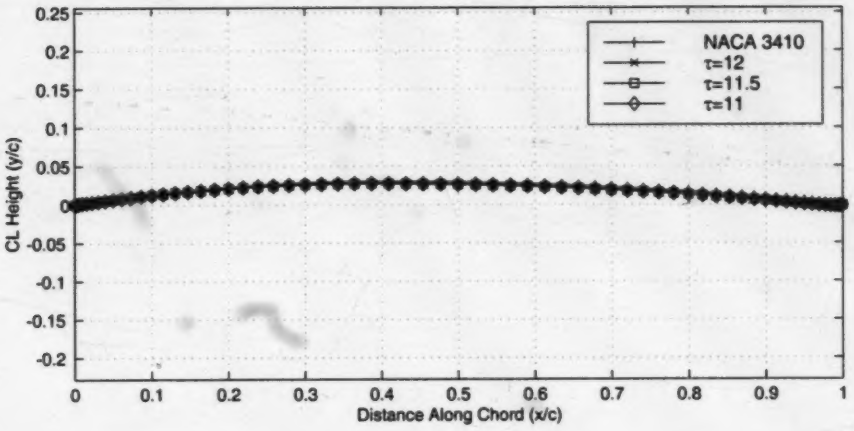

Figure 6.16a: Inversely Designed NACA 4-Digit Camber Lines - Increasing Thickness Specification

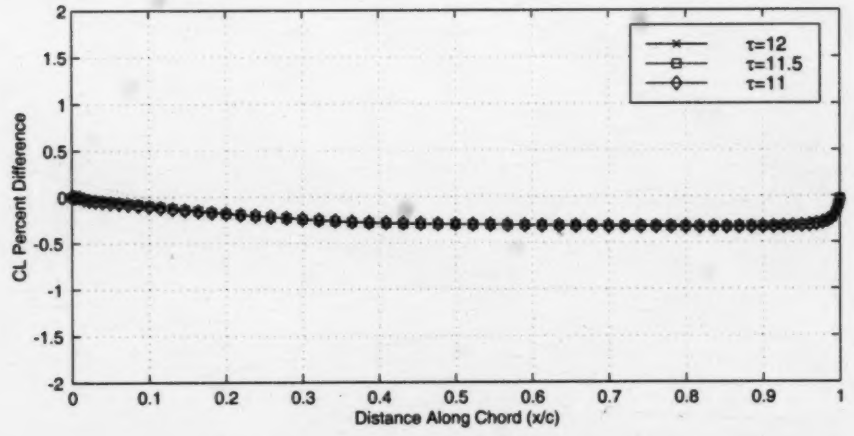

Figure 6.16b: Difference Of Inversely Designed NACA 4-Digit Camber Lines - Increasing Thickness Specification

6.2 NACA 4-Digit-Modified Airfoils

The next step in verifying the accuracy of the inverse method and the trending technique is to test the trending of a different group of airfoils. The NACA 4-digit-modified airfoils have trended $\bar{u}$ and Δv velocities that have different shapes than the NACA 4-digit group. The trending of the NACA 4-digit-modified group is less accurate than the trending of the NACA 4-digit group because of the different shapes of the $\bar{u}$ and Δv velocities. The specification of the NACA 4-digit-modified velocities, both analysis and trended, will also test to see if the shape of thickness distributions can be designed, as well as the heights. For the NACA 4-digit group, all of the thickness distributions have the same shape, with different values of maximum thickness. The NACA 4-digit-modified airfoils have different maximum thicknesses as well as different locations of maximum thickness. By recreating the NACA 4-digit-modified group of airfoils, the inverse method can be tested for accuracy in creating entirely different thickness distributions.

For all of the NACA 4-digit-modified test cases, the Δu and $\bar{v}$ velocities are taken from the analysis of a NACA 3410-44 airfoil. As with the NACA 4-digit group, the $\bar{u}$ and Δv velocities change for every test case, but the Δu and $\bar{v}$ velocities do not change.

6.2.1 NACA 3410-44 Airfoil

The purpose of the next set of test cases is to inversely design a NACA 3410-44 airfoil. For this set of test cases, the Δu and $\bar{v}$ velocities will be taken from the analysis of a NACA 3410-44 airfoil. The first calculation has $\bar{u}$ and Δv velocities that were calculated from the analysis of a NACA 3410-44

airfoil. The second calculation has $\bar{u}$ and Δv velocities that were created using the 4-digit-modified trending equations with a specified thickness ratio of 10%. The calculated thicknesses from the two inverse calculations can be seen in Figure 6.17 along with the thickness distribution of the original NACA 3410-44 airfoil.

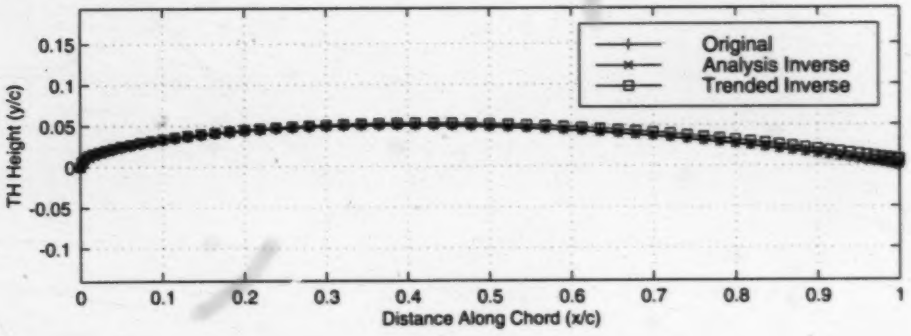

Figure 6.17: Original And Inversely Designed NACA 3410-44 Thickness Distributions

The difference between the thickness inversely designed using the analysis $\bar{u}$ and Δv velocities and the original thickness is calculated using Equation 6.1. The maximum percent difference calculated is 0.3%, as seen in Figure 6.18a.

The difference between the thickness designed with the analysis $\bar{u}$ and Δv velocities and the thickness designed with the trended $\bar{u}$ and Δv velocities is calculated with Equation 6.2. The maximum percent difference calculated is 0.8%, as seen in Figure 6.18b.

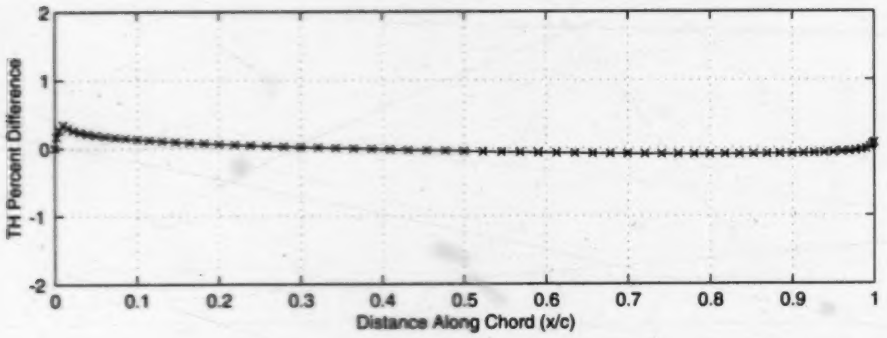

Figure 6.18a: Difference Of Original And Inversely Designed NACA 3410-44 Thickness Distributions

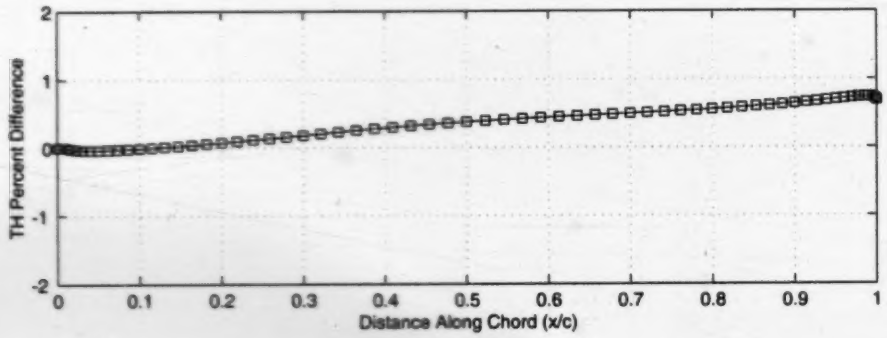

Figure 6.18b: Difference Of Analysis And Trended Inversely Designed NACA 3410-44 Thickness Distributions

The calculated camber lines from the two inverse calculations can be seen in Figure 6.19 along with the camber line of the original NACA 3410-44 airfoil.

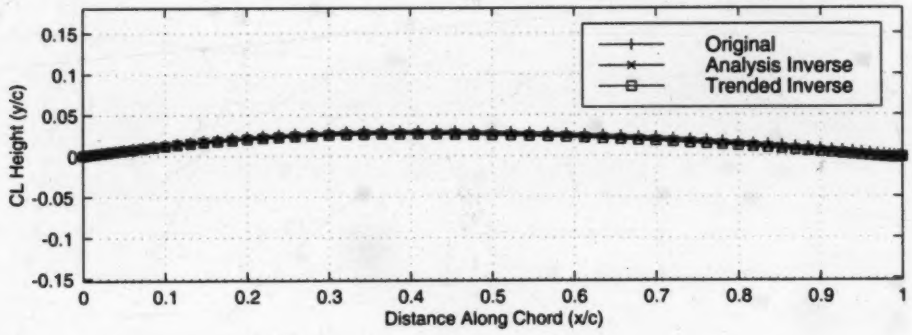

Figure 6.19: Original And Inversely Designed NACA 3410-44 Camber Lines

The difference between the camber inversely designed using the analysis $\bar{u}$ and Δv velocities and the original camber is calculated using Equation 6.3. The maximum percent difference calculated is 0.3%, as seen in Figure 6.20a.

The difference between the camber designed with the analysis $\bar{u}$ and Δv velocities and the camber designed with the trended $\bar{u}$ and Δv velocities is calculated with Equation 6.4. The maximum percent difference calculated is less than 0.1%, as seen in Figure 6.20b. Thus it can be shown that analysis and trended velocities can be specified to accurately recreate both the thickness distribution and the camber line of a NACA 3410-44 airfoil.

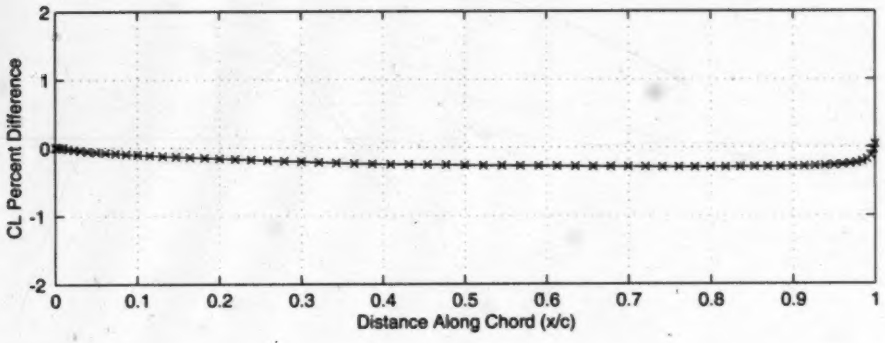

Figure 6.20a: Difference In Original And Inversely Designed NACA 3410-44 Camber Lines

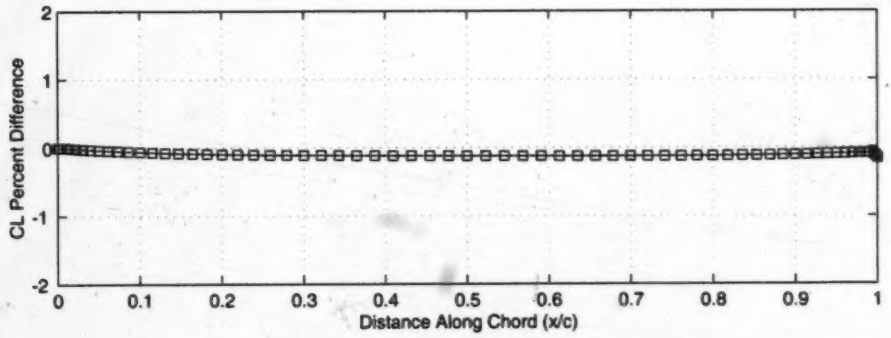

Figure 6.20b: Difference In Analysis And Trended Inversely Designed NACA 3410-44 Camber Lines

6.2.2 NACA 3406-42 Airfoil

The purpose of the next set of test cases is to inversely design a NACA 3406-42 airfoil. For this set of test cases, the Δu and $\bar{v}$ velocities will still be taken from the analysis of a NACA 3410-44 airfoil. The first calculation has $\bar{u}$ and Δv velocities that were taken from the analysis of a NACA 3406-42 airfoil. The second calculation has $\bar{u}$ and Δv velocities that were created using the 4-digit-modified trending equations with a specified thickness ratio of 6%. The calculated thicknesses from the two inverse calculations can be seen in Figure 6.21 along with the thickness distribution of the original NACA 3406-42 airfoil.

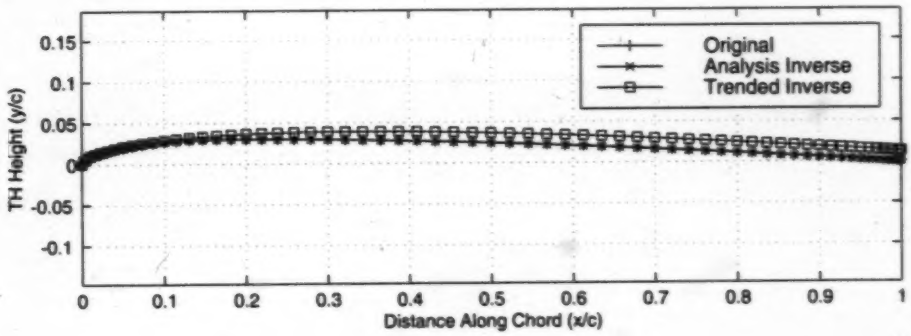

Figure 6.21: Original And Inversely Designed NACA 3406-42 Thickness Distributions

The difference between the thickness inversely designed using the analysis $\bar{u}$ and Δv velocities and the original thickness is calculated using Equation 6.1. The maximum percent difference calculated is 0.2%, as seen in Figure 6.22a.

The difference between the thickness designed with the analysis $\bar{u}$ and Δv velocities and the thickness designed with the trended $\bar{u}$ and Δv velocities is calculated with Equation 6.2. The maximum percent difference calculated is 1.3%, as seen in Figure 6.22b.

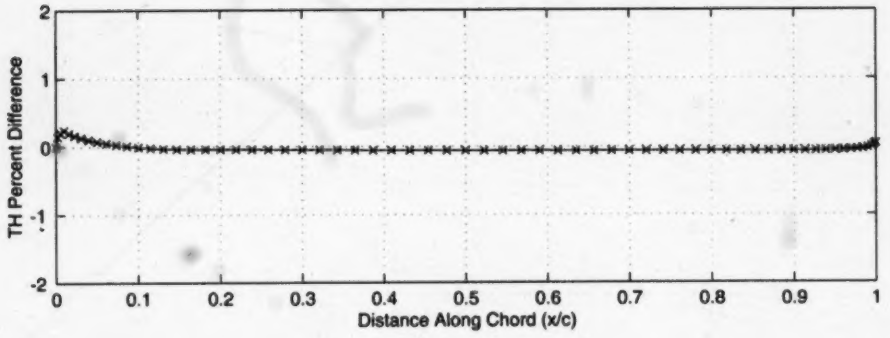

Figure 6.22a: Difference Of Original And Inversely Designed NACA 3406-42 Thickness Distributions

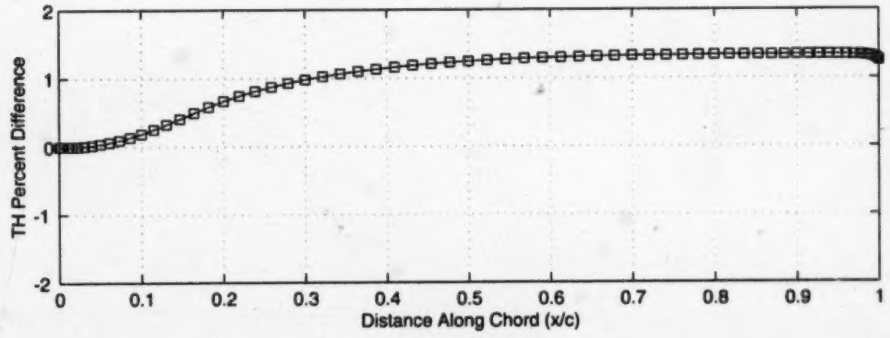

Figure 6.22b: Difference Of Analysis And Trended Inversely Designed NACA 3406-42 Thickness Distributions

The calculated camber lines from the two inverse calculations can be seen in Figure 6.23 along with the camber line of the original NACA 3406-42 airfoil.

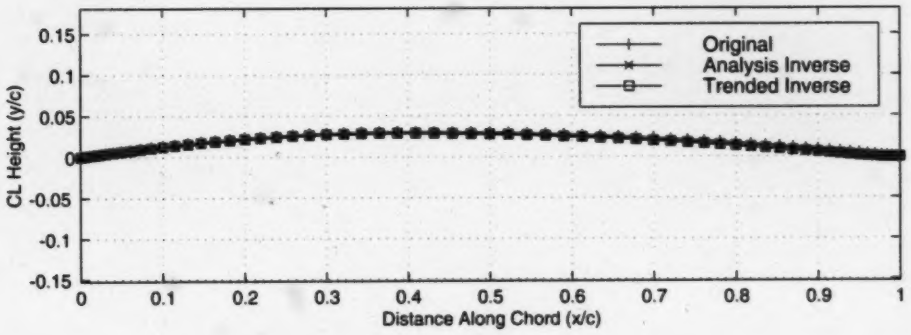

Figure 6.23: Original And Inversely Designed NACA 3406-42 Camber Lines

The difference between the camber inversely designed using the analysis $\bar{u}$ and Δv velocities and the original camber is calculated using Equation 6.3. The maximum percent difference calculated is 0.4%, as seen in Figure 6.24a.

The difference between the camber designed with the analysis $\bar{u}$ and Δv velocities and the camber designed with the trended $\bar{u}$ and Δv velocities is calculated with Equation 6.4. The maximum percent difference calculated is less than 0.1%, as seen in Figure 6.28b. These results show that by changing the $\bar{u}$ and Δv velocities and keeping the same Δu and $\bar{v}$ velocities, the thickness distribution changes, but the camber line remains the same. Thus it has been shown that the inverse method is accurate at recreating the NACA 4-digit-modified airfoils as well as the NACA 4-digit airfoils. The results prove that the trending method applies equally as well to the NACA 4-digit-

modified group. The results also prove that the ability to design thickness distributions using only the $\bar{u}$ and Δv velocities occurs with airfoils other than the NACA 4-digit airfoils.

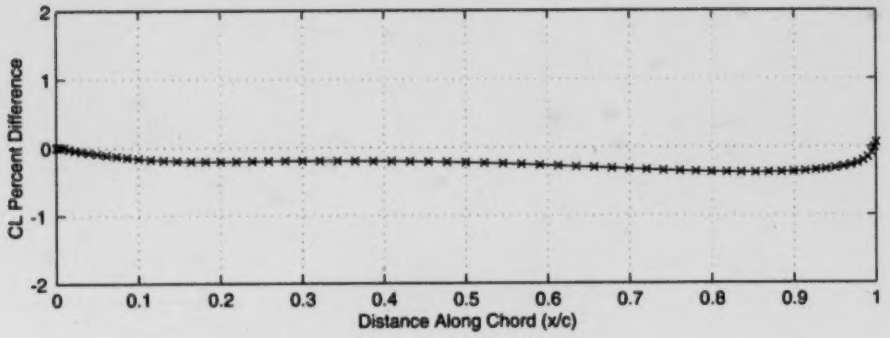

Figure 6.24a: Difference In Original And Inversely Designed NACA 3406-42 Camber Lines

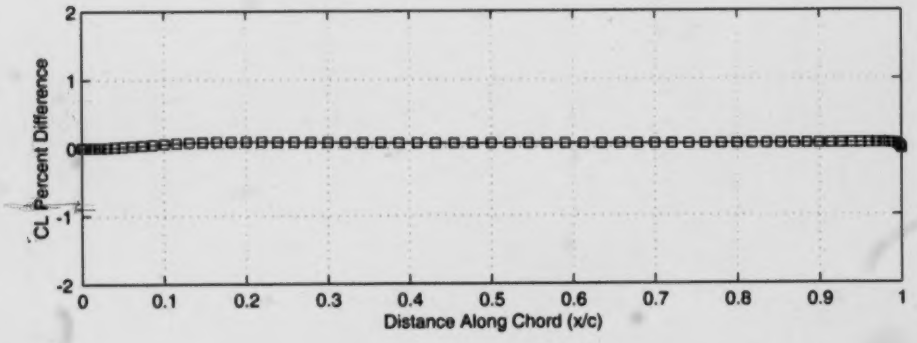

Figure 6.24b: Difference In Analysis And Trended Inversely Designed NACA 3406-42 Camber Lines

6.2.3 NACA 3414-46 Airfoil

The purpose of the next set of test cases is to inversely design a NACA 3414-46 airfoil. For this set of test cases, the Δu and $\bar{v}$ velocities will still be taken from the analysis of a NACA 3410-44 airfoil. The first calculation has $\bar{u}$ and Δv velocities that were taken from the analysis of a NACA 3414-46 airfoil. The second calculation has $\bar{u}$ and Δv velocities that were created using the 4-digit-modified trending equations with a specified thickness ratio of 14%. The calculated thicknesses from the two inverse calculations can be seen in Figure 6.25 along with the thickness distribution of the original NACA 3414-46 airfoil.

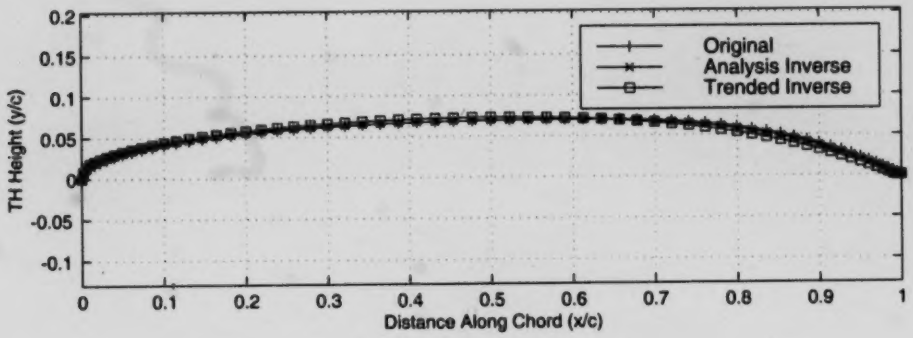

Figure 6.25: Original And Inversely Designed NACA 3414-46 Thickness Distributions

The difference between the thickness inversely designed using the analysis $\bar{u}$ and Δv velocities and the original thickness is calculated using Equation 6.1. The maximum percent difference calculated is 0.5%, as seen in Figure 6.26a.

The difference between the thickness designed with the analysis $\bar{u}$ and Δv velocities and the thickness designed with the trended $\bar{u}$ and Δv velocities is calculated with Equation 6.2. The maximum percent difference calculated is 0.5%, as seen in Figure 6.26b.

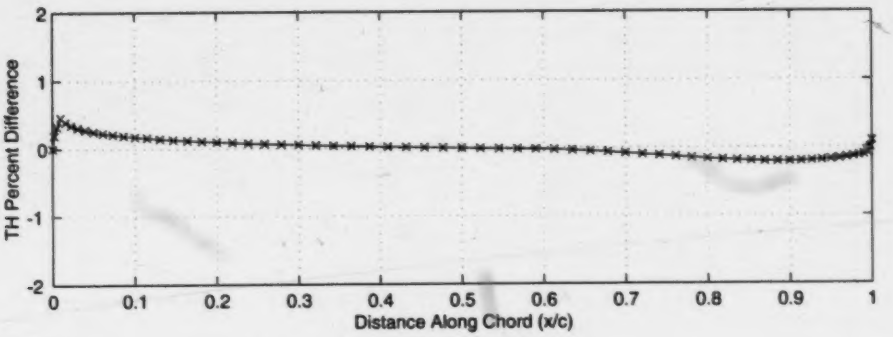

Figure 6.26a: Difference Of Original And Inversely Designed NACA 3414-46 Thickness Distributions

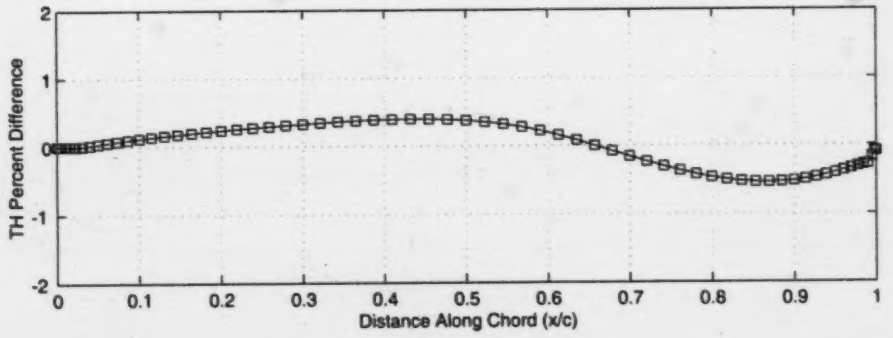

Figure 6.26b: Difference Of Analysis And Trended Inversely Designed NACA 3414-46 Thickness Distributions

The calculated camber lines from the two inverse calculations can be seen in Figure 6.27 along with the camber line of the original NACA 3414-46 airfoil.

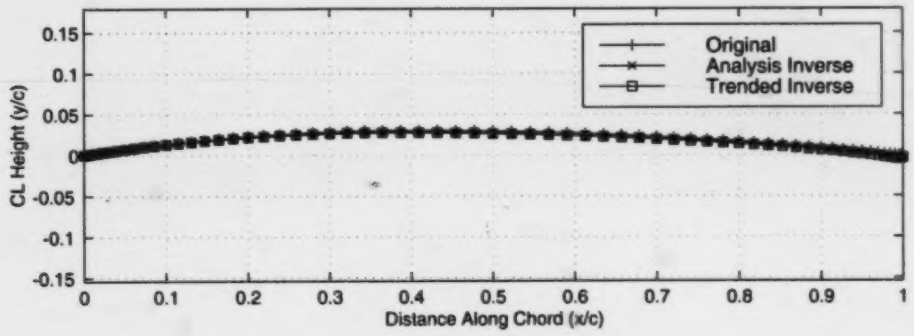

Figure 6.27: Original And Inversely Designed NACA 3414-46 Camber Lines

The difference between the camber inversely designed using the analysis $\bar{u}$ and Δv velocities and the original camber is calculated using Equation 6.3. The maximum percent difference calculated is 0.3%, as seen in Figure 6.28a.

The difference between the camber designed with the analysis $\bar{u}$ and Δv velocities and the camber designed with the trended $\bar{u}$ and Δv velocities is calculated with Equation 6.4. The maximum percent difference calculated is less than 0.1%, as seen in Figure 6.28b.

These six test cases show that the NACA 4-digit-modified airfoils can be recreated using the analysis $\bar{u}$ and Δv velocities as well as the trended $\bar{u}$ and Δv velocities. The percent difference between the analysis velocity inverse designs and the original airfoils, which is never larger than 0.5%, is small enough to be considered negligible. The largest percent differences, namely

1.3% and 0.8%, occurred when trended velocities were used to recreate the NACA 3406-42 and NACA 3410-44 airfoils, respectively. This difference, while still within acceptable limits, is likely due to the trending error which was slightly higher for the 4-digit-modified airfoils than the 4-digit group. These six test cases further prove that the constant camber line assumption is correct. The camber line used in the NACA 4-digit-modified group had a different shape, and therefore different Δu and $\bar{v}$ velocities, but the camber lines for each of the test cases had low percent difference, all below 0.5%. This low difference proves that $\bar{u}$ and Δv velocities control the thickness distribution only, and Δu and $\bar{v}$ velocities control the camber line. The test results also show that the inverse method can accurately recreate any airfoil from both the NACA groups using either the analysis velocities or the trended velocities.

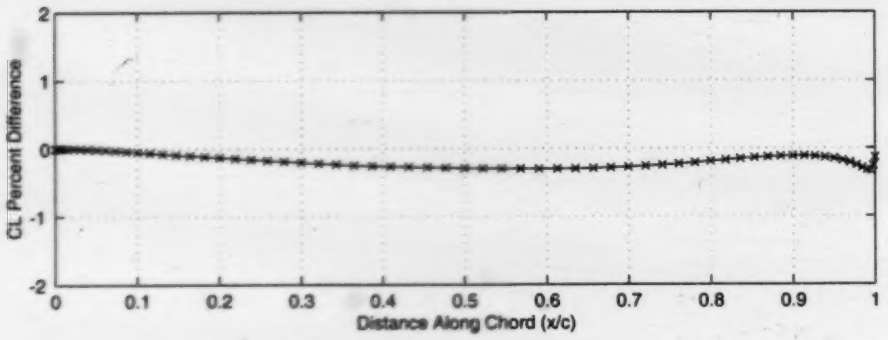

Figure 6.28a: Difference In Original And Inversely Designed NACA 3414-46 Camber Lines

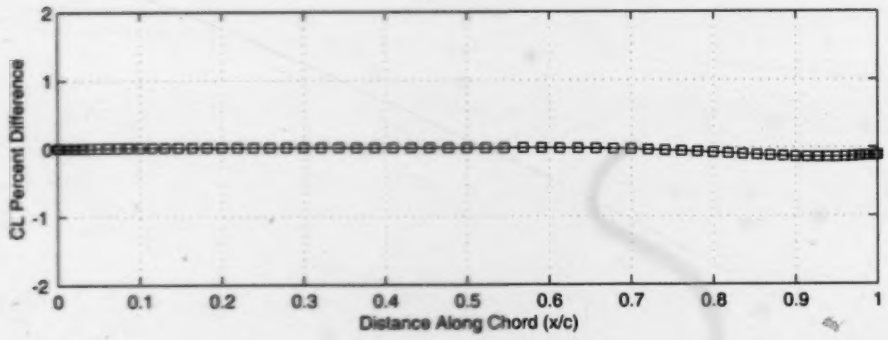

Figure 6.28b: Difference In Analysis And Trended Inversely Designed NACA 3414-46 Camber Lines

6.2.4 NACA 4-Digit-Modified Airfoil Design Space

The next step in verifying the accuracy of the inverse design method and trending technique is to use the system of equations created by trending the NACA 4-digit-modified $\bar{u}$ and Δv velocities to design airfoils that were not included in the trending. While this test was already completed with the NACA 4-digit airfoils, by repeating it with the 4-digit-modified airfoils the validity of the assumptions and the accuracy of the techniques is further assessed. The 4-digit-modified trending used airfoils that were 6%, 8%, 10%, 12% and 14% thick. It has already been shown that the 6%, 10% and 14% thick airfoils can be accurately recreated. For this set of calculations, the $\bar{u}$ and Δv velocities all come from the 4-digit-modified trending but the trending is again used to calculate $\bar{u}$ and Δv velocities corresponding to thickness ratios of 8%, 8.5% and 9%. The Δu and $\bar{v}$ velocities for all of the calculations are taken from the analysis of a NACA 3410-44 airfoil. The inversely designed thickness distributions, as well as the thickness distribution of the original NACA 3410-44 airfoil can be seen in Figure 6.29a.

The difference between each of the three designed thickness distributions and the NACA 3410-44 airfoil is calculated with Equation 6.5. The calculated difference between each of the designed thickness distributions and the NACA 3410-44 thickness distribution can be seen in Figure 6.29b.

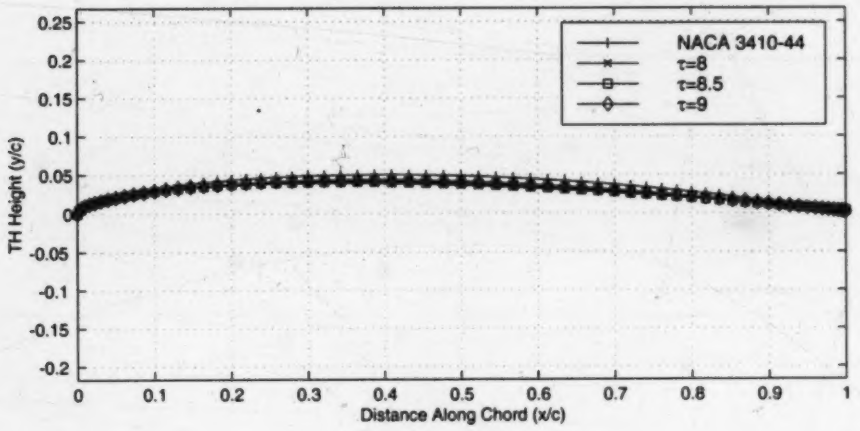

Figure 6.29a: Inversely Designed NACA 4-Digit-Modified Thickness Distributions - Decreasing Thickness Specification

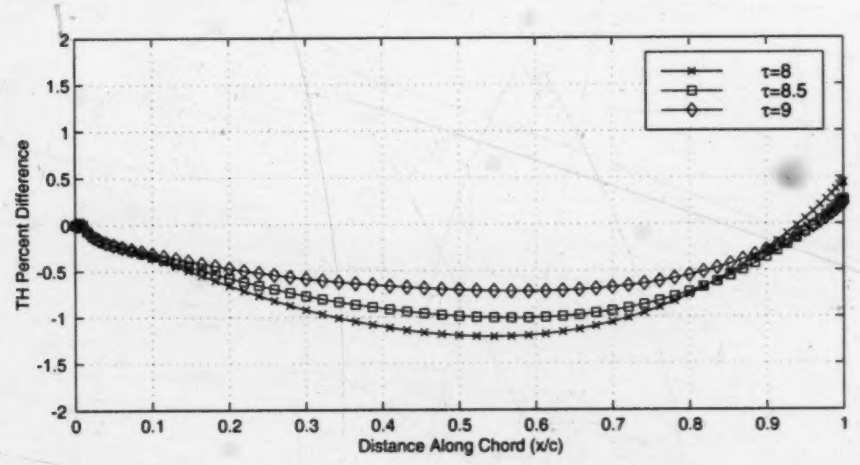

Figure 6.29b: Difference Of Inversely Designed NACA 4-Digit-Modified Thickness Distributions - Decreasing Thickness Specification

The percent differences show that the trending specification of 9%, 8.5%, and 8% created airfoils that decrease in thickness. As previous design space tests have shown, the relationship between specified thickness and designed thickness is not one-to-one.

The inversely designed camber lines corresponding to the specified thickness ratios, as well as the camber line of the original NACA 3410-44 airfoil can be seen in Figure 6.30a. The difference between each of the designed camber lines and the NACA 3410-44 camber line is calculated using Equation 6.6. The differences can be seen in Figure 6.30b. The maximum difference between any of the designed camber lines and the original camber line is less than 0.4%. This provides further proof that the accuracy of the inverse method and the camber line assumptions extend from the NACA 4-digit group to the NACA 4-digit-modified group.

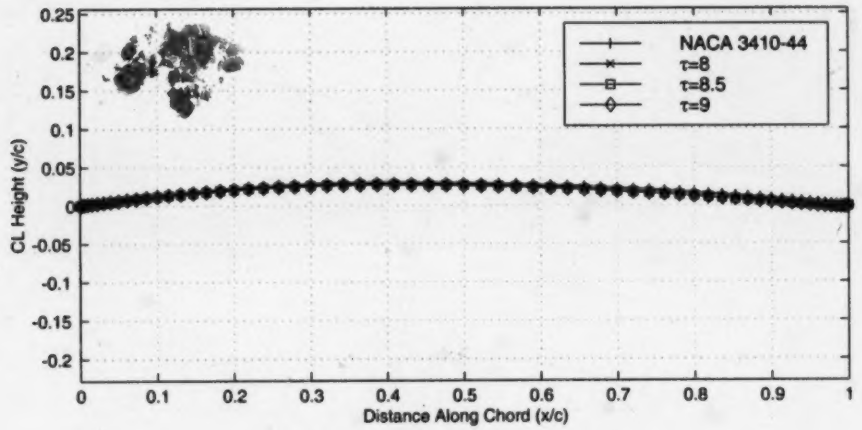

Figure 6.30a: Inversely Designed NACA 4-Digit-Modified Camber Lines - Decreasing Thickness Specification

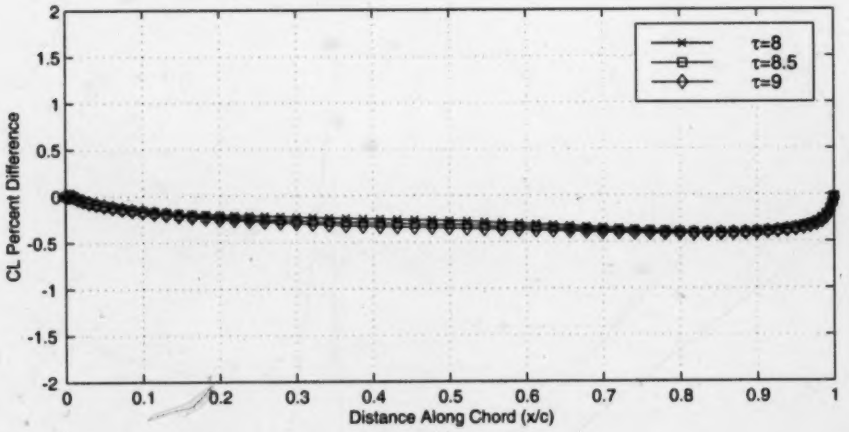

Figure 6.30b: Difference Of Inversely Designed NACA 4-Digit-Modified Camber Lines - Decreasing Thickness Specification

The design space test was repeated for thickness ratios greater than 10%. The three specified thickness ratios included 11%, 11.5% and 12%. As with the previous design space test, the NACA 4-digit-modified velocity trending equations were used to create the $\bar{u}$ and Δv velocities. The Δu and $\bar{v}$ velocities for all three calculations were taken from the analysis of a NACA 3410-44 airfoil. The designed thickness distributions, as well as the thickness distribution of the original NACA 3410-44 airfoil can be seen in Figure 6.31a. The difference between each of the designed thicknesses and the NACA 3410-44 thickness was calculated using Equation 6.5. The difference of each of the designed thickness distributions can be seen in Figure 6.31b.

As with the decreasing thickness design space test, the relationship between specified thickness for the trended velocities and the designed thickness distribution is not one-to-one. However, the validity of the trending method is verified by the fact that as the specified thickness was increased, the designed thickness distribution increased as well.

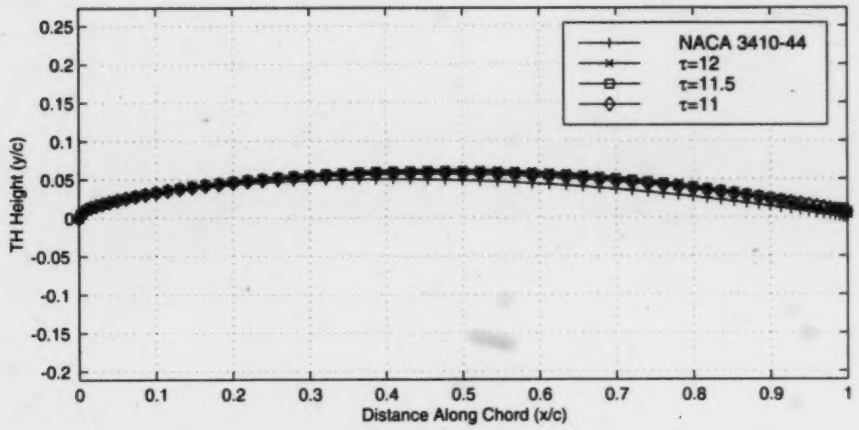

Figure 6.31a: Inversely Designed NACA 4-Digit-Modified Thickness Distributions - Increasing Thickness Specification

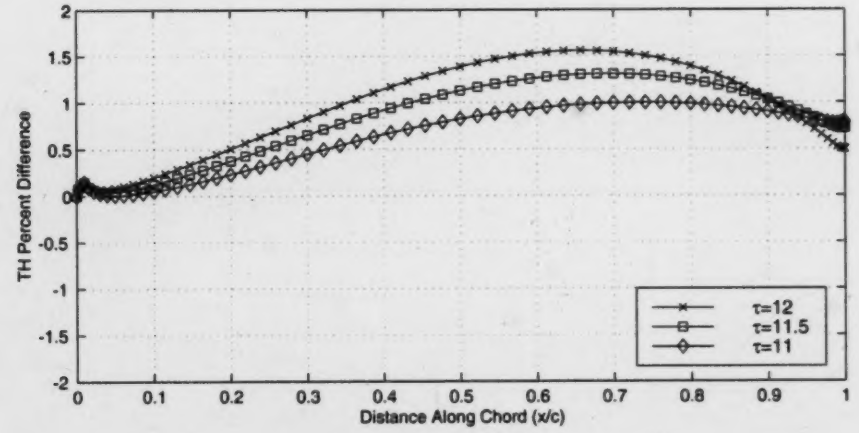

Figure 6.31b: Difference Of Inversely Designed NACA 4-Digit-Modified Thickness Distributions - Increasing Thickness Specification

The inversely designed camber lines corresponding to the specified thickness ratios, as well as the camber line of the original NACA 3410-44 airfoil can be seen in Figure 6.32a. The difference between each of the designed camber lines and the NACA 3410-44 camber line is calculated using Equation 6.6. The differences can be seen in Figure 6.32b. The maximum difference between any of the designed camber lines and the original camber line is less than 0.4%. The designed camber lines provides further proof of the accuracy of the inverse method, and add to the validity of the assumption that the camber line can be described by Δu and $\bar{v}$ velocities alone.

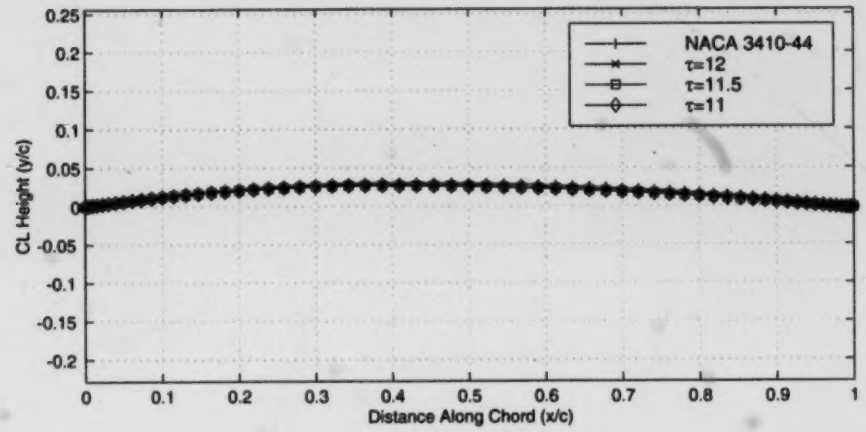

Figure 6.32a: Inversely Designed NACA 4-Digit-Modified Camber Lines - Increasing Thickness Specification

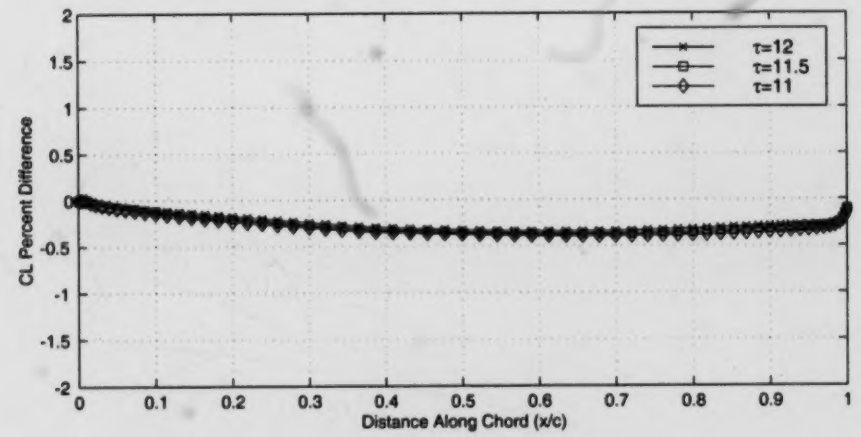

Figure 6.32b: Difference Of Inversely Designed NACA 4-Digit-Modified Camber Lines - Increasing Thickness Specification

6.3 General Airfoils

The next step in verifying the accuracy of the inverse method and the trending technique is to test the trending of a different group of airfoils. The General airfoils have $\bar{u}$ and Δv velocities that do not resemble each other, so the trending does not represent the velocities of the General airfoil group as accurately as with the NACA groups. The specification of the General airfoil velocities, both analysis and trended, will test to see if any general shape of thickness distribution can be designed.

For all of the General airfoil test cases, the Δu and $\bar{v}$ velocities are taken from the analysis of a GEN03 airfoil. As with the previous groups, the $\bar{u}$ and Δv velocities change for every test case, but the Δu and $\bar{v}$ velocities do not change.

6.3.1 GEN03 Airfoil

The purpose of the next set of test cases is to inversely design a GEN03 airfoil. For this set of test cases, the Δu and $\bar{v}$ velocities will be taken from the analysis of a GEN03 airfoil. The first calculation has $\bar{u}$ and Δv velocities that were taken from the analysis of a GEN03 airfoil. The second calculation has $\bar{u}$ and Δv velocities that were created using the general airfoil trending equations with a specified thickness ratio corresponding to the GEN03 airfoil. The calculated thicknesses from the two inverse calculations can be seen in Figure 6.33 along with the thickness distribution of the original GEN03 airfoil.

The difference between the thickness inversely designed using the analysis $\bar{u}$ and Δv velocities and the original thickness is calculated using Equation

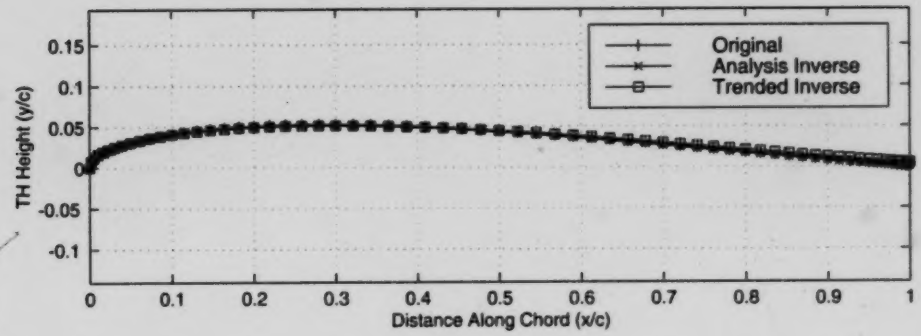

Figure 6.33: Original And Inversely Designed GEN03 Thickness Distributions

6.1. The maximum percent difference calculated is 0.4%, as seen in Figure 6.34a.

The difference between the thickness designed with the analysis $\bar{u}$ and Δv velocities and the thickness designed with the trended $\bar{u}$ and Δv velocities is calculated with Equation 6.2. The maximum percent difference calculated is 0.5%, as seen in Figure 6.34b.

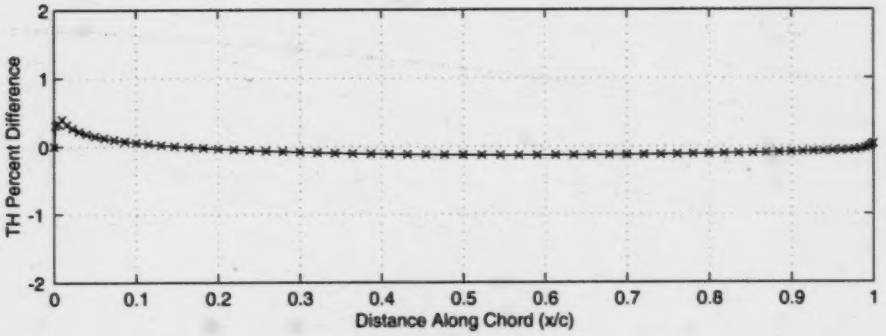

Figure 6.34a: Difference Of Original And Inversely Designed GEN03 Thickness Distributions

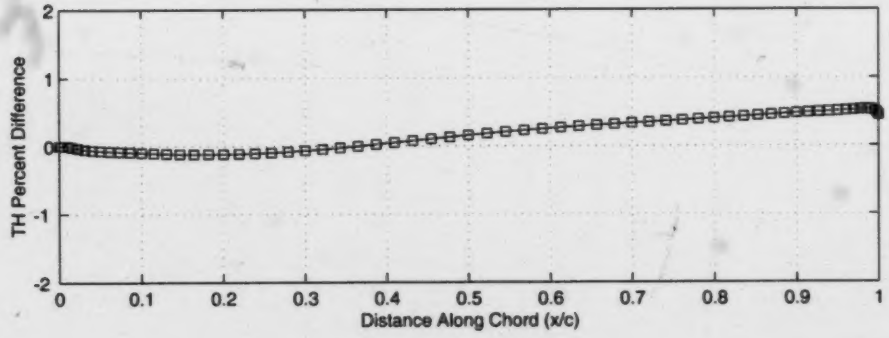

Figure 6.34b: Difference Of Analysis And Trended Inversely Designed GEN03 Thickness Distributions

The calculated camber lines from the two inverse calculations can be seen in Figure 6.35 along with the camber line of the original GEN03 airfoil.

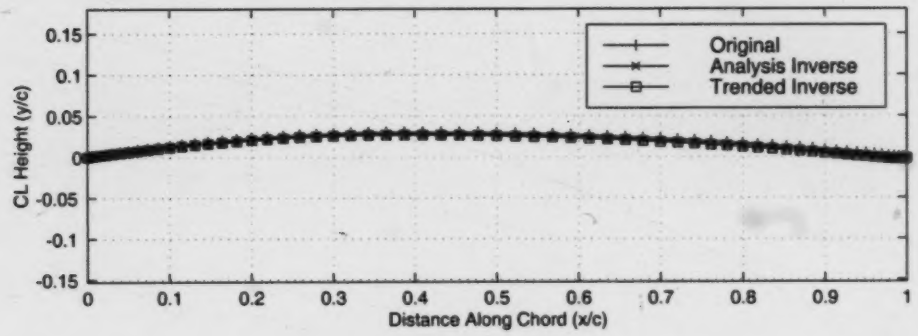

Figure 6.35: Original And Inversely Designed GEN03 Camber Lines

The difference between the camber inversely designed using the analysis $\bar{u}$ and Δv velocities and the original camber is calculated using Equation 6.3. The maximum percent difference calculated is 0.3%, as seen in Figure 6.36a.

The difference between the camber designed with the analysis $\bar{u}$ and Δv velocities and the camber designed with the trended $\bar{u}$ and Δv velocities is calculated with Equation 6.4. The maximum percent difference calculated is 0.1%, as seen in Figure 6.36b. These results show that the inverse design method can accurately recreate a general airfoil, not only airfoils that belong to certain groups. The accurate recreation of the thickness distribution and camber line of the GEN03 airfoil using both analysis and trended velocities proves that the trending technique and inverse design methodology can be used for any shape airfoil.

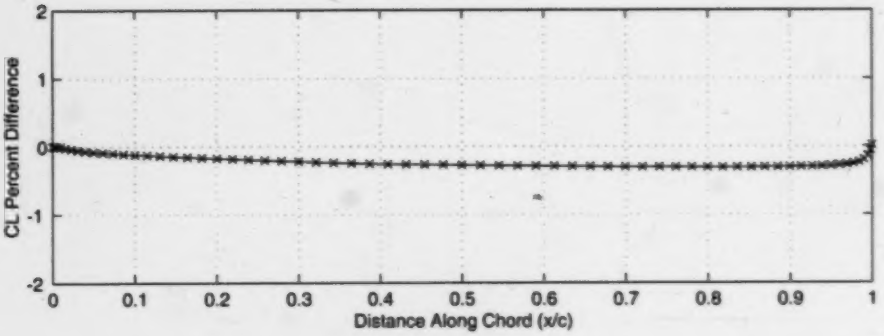

Figure 6.36a: Difference In Original And Inversely Designed GEN03 Camber Lines

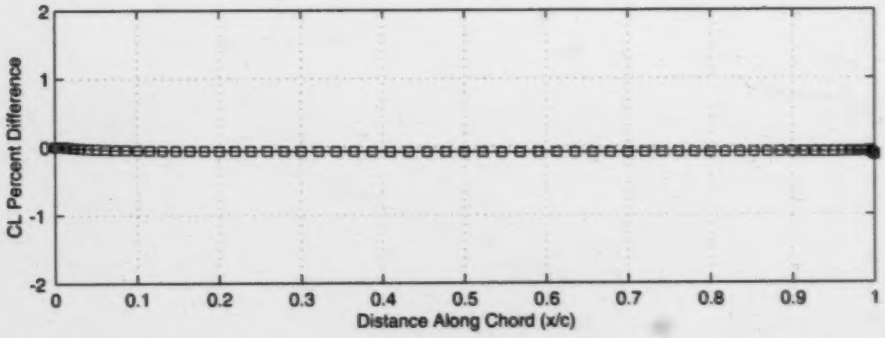

Figure 6.36b: Difference In Analysis And Trended Inversely Designed GEN03 Camber Lines

6.3.2 GEN01 Airfoil

The purpose of the next set of test cases is to inversely design a GEN01 airfoil. For this set of test cases, the Δu and $\bar{v}$ velocities will still be taken from the analysis of a GEN03 airfoil. The first calculation has $\bar{u}$ and Δv velocities that were taken from the analysis of a GEN01 airfoil. The second calculation has $\bar{u}$ and Δv velocities that were created using the general airfoil trending equations with a specified thickness ratio corresponding to the GEN01 airfoil. The calculated thicknesses from the two inverse calculations can be seen in Figure 6.37 along with the thickness distribution of the original GEN01 airfoil.

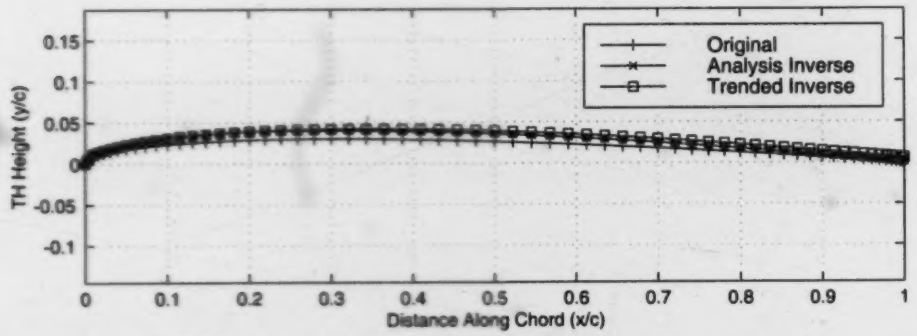

Figure 6.37: Original And Inversely Designed GEN01 Thickness Distributions

The difference between the thickness inversely designed using the analysis $\bar{u}$ and Δv velocities and the original thickness is calculated using Equation 6.1. The maximum percent difference calculated is 1.0%, as seen in Figure 6.38a.

The difference between the thickness designed with the analysis $\bar{u}$ and Δv velocities and the thickness designed with the trended $\bar{u}$ and Δv velocities is calculated with Equation 6.2. The maximum percent difference calculated is 0.6%, as seen in Figure 6.38b.

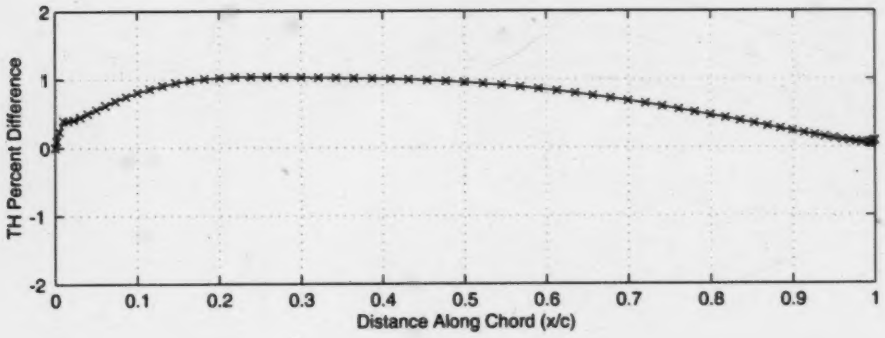

Figure 6.38a: Difference Of Original And Inversely Designed GEN01 Thickness Distributions

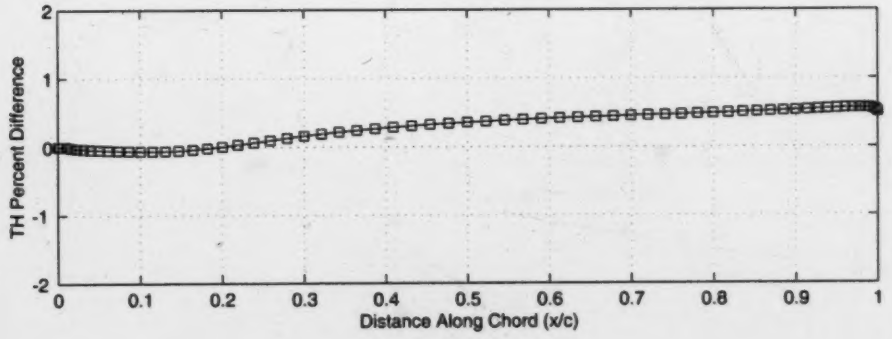

Figure 6.38b: Difference Of Analysis And Trended Inversely Designed GEN01 Thickness Distributions

The calculated camber lines from the two inverse calculations can be seen in Figure 6.39 along with the camber line of the original GEN01 airfoil.

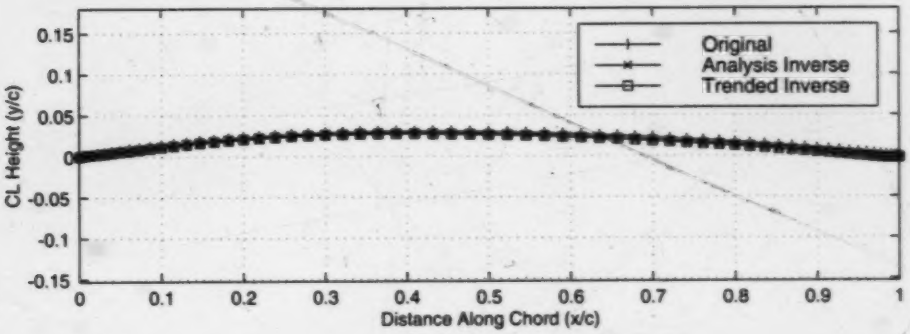

Figure 6.39: Original And Inversely Designed GEN01 Camber Lines

The difference between the camber inversely designed using the analysis $\bar{u}$ and Δv velocities and the original camber is calculated using Equation 6.3. The maximum percent difference calculated is 0.3%, as seen in Figure 6.40a.

The difference between the camber designed with the analysis $\bar{u}$ and Δv velocities and the camber designed with the trended $\bar{u}$ and Δv velocities is calculated with Equation 6.4. The maximum percent difference calculated is less than 0.1%, as seen in Figure 6.40b. These results show that the inverse methods can accurately recreate the GEN01 airfoil, using both the analysis and trended velocities. The results also show that the camber line of the GEN01 is described by the Δu and $\bar{v}$ velocities of the GEN03 airfoil, further proving that Δu and $\bar{v}$ velocities control the camber line and $\bar{u}$ and Δv velocities control the thickness distribution.

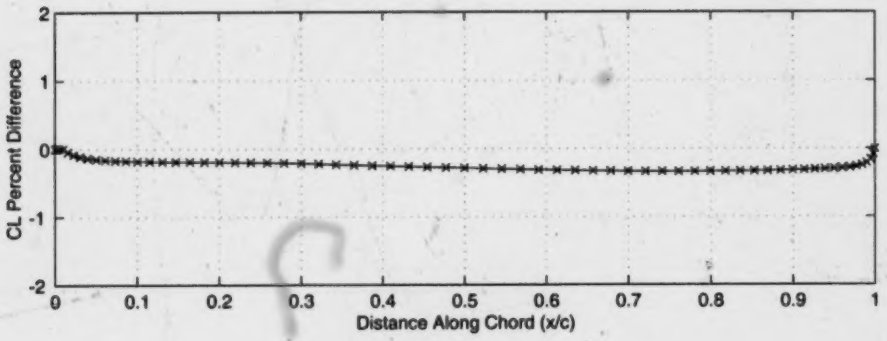

Figure 6.40a: Difference In Original And Inversely Designed GEN01 Camber Lines

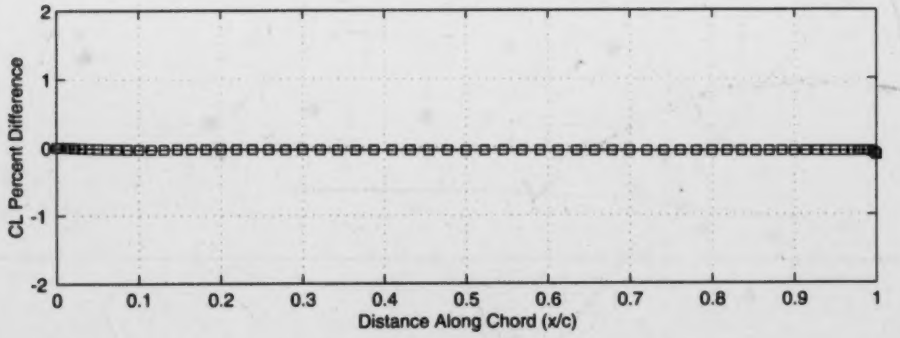

Figure 6.40b: Difference In Analysis And Trended Inversely Designed GEN01 Camber Lines

6.3.3 GEN05 Airfoil

The purpose of the next set of test cases is to inversely design a GEN05 airfoil. For this set of test cases, the Δu and $\bar{v}$ velocities will still be taken from the analysis of a GEN03 airfoil. The first calculation has $\bar{u}$ and Δv velocities that were taken from the analysis of a GEN05 airfoil. The second calculation has $\bar{u}$ and Δv velocities that were created using the General airfoil trending equations with a specified thickness ratio corresponding to the GEN05 airfoil. The calculated thicknesses from the two inverse calculations can be seen in Figure 6.41 along with the thickness distribution of the original GEN05 airfoil.

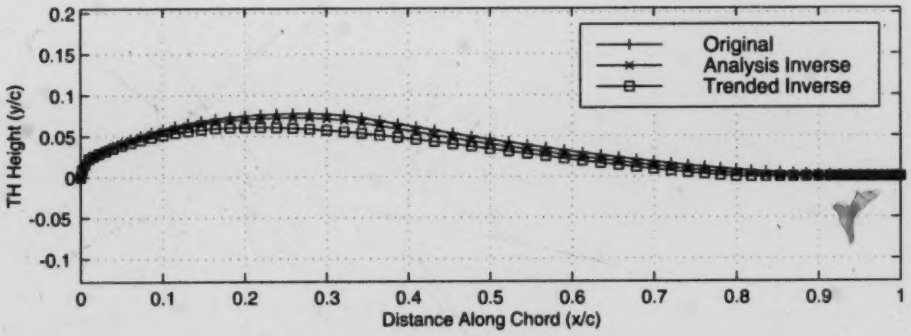

Figure 6.41: Original And Inversely Designed GEN05 Thickness Distributions

The difference between the thickness inversely designed using the analysis $\bar{u}$ and Δv velocities and the original thickness is calculated using Equation 6.1. The maximum percent difference calculated is 0.6%, as seen in Figure 6.42a.

The difference between the thickness designed with the analysis $\bar{u}$ and Δv velocities and the thickness designed with the trended $\bar{u}$ and Δv velocities is calculated with Equation 6.2. The maximum percent difference calculated is 1.4%, as seen in Figure 6.42b.

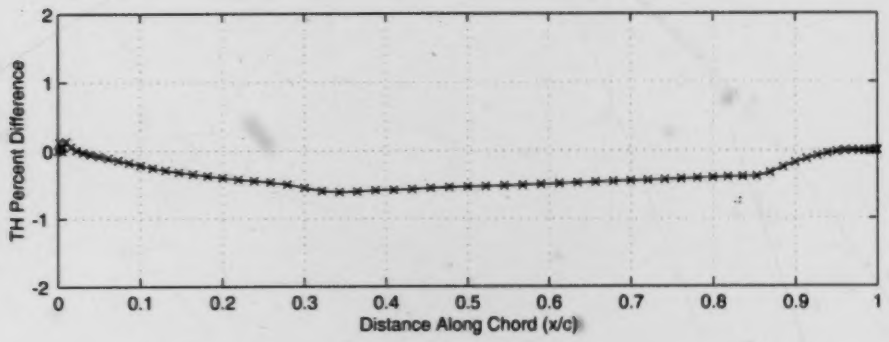

Figure 6.42a: Difference Of Original And Inversely Designed GEN05 Thickness Distributions

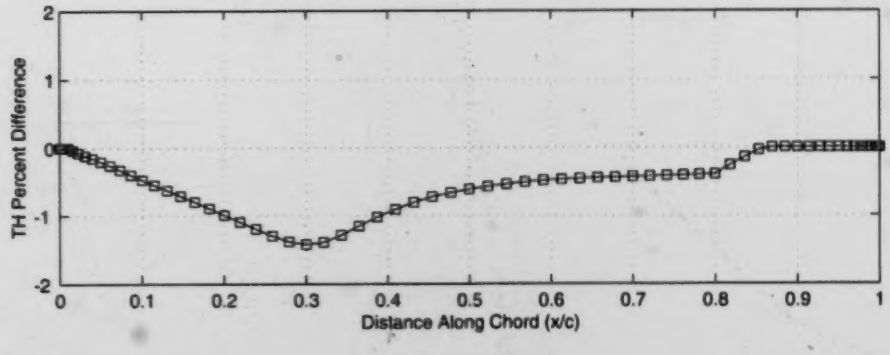

Figure 6.42b: Difference Of Analysis And Trended Inversely Designed GEN05 Thickness Distributions

The calculated camber lines from the two inverse calculations can be seen in Figure 6.43 along with the camber line of the original GEN05 airfoil.

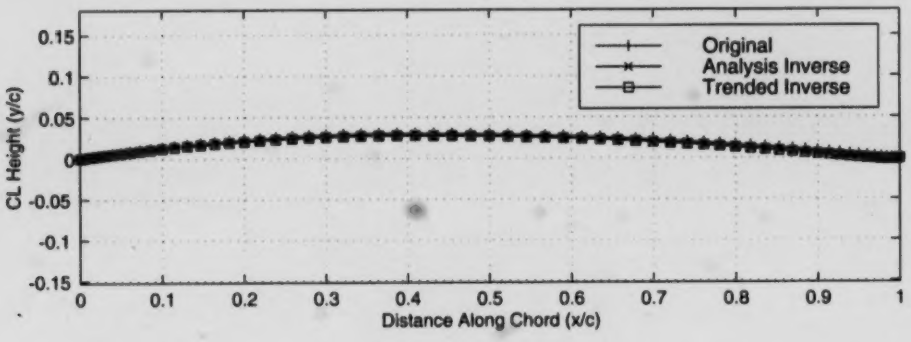

Figure 6.43: Original And Inversely Designed GEN05 Camber Lines

The difference between the camber inversely designed using the analysis $\bar{u}$ and Δv velocities and the original camber is calculated using Equation 6.3. The maximum percent difference calculated is 0.3%, as seen in Figure 6.44a.

The difference between the camber designed with the analysis $\bar{u}$ and Δv velocities and the camber designed with the trended $\bar{u}$ and Δv velocities is calculated with Equation 6.4. The maximum percent difference calculated is 0.1%, as seen in Figure 6.44b.

These six test cases show that the inverse method and trending technique work for airfoils where the shapes of the thickness distributions are vastly different. This group has the largest percent difference in the inverse calculation with analysis velocities at a maximum of 1.0%, still within acceptable limits. This group also has the largest percent difference created by changing from analysis $\bar{u}$ and Δv velocities to trended $\bar{u}$ and Δv velocities. The maximum

difference occurs with the design of the GEN05 airfoil. The GEN05 airfoil also had the largest error, 20%, produced in the trending of the $\bar{u}$ and Δv velocities. The 1.4% difference, while higher than other calculations, is still within acceptable limits. These test results prove that the inverse design methods and trending techniques apply to any shape airfoil, not just the NACA groups. The results also show that the trending technique can be used to describe the $\bar{u}$ and Δv velocities of any group of airfoils, no matter how dissimilar the individual airfoils are.

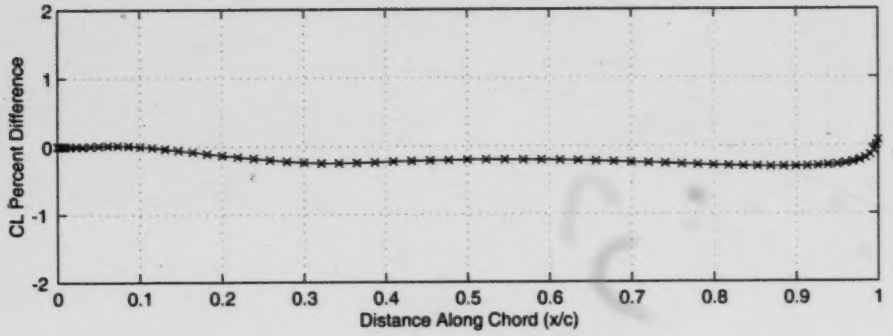

Figure 6.44a: Difference In Original And Inversely Designed GEN05 Camber Lines

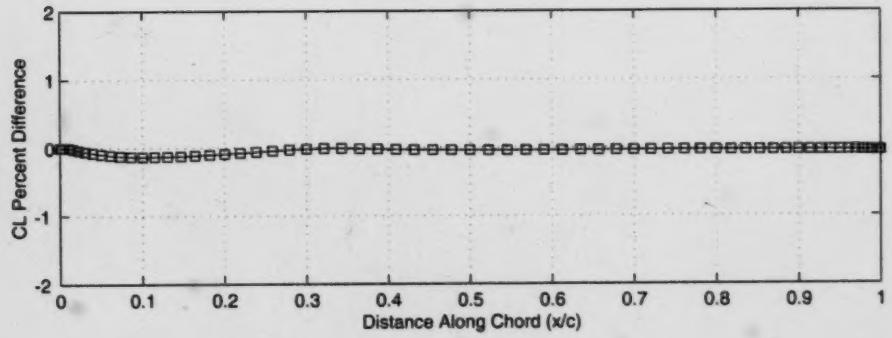

Figure 6.44b: Difference In Analysis And Trended Inversely Designed GEN05 Camber Lines

6.3.4 General Airfoil Design Space

The next step in verifying the accuracy of the inverse design method and trending technique is to use the system of equations created by trending the General airfoil $\bar{u}$ and Δv velocities to design airfoils that were not included in the analysis group. While this test was already completed with both the NACA groups, by repeating it with the General airfoils the validity of the assumptions and the accuracy of the techniques are further assessed. The General airfoil trending used velocities that corresponded to the GEN01, GEN02, GEN03, GEN04 and GEN05 airfoils. For this set of calculations, the $\bar{u}$ and Δv velocities all come from the General airfoil trending but the trending is again used to calculate $\bar{u}$ and Δv velocities corresponding to airfoils with thickness ratios between the GEN01 and GEN03 airfoils. The input $\bar{u}$ and Δv velocities are calculated from the trending equations with values of thickness ratio of 1.5, 2 and 2.5. The ratios are set so that specifying $\tau = 1$ recreates the velocities corresponding to the GEN01 airfoil, $\tau = 2$ recreates velocities corresponding to the GEN02 airfoil and so on. The intermediate values of 1.5 and 2.5 are used to design airfoils that have thickness distributions that exist between the analysis airfoils. The Δu and $\bar{v}$ velocities for all of the calculations are taken from the analysis of a GEN03 airfoil. The inversely designed thickness distributions, as well as the thickness distribution of the original GEN03 airfoil can be seen in Figure 6.45a.

The difference between each of the three designed thickness distributions and the GEN03 airfoil is calculated with Equation 6.5. The calculated difference between each of the designed thickness distributions and the GEN03 thickness distribution can be seen in Figure 6.45b.

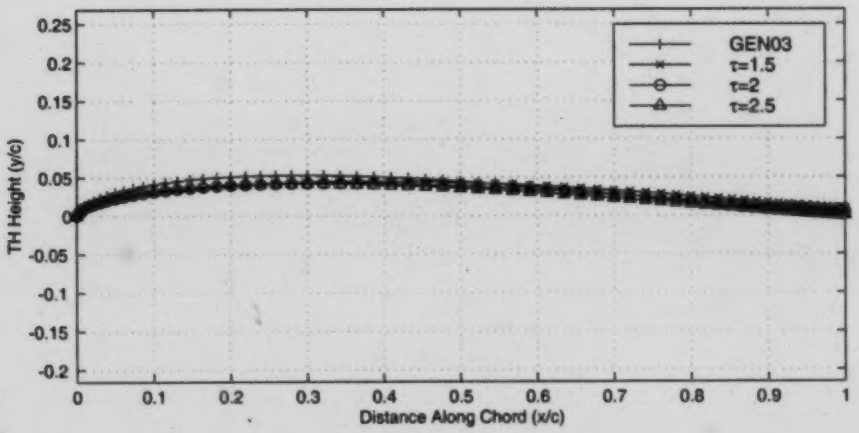

Figure 6.45a: Inversely Designed General Airfoil Thickness Distributions - Decreasing Thickness Specification

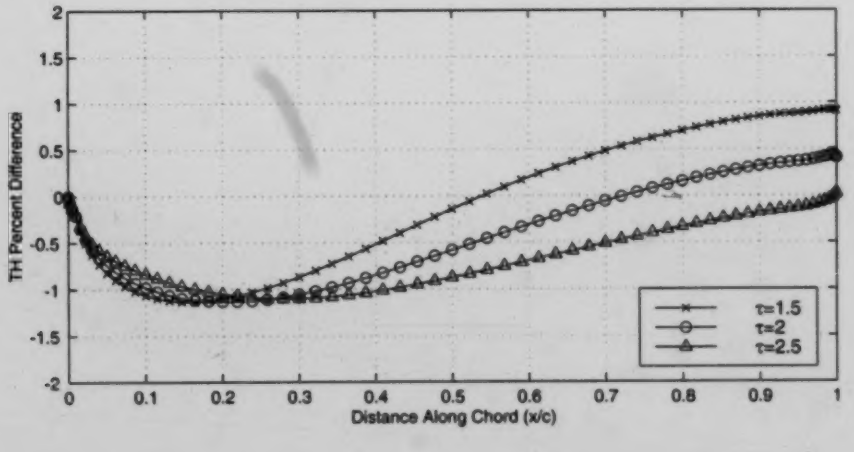

Figure 6.45b: Difference Of Inversely Designed General Airfoil Thickness Distributions - Decreasing Thickness Specification

The percent differences show that the trending specification of decreasing ratios create airfoils that decrease in thickness distribution. As previous design space tests have shown, the relationship between specified thickness and designed thickness is not one-to-one.

The inversely designed camber lines corresponding to the specified thickness ratios, as well as the camber line of the original GEN03 airfoil can be seen in Figure 6.46a. The difference between each of the designed camber lines and the GEN03 camber line is calculated using Equation 6.6. The differences can be seen in Figure 6.46b. The maximum difference between any of the designed camber lines and the original camber line is less than 0.5%. This provides further proof that the accuracy of the inverse method and the camber line assumptions extend from the NACA groups to the General airfoil group.

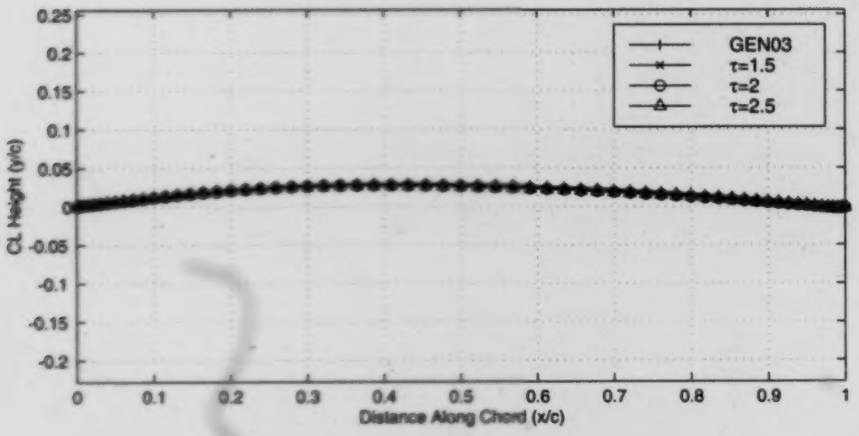

Figure 6.46a: Inversely Designed General Airfoil Camber Lines - Decreasing Thickness Specification

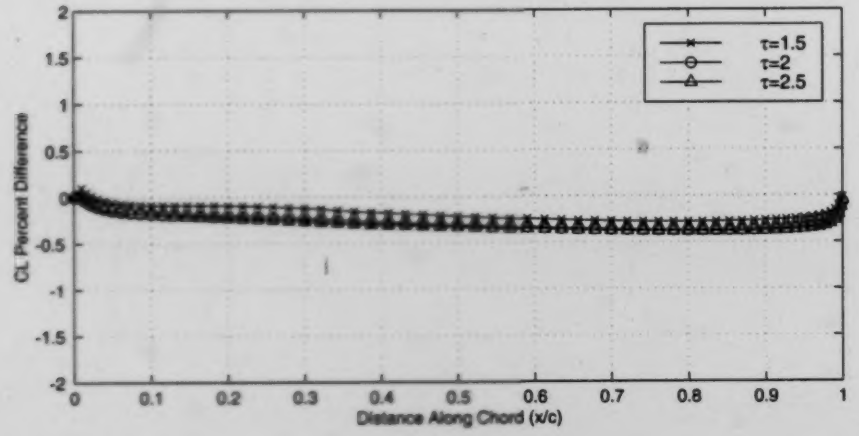

Figure 6.46b: Difference Of Inversely Designed General Airfoil Camber Lines - Decreasing Thickness Specification

The design space test was repeated for thickness distributions with ratios larger than that of the GEN03 airfoil. The three specified thickness ratios used had τ set as 3.5, 4 and 4.5. As with the previous design space test, the General airfoil velocity trending equations were used to create the $\bar{u}$ and Δv velocities. The Δu and $\bar{v}$ velocities for all three calculations were taken from the analysis of a GEN03 airfoil. The designed thickness distributions, as well as the thickness distribution of the original GEN03 airfoil can be seen in Figure 6.47a. The difference between each of the designed thicknesses and the GEN03 thickness was calculated using Equation 6.5. The difference of each of the designed thickness distribution can be seen in Figure 6.47b.

As with the decreasing thickness specification test, the relationship between specified thickness for the trended velocities and the designed thickness distribution is not one-to-one. However, the validity of the trending method is verified by the fact that as the specified thickness was increased, the designed thickness distribution increased as well.

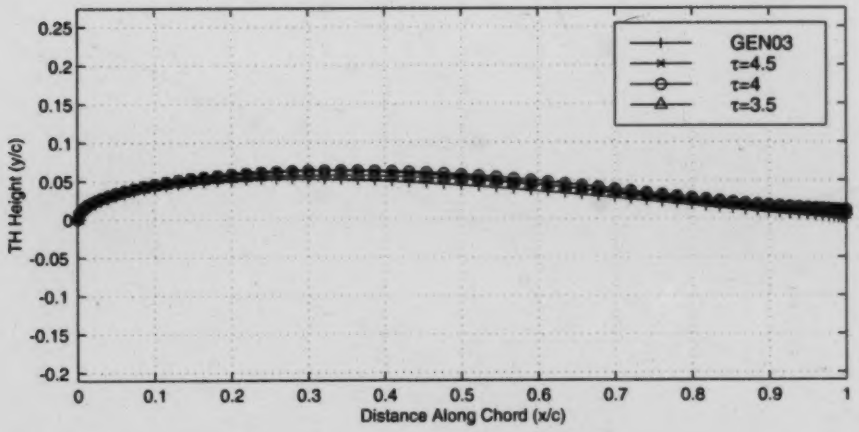

Figure 6.47a: Inversely Designed General Airfoil Thickness Distributions - Increasing Thickness Specification

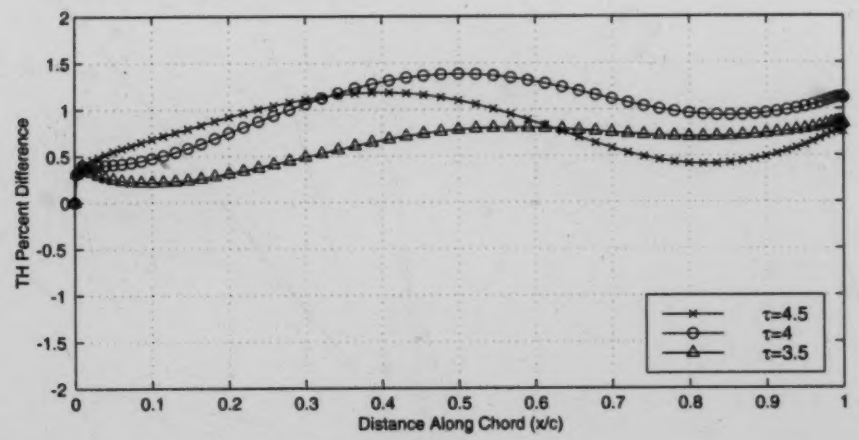

Figure 6.47b: Difference Of Inversely Designed General Airfoil Thickness Distributions - Increasing Thickness Specification

The inversely designed camber lines corresponding to the specified thickness ratios, as well as the camber line of the original GEN03 airfoil can be seen in Figure 6.48a. The difference between each of the designed camber lines and the GEN03 camber line is calculated using Equation 6.6. The differences can be seen in Figure 6.48b. The maximum difference between any of the designed camber lines and the original camber line is less than 0.4%. The designed camber lines provides further proof of the accuracy of the inverse method, and add to the validity of the assumption that the camber line can be described by Δu and $\bar{v}$ velocities alone.

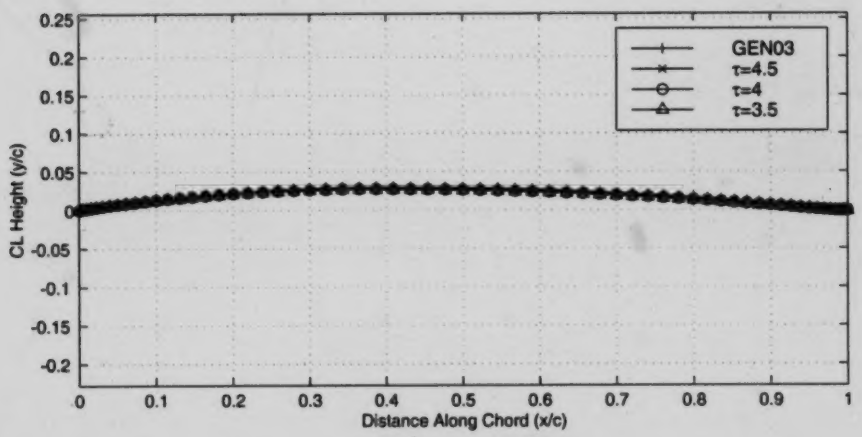

Figure 6.48a: Inversely Designed General Airfoil Camber Lines - Increasing Thickness Specification

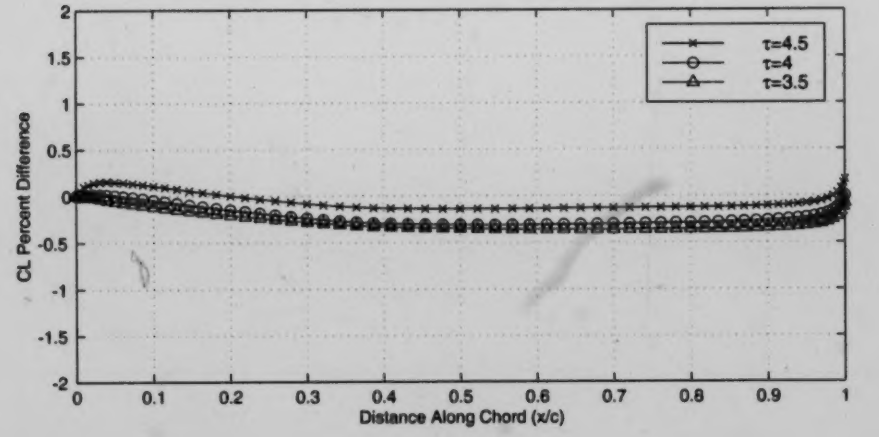

Figure 6.48b: Difference Of Inversely Designed General Airfoil Camber Lines - Increasing Thickness Specification

6.4 Direct Calculation Of Geometry

For this inverse design method, the specified velocities are used in the calculation of the residuals and the geometry is calculated with the flow field. The specified velocities are used in the residual determination, not the geometry calculation because the direct calculation of a geometry from the specified velocities does not guarantee that the thickness distribution and camber line will combine to form a true airfoil. When the input velocities are used to control the potential field, the influence of the true initial geometry is felt as well as the specified velocities. The two influences of the initial geometry and the specified velocities combine to create a more realistic result. Also, by using the specified velocities in the calculation of the residual, the converged flow field guarantees that the continuity condition is met, and therefore the conservation of mass is satisfied.

The purpose of the final test case is to determine the difference between using the specified velocities in the flow field versus directly calculating the geometry. For this test case, a GEN03 airfoil is recreated using the analysis $\bar{u}$, Δu, $\bar{v}$, and Δv velocities. The first calculation is performed with the flow field inverse calculation that has been used previously. The second calculation is performed with the geometry equations described in Section 5.3. The thickness distributions calculated by both of these methods, along with the original GEN03 thickness distribution can be seen in Figure 6.49a.

The difference between each of the designed thickness distributions and the original GEN03 thickness is calculated using Equation 6.5. The differences can be seen in Figure 6.49b.

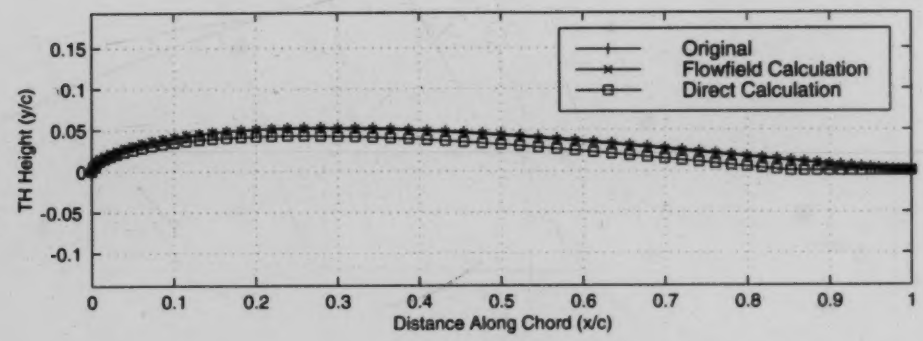

Figure 6.49a: Original And Inversely Designed Thickness Distributions From Two Calculation Methods

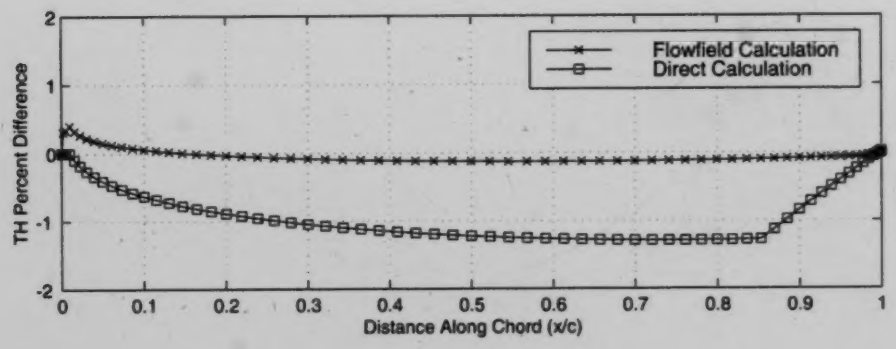

Figure 6.49b: Difference In Original And Inversely Designed Thickness Distributions From Two Calculation Methods

The camber lines calculated by both of the design methods, along with the original GEN03 camber line can be seen in Figure 6.50a. The difference between each of the designed camber lines and the original GEN03 camber line is calculated using Equation 6.6. The differences can be seen in Figure 6.50b.

By calculating the geometry directly, instead of with the flow field formulations, the percent difference in the thickness distributions has increased from 0.4% to 1.3%. The percent difference in the camber lines has increased from 0.3% to 0.7%. The thickness distribution calculated directly from the specified velocities also collapses to zero thickness at approximately 85% chord. This test proves the necessity of using the specified velocities in the calculation of the flow field residual, not the calculation of the geometry.

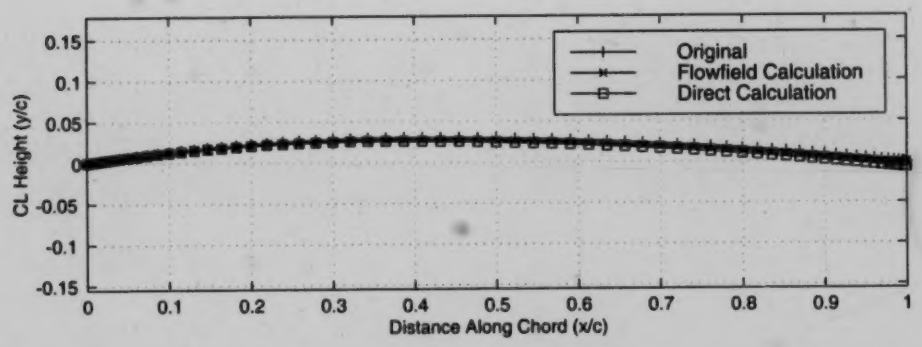

Figure 6.50a: Original And Inversely Designed Camber Lines From Two Calculation Methods

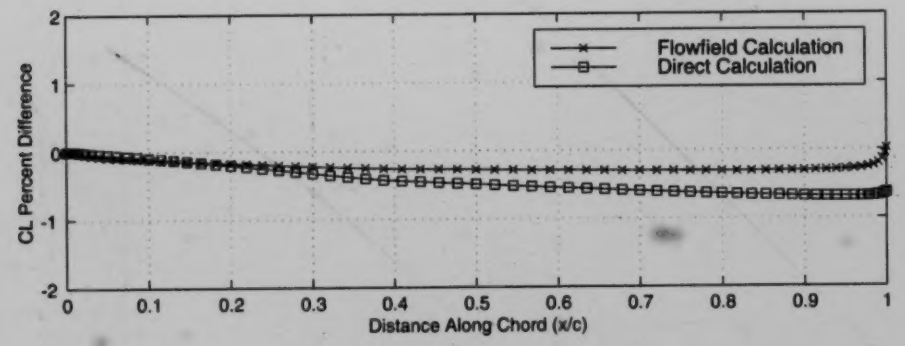

Figure 6.50b: Difference In Original And Inversely Designed Camber Lines From Two Calculation Methods

CHAPTER 7

CONCLUSIONS

Within this work, a numerical scheme has been developed for both the inviscid, incompressible flow analysis of airfoils, and the design of airfoil thickness distributions in inviscid, incompressible flow. An approximately factored LU implicit scheme for the solution of the potential equation has been devised for both the analysis and the design calculations. The algorithm employs a complex-lamellar decomposition to calculate the flow field around an airfoil within an infinite cascade.

After completing a potential flow analysis of a series of airfoils, it was discovered that surface velocities constructed from the potential flow field solution showed a characteristic dependence on changing thickness distributions and camber lines. Specific combinations of surface velocities, namely $\bar{u}$, Δu, $\bar{v}$, and Δv, show a relationship between thickness distribution and camber line. By testing different groups of airfoils, it was discovered that the $\bar{u}$ and Δv velocities changed with changing thickness distribution only, while the Δu and $\bar{v}$ velocities remained relatively constant with a constant camber line. Analysis of four different airfoil groups proved that the surface velocity

dependence occurred for any shape of thickness distribution. Therefore, the design of an airfoils thickness distribution can be controlled by adjusting the $\bar{u}$ and Δv velocities while keeping the Δu and $\bar{v}$ velocities constant.

Knowing that thickness distributions are designed by two specific surface velocity combinations, a method of trending the $\bar{u}$ and Δv velocities for a group of airfoils was developed. Through the use of Bezier curves, a method to mathematically recreate the $\bar{u}$ and Δv velocities from a group of airfoils with various thickness distributions was developed. Through a system of linear equations a Bezier curve allows the recreation of all the analysis velocities through a single control, the thickness ratio of the corresponding airfoil. Since the system of equations describing the Bezier velocities were smooth and continuous, any thickness distribution ratio within the group of airfoils could be specified, and a corresponding set of $\bar{u}$ and Δv velocities could be calculated.

The inverse design method requires the specification of surface velocities in order to calculate an airfoil geometry. The end result of an inverse calculation includes both a designed geometry corresponding to the input velocities and a converged flow field around the designed airfoil. The design method used the specified velocities in the calculation of the flow field residual, not the determination of the geometry. The use of the specified velocities in the residual formulation was to ensure that a realistic airfoil was designed. With the input velocities controlling the potential flux, the influence of a true geometry (the initial condition) was felt. The influences of both the true geometry of the initial condition and the specified surface velocities combine to create an true airfoil.

The accuracy of the inverse method was verified in three steps. First, the surface velocities calculated from the analysis of airfoils were used as input to determine if the inverse design method was able to recreate the original airfoils. Second, the trended $\bar{u}$ and Δv velocities were used to test the accuracy of the trending techniques along with the accuracy of the inverse method. Finally the continuous trending equations were used to determine if a small adjustment in the specified velocities created corresponding changes in the designed airfoil geometries.

The first inverse design calculations used specified velocities from the analysis of an airfoil as input. The designed thickness distribution and camber line was then compared to the thickness and camber of the original airfoil. The design method displayed high accuracy in being able to recreate the airfoil geometries using the analysis velocities. Two other airfoils from the group were recreated using analysis $\bar{u}$ and Δv velocities, but the Δu and $\bar{v}$ velocities remained identical to the velocities used for the first calculation. The accurate recreation of three different thickness distributions from the same group of airfoils proved that $\bar{u}$ and Δv velocities can be used to design the thickness distribution of an airfoil, and that constant Δu and $\bar{v}$ velocities created nearly identical camber lines.

The second step of evaluating the accuracy of the inverse design method included the use of the velocity trending. For this set of test cases, the $\bar{u}$ and Δv velocities were calculated using the trending equations, and the Δu and $\bar{v}$ velocities were kept as the analysis velocities. The thickness distributions and camber lines designed with the trended velocities were compared with the geometries calculated using only analysis velocities. The tests proved the

high accuracy of the trending technique, as the percent difference between the trended velocity designs and the analysis velocity designs remained low.

The third step included the use of the trending equations to interpolate a series of specified $\bar{u}$ and Δv velocities that corresponded to airfoils that were not originally in the analysis group. With these tests it was proven that an increase in the specified thickness ratio used to calculate the trended input velocities corresponded to an increase in the thickness of the designed airfoil. Conversely, a decrease in the thickness ratio used to calculate the trended input velocities corresponded to a decrease in the thickness distribution of the designed airfoil. This series of tests proved the validity of the trending to be used as a design tool. When designing for viscous performance, the thickness distribution of the airfoil limits the practical use of the airfoil. Therefore, the trending technique can be used to gradually adjust the thickness profile of the design while optimizing the viscous characteristics.

The final test case was used to evaluate the appropriateness of the flow field method of specifying the input velocities. In this test, two geometries were calculated using identical input velocities. The first design used the velocities to calculate the potential field residuals, and the potential field to calculate the thickness distribution and camber line. The second design used the velocities directly to calculate a thickness distribution and camber line. This test case proved that the direct geometry calculation does not guarantee a realistic airfoil, while the flow field method displayed high accuracy in recreating the airfoil corresponding to the input velocities. This is because without the influence of a real geometry (the initial condition in the calculation with the flow field) there is not enough control in the specified velocities

alone to ensure a realistic design.

Once the concept of the relationship between the surface velocity components and the geometry components was proven on the 4-digit, 5-digit 16-series, 4-digit-modified and General group of airfoils, the velocity trending was used to prove that any of the analysis velocities could be recreated. The initial test cases proved the accuracy of the inverse design and validity of the trending. After using both analysis velocities and velocities calculated through the trending to recreate the majority of the analysis airfoils, the full capabilities of trending technique were tested. The continuous system of equations from the velocity trending were used so that the geometry of any airfoil within each group could be calculated. Not only could the trending be used to recreate a 10% thick airfoil for instance, it could also be used to calculate any thickness ratio within the specific group.

After completing the test cases with the General airfoil group, it became obvious that the velocities of any set of arbitrarily chosen airfoils could be trended and the geometry of any airfoil within that design space could be calculated. The true advantage of this inverse method and trending technique is that given a finite number of airfoils, a designer can use the trending to define the interior design space encompassed by the entire group of airfoils. Therefore, when trying to benefit from past designs, a designer does not need to choose a single existing airfoil to adapt and redesign, instead the designer can use the influence of a group of existing designs to create a new, improved airfoil. The trending technique allows the designer to create a map of existing useful designs and then determine a new airfoil geometry based on past successes.

BIBLIOGRAPHY

[1] Abbott, I.H. and von Doenhoff, A.E., *Theory of Wing Sections*. Dover Publications, New York, USA, 1959

[2] von Mises, R., *Theory Of Flight*. Dover Publications, New York, USA, 1959

[3] Thwaites, B., *Incompressible Aerodynamics*. Dover Publications, New York, USA, 1960

[4] Abbott, I.H., von Doenhoff, A.E., and Stivers, L.S., "Summary of Airfoil Data," NACA Report No. 824, 1945

[5] Kennedy, J.l., and Marsden, D.J., "Potential Flow Velocity Distributions On Multi-Component Airfoil Sections," *Canadian Aeronautics and Space Journal*, Vol. 22, No. 5, Sept./Oct. 1976, pp. 243-56

[6] Hess, J.L., "Panel Methods In Computational Fluid Dynamics," *Annual Review of Fluid Mechanics*, Vol. 22, 1990, pp. 255-74

[7] Drela, M, and Giles, M.B., "Viscous-Inviscid Analysis of Transonic and Low Reynolds Number Airfoils," *AIAA Journal*, Vol. 25, No. 10, Oct. 1987, pp. 1347-55

[8] Bonataki, E., Chaviaropoulos, P., and Papailiou, K.D., "An Inverse Inviscid Method for the Design of Quasi-Three-Dimensional Turbomachinery Cascades," *Journal of Fluids Engineering*, Vol. 115, Mar. 1993, pp. 121-7

[9] Giles, M.B., and Drela, M., "Two-dimensional Transonic Aerodynamic Design Method," *AIAA Journal*, Vol. 25, No. 9, Sept. 1987, pp. 1199-206

[10] Selig, M.S., and Maughmer, M.D., "Multipoint Inverse Airfoil Design Method Based on Conformal Mapping", *AIAA Journal*, Vol. 30, No. 5, May 1992, pp. 1162-70

[11] Carlson, L.A., "Transonic Airfoil Analysis and Design Using Cartesian Coordinates," *Journal of Aircraft*, Vol. 13, No. 5, May 1976, pp. 349-56

[12] Liebeck, R.H., "Design of Subsonic Airfoils for High Lift," *Journal of Aircraft*, Vol. 15, No. 9, Sept. 1978, pp.547-61

[13] Obayashi, S., Jeong, S., and Matsuo, Y., "New Blunt Trailing-Edge Airfoil Design by Inverse Optimization Method," *Journal of Aircraft*, Vol. 34, No. 2, Mar./Apr. 1997, pp. 255-7

[14] Gopalarathnam, A. and Selig, M.S., "Multipoint Inverse Method for Multielement Airfoil Design," *Journal of Aircraft*, Vol. 35, No. 3, May-June 1998, pp.398-404

[15] Dang, T.Q., "Design of Turbomachinery Blading in Transonic Flows by the Circulation Method," *Journal of Turbomachinery*, Vol. 114, Jan. 1992, pp. 141-6

[16] Dang, T.Q., "Inverse Method for Turbomachine Blades Using Shock-Capturing Techniques," AIAA Paper No. 95-2465, 1995

[17] Eppler, R., *Airfoil Design And Data*. Springer-Verlag, Berlin, Germany, 1990

[18] Scholz, N., and Klein, A., *Aerodynamics of Cascades*, Advisory Group for Aerospace Research and Development, North Atlantic Treaty Organization, Neuilly sur Seine, France, 1977.

[19] Batchelor, G.K., *An Introduction To Fluid Dynamics*, Cambridge University Press, Cambridge, United Kingdom, 1999

[20] Mattingly, J.D., *Elements of Gas Turbine Propulsion*, McGraw-Hill, New York, USA, 1996

[21] Milne-Thomson, L.M., *Theoretical Aerodynamics*, Dover Publications, New York, USA, 1966

[22] Ladson, C.L., Brooks, C.W., Hill, A.S. and Sproles, D.W., "Computer Program To Obtain Ordinates for NACA Airfoils", NASA Technical Memorandum 4741, 1996

[23] Lakshminarayana, B., *Fluid Dynamics and Heat Transfer of Turbomachinery*, John Wiley & Sons, New York, USA, 1996

[24] Private Communication

[25] Strand, T., "Exact Method Of Designing Airfoils With Given Velocity Distribution In Incompressible Flow," *Journal Of Aircraft*, Vol. 10, No. 11, Nov. 1973, pp. 651-659

[26] Ferziger, J.H., and Perić, M., *Computational Methods for Fluid Dynamics*. Springer-Verlag, Berlin, Germany, 1996

[27] Yokota, J.W., *An LU Implicit Multigrid Algorithm to Solve the Euler Equations for Transonic Flow in Rotating Turbomachinery Passages*. PhD Thesis, Cornell University, 1987

[28] Hirsch, C., *Numerical Computation of Internal and External Flows, Vol. 2*. John Wiley & Sons, West Sussex, England, 1990

[29] Mortenson, M.E., *Geometric Modeling (Second Edition)*, John Wiley & Sons, New York, USA, 1997